UNIVERSITAT POLITÈCNICA DE CATALUNYA BARCELONATECH

Research on fluidic oscillators under incompressible and compressible flow conditions

Masoud Baghaei

Research on fluidic oscillators under incompressible and compressible flow conditions

Masoud Baghaei

Supervisor : Dr.Josep Maria Bergadà Granyó

Fluid Mechanics Department, Universitat Politècnica de Catalunya, 08222, colon 7-11, Terrassa, Barcelona, Spain

Universitat Politècnica de Catalunya

A thesis submitted for the degree of

Doctor by the UPC

2020

Contents

1 Introduction. 1

1.1 Introduction . . . 1

1.1.1 Introduction for flow control . . . 1

1.1.2 Fluidic oscillators . . . 2

1.1.3 Fluidic oscillators applications . . . 5

1.1.4 State of the art . . . 9

1.1.5 Main objectives . . . 13

2 Forces driving the oscillations in 3D fluidic oscillators. 15

2.1 Introduction . . . 15

2.2 Fluidic Oscillator Main Characteristics and Model Validation . . . 19

2.3 Parameters Used to Non-Dimensionalize the Results . . . 27

2.4 Results . . . 28

2.4.1 Original Fluidic Oscillator at Reynolds Number 16,034 . . . 28

2.4.2 Variation of the Fluidic Oscillator Momentum with the Reynolds Number . . . 39

2.5 Conclusions . . . 43

3 The effect of some design modifications. 45

3.1 Introduction . . . 45

3.2 Fluidic Oscillator main characteristics . . . 47

3.3 Geometry modifications considered . . . 50

3.4 Momentum acting on the jet entering the mixing chamber . . . 51

3.5 Results . . . 52

3.5.1 Modifying the (MC) inlet width . . . 52

3.5.2 Modifying (MC) outlet width . . . 60

3.5.3 Modifying the (MC) outlet angle . . . 67

3.5.4 Modifying the (MC) inlet angle . . . 73

3.5.5 Relation Reynolds frequency for all dimensional modifications performed . . . 78
3.5.6 Stagnation pressure at the (MC) converging walls and net momentum acting on the (MC) incoming jet as a function of the Reynolds number. . . . 80
3.6 Conclusions . . . 86

4 Feedback channel effect under compressible flow conditions. 88
4.1 Introduction . . . 88
4.2 Fluidic oscillator test of independence and cases studied . . . 90
4.3 Non-dimensional parameters . . . 93
4.4 Results . . . 94
4.4.1 Baseline case at two different inlet velocities . . . 94
4.4.2 The effect of the feedback channel length . . . 102
4.5 Conclusions . . . 112

5 Thesis conclusions. 118
5.1 Conclusions . . . 118
5.2 Future work . . . 120

Bibliography 128

Appendices 129

Appendix A Published journal papers 130

Appendix B Published conference papers 131

List of Figures

1.1 Schematic design of feedback-free fluidic oscillators (vortex oscillators) [1]. . . . 3
1.2 Traditional designs of fluidic Oscillator [1]. . . . 3
1.3 Schematic drawing of asymmetric monostable and symmetric bistable oscillators [1]. . . . 4
1.4 Sweeping jet fluidic oscillator [1]. . . . 5
1.5 Oscillator feedback channels diameter, length and jet impingement angle [1]. . . . 5
1.6 Mixing chamber entrance-exit diameter, feedback channel entrance and wedge angle [1]. . . . 5
1.7 Active flow control (sweeping jet) actuators on a Boeing 757 tail [2]. . 7
1.8 (**a**) Terminology of the fluidic oscillator, (**b**) Visualisation of the vertical stabilizer left: without AFC; right: with AFC [3]. . . . 7
1.9 Schematic view of wind turbine performance improvement using vortex generators [4]. . . . 8
1.10 Flow separation over an airfoil with varying angle of attack [5]. . . . 8
1.11 Experimental study of cavity noise reduction using sweeping jet actuator [6] 9
1.12 Sketch of a compact array of fluidic oscillator and integration into airfoil sections [7]. . . . 9
1.13 (**a**) Schematic of the oscillator, (**b**) Isosurface of nondimensional Q with streamwise velocity contours obtained from 3-D IDDES [8]. . . . 11
1.14 (**a**) Schematic of the fluidic oscillator, (**b**) Flow field inside the fluidic oscillator [9]. . . . 11
1.15 (**a**) A simple schematic of the experimental setup, (**b**) Comparison of calculated and measured oscillation frequencies of the fluidic diverter versus Mach number [10]. . . . 12

1.16 (**a**) Fluidic oscillator geometric parameters, (**b**) Jet oscillation frequency for varying feedback channel height for different mass flow rates [11]. 13

2.1 Fluidic oscillator general view and its different parts, (**a**) original fluidic oscillator, (**b**) fluidic oscillator with buffer zone, (**c**) fluidic oscillator main parts. Flattered pipe, 1; mixing chamber (MC), 2; feedback channels (FC), 3; external chamber (EC), 4; buffer zone (BZ), 5. . . . 19
2.2 Grid used in the present study, (**a**) plane view, (**b**) zoom view, (**c**) side view of the mesh at the center of the mixing chamber, see the vertical line. 22
2.3 (**a**) Comparison of experimental and computational fluid dynamics (CFD) results, (**b**) FFT of the different Reynolds numbers studied. . 23
2.4 Mixing chamber period of oscillation divided in six equally spaced times, Reynolds number 16,034. Figures a, b, c, g, h and i, present the streamlines plots, figures d, e, f, j, k and l, introduce the pressure contours. 31
2.5 Mass flow through the oscillator upper and lower outlets, (**a**); mass flow through the feedback channels, (**b**); mixing chamber inlet jet inclination angle, (**c**); and mixing chamber outlet jet inclination angle, (**d**). Reynolds number 16,034. 32
2.6 Mixing chamber outlet converging walls pressure, (**a**); pressure at both feedback channels outlets, (**b**); and pressure at the feedback channel inlet and outlet, (**c**). Overall momentum at the feedback channels outlet, which is acting on the jet entering the mixing chamber. The momentum is split in the component due to the mass flow flowing along the feedback channels and due to the pressure acting onto the feedback channels outlet (**d**). Reynolds number 16,034. 34
2.7 (**a**) Mixing chamber volume growth at three different Reynolds numbers, 8711, 16,034, and 32,068. Comparison with the fluid volume provided by the FC. (**b**) Zoomed view of the mixing chamber inlet, where it is seen that part of the incoming fluid helps the mixing chamber bubble to grow. 37
2.8 Instantaneous velocity fields at the, (**a**) mixing chamber, (**b**) spanwise section, slice (1), (**c**) spanwise section at the fluidic oscillator outlet, slice (2). Reynolds number 16,034. 38

2.9 Q criterion at the mixing chamber period of oscillation divided into six equally spaced times, Reynolds number 16,034. 39
2.10 Net momentum pressure and mass flow terms for different Reynolds numbers. 40
2.11 Fluidic oscillator net momentum frequency (FFT) and amplitude for different Reynolds numbers studied. 41
2.12 Comparison of the stagnation pressure at the mixing chamber lower converging surface, the total momentum acting on the jet, the mixing chamber inlet oscillation angle, and the oscillator output mass flow. Reynolds numbers, 8711 (**a**), 16,034 (**b**), 32,068 (**c**). 43

3.1 Fluidic oscillator mixing chamber internal dimensions modifications. . 48
3.2 Grid used in the present study, (a) plane view, (b) zoom view, (c) side view of the mesh at the center of the mixing chamber, see the vertical line. 48
3.3 Fluidic oscillator output mass flow frequency and peak to peak amplitude as a function of the mixing chamber inlet width and for three different Reynolds numbers, 8711, 16034 and 32068. 53
3.4 Fluidic oscillator internal velocity field (a, b), and pressure magnitude (c, d). Maximum inlet width (a, c), minimum inlet width (b, d). Reynolds number 16034. 54
3.5 Q criterion at the mixing chamber period of oscillation divided into six equally spaced times, Reynolds number 16,034. Maximum inlet width. 55
3.6 Q criterion at the mixing chamber period of oscillation divided into six equally spaced times, Reynolds number 16,034. Minimum inlet width. 55
3.7 Dynamic effects of the (MC) inlet width modification on the main flow parameters, Reynolds number 16034. Each graph presents three non-dimensional curves characterizing results from the baseline, the lowest inlet width and the highest inlet width cases, and as a function of the dimensional time. In figure (a) the mass flow across the upper oscillator outlet is presented. Figure (b) introduces the temporal variation of the (MC) inlet inclination angle. Figure (c) presents the pressure at the (MC) lower inclined wall. The net momentum acting on the lateral sides of the main jet is presented in figure (d). Figure (e) characterizes the mass flow at the lower feedback channel outlet. 58

3.8 Comparison of the pressure and mass flow terms of the net-momentum and for three characteristic inlet widths, Reynolds number 16034. . . 59
3.9 Fluidic oscillator output mass flow frequency and peak to peak amplitude as a function of the mixing chamber outlet width and for three different Reynolds numbers, 8711, 16034 and 32068. 61
3.10 Fluidic oscillator internal velocity field (a, b) and pressure magnitude (c, d). Maximum outlet width (a, c), minimum outlet width (b, d). Reynolds number 16034. 62
3.11 Q criterion at the mixing chamber period of oscillation divided into six equally spaced times, Reynolds number 16,034. Maximum outlet width. 63
3.12 Q criterion at the mixing chamber period of oscillation divided into six equally spaced times, Reynolds number 16,034. Minimum outlet width. 63
3.13 Dynamic effects of the (MC) outlet width modification on the main flow parameters, Reynolds number 16034. Each graph presents three non-dimensional curves characterizing results from the baseline, the lowest and highest outlet width cases, and as a function of the dimensional time. In figure (a) the mass flow across the upper oscillator outlet is presented. Figure (b) introduces the temporal variation of the (MC) inlet inclination angle. Figures (c) presents the pressure at the (MC) lower inclined wall. The net momentum acting on the lateral sides of the main jet is presented in figure (d). Figure (e) characterizes the mass flow at the lower feedback channel outlet. 65
3.14 Comparison of the pressure and mass flow terms of the net-momentum and for three characteristic outlet widths, Reynolds number 16034. . . 66
3.15 Frequency and amplitude of the (FO) outlet dynamic mass flow, as a function of the mixing chamber outlet angle and for three different Reynolds numbers, 8711, 16034 and 32068. 68
3.16 Fluidic oscillator internal velocity field (a, b) and pressure magnitude (c, d). Maximum outlet angle (a, c), minimum outlet angle (b, d). Reynolds number 16034. 70
3.17 Q criterion at the mixing chamber period of oscillation divided into six equally spaced times, Reynolds number 16,034. Maximum outlet angle. 70
3.18 Q criterion at the mixing chamber period of oscillation divided into six equally spaced times, Reynolds number 16,034. Minimum outlet angle. 71

3.19 Dynamic effects of the (MC) outlet angle modification on the main flow parameters, Reynolds number 16034. Each graph presents three non-dimensional curves characterizing results from the baseline, the lowest and highest outlet angle cases, and as a function of the dimensional time. In figure (a) the mass flow across the upper oscillator outlet is presented. Figure (b) introduces the temporal variation of the (MC) inlet inclination angle. Figures (c) presents the pressure at the (MC) lower inclined wall. The net momentum acting on the lateral sides of the main jet is presented in figure (d). Figure (e) characterizes the mass flow at the lower feedback channel outlet. 72
3.20 Comparison of the pressure and mass flow terms of the net-momentum and for three characteristic outlet angles, Reynolds number 16034. . . 73
3.21 Fluidic oscillator output mass flow Frequency and amplitude as a function of the mixing chamber inlet angle and for three different Reynolds numbers, 8711, 16034 and 32068. 74
3.22 Fluidic oscillator internal velocity field (a, b) and pressure magnitude (c, d). Maximum inlet angle (a, c), minimum inlet angle (b, d). Reynolds number 16034. 75
3.23 Q criterion at the mixing chamber period of oscillation divided into six equally spaced times, Reynolds number 16,034. Maximum inlet angle. 76
3.24 Q criterion at the mixing chamber period of oscillation divided into six equally spaced times, Reynolds number 16,034. Medium inlet angle. . 76
3.25 Dynamic effects of the (MC) inlet angle modification on the main flow parameters, Reynolds number 16034. Each graph presents three non-dimensional curves characterizing results from the baseline, the medium and highest inlet angle cases, and as a function of the dimensional time. In figure (a) the mass flow across the upper oscillator outlet is presented. Figure (b) introduces the temporal variation of the (MC) inlet inclination angle. Figures (c) presents the pressure at the (MC) lower inclined wall. The net momentum acting on the lateral sides of the main jet is presented in figure (d). Figure (e) characterizes the mass flow at the lower feedback channel outlet. 77
3.26 Comparison of the pressure and mass flow terms of the net-momentum and for three characteristic inlet angles, Reynolds number 16034. . . . 78
3.27 Relation Reynolds number versus mass flow output frequency, for all dimensional modifications studied. 79

3.28 Net momentum acting on the fluidic oscillator inlet jet and for two different mixing chamber inlet widths, two different Reynolds numbers, 16034 and 32068, were considered. 86

4.1 (a) Fluidic oscillator mesh, main view; (b) mixing chamber computational domain; (c) mesh side view; (d) fluidic oscillator output frequency for the three meshes studied; (e) mixing chamber main zones. 92

4.2 Baseline case fluidic oscillator with the different feedback channel lengths studied. (a) Original feedback channel length L; (b) feedback channel length 2L; (c) feedback channel length 3L; (d) feedback channel length 9L. 92

4.3 Q criterion at the mixing chamber period of oscillation divided into six equally spaced times, power nozzle velocity 65m/s. Baseline case. . . 95

4.4 Q criterion at the mixing chamber period of oscillation divided into six equally spaced times, power nozzle velocity 97m/s. Baseline case. . . 96

4.5 Mixing chamber instant velocity field (a), pressure distribution (b), density (c), temperature (d) and (e) Q criterion fields. Power nozzle velocity 65m/s. Baseline case. 97

4.6 Mixing chamber instant velocity field (a), pressure distribution (b), density (c), temperature (d) and (e) Q criterion fields. Power nozzle velocity 97m/s. Baseline case. 98

4.7 Mixing chamber instant velocity field (a), pressure distribution (b), density (c), temperature (d). Power nozzle velocity 65m/s.feedback channel length L2. 99

4.8 Mixing chamber instant velocity field (a), pressure distribution (b), density (c), temperature (d). Power nozzle velocity 97m/s.feedback channel length L2. 99

4.9 Mixing chamber instant velocity field (a), pressure distribution (b), density (c), temperature (d). Power nozzle velocity 65m/s.feedback channel length L3. 100

4.10 Mixing chamber instant velocity field (a), pressure distribution (b), density (c), temperature (d). Power nozzle velocity 97m/s.feedback channel length L3. 101

4.11 Non dimensional pressure at the mixing chamber lower converging wall, oscillator mass flow, feedback channels mass flow and total net momentum applied to the incoming jet from both feedback channel outlets. (a) (b) Baseline case. (c) (d) Feedback channels length 2L . (a) (c) Power nozzle velocity 65m/s. (b) (d) Power nozzle velocity 97m/s. . . 102
4.12 Non dimensional pressure at the mixing chamber lower converging wall, oscillator mass flow, feedback channels mass flow and total net momentum applied to the incoming jet from both feedback channel outlets. (a) (b) Feedback channels length 3L. (c) (d) Feedback channels length 9L. (a) (c) Power nozzle velocity 65m/s. (b) (d Power nozzle velocity 97m/s. 103
4.13 Fluidic oscillator outlet mass flow as a function of the different feedback channels length. (a) Power nozzle velocity 65m/s. (b) Power nozzle velocity 97m/s. 104
4.14 Feedback channel outlet mass flow as a function of the different feedback channels length. (a) Power nozzle velocity 65m/s. (b) Power nozzle velocity 97m/s. 105
4.15 Feedback channel outlet pressure as a function of the different feedback channels length. (a) Power nozzle velocity 65m/s. (b) Power nozzle velocity 97m/s. 105
4.16 Fluidic oscillator outlet mass flow frequency (FFT) and amplitude for different feedback channel lengths. Power nozzle velocity 65m/s. . . . 107
4.17 Fluidic oscillator outlet mass flow frequency (FFT) and amplitude for different feedback channel lengths. Power nozzle velocity 97m/s. . . . 108
4.18 Net momentum applied to the jet entering the mixing chamber as a function of the different feedback channels length. (a) Power nozzle velocity 65m/s. (b) Power nozzle velocity 97m/s. 110
4.19 Comparison of the net momentum pressure term with the mass flow term, for the baseline case L1, and for the maximum (FC) length L9. (a) Power nozzle velocity 65m/s. (b) Power nozzle velocity 97m/s. . . 110
4.20 Fluidic oscillator net momentum frequency (FFT) and amplitude for different feedback channel lengths. Power nozzle velocity 65m/s. . . . 114
4.21 Fluidic oscillator net momentum frequency (FFT) and amplitude for different feedback channel lengths. Power nozzle velocity 97m/s. . . . 114
4.22 Mixing chamber instant density and temperature fields. Power nozzle velocity 65m/s, feedback channel length L9. 115

4.23 Mixing chamber instant density and temperature fields. Power nozzle velocity 97m/s, feedback channel length L9. 116

List of Tables

2.1 Main characteristic parameters of the initial simulations done in 3D using DDES turbulent model. 21

3.1 Comparison experimental and simulated results. 49
3.2 List of the different geometry ratios evaluated. 51
3.3 Equations characterizing the evolution of non dimensional average pressure at the (MC) outlet converging walls, and as a function of the Reynolds number. These equations are valid in the range 8711 < Re < 32068. The coefficient of determination was $(R)^2 = 1$ for all curves presented. 81
3.4 Equations characterizing the evolution of non-dimensional average net momentum acting on the jet entering the (MC), and as a function of the Reynolds number. These equations are valid in the range 8711 < Re < 32068. The coefficient of determination was $(R)^2 = 1$ for all curves presented. 82
3.5 Equations characterizing the evolution of non-dimensional peak to peak stagnation pressure amplitude at the (MC) outlet converging walls, and as a function of the Reynolds number. These equations are valid in the range 8711 < Re < 32068. 83
3.6 Equations characterizing the evolution of non-dimensional peak to peak net momentum amplitude at the (MC) incoming jet, and as a function of the Reynolds number. These equations are valid in the range 8711 < Re < 32068. 84
3.7 Evaluation of the peak to peak net momentum amplitude at the (MC) incoming jet due to the pressure term, divided by the net momentum amplitude due to the (FC) mass flow term, and for the three Reynolds numbers studied. 85

4.1 Fluidic Oscillator output mass flow frequency and peak to peak amplitude as a function of the power nozzle velocity and the feedback channel length. 109
4.2 Frequencies obtained from the net-momentum signals measured at the feedback channels outlets.The two power nozzle velocities 65m/s and 97m/s and all feedback channels lengths are evaluated. 112
4.3 Maximum and minimum values of the velocity, pressure, density and temperature variables inside the mixing chamber. Both power nozzle velocities and the four feedback channel lengths are considered. . . . 113

Chapter 1

Introduction.

1.1 Introduction

1.1.1 Introduction for flow control

Over the past decades, many flow control devices have been developed and also implemented in a wide variety of applications [1–11]. Flow control devices can be categorized into two groups, passive and active. Passive control devices always consist of geometrical modifications, such as chevrons on the exhaust nozzle of an aircraft to reduce noise or vortex generators on an aircraft's wing to reduce drag and increase lift. Passive flow control devices are always at work because of changes in geometry and cannot be turned on or off. This is a big disadvantage for passive flow control devices. On the other hand, active flow control involves adding energy and momentum to the flow in a regulated manner. Active flow control is preferable to passive flow control because it can be turned on and off as needed but its reliability and cost is a problem in some applications. Most of the research has been carried out on passive control devices, while there is not enough information on active control devices. Actuators are at the center of active flow control devices and have many benefits such as no moving parts, high durability, rapid response, capable of generating high amplitudes and frequencies, energy efficiency and scalability.

Flow control actuators and their performance should be examined in real applications to assure their reliability, ease of use and high lifetime. There are many types of actuators such as ZNMF (zero net mass flux), plasma actuators, MEMS (Micro-Electro-Mechanical Systems), fluidic oscillators and combustion driven jet actuators [12, 13]. Among them only plasma, combustion and fluidic actuators have no moving parts, so they are expected to have higher reliability compared to other actuators. Pulse combustion actuators provide high momentum but can be used in some specific

applications due to the high temperature associated. Plasma actuators are not able to create high momentum to modify the boundary layer in real applications. On the other hand fluidic oscillators can produce the required momentum by creating pulsating jets but their geometry and design needs to be adapted for each specific application. MEMS actuators are used widely especially in the microfluidics field when a small amount of flow is required [14, 15]. They can also be used in flow measurement applications, including semiconductor manufacturing processes, chemical processes, medical devices, natural gas metering, etc. ZNMF actuators provide enough momentum to modify the flow boundary layer but their reliability can be compromised due to their moving parts. Relevant papers about the development and applications of ZNMF actuators are from references [16–20]. Most devices used in the flow control field demonstrate high degrees of flow control in experiments and laboratories but their use in real applications can be challenging. The use of moving parts, high operating temperatures and voltages, and using electronics in them can decrease the chance of integrating them into actual applications. These devices must be able to operate in harsh environments, rain, snow, dust, high noise, high vibrations, a wide range of temperatures and material stresses and also be easy to maintain. Another challenge is finding housing for electrical and electronic systems, air supply systems if the actuator uses air and protection from electromagnetic interferences. Therefore the actuator and its components should be small and simple and easily integrated into different applications. The design of fluidic actuators goes back to 50s and 60s and many designs have not changed for over 40 years. These actuators can produce frequencies ranging from several Hz to KHz at different flow rates.

1.1.2 Fluidic oscillators

The most interesting feature of fluidic oscillators is that they produce periodically oscillating pulsating jets without having any moving mechanical parts. This capability makes fluidic oscillators more robust and reliable and means that they are not sensitive to electromagnetic interferences. A fluidic oscillator produces a continuous oscillating jet when pressurized with fluid and generally consists of one supply port, two exit ports and two feedback control ports. They can be categorized into three main designs. One of the designs of fluidic oscillators is feedback-free fluidic oscillators (vortex oscillators), as shown in figure 1.1. This design consist of two inlet power nozzles, an interaction chamber and one exit port. Jet interaction in the interaction chamber lead to self-sustained oscillation of the exiting jet at the outlet. In this oscillator design, two interaction jets from the inlet nozzles create an unsteady shear

layer by collision, and this shear layer is driven by two counter- rotating side vortices and the creation of vortices leads to oscillating behavior. The traditional way of producing oscillation is by using feedback channels in the design. Other two designs of oscillators consist of feedback channels which are control loaded fluidic oscillators and vent-fed fluidic oscillators as shown in figures 1.2a and 1.2b. Both types of the above fluidic oscillators operate by the same principle at the beginning stage of their operation. A power jet is supplied to the inlet nozzle and by applying the Coanda effect [21], it chooses to attach to one side of the attachment walls in the mixing chamber. If the oscillator is symmetric bistable, then the power jet can attach to one side or both side of the attachment walls equally but if the oscillator is asymmetric monostable, then the power jet always choses to attach to the side where the creation of bubbles is more restricted and this create continuous oscillation. Figures 1.3a and 1.3b shows schematic drawings of asymmetric monostable and symmetric bistable oscillators.

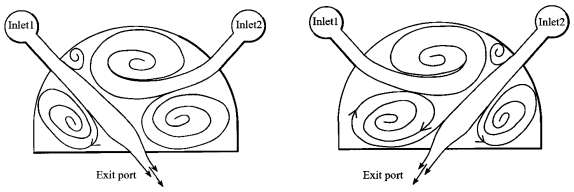

Figure 1.1: Schematic design of feedback-free fluidic oscillators (vortex oscillators) [1].

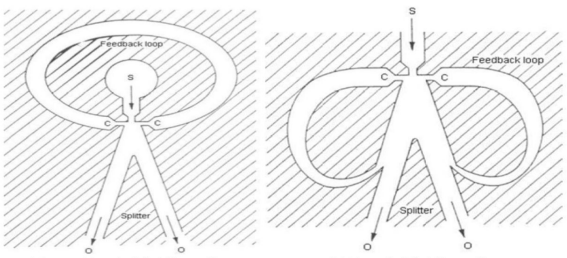

Figure 1.2: Traditional designs of fluidic Oscillator [1].

In vent-fed fluidic oscillators, as inlet supplied working fluid passes though the oscillator, the Coanda bistable effect cause the jet to attach to either side of mixing chamber wall. At the exit, a small portion of jet guided through the feedback channel back to the inlet. At the inlet the interaction of small portion jet with the main jet causes the jet to separate from that side of the wall and attach to the opposite side of the mixing chamber wall and this process is then repeated. This phenomena

creates a switching mechanism which can produce a range of frequencies from 10 Hz to 20 KHz at the outlet depending on different geometry, size and supplied flowrate. On the other hand, in the control loaded fluidic oscillator, a separation bubble is created on the attached side of the wall between the mixing chamber wall and the jet which produces a pressure difference and creates an expansion wave on that side of the feedback channel port while a compression wave is produced on the other side of the feedback channel port. The continuous generation and interaction of these waves through the feedback loop is a fundamental principle of operation for these types of oscillators. Control loaded fluidic oscillators are mainly pressure driven devices due to their switching characteristics. Fluidic oscillators can generate pulsating jets without any mechanical moving parts, therefore they have many advantages over conventional actuators. The oscillator based on the Coanda effect, had an early application in temperature, pressure and flow measuring devices but the oscillator based on a jet mixing chamber was used more often in flow control devices.

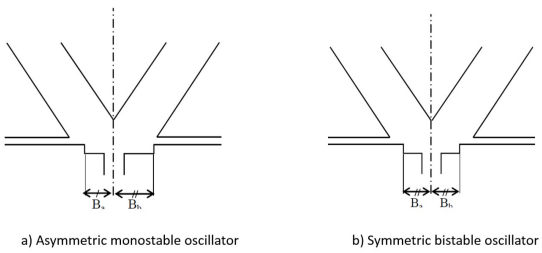

Figure 1.3: Schematic drawing of asymmetric monostable and symmetric bistable oscillators [1].

Sweeping jet fluidic oscillators are vent-fed type oscillators and consist of different regions as shown in figure 1.4. Oscillator parameters and the feedback channel characteristics determine frequency, temperature and pressure under compressible flow conditions as discussed in chapter 4 of this thesis. The fluid supplied from the inlet nozzle and exit from outlets (outlet1 and 2), also this design consist of two feedback channels. The oscillator can be modified to fit each specific application. Increasing the feedback channel length can decrease the oscillation frequency and increasing the feedback channel diameter can also cause reduction of the frequency. In conclusion, increasing the feedback channel volume, decrease the oscillation frequency as shown in figures 1.5a, b. Jet impingement angle modification can change the stagnation pressure in the wall and the flow momentum across the feedback channels. Jet angle increase can reduce the stagnation pressure and mass flow across the feedback channels, thus reducing the oscillation frequency as shown in figure 1.5c. Modifying the

mixing chamber entrance and exit diameters also has an effect on the frequency. An increase in the diameter, will decrease the jet sensibility and reduce the frequency of oscillation for both the entrance and exit as shown in figures 1.6a, b. Feedback channel entrance modification has an effect on the mass flow entrance to the channels and can also shape the vortex which forms at the end of the chamber as shown in figure 1.6c. The nearer the wedge position is to the jet entrance, the lower the oscillation frequency while increasing the wedge angle might slightly increase the frequency as shown in figure 1.6d. These internal modifications will be investigated in the chapter 3 of this thesis.

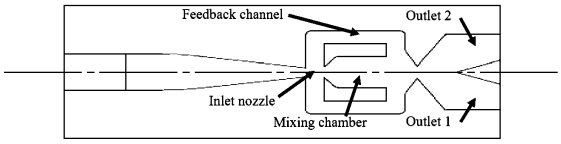

Figure 1.4: Sweeping jet fluidic oscillator [1].

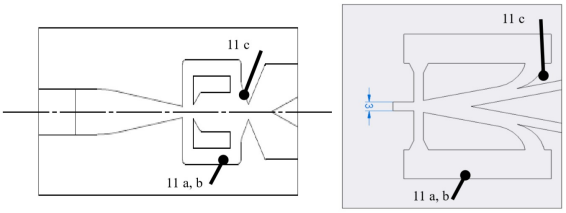

Figure 1.5: Oscillator feedback channels diameter, length and jet impingement angle [1].

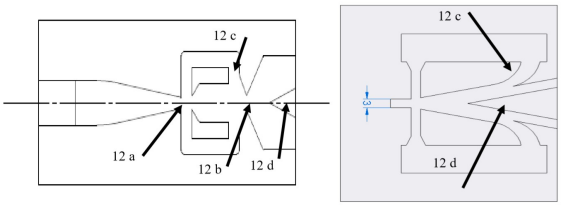

Figure 1.6: Mixing chamber entrance-exit diameter, feedback channel entrance and wedge angle [1].

1.1.3 Fluidic oscillators applications

There are wide range of applications for active flow control and some of them are currently being tested in actual experiments. This type of flow control can be used in

boundary layer control in turbomachinery [22], combustion control [23], mixing enhancement, flow separation control on stator vanes of compressors [24], cavity noise reduction [6], modifying flow separation on airfoils [7], and drag reduction on vehicles mainly trucks [25]. Fluidic oscillators can produce a range of frequencies from 5 Hz up to 20 KHz depending on their geometry, size and supplied flowrate. In the past most fluidic oscillators used water as a working fluid in shower heads, Jacuzzis, windshield washers and sprinklers. However, recent studies on combustion and flow separation control has used air or gas as the working fluid. Aerodynamic improvements also can be made by controlling flow separation on airfoils using fluidic oscillators and several experiments have been performed on two-dimensional airfoils such as a NACA 0021 airfoil [26], a generic airfoil [27], and three- dimensional airfoil models such as a 1/10th-scale powered V-22 model [7]. Fluidic oscillators are also used in turbomachinery for boundary layer control, vehicles aerodynamic improvements and in wind turbines.

The aerospace industry has a particular interest in active flow control (AFC) and is focusing on producing more efficient and aerodynamic aircrafts and space vehicles. The effects of this technology have been investigated for wing flow separation control, for both swept and unswept design and researchers found that the flow control helps to delay the flow separation and stall, especially in the swept wing case. Recently, a full scale Boeing 757 tail [2], equipped with active flow control devices was tested as shown in figure 1.7 and it was found that it can increase rudder effectiveness which lead to designing smaller vertical tails and lowering drag. In the case of engine failure on takeoff, the rudder must generate enough sideforce to counteract the asymmetric thrust from a high-bypass engine slung under the wing, so only because of this problem, aircraft tails were made bigger than they should be to operate safely in the event of engine loss. In this experiment by Boeing and NASA [2], "Sweeping jet" AFC actuators were mounted on one side of a vertical tail, upstream of the rudder hinge line to blow air on the leading edge of the surface. 37 actuators were supplied by a variable mass flow air pump from an external source. This project, which used active flow control, increased sideforce by 20% and reduced the vertical tail size by 17% which reduced the amount of fuel the aircraft burnt by 1-2%. All the research conducted on different parts of aircraft and space vehicles, has found that this technology is beneficial in many aspects and may lead to the design of more efficient and aerodynamic aircrafts.

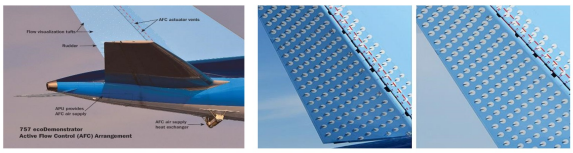

Figure 1.7: Active flow control (sweeping jet) actuators on a Boeing 757 tail [2].

In a recent study [3], a new array of six Fluidic Oscillators connected together was designed, and they simulated it using OpenFOAM in order to understand the flow physics inside the actuators. The performance of this fluidic oscillator investigated on a vertical stabilizer inside the wind tunnel experimentally. They concluded that by using fluidic oscillators, the side forces can be reduced and this may lead to a reduction of the vertical stabilizer size. Figures 1.8a,b shows the fluidic oscillator design.

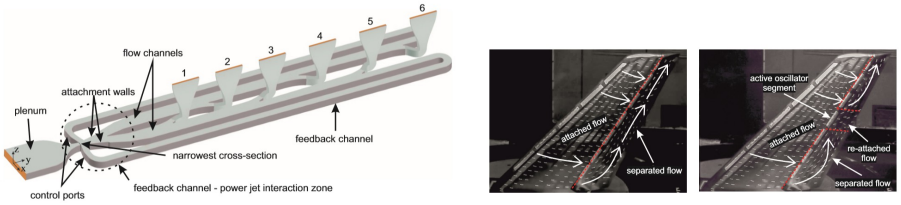

(a) (b)

Figure 1.8: (**a**) Terminology of the fluidic oscillator, (**b**) Visualisation of the vertical stabilizer left: without AFC; right: with AFC [3].

Active flow control (AFC) can effect load and performance of wind turbines. Wind turbines rapid response to changing wind velocity can be affected by the mass of individual blades and the massive rotational inertia of the rotor assembly. Therefore wind turbines always operate with less optimal performance with respect to the wind velocity and a wind turbine can suffer a loss in energy extraction due to blading stall. The interaction of a wind turbine with a constantly fluctuating wind can cause severe structural failure. AFC enable us to control and reduce the magnitude of regional flow separation over an airfoil as shown in figure 1.9 which can have a significant role in reducing the negative effects of the interaction between a turbine and wind velocity. AFC also provides net increases in power output in wind turbines and improves the fluctuating aerodynamic loads associated with dynamic stall. There are many types of devices which can be used in wind turbine technology such as Air Jet Vortex Generators (AJVG), fixed Vane Vortex Generators (VVG) and plasma actuators [28].

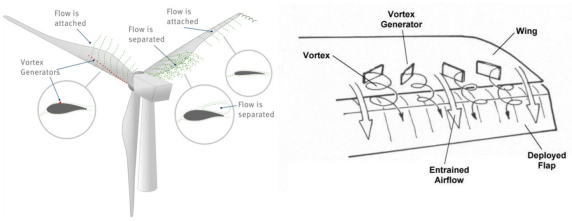

Figure 1.9: Schematic view of wind turbine performance improvement using vortex generators [4].

Fluidic oscillators can be used to delay the flow separation in aerodynamic and hydrodynamic bodies and keep the local flow attached as long as possible. Flow separation can produce pressure drag which is caused by the pressure difference between the front and rear surfaces of the solid object in aerodynamic applications. Flow separation on aircraft body and wing sections can increase pressure drag and hence reduce lift and overall performance of the aircraft. In some cases it can cause a loss of control of the aircraft in high angles of attack. Figure 1.10 shows flow separation over an airfoil. Flow separation control can improve lift characteristics and decrease drag, which lead to more aircraft maneuverability, reduce fuel consumption and lower the landing speed [29]. Flow separation control can offer a reduction in the aircraft industry's operational costs and enables aircraft designers to work with broader flight envelopes. Flow separation can also accrue on wind turbine blades which can reduce their performance and ability to operate relative to the fluctuating wind velocity.

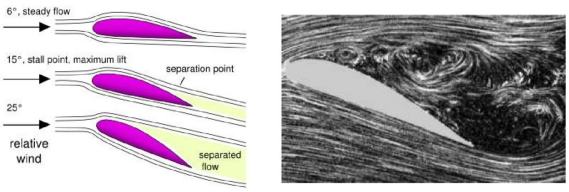

Figure 1.10: Flow separation over an airfoil with varying angle of attack [5].

Fluidic oscillators can also be used in noise reduction applications. Raman and Raghu [6], used fluidic oscillators and successfully reduced the acoustic frequency of the cavity tone by over 10 dB as shown in figure 1.11 and concluded that oscillators can be used in noise control applications.

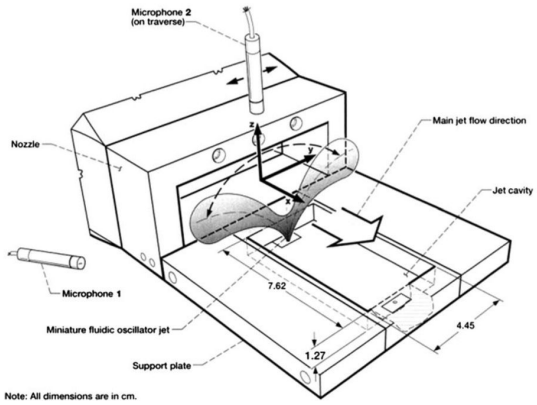

Figure 1.11: Experimental study of cavity noise reduction using sweeping jet actuator [6]

Recently, arrays of actuators have been used in different experiments for flow separation control over airfoils and flaps [7, 27]. Results from experiments on 2-D symmetric airfoils with a sweeping jet array show an improvement in lift and drag coefficients. In most of the practical experiments, it's required to distribute arrays of fluidic oscillators over the large surface of the aerodynamic body with a common plenum chamber as an air supply (working fluid) to all actuators such as shown in figure 1.12. This design can minimize the number of air supply connections and length of tubing required and it's also easy to maintain. Figures 1.12b,c show the integration of arrays of actuators on the leading and trailing edges of an airfoil. The array is fabricated using rapid prototyping or micromilling and inserted into a slot at a selected location. Based on the aerodynamic surface where the control is needed, different arrays of actuators with varying configurations, orientations and patterns may be needed.

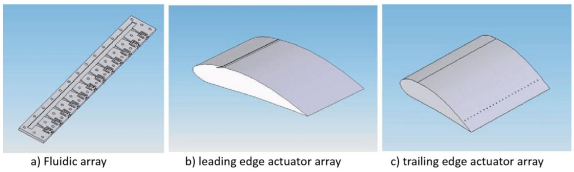

Figure 1.12: Sketch of a compact array of fluidic oscillator and integration into airfoil sections [7].

1.1.4 State of the art

In previous studies, both numerical and experimental methods were conducted on various actuator designs and different applications for the purpose of active flow con-

trol. Different techniques and methods of investigation were used both on numerical and experimental studies which helped other researchers and created a foundation for future work. Uzol and Camci [30], studied a fluidic oscillator with two elliptical cross-sections placed transversally and an afterbody located in front of them both experimentally and with computational fluid dynamics (CFD). In this case, the relation between the Reynolds number and frequency was perfectly linear and the oscillator was able to produce a frequency of 30 Hz under laminar flow condition. Khelfaoui et al. [31], also conducted experimental and numerical studies on symmetrical micro and mini oscillators under incompressible flow conditions. The oscillator feedback was modeled analytically and the central part of the oscillator was simulated using CFD. They found a linear relation between feedback channel volume and frequency of oscillation. In this design, above a certain pressure point choked flow appears and from this point the relation between frequency and pressure threshold difference decreased linearly. Huang and Chang [32], performed an investigation on a V-shape fluidic oscillator. They modified its internal dimensions and defined some regions where oscillation can occur and found that a range of frequencies from a few Hz to several KHz can be produced by modifying the oscillator internal dimensions and parameters.

Gregory and Raghu [33], created a fluidic oscillator based on the Coanda effect but driven by piezoelectric devices. One of the main advantages of this device is that the frequency can be decoupled from the input flow and pressure and the frequency just depends on the input electrical signal which enables this device to work at a range of velocities. Raman et al. [6], used a single sweeping jet actuator located at the upstream end of the cavity to suppress cavity noise, up to 10 dB reduction was achieved in the noise level in the cavity. Also a similar actuator was used in a thrust vectoring experiment in a round jet. In all of these experiments just one actuator was used because of the small experimental setups.

In a recent study by Aram et al. [8], a design of the fluidic oscillator simulated both in 2D and 3D using OpenFOAM and air as a working fluid. The main objective of their study was to validate the computational fluid dynamics (CFD)-based simulations of a fluidic oscillator. Both URANS and the improved delayed detached-eddy simulation (IDDES) were used to simulate and resolve the flow structures in the internal flow passages of the fluidic oscillator and outside of the actuator outlet. The 2-D URANS simulation, 3-D URANS simulation, and IDDES of flow inside and outside the actuator in quiescent air were compared with the experimental work of [34]. Based on the computational results validated against experiments, it was found that

the 3-D IDDES model provided the most accurate prediction of the flowfield among the three models used in this study. Figures 1.13a,b shows the schematic veiw of the oscillator and 3-D Q criterion.

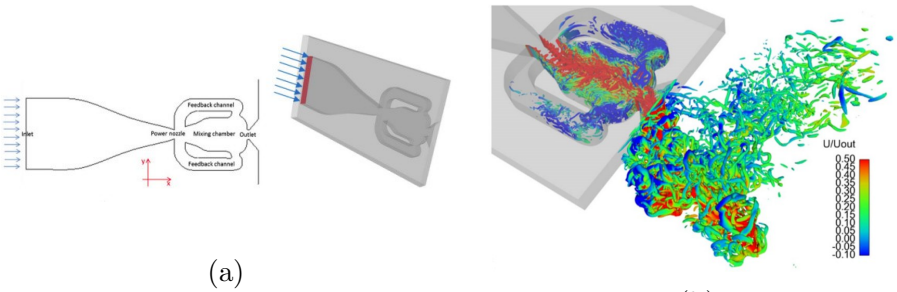

(a) (b)

Figure 1.13: (**a**) Schematic of the oscillator, (**b**) Isosurface of nondimensional Q with streamwise velocity contours obtained from 3-D IDDES [8].

In a recent study, the output frequency and amplitude effects whenever the feedback channel and the mixing chamber lengths were modified, was studied by Seo et al. [9] using a 2D numerical model, the fluid was considered as incompressible, the Reynolds number employed was 5000. The observation was that an increase of the feedback channel length generated no modifications on the output frequency, as in this case the flow is incompressible, being the reason why the simulations could not provide the correct information. On the other hand, the increase of the mixing chamber length, generated a clear reduction on the actuator output frequency. They defined the length scale to be employed to properly non-dimensionalize the oscillation frequency. Figures 1.14a,b shows a Schematic of fluidic oscillator considered in this study and the flow field inside the oscillator respectively.

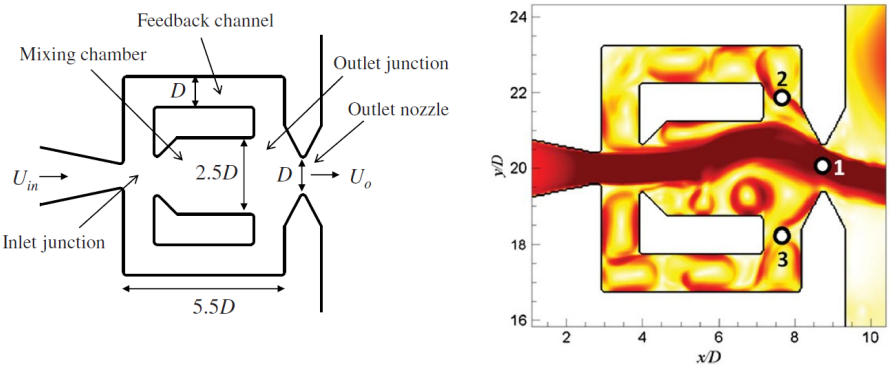

(a) (b)

Figure 1.14: (**a**) Schematic of the fluidic oscillator, (**b**) Flow field inside the fluidic oscillator [9].

Several recent studies on the performance of fluidic oscillators under compressible flow conditions undertaken as shown in references [10, 11, 35, 36]. Gokoglu et al. [10], analyzed via 2D-CFD a very similar fluidic oscillator configuration to the one evaluated in the current thesis, under supersonic flow conditions. Their objective was to create reasonable, unsteady fluidic actuators with high control specialist and furthermore enhance their execution proficiency by limiting pressure losses in propulsion systems and on airframes working in a wide range of flow speeds. The predicted oscillation frequencies had excellent agreement with the experimental measurements of the device for both air and helium operating gases. It was resolved numerically that this diverter was capable for creating supersonic exit velocities. Figures 1.15a,b shows a schematic of the setup and measured oscillation frequencies of the fluidic diverter versus Mach number.

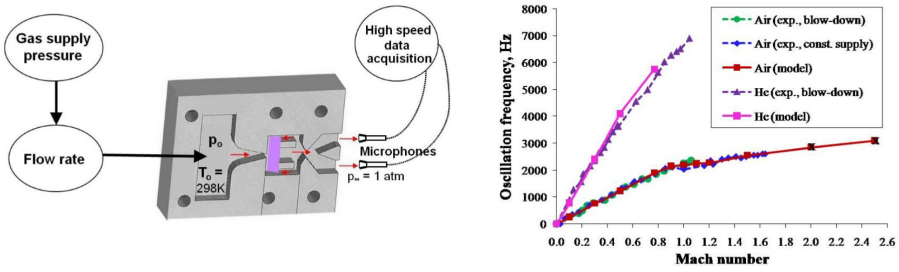

(a) (b)

Figure 1.15: (**a**) A simple schematic of the experimental setup, (**b**) Comparison of calculated and measured oscillation frequencies of the fluidic diverter versus Mach number [10].

Slupski and Kara [11], studied the effects of feedback channel geometric parameters on the Performance of the sweeping jet actuator. In this study, unsteady flow fields produced by sweeping jet (SWJ) actuator are investigated using two-dimensional, unsteady, Reynolds-Averaged Navier Stokes (2D-URANS) simulations with Ansys Fluent programming. All the simulations were performed for a fully-turbulent compressible flow. Figure 1.16a present a schematic view of the fluidic oscillator with different geometric parameters. In figure 1.16a, parameters D1 and D2 represent feedback channel height and width. The parameters were varied systematically to investigate the effect of feedback channel geometry on jet oscillation frequency. One of the main conclusions they obtained was that the oscillation frequency increase with increasing feedback channel height and after that remains unaffected. An opposite behaviour is observed with feedback channel width as shown in figure 1.16b.

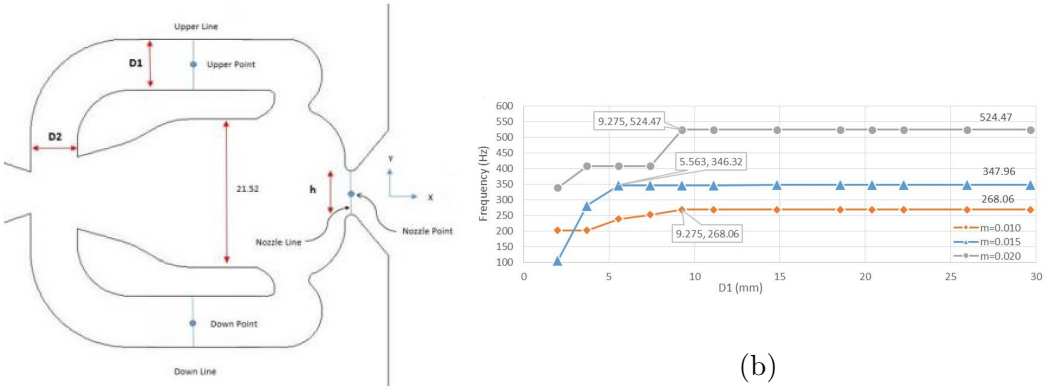

(a) (b)

Figure 1.16: (**a**) Fluidic oscillator geometric parameters, (**b**) Jet oscillation frequency for varying feedback channel height for different mass flow rates [11].

At this point, most of the research on fluidic actuators including the evaluation of new configurations, performing numerical and CFD models usually using laminar condition and performing different experiments on their applications. It's crucial to understand the internal flow physics of fluidic actuators and be able to design these devices for each specific application.

1.1.5 Main objectives

In this PhD, a specific design of the fluidic oscillator will be examined carefully. In chapter 2, different forces applying to the main jet, and driving the oscillation will be investigated to understand the origin of the oscillation. In chapter 3, different internal geometry modifications will be applied to the main shape to investigate how geometry influences flow physics and the dynamic performance of fluidic oscillators. The forces driving the oscillation will be evaluated for each case in this chapter. This knowledge will enable us to design the devices required for each individual specific applications and enable us to understand how different sizes and geometries can be added to real-world engineering systems. The effect of the feedback channel length on the performance of the fluidic oscillator under compressible flow conditions will be studied in chapter 4 of this thesis. This study is performed numerically using the open-source computational software OpenFOAM considering fluid as incompressible and compressible. Most of the research so far was performed using two-dimensional meshes, but this can cause some resolution and accuracy problems in some cases and

especially when dealing with high Reynolds numbers. All the simulations performed in this thesis are using 3D meshes.

Chapter 2

Forces driving the oscillations in 3D fluidic oscillators.

2.1 Introduction

Flow control actuators have traditionally been a research topic in the fluid mechanics field. Their use on bluff bodies allows modifying lift and drag, reducing flow instabilities, as well as the energy required for the body to move. From the different existing actuators, plasma actuators, ZNMF (zero net mass flow), MEMS (Micro-Electro-Mechanical Systems), fluidic oscillators, and combustion driven jet actuators [12, 13], only plasma, pulsed combustion actuators, and fluidic oscillators do not have moving parts, which a priori gives confidence regarding their reliability.

Plasma actuators are just beginning to be able to produce the required momentum to interact with the boundary layer in real applications, but the voltage differential used often does not sufficiently ionize the fluid to create the required fluid jet momentum. Pulsed combustion actuators provide a large flow momentum, but, due to the high temperatures associated with them, these actuators can only be used in very particular applications in which high fluid temperatures are acceptable. Fluidic oscillators are able to produce pulsating jets with the required momentum to interact with the main flow boundary layer, although it appears that their design needs to be adapted to each particular application.

Original fluidic oscillators design goes back to the 60 s and 70 s. Their outlet frequency ranges from several Hz to KHz and the flow rate is usually of a few dm^3/min. From their applications in flow control, it is interesting to mention their use in combustion control [23], flow deflection and mixing enhancement [37], flow separation modification in airfoils [7], boundary layer modification on hump diffusers used in turbomachinery [22], flow separation control on compressors stator vanes [24],

gas turbine cooling [38], drag reduction on lorries [25], and noise reduction in cavities [6].

Despite the existence of particular fluidic oscillator configurations, like the one introduced by Uzol and Camci [30], which was based on two elliptical cross-sections placed transversally and an afterbody located in front of them, or the one proposed by Huang and Chang [32], which was a V-shaped fluidic oscillator, most of the recent studies on oscillators focused on two main, very similar, canonical geometries, which Ostermann et al. [34] called the angled and the curved oscillator geometries. Some very recent studies on the angled geometry are [9, 10, 34, 39–46], while the curved geometry was studied by [6, 8, 11, 34, 37, 46–54]. Ostermann et al. [34], compared both geometries, concluding that the curved one was energetically the most efficient.

One of the first analyses of the internal flow on an angled fluidic oscillator was undertaken by Bobusch et al. [41]. Experiments were performed using water to visualize and quantify the internal flow patterns. The results provided detailed insight into the oscillation mechanism and also of the interaction between the mixing chamber and the feedback channels.

Via employing the same fluidic oscillator configuration previously analyzed by Bobbusch et al. [41], Gartlein et al. [42] carefully evaluated the internal fluid structures as well as the output jet oscillation parameters using high speed PIV, and they also used time-resolved pressure measurements. The Reynolds numbers studied ranged between 10,000 and 50,000, and air was employed as working fluid. They observed a linear dependency between the oscillation frequencies and the input Reynolds number. Several fluid properties, such as the deflection angle, jet width, and jet velocity, were examined. It was found that these properties remained rather constant for a certain range of Reynolds numbers, and suffered a strong change once a certain Reynolds number was overcome. Woszidlo et al. [43] studied the same configuration previously evaluated by Gartlein et al. [42]. Their attention focused on analyzing the flow phenomena inside the mixing chamber and the feedback channels, and highlighted that increasing the mixing chamber inlet width tended to increase the output frequency, and rounding the feedback channels should diminish the generation of the separation bubbles on these channels.

Vatsa et al. [55] studied the same two fluidic oscillators recently analyzed by [34], which resemble the ones previously studied by Bobusch et al. [41] and Aram et al. [8]. Results showed that the fluidic oscillator with sharp internal corners generated a much more homogeneous output velocity distribution than the actuator with rounded internal corners.

Aram et al. [8] studied numerically the curved geometry sweeping jet fluidic oscillator, and a large buffer zone was also considered in the simulation. The simulations were performed in 2D and 3D using the URANS-K-omega turbulence model, additionally a 3D simulation was undertaken using the IDDES turbulence model. An oscillator with an outlet diameter of 25 mm using air as working fluid and at Reynolds 12,000 and 50,000 was initially studied, but a second oscillator with an outlet diameter of 1.3 mm using water as working fluid at Reynolds number 12,000 was considered. Based on the computational results validated against experiments undertaken by previous researchers, it was found that the IDDES model provided the most accurate prediction of the flow field.

Ostermann et al. [34] experimentally studied, via PIV, the internal and external flow fields of the same two oscillator configurations previously studied by Vatsa et al. [55]. Both oscillators were characterized by a linear dependence of the oscillation frequency on the supply flow—in fact, and for the Reynolds numbers studied, the output frequency of both configurations was almost identical. The curved configuration studied by Aram et al. [8] had a larger mixing chamber inlet width than the angled one employed by Bobusch et al. [41] and Gokoglu et al. [10], which prevented the existence of reversed flow into the feedback channel. This configuration also prevented the flow separation on the feedback channel's corners. As a result, this particular configuration appeared to be more efficient in terms of energy requirements. In fact, there are considerable differences in external flow fields caused by the different external chamber configurations. The configurations of Bobusch et al. [41] and Gokoglu et al. [10] have a smaller deflection angle and a higher homogeneous distribution of the output flow field, when compared with the flow distribution generated by the Aram et al. [8] configuration.

Slupski and Kara [11] studied a range of feedback channel geometric parameters, where the actuator configuration was the same as the one analyzed by Aram et al. [8]. The effects of varying the feedback channel height and width for different fluidic oscillator mass flow rates were studied. Oscillation frequencies increased when increasing the feedback channel height up to a certain point and then remained unaffected, however, frequencies decreased by further increasing the feedback channel width.

The oscillation frequency response for different lengths of the feedback channels of a fluidic oscillator which could generate a wide range of frequencies (50–300 Hz) was studied by Wang et al. [35]. An inverse linear relation between frequency and the length of the feedback channels was observed.

The same configuration previously employed by [41], although using a single exit, was numerically evaluated in 3D by [45]. Two geometrical parameters, the mixing chamber inlet and outlet widths, were modified. They observed a significant effect of the flow structure and the feedback channel flow rate when modifying the inlet width, while negligible effects were observed when modifying the outlet width. The effect of modifying the feedback channel and mixing chamber lengths on the oscillator mass flow frequency and amplitude was studied using a 2D numerical model by Seo et al. [9], where the fluid was considered as incompressible. Increasing the mixing chamber length generated a clear reduction in the actuator output frequency. An increase of the feedback channel length generated no modifications on the output frequency, the same observation that was previously obtained by [56].

In Hirsch and Gharib [36], the dynamics of a sweeping jet actuator were analyzed via Schlieren visualizations. Subsonic Mach numbers and the transition to sonic conditions were evaluated. They observed the oscillations started from small asymmetries caused by small differences in geometry. The properties of a sweeping jet emitted by a fluidic oscillator were recently investigated by Ostermann et al. [50]. They observed the maximum jet velocity decays much faster than a comparable steady jet, and the entrainment rate was four times the one of a steady jet. Among the latest studies on fluidic oscillators, it is relevant to highlight the ones performed by [53, 54], where novel phase-synchronized and adjustable frequency fluidic oscillators were introduced. In Staats et al. [3], a new array of six Fluidic Oscillators (FOs) connected together was designed, and they simulated it using OpenFOAM in order to understand the flow physics inside the actuators. The array was employed to experimentally modify the side forces acting on a model of a vertical stabilizer.

The current paper presents a numerical evaluation of the same fluidic oscillator configuration employed in [41]. Initially, the experimental results obtained in [41] are compared with the 3D-computational fluid dynamics (CFD) simulations performed. A discussion regarding why the stagnation pressure generated at the mixing chamber converging surfaces and why the pressure momentum term acting onto the main jet at the mixing chamber inlet are responsible of the jet oscillations is undertaken. The effect of the Reynolds number on the dynamic stagnation pressure and on the pressure momentum term acting on the jet shall further clarify the origin of the oscillations. At this point it is very relevant to recall the work done by Wu et al. [46], where they applied the curved and angled fluidic oscillator configurations to enhance heat transfer. As in the present paper, they presented the temporal pressure fields inside the oscillator and concluded that for the two configurations they studied, the

oscillations were pressure driven. As a matter of a fact, in microfluidics there are several fluidic oscillator configurations which are known to be pressure driven [57,58]. In the present paper and for a different angled configuration than the ones evaluated by [46], the same conclusion is obtained and is proven fully.

2.2 Fluidic Oscillator Main Characteristics and Model Validation

According to the introduction just presented, fluidic oscillators were mostly studied experimentally. The vast majority of the CFD simulations were carried out in two dimensions, although some recent three dimensional simulations were performed by [8, 45,46,53]. In the present study, the flow was considered as turbulent, incompressible, and isothermal, all simulations were 3D, and the fluid used was water. The 3D Fluidic Oscillator (FO) considered in the present chapter is introduced in figure 2.1. The incoming flow enters the actuator Mixing Chamber (MC) (2) through the flattered pipe (1), and on both sides of the MC there are the Feedback Channels (FC) (3), their function is to allow transporting fluid from the downstream mixing chamber site to the upstream one and vice-versa. The fluid leaves the oscillator alternatively through the two exit surfaces located on both sides of the External Chamber (EC) (4). Notice that a second FO with a buffer zone (5) is also presented in figure 2.1b. This second configuration was used to evaluate the effects of the outlet boundary conditions on the FO outlet mass flow frequency. In order to properly understand the following explanations, figure 2.1c was generated, and the different sections, actuator angles, and relevant walls are defined in this figure.

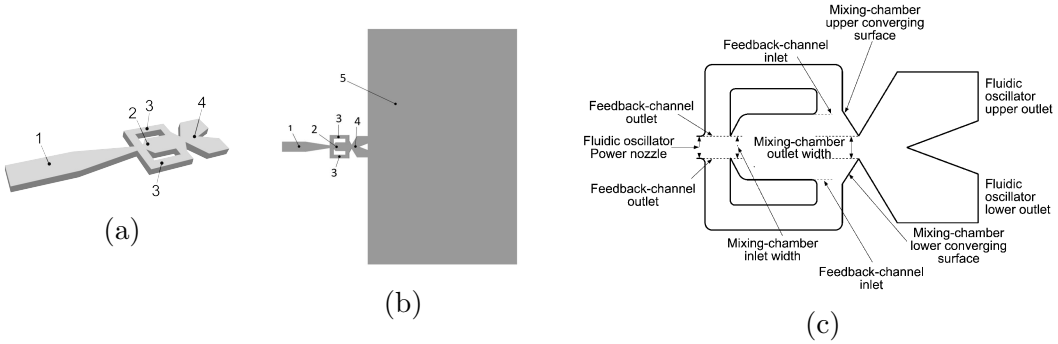

Figure 2.1: Fluidic oscillator general view and its different parts, (**a**) original fluidic oscillator, (**b**) fluidic oscillator with buffer zone, (**c**) fluidic oscillator main parts. Flattered pipe, 1; mixing chamber (MC), 2; feedback channels (FC), 3; external chamber (EC), 4; buffer zone (BZ), 5.

A zoomed view of the grid used to perform the 3D simulations is presented in figure 2.2. Initial simulations were done employing three different grid sizes—the number of cells were respectively 142,000, 2,242,000, and 5,933,900—and the Reynolds number was set to 16,034. The Reynolds number definition used to characterize the main flow was $R_e = \frac{\rho V D_h}{\mu}$, where ρ and μ are the density and dynamic viscosity of the fluid respectively. The characteristic length was chosen to be the oscillator's power nozzle hydraulic diameter D_h, and the fluid velocity at the same section was employed as the dimensional characteristic velocity.

The output oscillation frequencies obtained with the three different meshes were 24.6 Hz, 22.7 Hz, and 22.63 Hz respectively. When comparing these values with the experimental results undertaken by [41], it was noticed that for the coarsest grid, the error produced was 12.8%, when using the intermediate mesh, the error reduced to around 4.1%, and this error further reduced to 3.8% for the finest mesh. The typical computational time required for each of these simulations was respectively 2480 CPUh for the coarsest grid, 9950 CPUh for the medium one, and 14,900 CPUh when using the finest mesh, where the computational time was calculated based on a 16 core CPUs server, and each processor had a speed of 2.3 GHz. All three grids were structured, for a Reynolds number of 16,034, the maximum respective $x+$, $y+$, and $z+$ were 5.2, 8.4, and 14.8 when employing the coarsest grid, 1.8, 4.7, and 1.2 for the case of the medium mesh, and 0.5, 0.65, and 0.4 when the finest mesh was employed. The locations of the maximum $x+$, $y+$, and $z+$ were, for the coarsest grid case, at the actuator inlet section, just before the mixing chamber entrance. For the other two meshes, the location of the maximum $x+$ was the same, yet the locations of the maximum $y+$ and $z+$ were found at the mixing chamber outlet section. The definition of $y+$ is given as $y+ = (\rho y U_\tau)/\mu$, where $U_\tau = \sqrt{\tau_w/\rho}$, and τ_w characterizes the shear stresses at the wall point where $y+$ is determined, y is the distance to the first grid cell measured in the y direction. To obtain the $x+$ and $z+$ values, the cell distances in these respective directions were used instead of y, and the maximum shear stresses at each particular point were used for all cases. Based on the previous simulations undertaken in this paper, it was concluded that the medium grid was precise enough to evaluate the cases under study and when using Reynolds numbers below 16,034. The mesh with 5,933,900 cells was used to perform simulations at Reynolds number of 32,068. The maximum values of $x+$, $y+$, and $z+$ obtained with the finest mesh at Reynolds 32,068 were 0.9, 1.2, and 0.7 respectively. Table 2.1 summarizes this information.

Table 2.1: Main characteristic parameters of the initial simulations done in 3D using DDES turbulent model.

Reynolds Number	**Number of Grid Cells**	**Output Frequency (Hz)**	**Error (%)**	**Time CPUh**	$x+$	$y+$	$z+$
16,034	142,000	24.6	12.8	2480	5.2	8.4	14.8
16,034	2,242,000	22.7	4.1	9950	1.8	4.7	1.2
16,034	5,933,900	22.63	3.8	14,900	0.5	0.65	0.4
16,034	11,292,000 (buffer zone)	22.38	2.7	26,100	1.8	4.7	1.2
16,034	Experimental [41]	21.8	0	-	-	-	-
32,068	5,933,900	40.43	-	17,700	0.9	1.2	0.7

As previously stated, and in order to characterize the possible effect of the boundary conditions on the flow performance, a fluidic actuator with a buffer zone was generated. For this particular case, the outlet boundary conditions were maintained the same as in the original case, but the outlet was located at the end of the buffer zone. The total number of cells used in this new model was 11,292,000. A single Reynolds number of 16,034 was studied, being the maximum $x+$, $y+$, and $z+$ values, the same as the ones obtained for the medium mesh previously introduced. The frequency obtained when using this particular buffer zone model increased by 2.7% versus the one obtained experimentally [41]. The use of the buffer zone increased the computational time by 162% and the oscillation frequency obtained differed by 1.4% versus the one obtained without buffer and using the medium mesh. Considering the number of 3D simulations to be undertaken, it was decided to simulate the FO without the buffer zone.

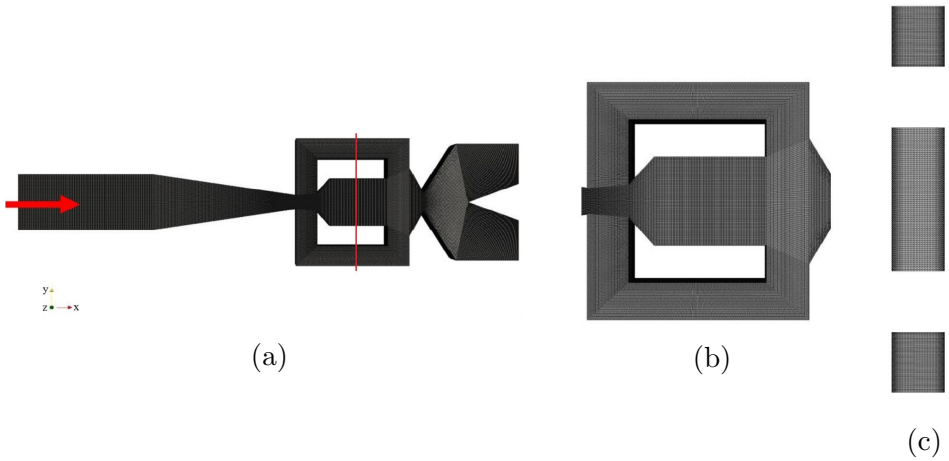

Figure 2.2: Grid used in the present study, (**a**) plane view, (**b**) zoom view, (**c**) side view of the mesh at the center of the mixing chamber, see the vertical line.

The boundary conditions employed in all simulations were Dirichlet conditions for velocity and Neumann for pressure at the inlet. A relative pressure of 10^4 Pa and Neumann conditions for velocity were employed at the two outlets. The same boundary conditions were used at the single outlet when the buffer zone was employed. Dirichlet boundary conditions for velocity and Neumann for pressure were set to all walls. The different velocities evaluated and defined at the inlet of the flattered pipe where the section was $10.3 \times 3.25 = 33.475$ mm^2, see figure 2.1a, were 0.671 m/s, 0.8588 m/s, 1.0479 m/s, 1.2347 m/s, and 2.46 m/s. Their respective associated volumetric flows were 22.47 cm^3/s, 28.75 cm^3/s, 35.08 cm^3/s, 41.33 cm^3/s, and 82.349 cm^3/s, with the corresponding Reynolds numbers being 8711, 11,152, 13,593, 16,034, and 32,068. The Reynolds numbers are based on the hydraulic diameter D_h and the fluid velocity V at the power nozzle, mixing chamber inlet, and the same location was already used by [41]. One of the main characteristics of a fluidic oscillator is its linear frequency behavior versus the inlet mass flow, usually represented as a function of the Reynolds number. The results obtained from the first four Reynolds numbers were used for comparison with the experimental results obtained by [41]. This comparison is presented in figure 2.3, and clarifies that the expected linear behavior appears in both cases. The frequency obtained when simulating the Reynolds number 32,068 with a mesh of 5,933,900 cells is also plotted in the same figure, proving that the oscillator linearity still exists at this particular Reynolds number. Notice that the straight line showing the relation between the FO outlet frequency with the Reynolds number, see figure 2.3a, would have been even better if the finest mesh was used for all Reynolds numbers evaluated.

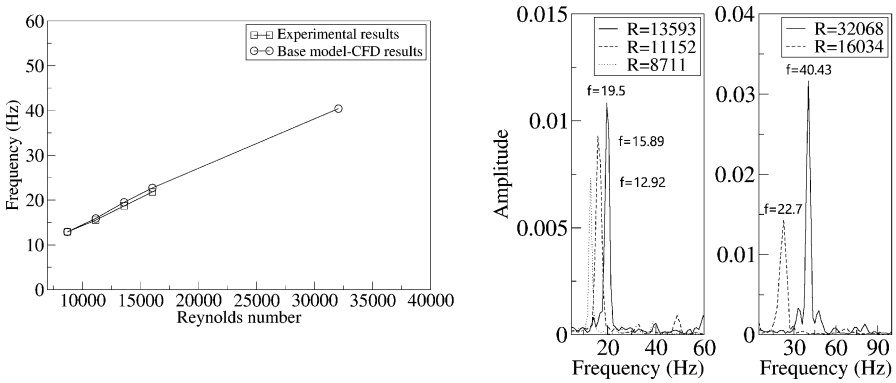

(a) (b)

Figure 2.3: (**a**) Comparison of experimental and computational fluid dynamics (CFD) results, (**b**) FFT of the different Reynolds numbers studied.

Fluid dynamic viscosity was chosen as 0.001003 Kg/(m s), with the fluid density being 998.2 Kg/m^3. The software OpenFOAM was employed for all 3D simulations, and finite volumes is the approach OpenFOAM uses to discretize Navier Stokes equations. Inlet turbulence intensity was set to 0.05% in all cases, Pressure Implicit with Splitting Operators (PISO) was used to solve the Navier Stokes equations, the time step being 10^{-6} s, and spatial discretization was set to second order.

The DDES turbulent model uses a RANS model nearby the walls, (simply because the grid required by an LES model is too restrictive in many applications), and a LES model for the cells located a distance greater than a threshold distance d of the wall.

Equations 2.1 and 2.2 are the coupling momentum equations through viscosity for RANS and LES models respectively. The main difference is that the RANS models need to estimate the turbulent viscosity ν_t which characterizes the apparent Reynolds stress tensor, the rest of the parameters in equation 2.1 define average values. All parameters defined in equation 2.2 are instantaneous, and the LES model employed in the present paper uses the sub-grid scale viscosity ν_{SGS}, which characterizes the average temporal variation of the apparent Reynolds stress tensor. Notice that in RANS models the temporal variation of the Reynolds stress tensor were assumed to be zero, therefore the ν_t term characterizes the instantaneous fluctuation values.

$$\frac{\partial \mathbf{U}}{\partial t} + \nabla \cdot (\mathbf{U}\mathbf{U}) - \nabla \cdot \left((\nu + \nu_{\mathrm{t}}) \left(\nabla \mathbf{U} + (\nabla \mathbf{U})^{\mathrm{T}} \right) \right) = \nabla p \tag{2.1}$$

$$\frac{\partial \mathbf{U}}{\partial t} + \nabla \cdot (\mathbf{U}\mathbf{U}) - \nabla \cdot \left((\nu + \nu_{\mathrm{SGS}}) \left(\nabla \mathbf{U} + (\nabla \mathbf{U})^{\mathrm{T}} \right) \right) = \nabla p \tag{2.2}$$

Detached-eddy simulation (DES) is a hybrid model which makes use of the Spalart-Allmaras turbulent model and combines the benefits of RANS and LES model. Generally RANS models perform well when the boundary layers are attached and have some difficulties when facing with separated flows, see [59]. LES models need a very refined mesh near the walls and this can bring high computational costs and also difficulties to work with this model for complex flows and high Reynolds numbers [60]. The methodology behind this is that the DES model uses more efficient RANS approach near the walls with less grid spacing requirements and use the LES model away from the walls. The DES model is arranged to function in RANS mode in attached boundary layers and in LES mode in regions when the flow is separated. The DES is based on the Spalart-Allmaras one equation turbulence model [61] which Length scale, (d), is generally taken as the shortest distance at any point to the closest wall. In the DES model, this (d) is replaced with $(\tilde{d})$ which is the minimum length between the distance to the wall and a length proportional to the local grid spacing [62]. The DES turbulent model switches from RANS to LES formulation by modifying the distance (d) associated to the destruction term $(\left(\frac{\tilde{\nu}}{d}\right)^2)$ see equation 2.8. The parameters $(\tilde{d})$ and (Δ) are defined in equations 2.3 and 2.4.

$$\tilde{d} = \min\left(d, C_{DES} \cdot \Delta\right) \tag{2.3}$$

$$\Delta = \max(\Delta x, \Delta y, \Delta z) \tag{2.4}$$

Where C_{DES} is defined as a constant of the model, its value is 0.65 and Δ is the local grid spacing. As long as the distance between a point in the mesh domain and the nearest surface, (d), is smaller than the DES length scale (Δ) multiplied to the C_{DES} constant, then the simulation remains in RANS mode [63].

The DES model can be further modified into the delayed detached-eddy simulation (DDES) model, this model include the molecular and turbulent viscosity information into the switching mechanism to delay this switching in boundary layers. The idea of this model is to make sure that the turbulent modeling remains in RANS mode throughout the boundary layers and to overcome the possible issue of grid-induced separation (GIS) [64]. For DDES model a new formulation with a filter function f_d was introduced to avoid the so called grid-induced separation (GIS). In the DDES model, the switching mechanism between RANS and LES is not only dependent on the wall distance and grid spacing but also on the flow itself. The filter function f_d is designed to take a value of 0 in the region where the boundary layer is attached,

under this conditions the RANS model is used, and a value of 1 in the region where the flow is separated, under these conditions the original DES model is employed. For the DDES turbulent model, the parameter $\tilde{d}$ is now modified as shown in equation 2.5.

$$\tilde{d} = d - f_d \max\left(0, d - C_{DES} \cdot \Delta\right) \tag{2.5}$$

Where f_d is a filter function which is modified to take a value of 0 in the RANS region when the boundary layers are attached and take a value of 1 in the separated LES region [64]. The DDES formulation should be used as a standard model instead of DES as suggested by [65]. The filter function f_d of the DDES model is presented in equations 2.6 and 2.7.

$$f_d \equiv 1 - \tanh\left(\left[8r_d\right]^3\right) \tag{2.6}$$

$$r_d \equiv \frac{\nu_t + \nu}{\sqrt{U_{i,j}U_{i,j}}\kappa^2 d^2} \tag{2.7}$$

Where ν_t is the kinematic eddy viscosity, ν is the molecular viscosity, $U_{i,j}$ represent the velocity gradients, κ is the Karman constant which value is 0.41 and d is the distance to the wall.

The RANS model used in the present DDES simulation, is the Spalart-Allmaras, which is a one-equation turbulence model, being this equation a transport equation for the kinematic eddy viscosity. In the Spalart-Allmaras methodology, various terms such as diffusion, production and destruction are defined to achieve a complete transport equation for the kinematic eddy viscosity, as shown in equation 2.8, see as well the following reference, [61].

In reality, the working variable defined in equation 2.8 is $\bar{\nu}$, which is a the kinematic eddy viscosity multiplied by a non dimensional damping function $f_{\nu 1}$, see equation 2.9.

$$\frac{\partial \tilde{\nu}}{\partial t} + \tilde{u}_j \frac{\partial \tilde{\nu}}{\partial x_j} = \underbrace{c_{b1}\widetilde{S}\tilde{\nu}}_{\text{Production}} + \underbrace{\frac{1}{\sigma}\left[\frac{\partial}{\partial x_j}\left((\nu + \tilde{\nu})\frac{\partial \tilde{\nu}}{\partial x_j}\right) + c_{b2}\frac{\partial \tilde{\nu}}{\partial x_j}\frac{\partial \tilde{\nu}}{\partial x_j}\right]}_{\text{Diffusion}} - \underbrace{c_{w1}f_w\left(\frac{\tilde{\nu}}{d}\right)^2}_{\text{Destruction}} \tag{2.8}$$

The relation between the eddy viscosity, the damping function and the working variable used in equation 2.8, is presented in equation 2.9.

$$\mu_t = \bar{\rho}\tilde{\nu}f_{\nu 1} = \bar{\rho}\nu_t \tag{2.9}$$

The damping function $f_{\nu 1}$ is defined in the boundary layer buffer zone, viscous sublayer and in the logarithmic layer, and needs to be accomplished that $\tilde{\nu} = kyu_\tau$, k being the Karmann constant, y is the generic distance from the wall and any point inside the boundary layer, and u_τ is the friction velocity. Equation 2.10 defines the damping function.

$$f_{\nu 1} = \frac{\chi^3}{\chi^3 + c_{\nu 1}^3} \qquad \chi = \frac{\tilde{\nu}}{\nu} \tag{2.10}$$

The vorticity magnitude S associated to the production term of equation 2.8, is modified as $\tilde{S}$, to maintain its logarithmic layer performance characterized by $\left(\tilde{S} = u_\tau / ky\right)$ as shown in equation 2.11.

$$\begin{aligned} \widetilde{S} &= S f_{\nu 3} + \frac{\tilde{\nu}}{\kappa^2 d^2} f_{\nu 2} \\ \widetilde{S} &= \sqrt{2\Omega_{ij}\Omega_{ij}} f_{\nu 3} + \frac{\tilde{\nu}}{\kappa^2 d^2} f_{\nu 2} \\ \Omega_{ij} &= \frac{1}{2}\left(\frac{\partial \tilde{u}_i}{\partial x_j} - \frac{\partial \tilde{u}_j}{\partial x_i}\right) \end{aligned} \tag{2.11}$$

where $f_{\nu 2} = 1 - \frac{\chi}{1+\chi f_{\nu 1}}, \quad f_{\nu 3} = 1$

To enhance the decaying of the destruction term in the outer area of the boundary layer, see equation 2.8, a function f_w is used, equation 2.12 defines this particular function.

$$f_w(g) = g\left(\frac{1 + c_{w3}^6}{g^6 + c_{w3}^6}\right)^{1/6} \tag{2.12}$$

where $g = r + c_{w2}\left(r^6 - r\right)$, and $\quad r = \frac{\tilde{\nu}}{\widetilde{S}\kappa^2 d^2}$

In this equation, g is a limiter which prevents the large values of f_w, f_w and r are equal to 1 in the logarithmic layer and decrease in the outer areas. The constants employed in the present model are introduced in equation 2.13.

$$\begin{aligned} &c_{b1} = 0.1355, \quad c_{b2} = 0.622, \quad \sigma = \frac{2}{3} \\ &\kappa = 0.41, \quad c_{w1} = \frac{c_{b1}}{\kappa^2} + \frac{1+c_{b2}}{\sigma}, \quad c_{w2} = 0.3 \\ &c_{w3} = 2, \quad c_{v1} = 7.1 \end{aligned} \tag{2.13}$$

Basically the most important part of the Spalart-Allmaras equation is the destruction term as shown in equation 2.8, being particularly important the parameter d, which characterizes a generic distance of any mesh cell to the closest wall. When using the (LES sub-model) from the DDES model, this term d is replaced with a length proportional to Δ. The definition of the length scale $\tilde{d}$ is to make sure that

when in the boundary layer $d < C_{\mathrm{DES}}\Delta$, then $\tilde{d} = d$ and the original RANS model, Spalart-Allmaras for the present case, is used. On the other hand, outside the boundary layer where $d > C_{\mathrm{DES}}\Delta$, then $\tilde{d} = C_{\mathrm{DES}}\Delta$, and for the present simulation, the Spalart-Allmaras model serves as a one-equation SGS model for the LES [63].

In other words, when applying equation 2.8 to the cells located outside the boundary layer, the production and destruction terms are rather balanced, as a result it can be established that $\tilde{S}\tilde{\nu} \cong \left(\frac{\tilde{\nu}}{\tilde{d}}\right)^2$, which in reality means $\tilde{\nu} \cong \tilde{d}^2\tilde{S}$, when using the LES (SGS) sub-model inside the DDES model, the previous equation can be given as $\tilde{\nu} \cong (C_{DES}\Delta)^2\,\tilde{S}$ and the same transport equation for Spalart-Allmaras model is employed for the SGS model.

2.3 Parameters Used to Non-Dimensionalize the Results

In order to be able to compare the present results with the previous researchers' ones, the majority of the graphs introduced in this paper were made dimensional, yet, the final graphs in which for a given Reynolds number several parameters are compared, the results are presented in non-dimensional form. To proceed with the non-dimensionalization and in order to generate graphs showing values around unity, the following dimensional parameters were employed. All dimensional parameters are based on values obtained for the baseline oscillator case at Reynolds number 16,034.

The FO outlet mass flow was non-dimensionalized using the maximum value of the mass flow measured at one of the FO outlets. The maximum inclination angle of the main jet at the mixing chamber inlet was used to non-dimensionalize the jet inclination angle at the mixing chamber inlet. The maximum momentum measured at one of the FC outlets was employed to non-dimensionalize the momentum acting over the jet. The maximum value of the stagnation pressure measured at the mixing chamber outlet converging walls was defined as the characteristic pressure for non dimensionalization. The characteristic length was chosen to be the oscillator's power nozzle inlet hydraulic diameter D_h, and the fluid velocity at the oscillator's power nozzle was employed as the dimensional characteristic velocity.

One of the main concepts which needs to be understood in the present paper is the momentum associated with the fluid in a given section. Equation (2.14) defines this concept for any of the two FC outlets.

$$M = \dot{m}_{out} \times V_{out} + P_f \times S_{out} = \dot{m}_{out}^2/(S_{out} \times \rho) + P_f \times S_{out} \tag{2.14}$$

where $\dot{m}_{out}, V_{out}, S_{out}$, and P_f are respectively the mass flow, the spatial average fluid velocity, the surface at the FC outlet, and the pressure instantaneously appearing at any of the FC outlets, and ρ is the fluid density.

The momentum associated with the flow at any given section consists of two parts: the momentum associated with the fluid mass flow and the one associated with the fluid pressure. To evaluate the mass flow momentum term, it is required to know the instantaneous mass flow, the fluid density, and the section through which the fluid flows. In the present paper, the instantaneous mass flow flowing though each grid cell belonging to the surface to be evaluated was determined. The total mass flow was obtained simply by adding the elementary mass flow of each cell corresponding to the chosen surface. The pressure momentum term was obtained when multiplying the instantaneous pressure acting on each cell by the cell surface, and then adding the elemental pressure momentum terms corresponding to the surface under study. The different momentum terms will be obtained at the feedback channel outlets. The net momentum characterizing the overall forces acting on the main jet lateral surfaces will consider the pressure and mass flow momentum terms acting on both feedback channels outlets.

2.4 Results

2.4.1 Original Fluidic Oscillator at Reynolds Number 16,034

As already presented in many of the studies on FO, see for example [9,41–43,45,46,53], the MC and FC internal flow configuration along a complete oscillation period was divided in several equally spaced time steps. In the present study, the streamlines and pressure contour plots at Reynolds number 16,034 are divided into six time steps, which correspond to 1/6 of a typical oscillation period. This information is introduced in figure 2.4. Notice that the streamline plots are almost identical to the ones experimentally obtained by [41], although in the present case, the pressure contours are also implemented and will be used to clarify the origin of the forces responsible of the oscillation. In order to properly understand the flow configuration and the forces acting inside the FO, figures 2.5 and 2.6, which introduce the dimensional values of the oscillator and FC volumetric flows, the MC inlet, and outlet jet inclination angles, the pressure at different locations inside the MC, and the net momentum acting on the jet at the feedback channels outlet will be linked with figure 2.4. Each graph in figures 2.5 and 2.6 is divided into six equally spaced time steps, see the dotted

vertical lines, which correspond to each of the time periods described in figure 2.4. This will allow to carefully evaluate the value of each parameter at each time period.

The initial time in figure 2.4, $T = 0$, was chosen at the instant at which the volumetric flow across the FO upper outlet was minimum. At this particular instant there is some negative flow entering the oscillator across the oscillator upper outlet, see figure 2.5a at a dimensional time of 1.255 s. The jet inside the MC is moving down and it is about to reach its lowest position, figure 2.5c clarifies this point. According to figure 2.4a, there is a considerable flow along the upper feedback channel, from figure 2.5b it is observed that such volumetric flow is almost at its maximum value and it tends to decrease over time. When comparing figure 2.5a,b, it is stated that the FC volumetric flow is one order of magnitude smaller than the oscillator volumetric flow. This characteristic agrees perfectly well with what was found in [34, 43] working with air, comparing figure 2.5a,b from the present paper with figures 6 and 8 in [43] or with figures 3 and 5 from [34]. At this initial instant, the volumetric flow along the lowest FC is almost zero, see figure 2.5b. The spatially averaged pressure at the MC upper converging surface is about 4000 Pa higher than the one corresponding to the lower converging wall, this can be seen in figures 2.4d and 2.6a, and both pressures are about to decrease versus time. Also, the pressure at the upper FC outlet, see figure 2.6b, is about 4000 Pa higher than the one appearing at the lower FC outlet, indicating there must be a force acting on the main jet inlet which pushes the jet down. The net momentum acting onto the lateral sides of the jet at the MC inlet is obtained when considering the pressure and mass flow on both FC outlets. The pressure at each grid cell multiplied by the cell area and summed across a feedback channel outlet provides the momentum due to the pressure at this particular section. However, the momentum due to the pressure needs to be added to the momentum due to the FC mass flow, which was determined via dividing the instantaneous mass flow raised to the power of two by the section of the feedback channel outlet and the fluid density, $M = ps + \dot{m}v = ps + \dot{m}^2/(\rho s)$. Each separate net momentum, pressure, and mass flow term on both FC outlets, and the addition of both terms, is presented in figure 2.6d, from which it is stated that the net momentum due to the mass flow is almost negligible when compared to the one generated by the pressure. The net momentum presented in figure 2.6d is almost the same as the net momentum due to pressure term, then the forces due to the FC mass flow are over an order of magnitude smaller. The net momentum at this initial time is negative, indicating the jet is being pushed down, in fact the net momentum has just reached its maximum negative value. Notice there is a very good agreement between figure

2.6b,d, in fact, the origin of figure 2.6d is the temporal pressure difference between both feedback channel outlets.

Going back to figure 2.4a, it is observed that the bubble located between the jet and the MC lower borders is about to reach its minimum volume, while the bubble above the jet is almost at its maximum dimension. Notice that these bubbles consist of a series of small vortical structures, instead of a main large structure as defined in previous papers, see for example [41, 43]. This is probably due to the high accuracy of the turbulent model employed along with a very realistic three dimensional model presented in this research. When analyzing the vortical structures generated, it needs to be considered that the Reynolds number studied is relatively high, hence the flow is chaotic. Evaluating a different FO configuration and using the Q criterion, the internal vortical structures were presented in [53].

At this initial instant, the jet leaves the FO through the lower outlet. On both sides of the (EC), a large vortex is observed, the lower vortex is smaller than the upper one and has a much higher intensity, see from figure 2.4d that the pressure is about 32% smaller than the upper one, indicating that the lower vortex turns much faster. The pressure inside the mixing chamber is quite homogeneous, and some particular low pressure spots are to be seen where the main lower and upper bubbles are located. The particularly low pressure spot located below the jet indicates the Coanda effect appears in this location. According to [66], from this low pressure location and when the flow is considered as compressible, weak expansion waves are being generated.

At this initial instant, on the MC upper converging surface, the pressure is about 16% higher than the one existing on the MC lower converging surface. This particularly high stagnation pressure point will move to the lower converging surface in the next time period $T = 1/6$, compare figure 2.4d,e. It appears the jet impinges alternatively on these surfaces during a small period of time. According to Gregory and Tomac [66], under compressible flow conditions, weak compression pressure waves are generated alternatively at these locations. The FC upper branch has a slightly higher pressure than the lower branch, see figure 2.4d, and this pressure difference between both feedback channels and measured at the feedback channels outlets is presented in figure 2.6b. The particular pressure difference between the upper feedback channel inlet and outlet is introduced in figure 2.6c. The pressure is very much alike along the channel, being just slightly higher at the inlet, but this small pressure difference is what drives the flow along the feedback channel. It is at this point relevant to clarify that all graphs presented, especially the pressure ones, show very scattered curves. The origin of this lack of smoothness is the intrinsic instabilities associated

with the chaotic flow. Another point to discuss is that the curves presented are not fully sinusoidal. As the flow inside the mixing chamber is fully turbulent, the jet inside the mixing chamber does not follow a perfect and symmetrical displacement, therefore the periods of all variables are not completely sinusoidal.

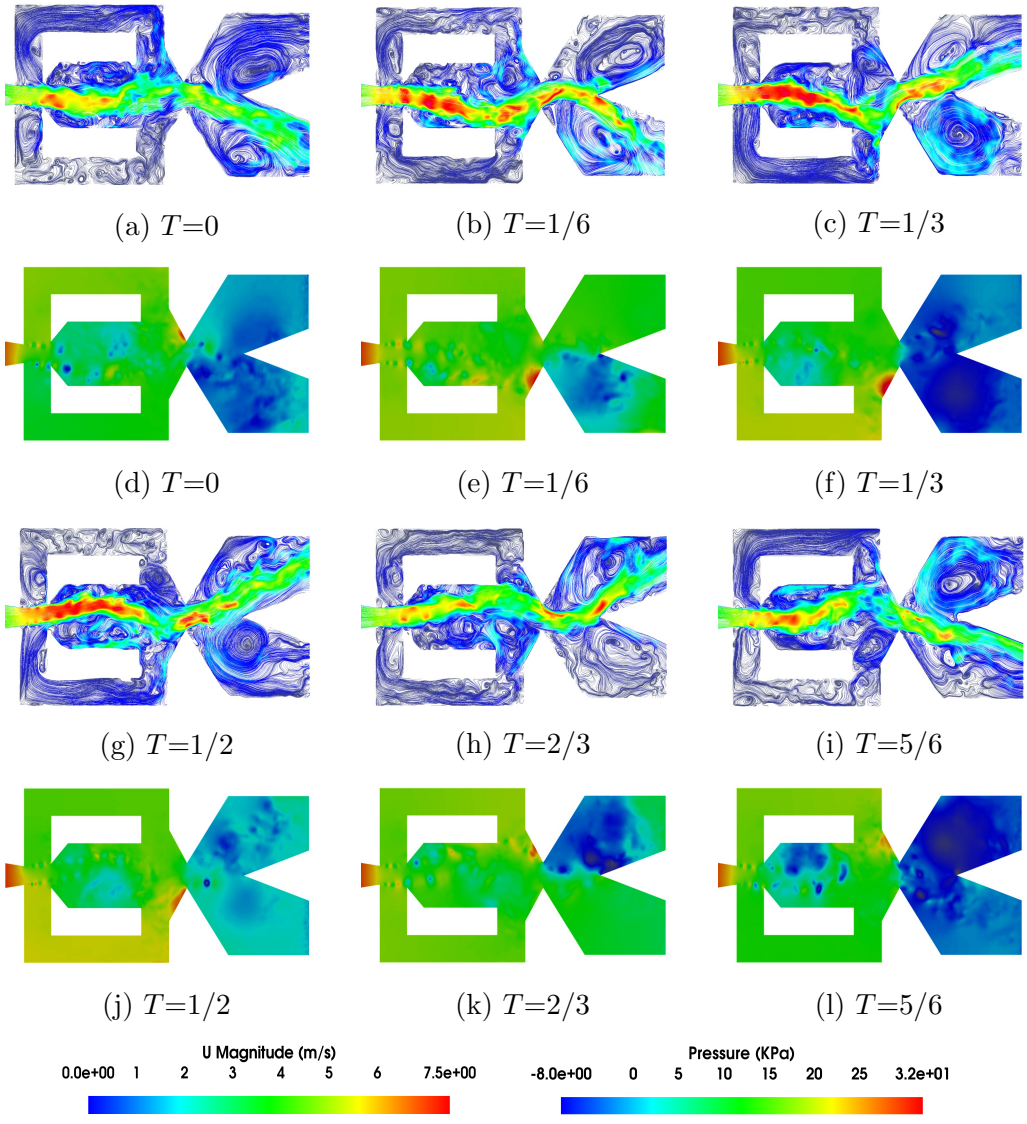

(a) T=0 (b) T=1/6 (c) T=1/3

(d) T=0 (e) T=1/6 (f) T=1/3

(g) T=1/2 (h) T=2/3 (i) T=5/6

(j) T=1/2 (k) T=2/3 (l) T=5/6

Figure 2.4: Mixing chamber period of oscillation divided in six equally spaced times, Reynolds number 16,034. Figures a, b, c, g, h and i, present the streamlines plots, figures d, e, f, j, k and l, introduce the pressure contours.

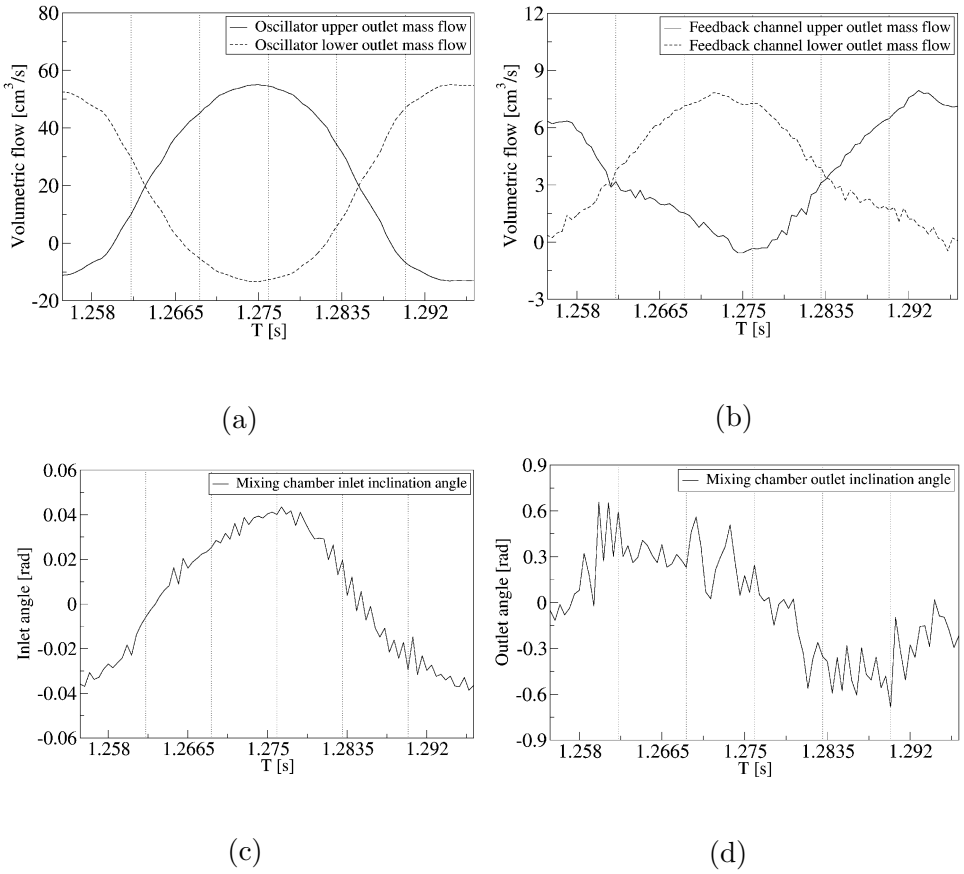

Figure 2.5: Mass flow through the oscillator upper and lower outlets, (**a**); mass flow through the feedback channels, (**b**); mixing chamber inlet jet inclination angle, (**c**); and mixing chamber outlet jet inclination angle, (**d**). Reynolds number 16,034.

In the next time period $T = 1/6$, the jet inside the MC has reached its lowest position and it is starting to move up. Most of the flow is leaving the oscillator through the lower oscillator outlet, but some amount of flow exits the oscillator through the upper outlet, see figures 2.4b and 2.5a. Two large vortices can be observed at the external chamber upper and lower outlets. The vortex associated with the upper outlet is much bigger than the one appearing at the lower outlet, yet the intensity associated with the lower vortex is higher, as can be extracted from the observation of the pressure field in figure 2.4e. In any case, when comparing figure 2.4d,e it is observed that the external chamber lower vortex has decreased its intensity versus the previous time period, which is because the mass flow leaving through the lower outlet is now smaller than the previous time period. The volumetric flow along both feedback channels is very similar and flows in both cases from the feedback channels inlets to the outlets. This fact can be observed from the streamlines plot presented in figure 2.4b and from the FC volumetric flow at a dimensional time of 1.2635 s, figure

2.5b. The maximum pressure is now to be observed at the MC lower converging wall, see figures 2.4e and 2.6a, which is why the lower FC has a slightly higher pressure than the upper one, yet as already mentioned, the volumetric flow is almost the same in both feedback channels, which seems to indicate that there is a phase lag between the instant an FC is pressurized and the instant the flow starts moving along the FC. In fact, at this particular instant and according to figure 2.6b, the pressure on both feedback channel outlets is almost the same, although on the verge of being higher at the lower FC outlet. From the information presented in figure 2.6b, the pressure term of the net momentum applied to the jet entering the FO is obtained, see figure 2.6d, where it can be stated that at this instant, the net momentum is almost zero. Figure 2.5c,d presents the jet inclination angle at the mixing chamber inlet and outlet, as already introduced by Seo et al. [9]. The jet inclination angle at the MC inlet is still negative and tending to zero, while at the MC outlet the jet inclination angle is now positive, see figures 2.4b and 2.5d. It is interesting to realize that at this instant the jet leaving the MC is facing upwards, but the jet still leaves the oscillator through the lower outlet, which is due to the reattachment the jet is having to the external chamber lower wedge surface.

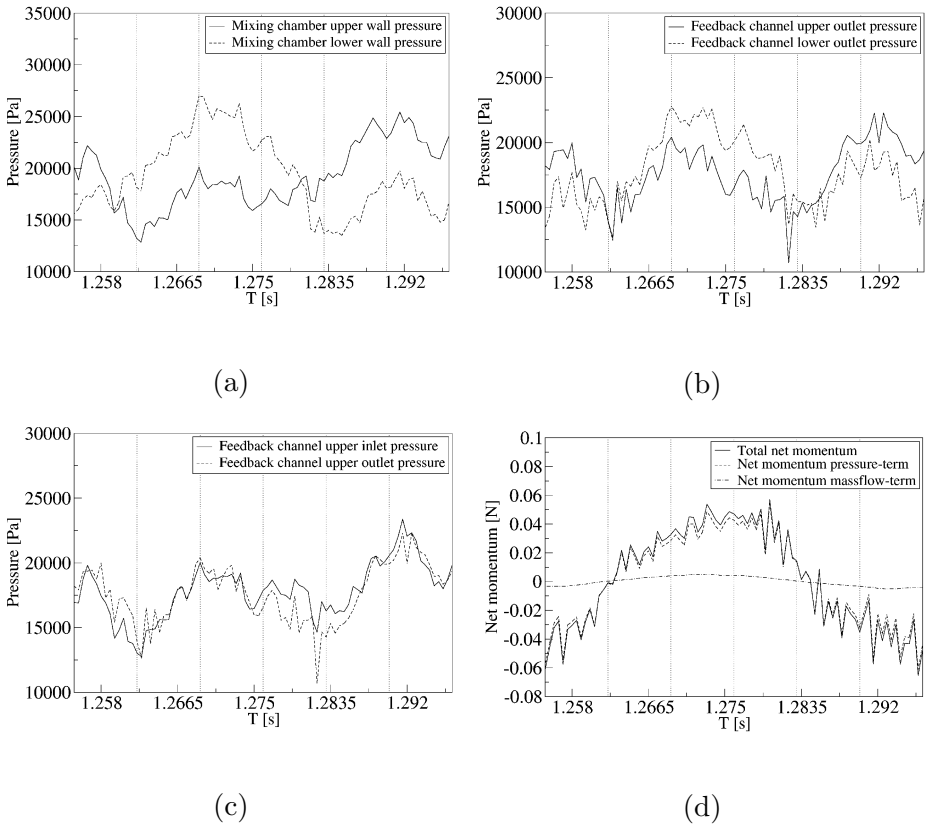

Figure 2.6: Mixing chamber outlet converging walls pressure, (**a**); pressure at both feedback channels outlets, (**b**); and pressure at the feedback channel inlet and outlet, (**c**). Overall momentum at the feedback channels outlet, which is acting on the jet entering the mixing chamber. The momentum is split in the component due to the mass flow flowing along the feedback channels and due to the pressure acting onto the feedback channels outlet (**d**). Reynolds number 16,034.

When moving to the next time period, $T = 1/3$, it is observed that the jet is now entering the MC almost perpendicular to it, see figure 2.4c and also figure 2.5c, where it can be stated that the jet inclination angle at the mixing chamber inlet is slightly positive. The flow is leaving the oscillator through the upper outlet, see figures 2.4c and 2.5a. This is why at the MC outlet, the jet inclination angle is positive and having almost its maximum value, figure 2.5d. The two typical vortices respectively appearing at each side of the external chamber are clearly seen, at this particular instant. The lower vortex, which is located at the center of the lower outlet, has a slightly higher intensity than the upper one, see figure 2.4f. This is particularly relevant because at this instant the jet leaves the actuator through the upper outlet, which in reality indicates that the jet has just flipped from the lower outlet to the upper one. Inside the MC, the maximum pressure is localized at the lower converging

surface, notice that the jet impinges on this surface, figure 2.4f. As a result of the location of the maximum stagnation pressure point, the lower feedback channel is pressurized and a large amount of flow is going from the feedback channel inlet to the outlet, with figures 2.4c,f and 2.5b are showing this situation. Despite the fact that the flow on the lower FC is almost at its maximum, on the upper FC there is still a small amount of flow from the FC inlet to the outlet. Regarding the streamlines at the lower FC, it is interesting to recall the work undertaken by Woszidlo et al. [43], where they defined the existence of a bubble at the FC inlet, which perfectly fits with what can be seen in figure 2.4c. At this particular instant, the pressure between the lower and upper mixing chamber converging walls is about 6500 Pa, also the pressure difference between the feedback channel lower and upper outlets reached a particularly high value of about 3000 Pa, see figure 2.6a,b. As a result of the relevant pressure difference at the feedback channel outlets, the positive net momentum acting on the jet is about to reach its maximum value, see figure 2.6d.

The next time period corresponds to $T = 1/2$, see figure 2.4g,j. The jet inside the MC is about to reach its maximum position, the flow is leaving the actuator through the upper outlet, and the jet inside the MC is still impinging onto the lower converging surface. The stagnation pressure is lower than the one existing in the previous time period. The pressure on the lower converging wall, see figures 2.4j and 2.6a, is much higher than the one in the upper converging wall. The lower FC is still pressurized, and the flow rate going from the lower FC inlet to the outlet is still very high, on the other hand the flow flowing along the upper FC is almost zero, see figures 2.4g and 2.5b. The pressure on the lower FC outlet is, according to figure 2.6b, about 4000 Pa higher than the one on the upper FC outlet. This is why the net momentum acting on the jet inlet is positive, pushing the jet upwards, figure 2.6d represents this case.

At $T = 2/3$, figure 2.4h,k, the jet at the MC has reached its highest position and is beginning to move down. At the MC inlet, the jet inclination angle is still positive, but tending to zero, see figure 2.5c. At the MC outlet, the jet inclination angle has changed from positive to negative, see figures 2.4h and 2.5d, but the jet still leaves the FO through the upper outlet, the volumetric flow through the FO upper outlet is represented in figure 2.5a. The vortex generated at the upper part of the external chamber is now more energetic than the one appearing at the lower external chamber outlet, and figure 2.4h,k clarifies this point. From figure 2.6a it is observed that the maximum stagnation pressure has moved to the upper converging wall, and the upper FC is about to be pressurized. The pressure at both feedback channel outlets is very much the same (figure 2.6b), as a result the volumetric flow along both feedback

channels is also very similar, see figure 2.5b, and flows from the feedback channels inlets to outlets. The net momentum applied to the jet entering the MC, as can be observed in figure 2.6d, is almost null, this is clearly understandable when realizing that the pressure on both feedback channels outlets is nearly the same, as represented in figure 2.6b.

Finally, when the time period is $T = 5/6$, the jet is located at the center of the MC and descending down, the jet inclination angle at the MC inlet is slightly negative and so is the jet at the MC outlet, see figures 2.4i and 2.5c,d. The flow is leaving the FO through the lower outlet, in fact, there is some reverse flow entering the FO through the upper outlet, as presented in figure 2.5a. At the external chamber upper outlet, a clear vortex is being observed, as can be seen in figure 2.4l. This vortex has a higher intensity than the one appearing at the external chamber lower outlet. This is particular because, as previously mentioned, the fluid leaves the oscillator through the lower outlet, which in reality indicates that the jet at the external chamber has just flipped over from up to down. Inside the MC, the jet is still impinging on the upper converging surface, figure 2.4l, as a result there is a relatively large flow moving along the upper FC. On the lower FC there is a small amount of flow still going from the FC inlet to the outlet, see figure 2.5b. The pressure difference between the upper and lower converging walls is at its maximum, about 6000 Pa, and so is the pressure difference between the feedback channel upper and lower outlets, about 3000 Pa, see figure 2.6a,b, respectively. As a result of the pressure difference existing between the feedback channels outlets, the net momentum acting on the lateral surfaces of the jet entering the mixing chamber is negative, see figure 2.6d, and the jet is being pushed down.

Based on the previous explanations, the following statement is made: What is needed to flip the jet from one side to another is a pressure gradient between the feedback channel outlets. Once a pressure threshold is overcome, the jet starts bending and the mass flow through the feedback channels provides the required volume for the mixing chamber bubbles to expand. The required pressure threshold originates at the mixing chamber outlet converging surfaces.

Figure 2.7 introduces, for the three Reynolds numbers studied, 8711, 16,034, and 32,068, the volume of fluid transferred through each FC during half cycle and during a full cycle. The estimated mixing chamber bubble volume increase, as the main jet flips from one side to the other, is also presented. According to the work undertaken by [42, 43], the maximum bubble volume remains constant and independent of the Reynolds number employed, and the volume of fluid transferred by the feedback

channel, according to [9, 42, 43], was always equal to the bubble volume growth. Figure 2.7a shows that both volumes are independent of the Reynolds number, yet they are not equal, which means the volume of fluid required for the mixing chamber bubble to expand may not be fully provided by one of the feedback channels flow, in fact both FCs are responsible for the MC bubble growth. It also appears that some of the required volume is provided by the mixing chamber incoming jet, and figure 2.7b clarifies this point. Notice that the jet expands as it enters the MC, filling up part of it.

At this point, it is necessary to remember that most of the previous work on fluidic oscillators was done in 2D, and even the results obtained experimentally were based on 2D PIV measurements. The present simulations are 3D, and this fact is likely to explain the small discrepancies found regarding the origin of the fluid required for the mixing chamber bubble to grow. In order to highlight the importance of performing the study in 3D, figure 2.8 introduces instantaneous slices of the mixing chamber and of the FO output exits. Clearly, the flow cannot be considered two dimensional at any point and clarifies the difficulty of measuring the exact bubble growth in the mixing chamber.

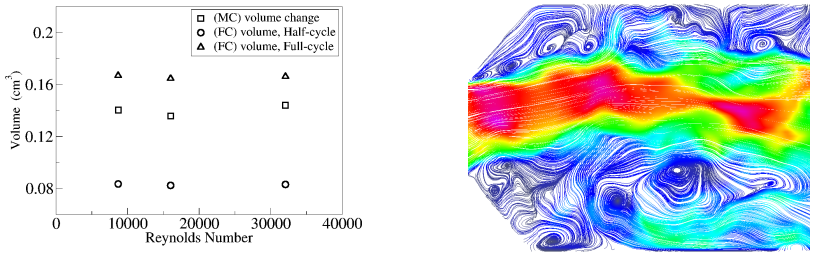

(a) (b)

Figure 2.7: (**a**) Mixing chamber volume growth at three different Reynolds numbers, 8711, 16,034, and 32,068. Comparison with the fluid volume provided by the FC. (**b**) Zoomed view of the mixing chamber inlet, where it is seen that part of the incoming fluid helps the mixing chamber bubble to grow.

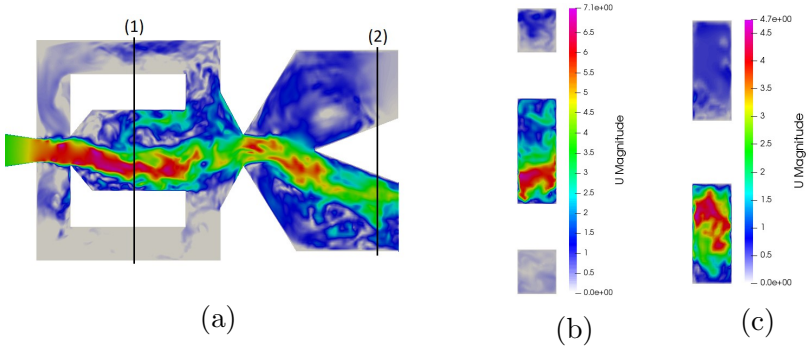

(a) (b) (c)

Figure 2.8: Instantaneous velocity fields at the, (**a**) mixing chamber, (**b**) spanwise section, slice (1), (**c**) spanwise section at the fluidic oscillator outlet, slice (2). Reynolds number 16,034.

A good way to illustrate the vortical structures appearing inside the FO is by means of isosurfaces based on the Q criterion, as presented in figure 2.9. The isosurfaces are colored by the vorticity about the Z axis. The color blue indicates the structures turn clockwise, the red color is associated with counterclockwise rotation. The snapshot sequence presented in figure 2.9 characterizes a full oscillation period divided into six evenly spaced time steps, which match with the time steps introduced in figure 2.4. It is interesting to see the coexistence of positive and negative structures at any instant. When the jet inside the MC is inclined downwards, $T = 0$ and $T = 1/6$, the negative structures dominate the flow, but the counterclockwise structures are the predominant ones when the jet inside the MC faces upwards, $T = 1/2$ and $T = 2/3$. The vortical structures inside the FCs and the external chamber (EC), which could clearly be seen in figure 2.4, can hardly be seen in figure 2.9, indicating that their vorticity is at least an order of magnitude smaller than the one associated with the MC vortical structures. The large coherent negative structures which can be seen in figure 2.9a,b break and move downstream of the MC at time $T = 1/3$. In the next two time periods, in figure 2.9d,e, coherent positive structures dominate the MC flow, also moving downstream, while breaking up on the next time step.

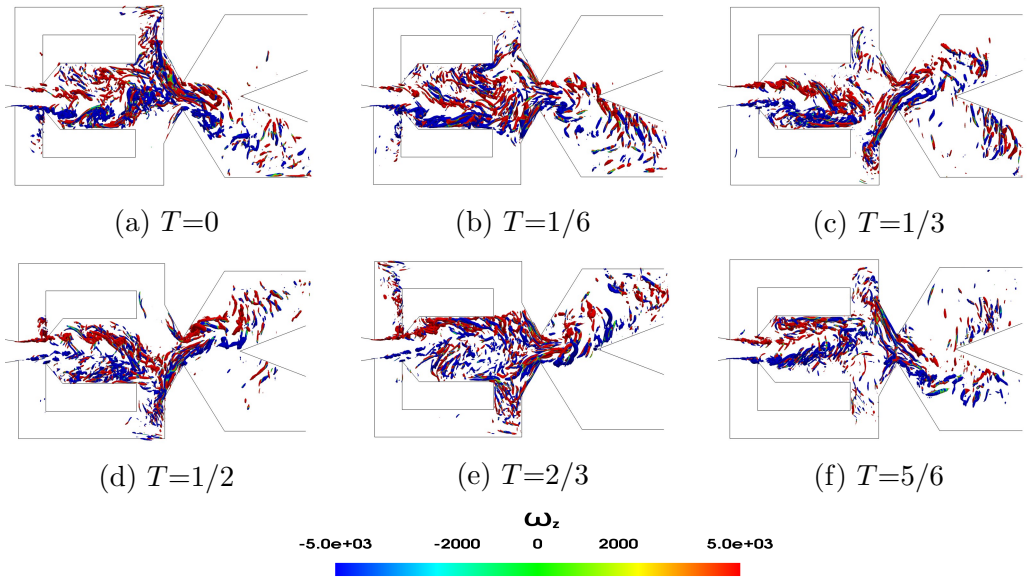

Figure 2.9: Q criterion at the mixing chamber period of oscillation divided into six equally spaced times, Reynolds number 16,034.

2.4.2 Variation of the Fluidic Oscillator Momentum with the Reynolds Number

When evaluating the forces which trigger the flapping motion of the incoming jet inside the mixing chamber, and according to previous studies, it seemed that the mass flow flowing along the feedback channels had a high degree of relevance. In the previous section, see figure 2.6d, the net momentum generated by the FC mass flow was compared with the one generated by the pressure, and both net momentums were determined at the feedback channels outlets. The conclusion was that the net momentum due to pressure is the relevant one. But one question still remains: Is the net momentum due to the pressure always the relevant one? In the present section and for three different Reynolds numbers, 8711, 16,034, and 32,068, the net momentum acting on the fluidic oscillator incoming jet and due to the feedback channels flow is compared with the net momentum generated by the static pressure. Figure 2.10 presents, for the three Reynolds numbers evaluated, both net momentums acting on the MC incoming jet lateral sides. The net momentum due to the static pressure and regardless of the Reynolds number studied is over one order of magnitude higher than the one generated by the feedback channel mass flow. The overall net momentum is mostly due to the pressure term, as shown in figure 2.6d for Reynolds number 16,034. The conclusion is, that for the present FO configuration, the mass flow transported by the FCs plays a negligible role when considering the flapping movement of the

jet inside the MC. The flapping movement is driven by the pressure difference acting onto the main jet lateral surfaces, the feedback channel output surfaces.

From figure 2.10 it is also observed that the net momentum due to the pressure field appears to be rather scattered. The curve is not smooth, and the authors believe this is due to the turbulence intensity associated with the chaotic flow. Another point to be highlighted from figure 2.10 is that the amplitude of the net momentum due to the pressure term increases as the Reynolds number increases. To understand why this is so, it just needs to be remembered that the kinetic energy $V^2/2$, and therefore the dynamic term of the stagnation pressure $P_{0d} = \rho V^2/2$, increases with the fluid velocity to the power of two. The peak to peak amplitude of the stagnation pressure, measured in Pascals, at the mixing chamber converging walls and as a function of the Reynolds number, was found to be having the following relation, $PA_{peaktopeak} = 6.476 \times 10^{(-5)} \times (Re)^{1.985}$. The reason why it is not increasing as a function of the velocity to the power two is due to the inclination of the MC converging walls where the jet impinges.

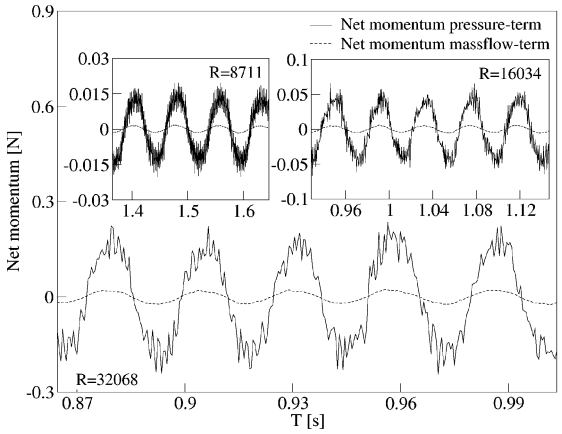

Figure 2.10: Net momentum pressure and mass flow terms for different Reynolds numbers.

For the Reynolds numbers studied, the net momentum peak to peak amplitude, given in Newtons, increases with the Reynolds number increase and obeys to the following expression, $MA_{peaktopeak} = 6.267 \times 10^{(-10)} \times (Re)^{1.981}$. At this point, it is important to recall that the fluid net momentum has two terms, the static pressure term and the mass flow one, the second being much smaller than the first. The fluid velocity increases linearly with the Reynolds number increase, the net momentum amplitude increases with the stagnation pressure increase at the MC converging walls, and the stagnation pressure increase is a function of the square of the fluid velocity,

$P_{0d} = \rho V^2/2$. Therefore, it seems the net momentum amplitude should increase as a function of the Reynolds number to the power of two, yet this is not happening and the reason why is related to the stagnation pressure increase, which in reality increases to the power of 1.985 as presented in the previous paragraph. The reason why the momentum increases to the power 1.981 instead of 1.985, which is the power increase of the pressure amplitude, is due to the pressure losses existing between the MC outlet inclined walls and the FC outlet. In reality, the fluidic oscillator internal configuration, and especially the angle of the MC converging walls, play a decisive role in the relation fluid velocity and stagnation pressure. Figure 2.11 shows the frequency (FFT) and amplitude from the net momentum as discussed in figure 2.10 for different Reynolds numbers studied. Notice that the frequency is matching with the frequency calculated based on the FO outlet mass flow as shown in figure 2.3b.

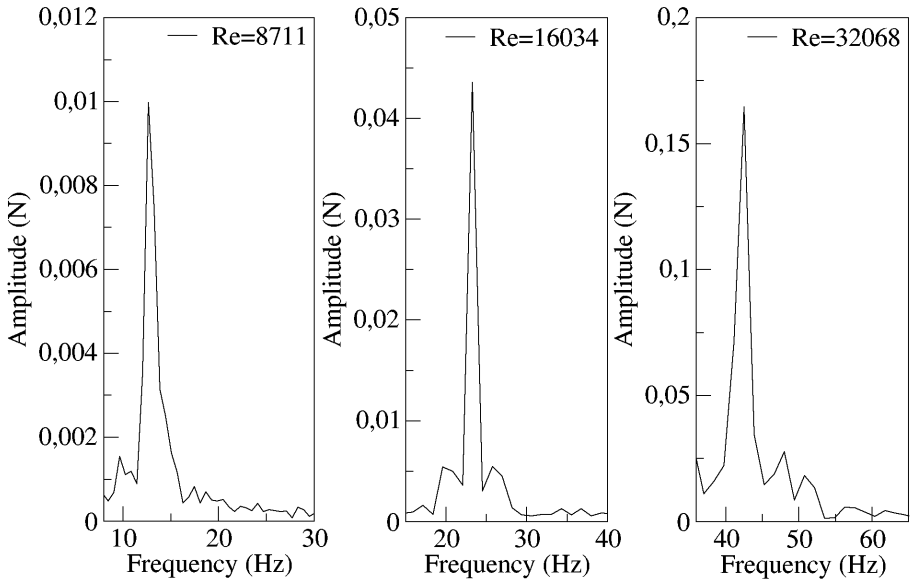

Figure 2.11: Fluidic oscillator net momentum frequency (FFT) and amplitude for different Reynolds numbers studied.

The statements made in the previous section were: the oscillation of the FO is triggered by the pressure difference between the FC outlets, and this pressure difference is generated at the MC outlet converging surfaces. In order to properly understand these statements, the following dynamic non-dimensional parameters were compared in figure 2.12: the stagnation pressure at the MC lower converging surface, the net momentum acting on the jet, the MC incoming jet oscillation angle, and the FO upper outlet mass flow. These parameters were compared for the three Reynolds numbers studied, 8711, 16,034, and 32,068.

The first thing to realize, when comparing the figure 2.12a–c, is that the outlet mass flow frequency and peak to peak amplitude increase as the Reynolds number increases. During approximately one fourth of the period the volumetric flow at the FO outlet enters the oscillator, the volumetric flow entering the oscillator increases as the Reynolds number increases, yet the time at which this is happening keeps being approximately one fourth of the oscillation period. The main conclusion from figure 2.12a–c is that there is a perfect agreement between the dynamic parameters evaluated. This agreement exists regardless of the Reynolds number studied. The stagnation pressure peak to peak amplitude increases as the Reynolds number increases, and the exact dimensional relation previously defined was $PA_{peaktopeak} = 6.476 \times 10^{(-5)} \times (Re)^{1.985}$. The net momentum applied to the jet, the FO output mass flow, and the MC inlet inclination angle follow the pressure dynamics generated at the MC outlet converging walls. Yet a small phase-lag between the stagnation pressure fluctuation and the net momentum acting on the MC incoming jet, to the order of 0.0017 s, is to be observed at Reynolds number 16,034, the phase-lag increases to 0.00287 s for a Reynolds number of 32,068.

Under compressible flow conditions, the time required by the pressure waves to travel from the FC inlet to outlet directly depends on the speed of the pressure waves, which is defined as $C = \sqrt{\beta/\rho}$, and considering the bulk modulus and the density for the working fluid, water, the resultant speed is of $C = 1460$ m/s. This speed is meant to be infinite when the fluid is considered incompressible. In any case and considering the actual FC length, the phase lag between all parameters studied has to be negligible regardless of the Reynolds number employed. Therefore, the phase lag observed in figure 2.12 is believed to estimate the time required for the pressure to be established at the FC outlets. In figure 2.7, it was shown that the maximum volume between the MC oscillating jet and the lateral walls remained constant and independent of the Reynolds number. Figure 2.12 also presents the jet inclination angle at the MC inlet. Notice that the maximum inlet inclination angle remains constant and independent of the Reynolds number, therefore explaining why the maximum volume at the MC remains constant.

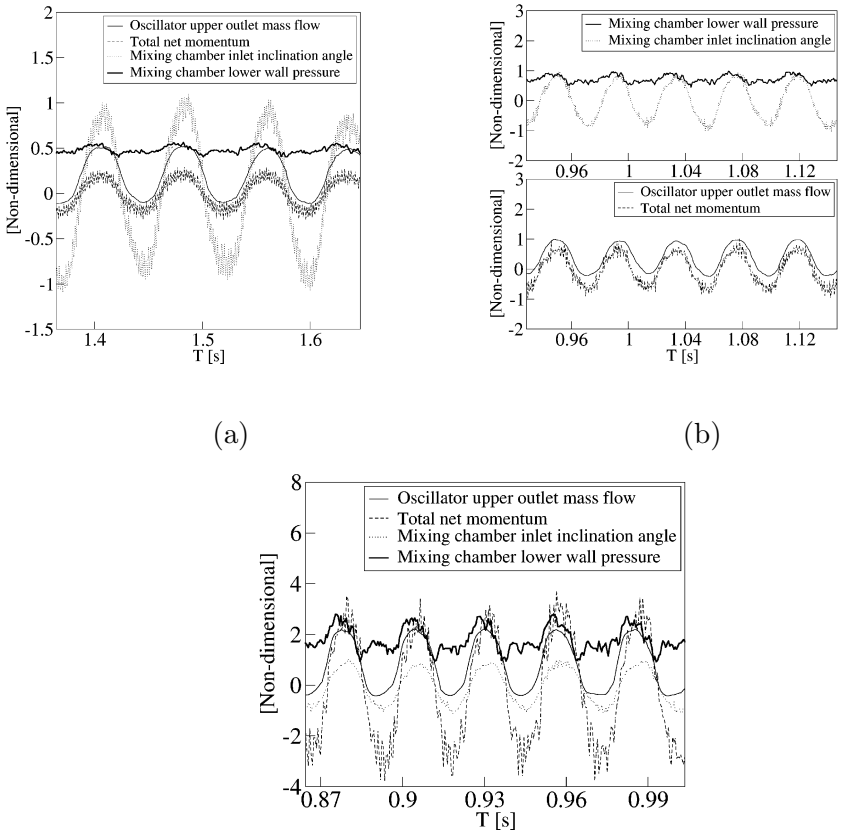

Figure 2.12: Comparison of the stagnation pressure at the mixing chamber lower converging surface, the total momentum acting on the jet, the mixing chamber inlet oscillation angle, and the oscillator output mass flow. Reynolds numbers, 8711 (**a**), 16,034 (**b**), 32,068 (**c**).

2.5 Conclusions

A careful 3D-CFD evaluation of a fluidic oscillator under turbulent conditions has been performed. Numerical results obtained were compared with previous experimental works, showing good agreement. For the Reynolds numbers studied, the flow is chaotic, therefore three dimensional simulations are needed to properly characterize the flow structures. The main jet oscillation at the mixing chamber inlet and outlet has been linked with the feedback channels mass flow, the oscillator mass flow, the pressure at the mixing chamber converging walls, and the pressure at the feedback channels outlet. The conclusion is that the forces acting onto the incoming jet at the mixing chamber inlet and feedback channel outlets are mostly due to the static pressure.

The net momentum pressure term acting onto the lateral sides of the mixing chamber incoming jet directs the oscillation of the jet in the MC, and therefore the oscillation at the fluidic oscillator output. For the actual FO, the momentum oscillation is generated by the stagnation pressure oscillation occurring at the mixing chamber outlet converging surfaces. The momentum due to the mass flow flowing along the feedback channels plays a negligible role, when considering the forces driving the oscillation. The amplitude of the net momentum oscillation is directly linked with the maximum and minimum values of the stagnation pressure appearing at the mixing chamber outlet converging surfaces, and the amplitude of the stagnation pressure increases the Reynolds number increases, according to the function $PA_{peaktopeak} = 6.476 \times 10^{(-5)} \times (Re)^{1.985}$. Regardless of the Reynolds number employed, the total dynamic momentum acting on the jet always follows the stagnation pressure dynamics observed at the mixing chamber converging walls, therefore indicating that the origin of the fluctuations is the same for all Reynolds numbers studied.

Chapter 3

The effect of some design modifications.

3.1 Introduction

The reduction or enhancement of the lift and drag forces on any bluff-body via modifying the boundary layer employing Active Flow Control (AFC), must be regarded as a novel technology. The use of pulsating flow in (AFC) applications, allows reducing the energy required to modify the boundary layer around a given bluff body. Zero Net Mass Flux Actuators (ZNMFA) and Fluidic Oscillators (FO), are two good candidates to generate pulsating jets, the later having the advantage of employing no moving parts, therefore increasing its reliability. Although there exist few canonical shapes on (FO), it is of major interest to investigate the (FO's) performance when modifying their internal dimensions, then oscillation amplitude and frequency are expected to change. The present paper aims to bring some light to this matter. One of the initial evaluations of the fluidic oscillators performance when modifying its internal shape, was made in 2013 by Bobusch et al. [41], they made some suggestions regarding the mixing chamber inlet width in order to modify the fluidic actuator output frequency. Vatsa et al [55] studied, using the lattice Boltzmann method and based on the solver PowerFLOW, two different configurations of sweeping jet fluidic oscillators (FO), which were further analyzed in 2015 by Ostermann et al [34]. The two (FO) considered, resemble the ones studied by Bobusch et al [41] and Aram et al [8] respectively. Velocity profiles generated by the (FO) in quiescent air were compared with experimental data, results showed that the (FO) having sharp internal corners, similar to the one employed in [41], generated an output velocity distribution much more homogeneous than the oscillator having rounded internal corners. The results from the two different configurations were compared to identify similarities

and differences between the designs, suggestions of how these differences may affect applications, were made.

Woszidlo et al [43], studied the same configuration previously evaluated by Gartlein et al [42]. Both configurations resemble the one studied by Bobbush et al [41], the main differences resided in the output shape. In Woszidlo et al [43] and Gartlein et al [42], just a single output was considered. In this new paper, Woszidlo et al [43], focused their attention in analyzing the flow phenomena inside the mixing chamber and the feedback channels. They also observed that, the increase of the mixing chamber inlet width was tending to increase the output frequency, and rounding the feedback channels would diminish the generation of the separation bubbles on these channels.

Slupski and Kara [11], studied using 2D-URANS with the software Fluent a range of feedback channel (FC) geometry parameters, the sweeping jet actuator configuration was the same as the one analyzed by Aram et al [8]. The effects of varying the feedback channel height and width for different mass flow rates were studied. All the simulations were performed for a fully-turbulent compressible flow, using SST k-omega turbulence model. It was found that, oscillation frequencies increased with increasing feedback channel height, up to a certain point and then remained unaffected, however, frequencies decreased by further increasing the feedback channel width.

An experimental and numerical study of a fluidic oscillator which could generate a wide range of frequencies (50-300 Hz), was studied by Wang et al [35]. Their study focused on the oscillation frequency response for different lengths of the feedback channels, 2D compressible simulations were performed using sonicFoam with k-epsilon as turbulence model. An inverse linear relation between frequency and the length of feedback loops was observed, frequency increased when decreasing the feedback channel length.

In 2018, the same configuration previously employed by [41], although now using a single exit, was numerically evaluated in 3D at Reynolds 30000 using the SST turbulent model by Pandley and Kim [45]. Two geometry parameters, the mixing chamber inlet and outlet widths were modified. They observed a significant effect of the flow structure and the feedback channel flow rate when modifying the inlet width, negligible effects were observed when modifying the outlet width. The output frequency and amplitude effects whenever the (FC) and the mixing chamber (MC) lengths were modified, was studied using a 2D numerical model by Seo et al. [9], the fluid was considered as incompressible, the Reynolds number employed was 5000.

They observed that an increase of the feedback channel length generated no modifications on the output frequency, the same observation was previously obtained by [56], in both cases the flow was defined as incompressible, being the reason why the simulations could not provide the correct information. On the other hand, the increase of the mixing chamber length, generated a clear reduction on the actuator output frequency. They defined the length scale to be employed to properly non-dimensionalize the oscillation frequency.

The present study is presenting a numerical evaluation of the same fluidic oscillator (FO) configuration experimentally evaluated in [41]. The effects on the stagnation pressure, net momentum acting onto the jet, output mass flow and mixing chamber incoming jet inclination angle, among other parameters, are analyzed for four different internal geometry modifications, the (MC) inlet and outlet widths and the (MC) inlet and outlet wall inclination angles. Three different Reynolds numbers are considered. The four geometry modifications chosen have a considerable impact on the flow inside the (MC) and the (FC's). The (MC) inlet width decisively affects the reverse flow in the (FC's) and the Coanda effect in the (MC), the (MC) outlet width drastically modifies the pressure inside the (MC), the (MC) inlet inclination angles, affect the Coanda effect and the bubble volume inside the (MC), finally, the (MC) outlet inclined walls drastically change the stagnation pressure in these particular walls, changing as well the (FC) dynamic pressure and amplitude.

3.2 Fluidic Oscillator main characteristics

The central part of the (FO) considered in the present study is introduced in figure 3.1, the four internal geometries modified, the mixing chamber (MC) inlet and outlet widths and angles, are clearly shown. Figure 3.1 also introduces the positive and negative directions taken for each geometry modification.

An orthogonal 3D mesh with 2242000 cells was used to evaluate the flow at Reynolds numbers up to 16034, the respective maximum x+, y+ and z+ were of 1.8, 4.7 and 1.2. A mesh with 5933900 cells was used to perform simulations at Reynolds number 32068. The maximum values of x+, y+ and z+ obtained with the finest mesh at Reynolds 32068, were of 0.9, 1.2 and 0.7 respectively. Figure 3.2 presents the mesh used for the simulations, showing the entire computational domain.

The boundary conditions employed in all simulations were, Dirichlet conditions for velocity and Neumann for pressure at the inlet. A relative pressure of 10^4 Pa

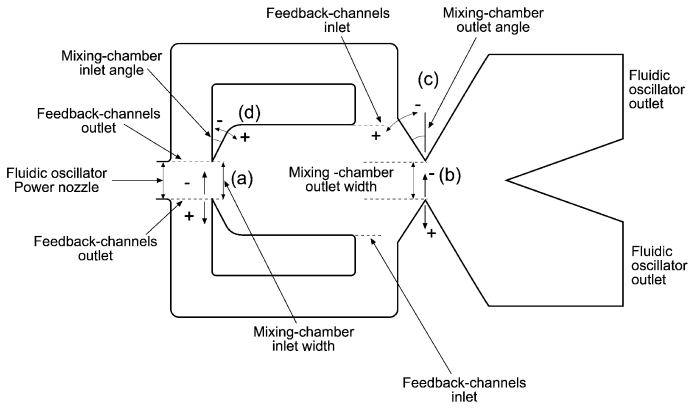

Figure 3.1: Fluidic oscillator mixing chamber internal dimensions modifications.

and Neumann conditions for velocity were considered at the two outlets. Dirichlet boundary conditions for velocity and Neumann for pressure were set to all walls.

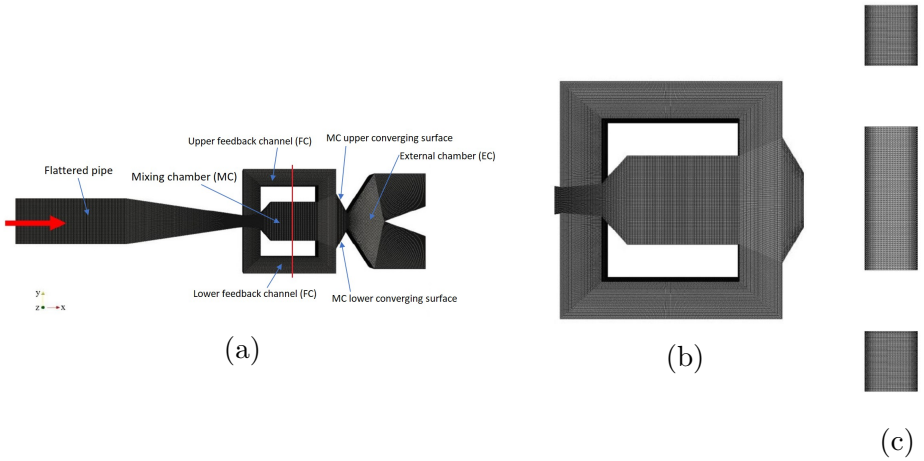

Figure 3.2: Grid used in the present study, (a) plane view, (b) zoom view, (c) side view of the mesh at the center of the mixing chamber, see the vertical line.

In the present study the flow was considered as turbulent, incompressible and isothermal, all simulations were three dimensional. The fluid used was water. Fluid dynamic viscosity was chosen to be $1.003*10^{-3}$ Kg/(m s), the fluid density was 998.2 Kg/m^3. The turbulence model used was the DDES, which is a hybrid model, since according to the research undertaken by [8], this model generates a very close approach to the experimental results. The software OpenFOAM was employed for all 3D simulations, finite volumes is the approach OpenFOAM uses to discretise Navier Stokes equations. Inlet turbulence intensity was set to 0.05% in all cases, Pressure Implicit with Splitting Operators (PISO), was used to solve the Navier Stokes equations, the time step being of 10^{-6}s, spatial discretization was set to second order.

Table 3.1: Comparison experimental and simulated results.

Reynolds number	8711	11152	13593	16034	32068
(CFD) mass flow output frequency (Hz)	12.92	15.89	19.5	22.7	40.43
Eperimental output frequency (Hz) [1]	12.9	15.5	18.7	21.8	-
Error in %	0.15	2.5	4.2	4.1	-

The different velocities evaluated and defined at the inlet of the flattered pipe where the section was $10.3 * 3.25 = 33.475mm^2$, see figure 3.2a, were $0.671m/s$, $1.2347m/s$, and $2.46m/s$, being the corresponding Reynolds numbers 8711, 16034 and 32068 respectively. The Reynolds numbers were based on the hydraulic diameter D_h and the fluid velocity V at the power nozzle, the same location was already used by [41]. One of the main characteristics of a fluidic oscillator is its linear output mass flow frequency behavior versus the inlet mass flow, usually represented as a function of the Reynolds number. The results obtained from the first four Reynolds numbers were used for comparison with the experimental results obtained by [41]. This comparison is presented in table 3.1, further validating the 3D-CFD model introduced. Notice that in table 3.1 the results obtained using two more Reynolds numbers 11152, 13593, are also presented.

To proceed with the non-dimensionalization and in order to generate graphs showing values around unity, the following dimensional parameters were employed. All dimensional parameters are based on values obtained for the baseline oscillator case at Reynolds number 16034. The (FO) outlet mass flow, was non-dimensionalised using the maximum value of the mass flow measured at one of the (FO) outlets. The maximum inclination angle of the main jet at the mixing chamber inlet, was used to non-dimensionalise the jet inclination angle at the mixing chamber inlet. The maximum momentum measured at one of the (FC) outlets, was employed to non-dimensionalise the momentum acting over the jet. The maximum value of the stagnation pressure measured at the mixing chamber outlet converging walls, was defined as the characteristic pressure for non dimensionalization. The characteristic length was chosen to be the oscillator′s power nozzle hydraulic diameter D_h, as already employed in [41]. The fluid velocity at the (FO) power nozzle was employed as the dimensional characteristic velocity. The Reynolds number definition used to

characterize the main flow, was: $Re = (\rho V D_h)/\mu$, where μ is the dynamic viscosity of the fluid. Time was maintained dimensional in all graphs.

3.3 Geometry modifications considered

The present study, is based on analyzing the effect of several geometry modifications on the (FO) outlet dynamic mass flow, frequency and amplitude. Four different modifications were evaluated, see figure 3.1 and table 3.2. Fluidic oscillator (MC) inlet width (a), was the first modification to be computed. Eight different widths were analyzed, the maximum and minimum width ratio was respectively 2.14 and 0.35. Width ratio was defined as the generic inlet width divided by the original one. The inlet width was decreased by 64.4% and increased by 114.7%.

The (MC) outlet width (b), was respectively increased and decreased by a ratio of 1.82 and 0.17. Outlet width ratio was defined as the generic outlet width divided by the original one. A total of 8 different outlet width ratios were analyzed. The outlet width increase and decrease was of 82.3%. The (MC) outlet angle (c), was progressively increased and decreased versus its original value until reaching an outlet angular ratio respectively of 2 and 0.63, the definition of the outlet angular ratio is similar to the previous definitions already given. A total of 8 different outlet angular ratios were studied. The outlet angle maximum increase and decrease was respectively of 100% and 36.6%. Finally, the (MC) inlet internal angle (d) was as well modified, two different angles which increase versus the original one was respectively of 74.3%, and 93% were evaluated. It is interesting to mention that the inlet angles are directly linked with the position, shape an intensity of the Coanda vortices generated alternatively at both sides of the (MC). This angles also modify the shape and dimension of the (MC) bubble generated alternatively on both sides of the main jet, and according to [9, 43, 56] among others, there is a direct link between the (MC) bubble volume increase and the feedback channels mass flow. Table 3.2 summarizes all the different internal geometry modifications performed. All geometry modifications presented were evaluated for three different Reynolds numbers, 8711, 16034 and 32068.

Table 3.2: List of the different geometry ratios evaluated.

Inlet width/Reference inlet width	Outlet width/Reference outlet width	Outlet angle/Reference outlet angle	Inlet angle/Reference inlet angle
0.35	0.17	0.63	1
0.57	0.38	0.82	1.74
0.78	0.58	1	1.93
0.9	0.79	1.16	
1	1	1.31	
1.21	1.2	1.44	
1.42	1.41	1.56	
1.64	1.61	1.66	
2.14	1.82	2	

3.4 Momentum acting on the jet entering the mixing chamber

In order to carefully evaluate the forces acting onto the main jet lateral surfaces, the momentum acting on any of the (FC) outlets is employed. The momentum is characterized by two terms, the (FC) mass flow and the static pressure at this particular location, equation 3.1 defines each of the two terms.

$$M = \dot{m}_{out} * V_{out} + P_f * S_{out} = \dot{m}_{out}^2/(S_{out} * \rho) + P_f * S_{out} \tag{3.1}$$

where, $\dot{m}_{out}, V_{out}, S_{out}$ and P_f, are respectively the instantaneous mass flow defined as $\dot{m} = \int_s \rho \vec{V} \vec{ds}$, the spatial averaged fluid velocity, the (FC) outlet surface and the pressure instantaneously appearing at any of the (FC) outlets, ρ is the fluid density. The net momentum acting on the jet entering the (MC), is obtained when considering the forces defined by equation 3.1 acting instantaneously on both (FC) outlets. The net momentum acting on the jet is composed by two terms, the net momentum due to the pressure term, which considers at each instant the pressure acting on both (FC) outlets, and the net momentum generated by the mass flow flowing along the (FC) and acting instantaneously on both (FC) outlets. At this point it is important to clarify that the momentum generated by the (FC) mass flow was obtained using the instantaneous mass flow to the power 2, divided by the section of the feedback channel and the fluid density, see the second term of equation 3.1.

In the following sections and thanks to the simulations undertaken, it will be clarified, for the different geometry modifications considered, which is the role played by the net momentum due to the mass flow transferred across the (FC). This net momentum will be compared with the role undertaken by the net momentum due to the pressure difference acting onto the jet at the (FC) outlets. The role of the Coanda effect generated alternatively on both sides of the mixing chamber will also be investigated, in fact, this point will be particularly addressed when evaluating the effect of the (MC) inlet angle.

3.5 Results

3.5.1 Modifying the (MC) inlet width

The first modification to be considered is the variation of the mixing chamber inlet width. Figure 3.3 introduces the variation of (FO) output mass flow peak to peak amplitude and frequency as a function of the different inlet widths evaluated. The first thing to notice is that whenever the inlet width falls below a minimum or is higher than a maximum value, the actual (FO) is not producing any outgoing frequency, see figure 3.3a. The explanation why there is no flow oscillation when the actuator inlet width falls to a minimum, is based on the fact that, the mixing chamber incoming jet borders impinge onto the feedback channels (FC's) outlet internal vertical walls, creating a flow stream in the (FC's) which goes from left to right, from upstream to downstream, and along both (FC's) at the same time. At both (FC's) outlet internal vertical walls, a stagnation pressure point is generated, from this point, pressure waves are generated and sent from the feedback channels outlets to the inlets. The combination of these two effects prevents any feedback flow to move from downstream to upstream. On the other hand, when the mixing chamber inlet width is too large, a gap appears between the incoming jet and the mixing chamber inlet width borders. This small gap is enough to prevent a pressure increase at the (FC's) outlets, then it allows the fluid coming up from the (FC) inlet, to escape through this gap towards the mixing chamber.

In figure 3.3b, is presented the effect of modifying the inlet width on the (FO) outlet mass flow peak to peak amplitude. As previously presented, for inlet widths exceeding a limit in any direction, whether too big or too small, the flow stops oscillating and the amplitude decays to zero. For the intermediate values it is seen that the amplitude is initially being highly affected by the inlet width, but as the width keeps increasing the amplitude decreases. It is also seen that the amplitude tendency

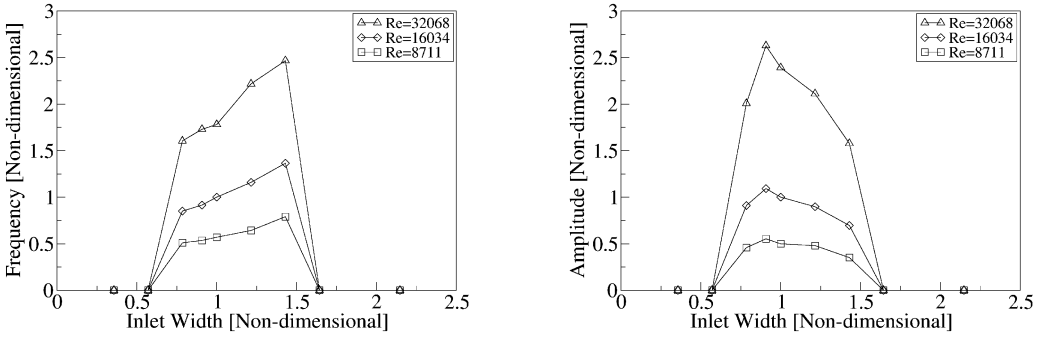

(a) (b)

Figure 3.3: Fluidic oscillator output mass flow frequency and peak to peak amplitude as a function of the mixing chamber inlet width and for three different Reynolds numbers, 8711, 16034 and 32068.

is opposed to that of the frequency, small frequencies are linked with high oscillation amplitudes and vice versa. The reason why this is happening, it is clearly seen when applying the mass conservation equation between the (FO) inlet and outlets. For the present modification, when high widths are considered, the jet entering the mixing chamber (MC), suffers a relatively small oscillation inside the mixing chamber (MC), causing a small variation of amplitude at the oscillator exit. As the mixing chamber (MC) inlet width decreases, the jet oscillation amplitude inside the mixing chamber increases, the jet deflection angle at the mixing chamber inlet and outlet also increases and so does the fluidic oscillator output amplitude, see figures 3.3, 3.4 and 3.7. Based on the results presented in figure 3.3, it can also be stated that the effects on output frequency and amplitude, are more relevant as the Reynolds number increases, but the trend already presented remains the same. The threshold at which the oscillation stops, appears to be rather independent of the Reynolds number. A good way to illustrate the vortical structures appearing inside the FO is by means of isosurfaces based on the Q criterion, as presented in figures 3.5 and 3.6 respectively for the maximum and minimum inlet width. The isosurfaces are colored by the vorticity about the Z axis. The color blue indicates the structures turn clockwise, the red color is associated with counterclockwise rotation. The snapshot sequence presented in figures 3.5 and 3.6 characterizes a full oscillation period divided into six evenly spaced time steps, which match with the time steps introduced in figure 3.4. It is interesting to see the coexistence of positive and negative structures at any instant. The vortical structures inside the FCs and the external chamber (EC), which could

clearly be seen in figure 3.4, can hardly be seen in figures 3.5 and 3.6 , indicating that their vorticity is at least an order of magnitude smaller than the one associated with the MC vortical structures. For the lowest inlet width, a lot of flow moving from the FCs inlets into the outlets in a opposite direction creating small structures at the FCs inlet parts as shown in figure 3.6.

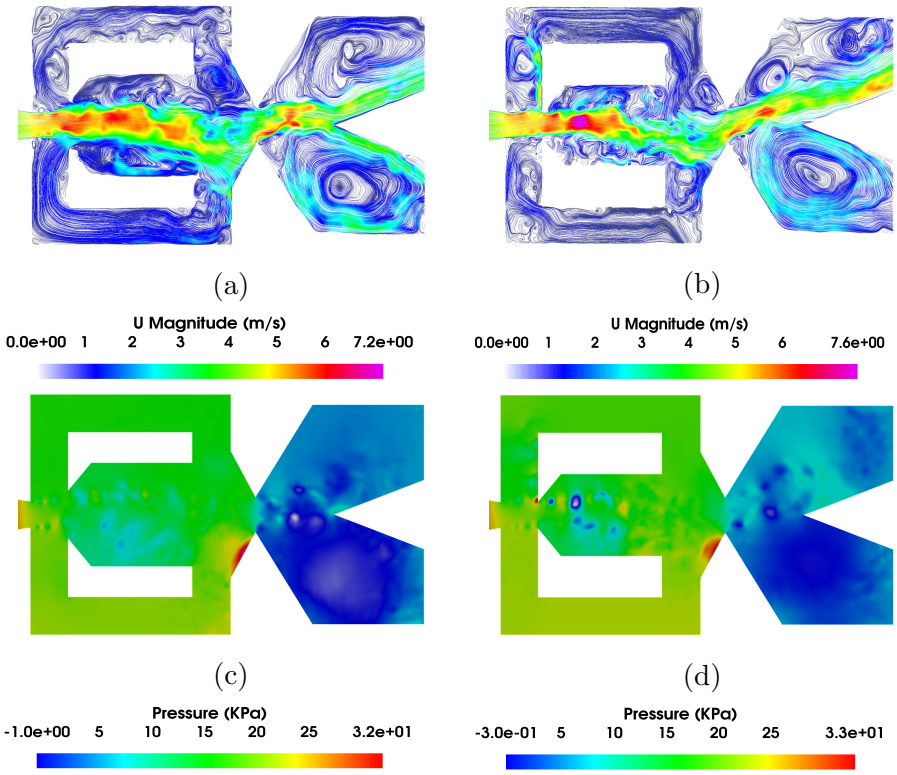

Figure 3.4: Fluidic oscillator internal velocity field (a, b), and pressure magnitude (c, d). Maximum inlet width (a, c), minimum inlet width (b, d). Reynolds number 16034.

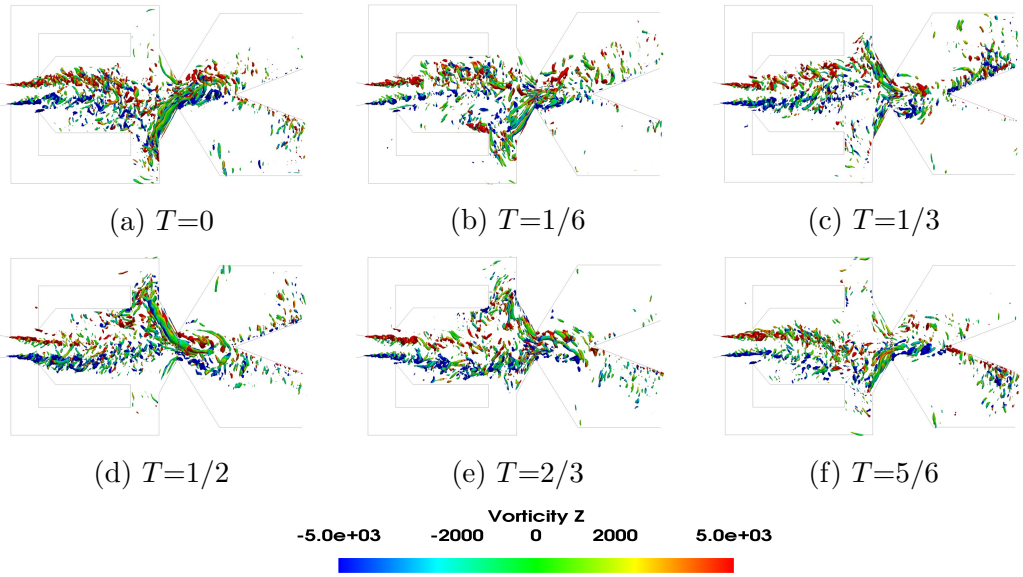

(a) T=0 (b) T=1/6 (c) T=1/3

(d) T=1/2 (e) T=2/3 (f) T=5/6

Figure 3.5: Q criterion at the mixing chamber period of oscillation divided into six equally spaced times, Reynolds number 16,034. Maximum inlet width.

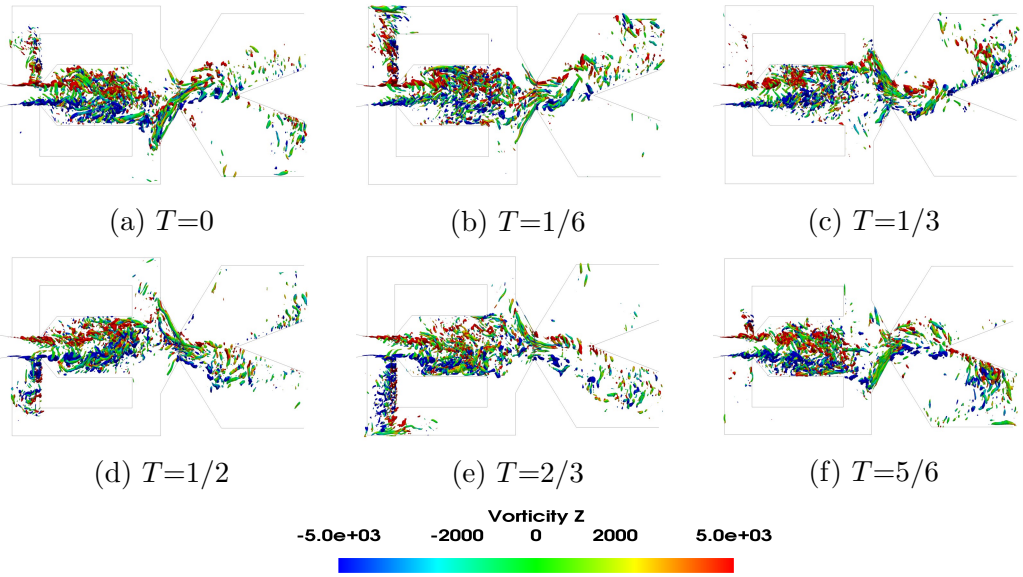

(a) T=0 (b) T=1/6 (c) T=1/3

(d) T=1/2 (e) T=2/3 (f) T=5/6

Figure 3.6: Q criterion at the mixing chamber period of oscillation divided into six equally spaced times, Reynolds number 16,034. Minimum inlet width.

Figure 3.4 introduces the flow field and pressure distribution inside the (FO), for the minimum and maximum (MC) inlet widths at which oscillation still appears, the Reynolds number is 16034. For the maximum inlet width, figures 3.4a,c, the jet bending inside the (MC) is supported by the low pressure below the jet generated by the Coanda effect, see figure 3.4c, at the external chamber the jet flows reattached to

the surface of the wedge, generating two alternative vortices of nearly the same size on both sides of the external chamber. From figure 3.7a, it is observed that no reverse flow appears at the (FO) upper outlet, see the curve characterizing the highest inlet width. Regarding the pressure distribution, the pressure is very much the same along the entire (MC), very small pressure fluctuations appear on the (FC's), alternatively pressurizing one (FC) or the other. The origin of the pressure waves, responsible of the (FC's) periodic pressurization, are the stagnation pressure points appearing alternatively at the (MC) outlet converging walls, see the red spots observed in figures 3.4c,d.

At small inlet widths, figures 3.4b,d, the (MC) incoming jet impinges alternatively at the (FC's) outlet internal vertical walls, generating an stagnation pressure point from which pressure waves are being sent alternatively from both (FC) outlets to the inlets, see the small red spot observed at the upper feedback channel outlet, figure 3.4d. Reverse flow, from (FC) outlets to inlets is therefore generated, although for this particular case, the oscillation still exists. This is because the stagnation pressure at the (MC) converging walls, is acting over a surface about 20 times bigger than the one affected by the pressure at the (FC's) outlet internal vertical walls, and despite the fact the maximum pressure at the (MC) outlet converging walls, is for the present case, about 22% smaller than the maximum pressure existing at the (FC's) outlet internal walls, the time the stagnation pressure is acting on the (MC) converging walls, is 6.4 times longer than the time the stagnation pressure point appears at the (FC) outlet internal vertical walls, being this time difference along with the area the stagnation pressure acts, what maintains the oscillation. Although no figure related is presented in the present manuscript, if the inlet width would be further reduced, the stagnation pressure points at the (FC's) outlet vertical walls, would be appearing simultaneously on both vertical walls, generating reverse flow on both feedback channels at the same time. Pressure waves would also be continuously transfered from the (FC's) upstream to downstream. Under these particular conditions oscillation would stop.

The evaluation of the dynamic values of the, net-momentum acting onto the jet entering the mixing chamber, the pressure at the (MC) outlet converging walls, the (MC) inlet inclination angle, the (FC's) mass flow and the (FO) output flow, greatly helps in understanding the (FO) dynamic performance. Figure 3.7 introduces the non-dimensional dynamic values of the mass flow through one of the (FO) outlets, the lower (FC) mass flow, the stagnation pressure at the (MC) outlet lower convergent wall, the net-momentum acting on the (MC) incoming jet and the (MC) inlet jet inclination angle. The Reynolds number was kept constant at 16034. In each graph it

is presented the non-dimensional dynamic value obtained for the baseline case, original actuator, and the corresponding ones characterizing the maximum and minimum inlet widths evaluated at which pulsating flow was observed. The first thing to notice is, that the dynamic stagnation pressure appearing alternatively at the (MC) converging walls, figure 3.7c, is driving the oscillation, the rest of the graphs presented simply follow these pressure pulsations. From the oscillator upper outlet mass flow graph, figure 3.7a, it is observed that the mass flow amplitude is directly linked with the reverse flow appearing at the (FO) outlets, the higher the reverse flow the higher the mass flow outlet amplitude, large reverse flows are associated to small inlet widths. This direct relationship is obvious when considering that the incoming (FO) mass flow is constant and given by the inlet boundary conditions, and at each instant, the mass flow through the two (FO) outlets must be the same as the inlet mass flow, the fluid is considered as incompressible. Therefore, if at some particular time, reverse flow appears at one of the (FO) outlets, the (FO) mass flow amplitude must increase to fulfill the continuity equation at each time instant.

When observing the effects of the inlet width on the (FC's), figure 3.7e, it is seen that, at small inlet widths the average mass flow is about zero, the flow inside the (FC's) is moving in both directions, yet the mass flow entering the (FC) outlet, reverse or negative flow, appears to be higher than the flow leaving such surface. If the inlet width would be further decreased, the reversed flow would keep increasing, eventually stopping the oscillation. As the inlet width increases, the mass flow inside the (FC's), although periodic, has a positive average value, meaning, there is a net mass flow moving from the feedback channels inlet to the outlet, at high inlet widths there is no reverse flow in the (FC's). The reason why at small inlet widths there is reverse flow in the (FC's), is the small stagnation pressure points generated alternatively at the (FC's) outlet internal vertical walls.

It is also relevant to highlight that, the peak to peak amplitude of the net momentum driving the jet oscillations inside the mixing chamber, is particularly small when the lowest inlet width is employed, figure 3.7d, the jet is prone to fluctuate under these conditions, therefore a small pressure difference at the (FC's) outlets is sufficient to flip the jet. The jet oscillation amplitude inside the (MC) appears not to be affected by this fact, then the amplitude is higher than the one appearing at highest inlet widths. In other words, small inlet widths require small net momentums to flip the jet and the jet oscillation amplitude inside the mixing chamber is maximum. The (MC) incoming jet inclination angle, figure 3.7b, suffers a reduction in the peak to peak amplitude of about 4.6% when comparing the maximum and minimum inlet

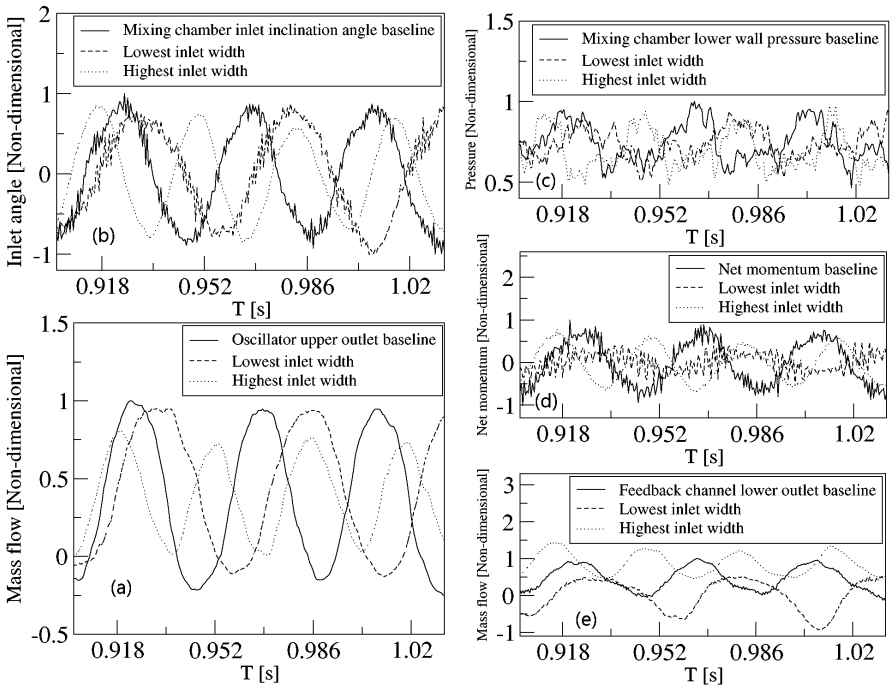

Figure 3.7: Dynamic effects of the (MC) inlet width modification on the main flow parameters, Reynolds number 16034. Each graph presents three non-dimensional curves characterizing results from the baseline, the lowest inlet width and the highest inlet width cases, and as a function of the dimensional time. In figure (a) the mass flow across the upper oscillator outlet is presented. Figure (b) introduces the temporal variation of the (MC) inlet inclination angle. Figure (c) presents the pressure at the (MC) lower inclined wall. The net momentum acting on the lateral sides of the main jet is presented in figure (d). Figure (e) characterizes the mass flow at the lower feedback channel outlet.

widths, for the same conditions, the variation of the outlet mass flow amplitude, is about 16%. It appears the oscillation inside the (MC) is delimited by the (MC) upper and lower internal horizontal walls.

To properly understand the forces acting on the main jet lateral sides, the pressure and the mass flow terms of the net momentum acting on the main jet lateral sides are compared for the lowest, baseline and highest inlet widths, see figure 3.8. Regardless of the inlet width studied, the pressure term of the net-momentum is much larger than the net-momentum mass flow term, indicating that the (FO) is pressure driven. Based on their observations and studding two different configurations of (FO), wu et al. [46] reached the same conclusion, although they could not bring a clear prove of it. From figure 3.8, it is also important to realize that at low inlet widths, the pressure term of the net momentum is particularly scattered, as previously explained under these conditions in any of the feedback channels there is reverse flow and pressure

waves travel in opposite directions.

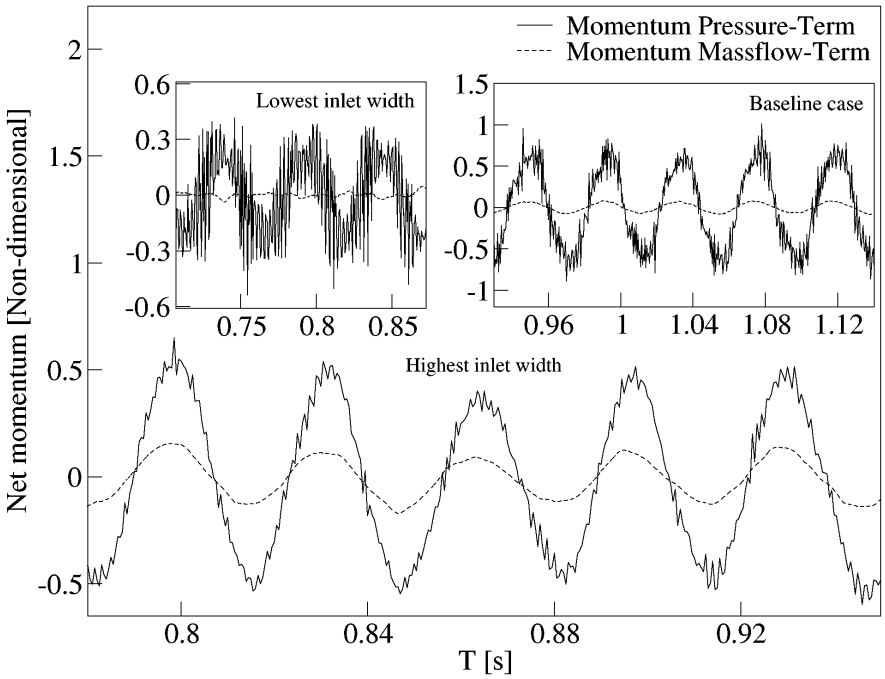

Figure 3.8: Comparison of the pressure and mass flow terms of the net-momentum and for three characteristic inlet widths, Reynolds number 16034.

From the dimensional temporal pressure plots at the (FC's) outlets, not presented in figure 3.7, and when comparing the highest and smallest inlet widths studied, it was observed that the average static pressure at both (FC) outlets, decreased about 3000Pa when the highest inlet width was used. Regarding the pressure fluctuation at both (FC) outlets, when the lowest inlet width was employed, the pressure was at any time, almost identical on both feedback channel outlets. While when the inlet width was maximum, the maximum pressure difference between the two (FC) outlets increased to about 2000Pa. From the results obtained, it can be stated that at higher inlets widths, a higher net momentum onto the mixing chamber incoming jet lateral sides is required to bend the jet towards the opposite direction and therefore generate flapping. This phenomenon is understood when realizing that at small inlet widths, the Coanda effect helps in generating the required pressure difference inside the mixing chamber, to flip the incoming jet.

As Reynolds number increases to 32064, there is an increase of the average pressure across the entire (MC) and therefore at the (FC's) outlets. The peak to peak amplitude of the mass flow inside the feedback channels, also increases. This is because the stagnation pressure is likely to increase with the velocity increase $P_0 = \rho V^2/2$. At

Reynolds number 32064 and for the lowest inlet width evaluated, the feedback channel mass flow reaches higher negative values than at Reynolds 16034, but its average value remains quite constant and close to zero. In other words, at high Reynolds numbers, a higher net momentum acting on the (MC) incoming jet is required, to produce the jet flapping. The effect of Reynolds number on all (FO) dynamic parameters studied is presented in the last section of the paper.

3.5.2 Modifying (MC) outlet width

The second dimensional evaluation undertaken consisted in analyzing the effect of modifying the mixing chamber outlet width. Figure 3.9, introduces the results obtained for the three Reynolds numbers studied. The first thing to observe, is that, an outlet width increase involves a reduction of the (FO) output frequency and amplitude, such reduction is more relevant as the Reynolds number increases. For example, at Reynolds 8711 and when comparing the values of the maximum and minimum outlet widths evaluated, the maximum decrease in frequency and amplitude was of about 7% and 60% respectively. At Reynolds 32068, the respective decrease of frequency and amplitude was about 9% and 74%. In other words, the range of frequencies and amplitudes a given fluidic oscillator can produce, when modifying the outlet width, increases with the Reynolds number increase. The variation of the outlet width affects mostly the (FO) outlet amplitude. A point to consider when comparing figures 3.3 and 3.9, is that the increase of the inlet width was bringing an increase in frequency and a decrease in amplitude, while an increase of outlet width generates a decrease in outlet frequency and amplitude. This opposite effect needs to be understood when evaluating the velocity fields under these four extreme conditions, these instantaneous velocity and pressure fields are presented in figure 3.10.

Figures 3.10a, b, show the velocity vectors magnitude inside the oscillator for the highest and lowest outlet widths evaluated. Notice that when the (MC) outlet width is minimum, the velocity of the jet leaving the external chamber is maximum, more than four times the maximum velocity found for the rest of the cases studied in this paper. The average pressure in the (MC) is about nineteen times higher than for the rest of the cases studied. The fluid is pressurized due to the restriction effect caused by the small outlet width. The fluid stiffness in the (MC) and therefore its dynamic response is particularly high, explaining why high frequencies are linked to small outlet widths. At the (EC) the pressure is particularly low, see figure 3.10d, in fact the relative negative pressure is of about 120KPa, which is physically not possible and in reality shows that for small outlet widths cavitation is likely to appear at the

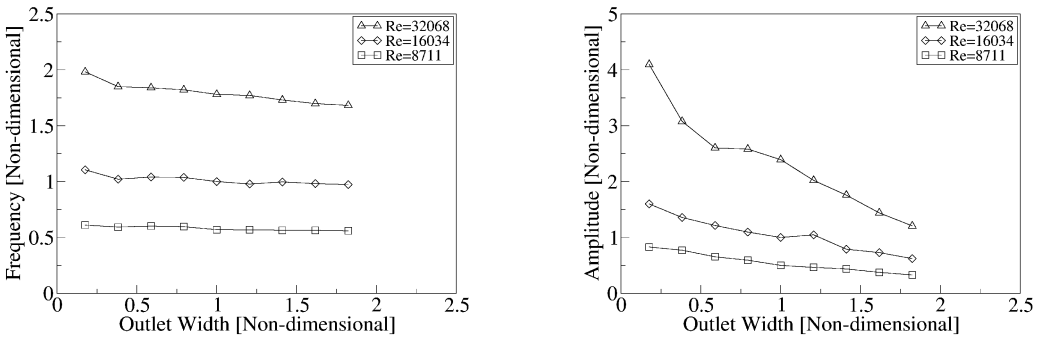

(a) (b)

Figure 3.9: Fluidic oscillator output mass flow frequency and peak to peak amplitude as a function of the mixing chamber outlet width and for three different Reynolds numbers, 8711, 16034 and 32068.

(EC). Under these conditions, at the (FO) outlets, the section used by the flow to leave the oscillator is being reduced, leaving a large part of the outlet section in which reverse flow exists, huge spatial velocity differences are to be seen at the (FO) outlets. As a result, high (FO) outlet mass flow amplitudes are expected.

Figure 3.10c shows, for the highest outlet width studied, there is a low pressure area generated below the jet due to the Coanda effect, it can also be seen that the (FC) located below the (MC) is beginning to be pressurized, a clear stagnation pressure point is observed at the (MC) outlet lower converging wall. The mass flow spatial distribution at the (FO) outlets, appears to be much uniform, the (FO) outlets have a smaller surface through which reverse flow exists, being this directly linked to smaller outlet amplitudes. The (MC) is slightly pressurized, the fluid stiffness is low and so it is the (FO) outlet mass flow oscillating frequency. For the present (FO) and regardless of the dimensional modification, the maximum mass flow amplitudes at the (FO) outlets, are directly linked with the reverse flow existing at the outlets, the bigger the reverse flow the higher the (FO) outlet oscillation amplitude. The outlet width can be effectively used to control the outlet oscillations amplitude.

Regardless of the outlet width, a vortex at the external chamber upper side, can be spotted, yet its intensity and turning speed associated are much smaller for the highest than for the lowest outlet widths studied. The turning speed of this particular vortex for the lowest and highest outlet widths studied, was respectively of 301 and 59 rad/s, which explains why the pressure at the (EC) is particularly low at small outlet widths. Figures 3.11 and 3.12 shows vortical structures appearing inside the

FO by means of isosurfaces based on the Q criterion respectively for the highest and lowest outlet width. The isosurfaces are colored by the vorticity about the Z axis. The color blue indicates the structures turn clockwise, the red color is associated with counterclockwise rotation. The snapshot sequence presented in figures 3.11 and 3.12 characterizes a full oscillation period divided into six evenly spaced time steps, which match with the time steps introduced in figure 3.10. It is interesting to see the coexistence of positive and negative structures at any instant. For the highest outlet width, the vortical structures inside the FCs and the external chamber (EC), which could clearly be seen in figure 3.10 can hardly be seen in figures 3.11 , indicating that their vorticity is at least an order of magnitude smaller than the one associated with the MC vortical structures. For the lowest outlet width, as the velocity is very high specially at the external chamber (EC), a lot of vortical structures can be seen in both parts of the external chambers. From all the cases studied, the vortical structures can only be seen for the case of lowest outlet width inside the EC.

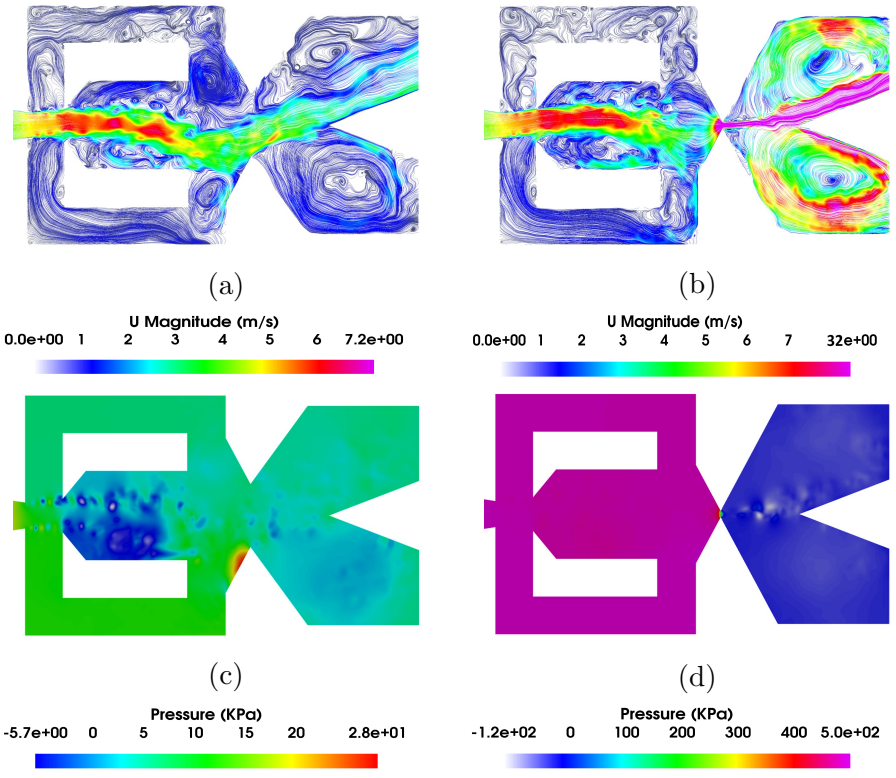

Figure 3.10: Fluidic oscillator internal velocity field (a, b) and pressure magnitude (c, d). Maximum outlet width (a, c), minimum outlet width (b, d). Reynolds number 16034.

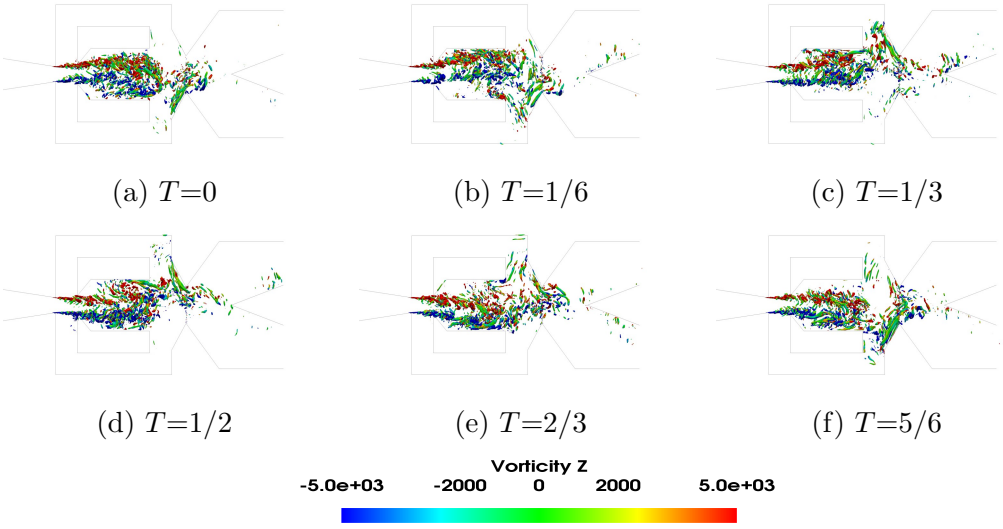

(a) T=0 (b) T=1/6 (c) T=1/3

(d) T=1/2 (e) T=2/3 (f) T=5/6

Figure 3.11: Q criterion at the mixing chamber period of oscillation divided into six equally spaced times, Reynolds number 16,034. Maximum outlet width.

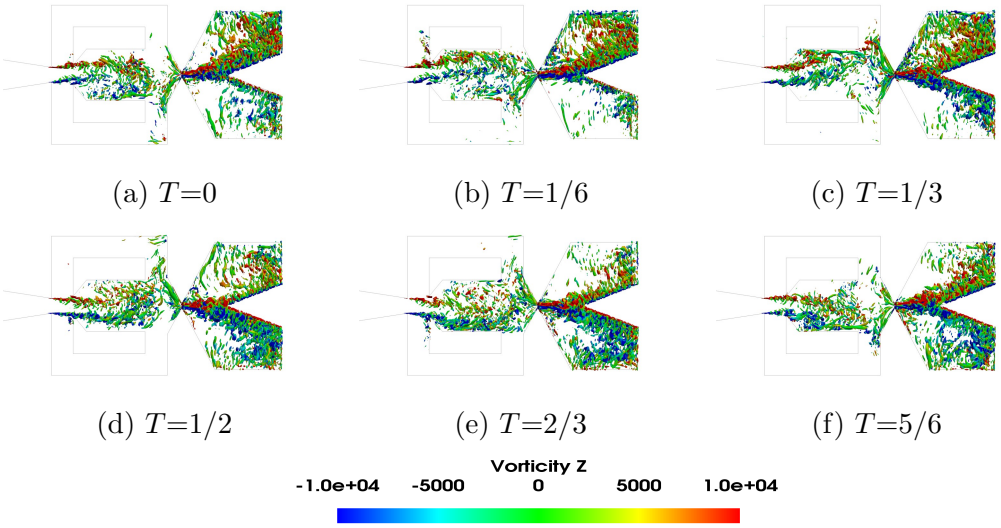

(a) T=0 (b) T=1/6 (c) T=1/3

(d) T=1/2 (e) T=2/3 (f) T=5/6

Figure 3.12: Q criterion at the mixing chamber period of oscillation divided into six equally spaced times, Reynolds number 16,034. Minimum outlet width.

The same dynamic parameters evaluated in the previous section and introduced in figure 3.7, are now being presented in figure 3.13 for the maximum, minimum and baseline (MC) outlet widths studied. When the highest (MC) outlet width is employed, the (FO) outlet mass flow amplitude is minimum, there is no reverse flow at any time. As the (MC) outlet width decreases, the reverse flow at the (FO) outlets keeps increasing, consequently the (FO) mass flow amplitude increases, see figure 3.13a. Another relevant effect associated to the decrease of the outlet width,

is the progressive increase of the (MC) pressure, notice that the average value of the stagnation pressure fluctuations presented in figure 3.13c, increases around 19 times when comparing the maximum and minimum outlet width values. For the lowest outlet width evaluated, the stagnation pressure fluctuations at the (MC) lower converging wall, show a quasi-chaotic behaviour, probably due to the stagnation pressure points appearing simultaneously on both (MC) converging walls, see figures 3.10d and 3.13c, although clear oscillation signs are still to be seen. Under these conditions, the curve representing the net momentum is particularly scattered. This fact is clearly understood when considering that the main term of the net momentum is the pressure term, as observed in figure 3.8 for the previous case. Regarding the net momentum responsible of the jet fluctuations inside the (MC), see figure 3.13d, its amplitude is about 38% smaller for high outlet widths than for the smaller ones. Notice as well that for the highest outlet width, the stagnation pressure peak to peak amplitude is about 40% smaller than for the smallest outlet width evaluated. These values suggest a direct relation between the stagnation pressure peak to peak amplitude and the net momentum driving the jet oscillations.

Another point to be discussed may be, why the net momentum shows rather a sinusoidal curve when the stagnation pressure oscillations, specially at the lowest outlet width, looks rather chaotic. The reason is the integration effect the (FC's) outlets are having on the pressure oscillations. The study of the (MC) incoming jet oscillation angle, see figure 3.13b, shows that the smallest oscillation amplitude appears when the highest outlet width is employed. The maximum jet oscillation angle amplitude, obtained for the minimum outlet width, is about 3% higher than the one generated for the baseline case, and about 29% higher than the one obtained when using the maximum outlet width. From figure 3.13, a direct correlation between the peak to peak stagnation pressure, the (MC) inlet angle amplitude, the (FO) output and (FC) mass flows amplitude, as well as the net momentum amplitude, appears to exist. Small stagnation pressure amplitudes generates small amplitudes in all these parameters.

When evaluating the feedback channel mass flow, figure 3.13e, regardless of the outlet width, it is observed there is an average mass flow flowing from both feedback channel inlets to the outlets. Its average value remains pretty much constant regardless of the outlet width chosen, although it was observed it increased with the Reynolds number increase. For the smallest (MC) outlet width evaluated, just a very small reverse mass flow exists on both feedback channel outlets, the reverse flow increases with the Reynolds number increase. (FC) reverse flow is associated to the

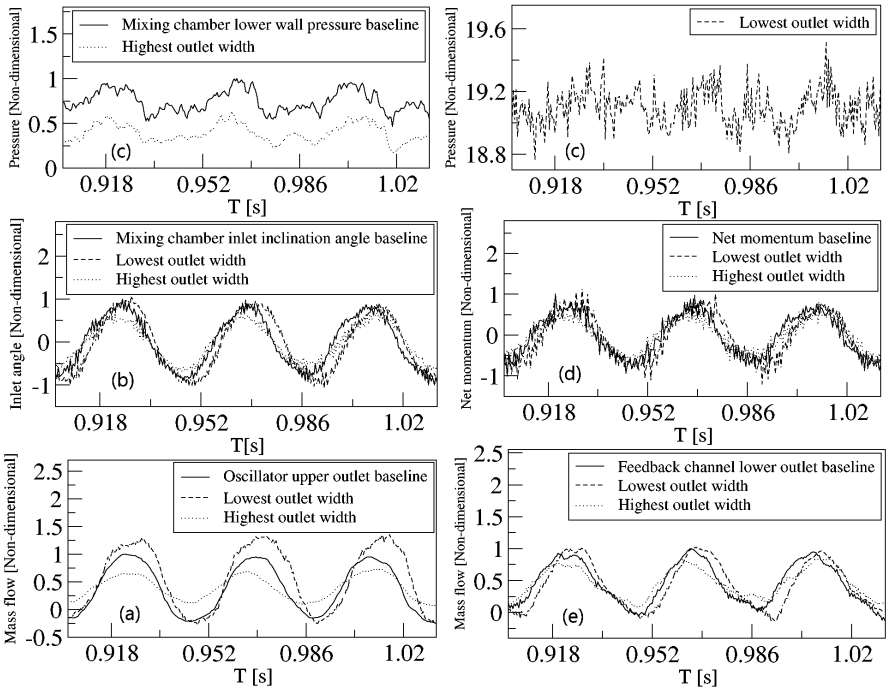

Figure 3.13: Dynamic effects of the (MC) outlet width modification on the main flow parameters, Reynolds number 16034. Each graph presents three non-dimensional curves characterizing results from the baseline, the lowest and highest outlet width cases, and as a function of the dimensional time. In figure (a) the mass flow across the upper oscillator outlet is presented. Figure (b) introduces the temporal variation of the (MC) inlet inclination angle. Figures (c) presents the pressure at the (MC) lower inclined wall. The net momentum acting on the lateral sides of the main jet is presented in figure (d). Figure (e) characterizes the mass flow at the lower feedback channel outlet.

alternative appearance of the stagnation pressure points at the (FC) outlets internal vertical walls, as it was observed in figure 3.4d and 3.7e for the smallest inlet width. At high mixing chamber outlet widths, there is no (FC) reverse flow. Regarding the (FC) mass flow amplitude, a decrease of about 32% is observed, when comparing the values of the highest outlet width with the ones obtained at the lowest outlet width. The decrease in feedback channel mass flow amplitude as outlet width increases can be more clearly seen at high Reynolds numbers, in general it can be said that all differences can be seen more clearly at high Reynolds numbers, the dynamic values at several Reynolds numbers are not presented in the present paper. The phase lag between the oscillator output mass flow and the feedback channel mass flow is about $4.4 * 10^{-3}$ and $2.4 * 10^{-3}$ seconds, respectively for the lowest and highest outlet widths at Reynolds 16034. It seems high phase lag values are related to high (FO) output mass flow amplitudes.

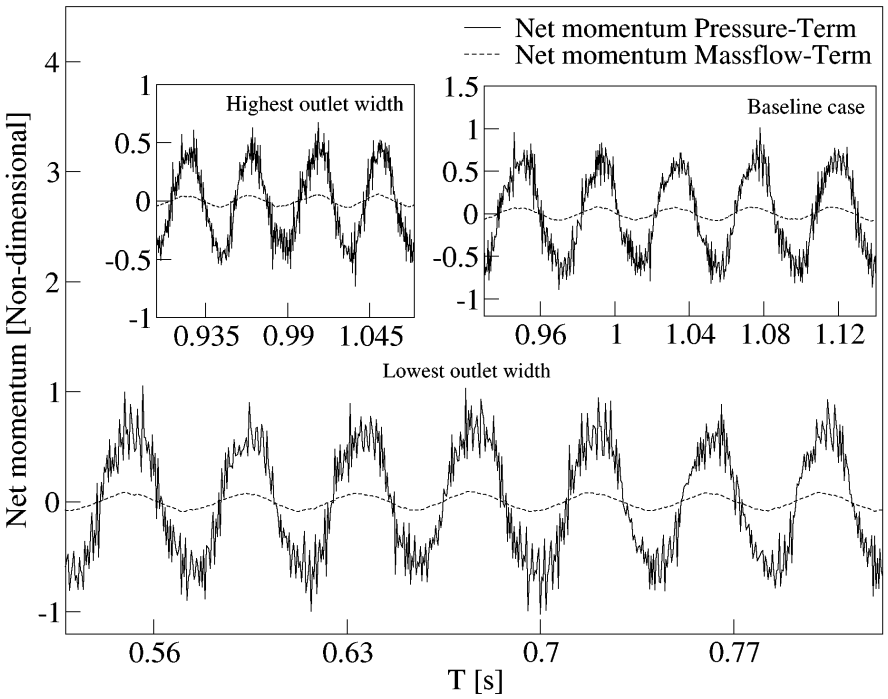

Figure 3.14: Comparison of the pressure and mass flow terms of the net-momentum and for three characteristic outlet widths, Reynolds number 16034.

Although not directly presented in the present manuscript, at low (MC) outlet widths, the pressure difference between the upper and lower (FC) channel outlets, was particularly high, a maximum pressure difference of 4200 Pascals was measured. For the highest outlet width studied, this maximum pressure difference was of 2500 Pa. The peak to peak stagnation pressure oscillations amplitude at the (MC) converging walls, was specially high at low outlet widths and high Reynolds numbers. From figures 3.13b and 3.13d, it is observed that for the lowest outlet width studied, the peak to peak net momentum amplitude acting onto the jet entering the (MC), and the peak to peak inlet angle amplitude of the jet at the same point, are respectively of 43% and 30% higher than the respective values obtained when evaluating the highest outlet width. A final relevant point to highlight on the average pressure, is that for most of the cases presented in this paper, and regardless of the modification considered, as Reynolds number increases from 16034 to 32068, the average pressure at the (MC) outlet converging walls, increased by approximately 150%. Yet there are two exceptions, one of them is whenever the highest (MC) outlet width is employed, for this particular case, the same increase of Reynolds number brings an increase of the average pressure of about 12.7%. The second exception appears when the lowest (MC) outlet width is employed, being the increase of average pressure of 316% for the

same increase of the Reynolds number. For highest outlet widths, the central core of the main jet flows towards the (EC) without impinging on the (MC) converging walls, just some fluid particles located at the lateral sides of the jet impinge on the (MC) converging walls, therefore explaining why the average spatial pressure on these walls is particularly small. Regardless of the geometry modification evaluated, the stagnation pressure peak to peak amplitude at the (MC) converging walls, increases with the Reynolds number increase. The detailed evaluation of this particular parameter is to be found in the final part of this chapter. Figure 3.14 shows the forces acting on the main jet lateral sides, the pressure and the mass flow terms of the net momentum acting on the main jet lateral sides are compared for the lowest, baseline and highest outlet widths. Regardless of the outlet width studied, the pressure term of the net-momentum is much larger than the net-momentum mass flow term, indicating that the (FO) is pressure driven. From figure 3.14, it is also important to realize that the both momentum terms regarding pressure and mass flow are smaller for the highest outlet width resulting in a smaller frequency and amplitude as shown in figure 3.9.

3.5.3 Modifying the (MC) outlet angle

Figure 3.15 presents the results obtained when modifying the (MC) outlet angle and for the three Reynolds numbers evaluated. The (FO) output mass flow frequency and amplitude keeps decreasing as the inclination angle increases. The frequency effect is perfectly understandable once it is realized that the (MC) outlet converging walls, play a key role regarding the flow directed towards the (FC's) and the pressure waves transmission. Not only the position of the stagnation pressure point is modified by this angle but also its magnitude will be affected. The stagnation pressure maximum value as well as the peak to peak pressure amplitude, was observed to decrease with the (MC) angle increase. High frequencies are linked to high stagnation pressure values and vice versa. Furthermore, high (MC) outlet angles tend to direct the pressure waves towards the (FC) located opposite to the wall where the main jet impinges, the main flow stream is directed towards the (FO) outlet. On the other hand, small (MC) outlet angles, have associated a much wider area where stagnation pressure exists, maximum stagnation pressure values and peak to peak amplitudes are obtained under these conditions. Small angles direct the mass flow and specially the pressure waves towards the (FC) located next to the wall the main jet impinges, periodically pressurizing the (FC), compare figures 3.16a, c with 3.16b, d. This is the reason why, small (MC) outlet angles, have associated higher frequencies and amplitudes.

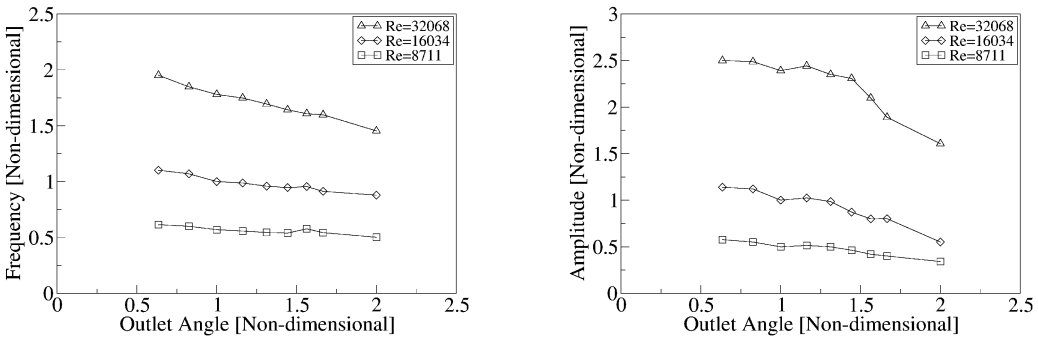

(a) (b)

Figure 3.15: Frequency and amplitude of the (FO) outlet dynamic mass flow, as a function of the mixing chamber outlet angle and for three different Reynolds numbers, 8711, 16034 and 32068.

The effect of the (MC) outlet angle on the (FO) outlet mass flow amplitude, can be further explained when taking into account that, higher angles tend to direct the main flow towards the (FO) outlet central horizontal axis, therefore tending to decrease the jet deflection. Notice from figure 3.19 that the amplitude of all parameters is particularly small at high outlet angles. The flow leaves the (EC) rather tangentially to the wedge walls and across one of the outlets at a time, generating a large vortex on the opposite outlet of the (EC). For high (MC) outlet angles, the fluid velocity at the (FO) outlets, is rather uniform across one of the exits at a time and always leaves the oscillator, there is no reverse flow, see figure 3.19a. As the angle decreases, the outlet maximum fluid velocity magnitude increases, for a given oscillation period and during approximately one third of the period, the mass flow in any of the two exits enters the oscillator, for the rest of the period the fluid leaves the oscillator at a relatively high speed, the peak to peak output mass flow amplitude is maximum under these conditions, see figure 3.19a. Again we are observing that large (FO) output mass flow amplitudes, have associated reverse flow at the (FO) outlets.

Figure 3.16 represents the oscillator overall velocity and pressure fields when the outlet angles are respectively the largest and smallest studied. From figure 3.16b, which characterizes the smallest angle evaluated, it is noticed that the jet impinges nearly perpendicular to the (MC) lower converging wall, generating a large area where the stagnation pressure acts, see figure 3.16d. The stagnation pressure and its peak to peak amplitude, reach their respective maximums under these conditions, see figure 3.19c. Pressure waves and some fluid flow are directed from the lower (FC) inlet to

the outlet. the lower feedback channel is pressurized, figure 3.16d. On the other hand, whenever the output angle increases, figure 3.16a, the jet leaving the (MC), tends to run tangential to the (MC) converging walls, therefore directing a smaller amount of fluid through the feedback channels, and even more important, the formation of a high pressure stagnation point is reduced to a very small converging walls section, its peak to peak amplitude and maximum value are also minimized, see figures 3.16c and 3.19c. As a result the time needed for the main jet to flip over increases, and accordingly the oscillation frequency decreases. It is also interesting to realize that at the external chamber (EC), a large vortex is generated at the opposite exit from the one the flow is leaving the amplifier. In fact the vortex covers the entire opposite exit, preventing flow from outside the (FO) to enter into the (EC). This vortex intensity was observed to be slightly higher as the angle decreased. For the smallest (MC) outlet angle, the turning speed associated to this particular vortex was of 117rad/s, while when highest outlet angle is used, the turning speed was of 67 rad/s. Figures 3.17 and 3.18 shows vortical structures appearing inside the FO by means of isosurfaces based on the Q criterion respectively for the highest and lowest outlet angle. The isosurfaces are colored by the vorticity about the Z axis. The color blue indicates the structures turn clockwise, the red color is associated with counterclockwise rotation. The snapshot sequence presented in figures 3.17 and 3.18 characterizes a full oscillation period divided into six evenly spaced time steps, which match with the time steps introduced in figure 3.16. For the highest outlet angle, less vortical structures can be seen inside the mixing chamber (MC) and external chamber (EC), also these structures are smaller and have less intensity. Only small part of the main jet reaches to the external chamber (EC) resulting lower frequency and aplitude as shown in figure 3.15. For the lowest outlet angle, the structures are larger and can be seen more clearly inside the external chamber (EC).

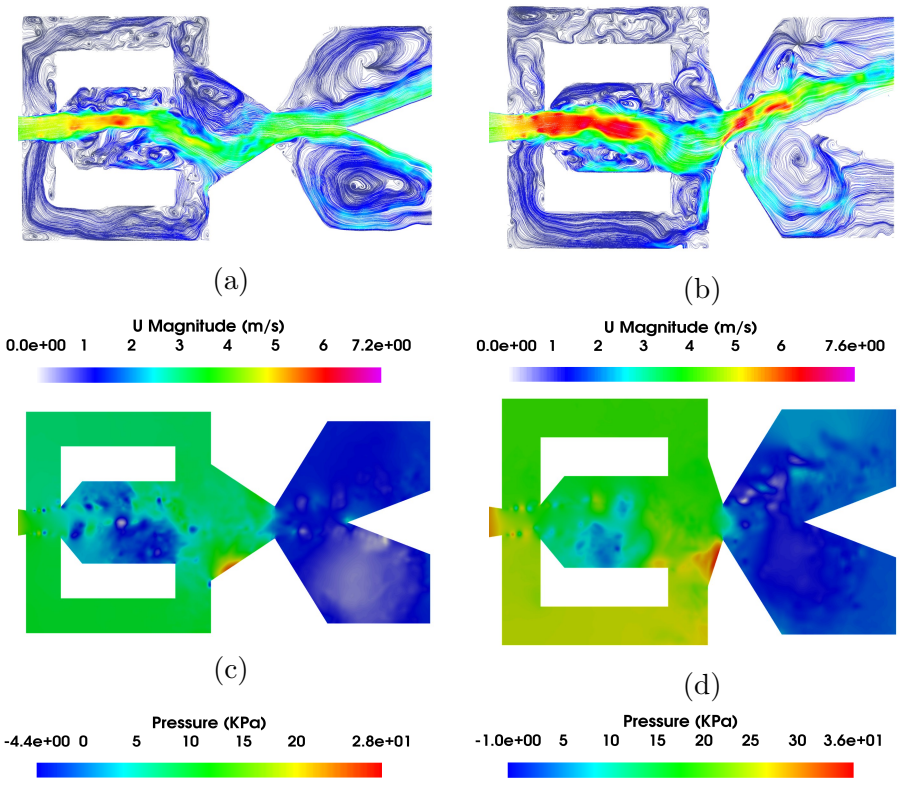

Figure 3.16: Fluidic oscillator internal velocity field (a, b) and pressure magnitude (c, d). Maximum outlet angle (a, c), minimum outlet angle (b, d). Reynolds number 16034.

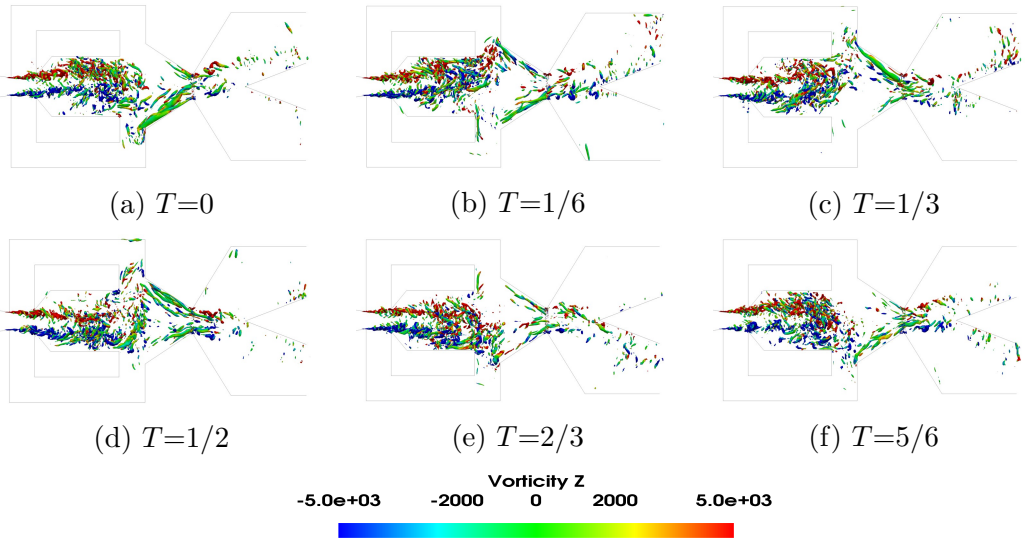

Figure 3.17: Q criterion at the mixing chamber period of oscillation divided into six equally spaced times, Reynolds number 16,034. Maximum outlet angle.

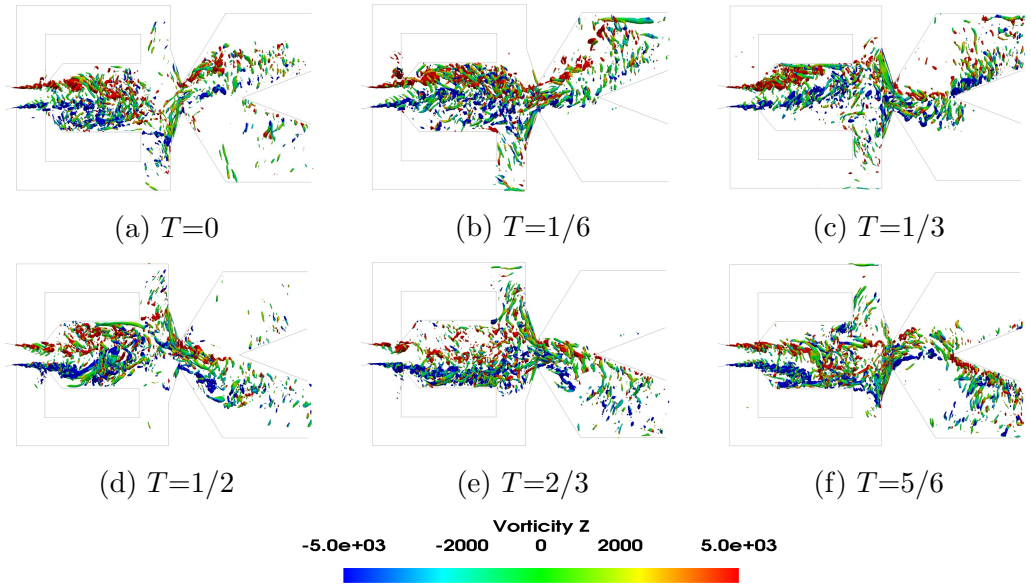

Figure 3.18: Q criterion at the mixing chamber period of oscillation divided into six equally spaced times, Reynolds number 16,034. Minimum outlet angle.

The effects on the (FO) outlet mass flow, the (FC) mass flow, the net momentum acting on the (FC) outlets, the stagnation pressure on the (MC) converging walls, and the (MC) jet oscillation angle, for the baseline case, the lowest and highest mixing chamber outlet angles evaluated, at Reynolds number 16034, are presented in figure 3.19. The first thing to observe is that the (MC) outlet angle modification, generates a clear effect on the (FO) main parameters. As the outlet angle increases, a clear peak to peak amplitude reduction of all measured parameters was observed. For the (MC) smallest outlet angle studied, the mass flow frequency and amplitude at the (FO) outlet are maximum, the reverse flow is also the largest. The peak to peak mass flow amplitude at the (FC's), is about 53% smaller when using the highest (MC) outlet angle than when using the smallest one. Under all (MC) outlet angles studied, the (FC) mass flow always goes from the (FC) inlets to outlets, for the lowest outlet angle, the minimum (FC) mass flow is about zero, see figure 3.19e. The average pressure at the (MC) lower converging wall, is around 22% lower for the highest (MC) outlet angle than for the lowest one. When the lowest (MC) outlet angle was employed, a clear difference between the static pressure at the (FC) outlets was observed, a maximum pressure difference between both outlets of over 3000Pa was measured. For the lowest (MC) outlet angle, the net momentum acting onto the lateral sides of the main jet entering the (MC), is about 38% higher than when the highest angle is used, figure 3.19d. This effect helps in generating a much larger jet oscillation amplitude in the (MC) and at the (FO) outlet mass flow, see figure 3.19a and 3.19b. The conclusion is

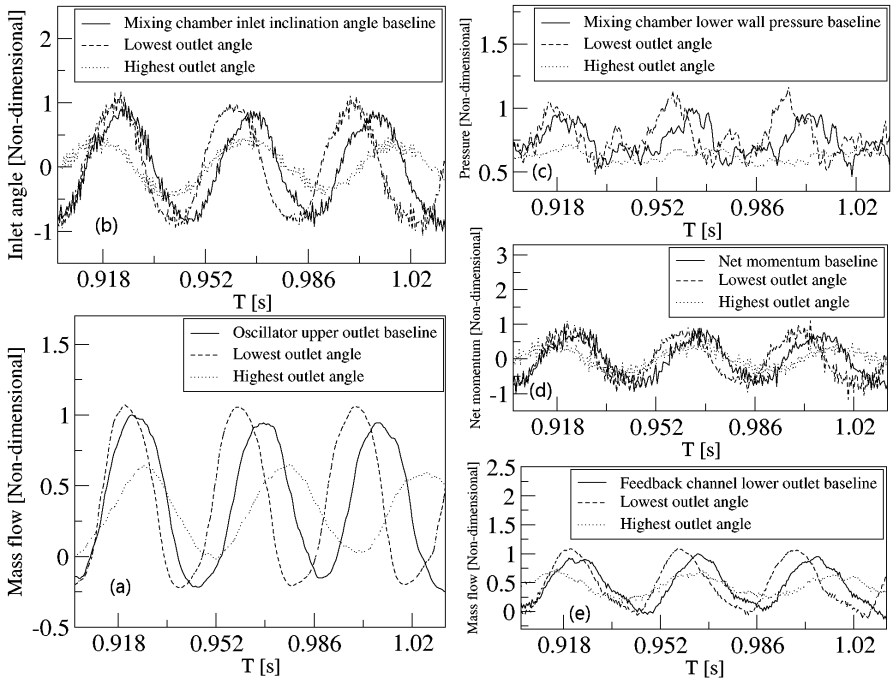

Figure 3.19: Dynamic effects of the (MC) outlet angle modification on the main flow parameters, Reynolds number 16034. Each graph presents three non-dimensional curves characterizing results from the baseline, the lowest and highest outlet angle cases, and as a function of the dimensional time. In figure (a) the mass flow across the upper oscillator outlet is presented. Figure (b) introduces the temporal variation of the (MC) inlet inclination angle. Figures (c) presents the pressure at the (MC) lower inclined wall. The net momentum acting on the lateral sides of the main jet is presented in figure (d). Figure (e) characterizes the mass flow at the lower feedback channel outlet.

that high oscillation amplitudes are linked with high pressure variations on the (MC) converging walls and therefore on the (FC) outlets.

Figure 3.20 shows the forces acting on the main jet lateral sides, the pressure and the mass flow terms of the net momentum acting on the main jet lateral sides are compared for the lowest, baseline and highest outlet angles. Regardless of the outlet width studied, the pressure term of the net-momentum is much larger than the net-momentum mass flow term, indicating that the (FO) is pressure driven. From figure 3.20, it is also important to realize that the both momentum terms regarding pressure and mass flow are smaller for the highest outlet angle resulting in a smaller frequency and amplitude as shown in figure 3.15. The opposite happen for the lowest outlet angle, as for this case higher momentum resulting higher frequency and amplitude as shown in figure 3.15.

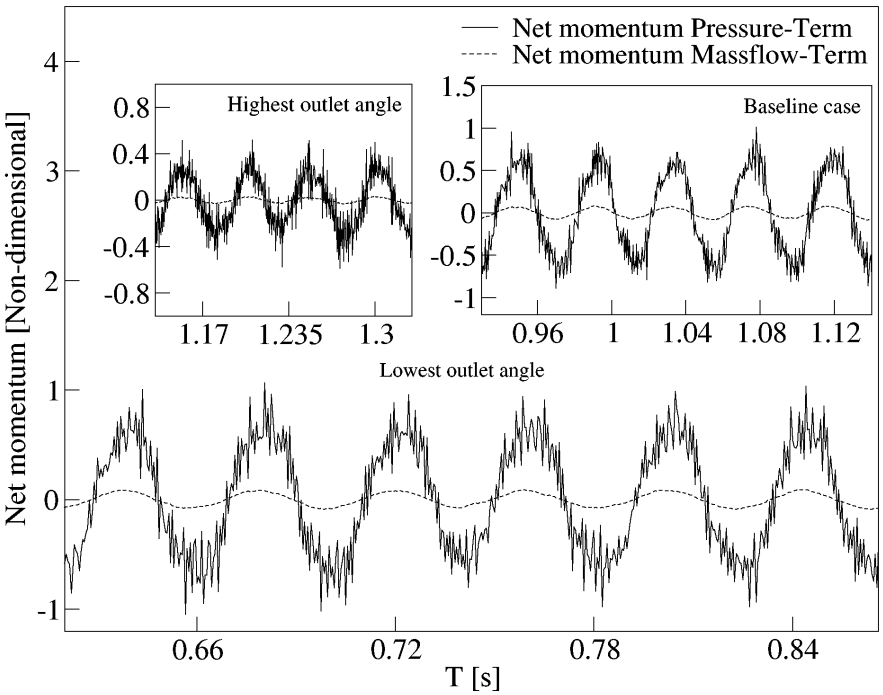

Figure 3.20: Comparison of the pressure and mass flow terms of the net-momentum and for three characteristic outlet angles, Reynolds number 16034.

3.5.4 Modifying the (MC) inlet angle

The flow effects caused by the modification of the (MC) inlet angle is presented in this section, just three angles including the baseline case, were considered, see figure 3.21. It was observed that, the (FO) outlet mass flow peak to peak oscillation amplitude, when compared with the baseline case, increased an 8.9% for an inlet angle increase of 74%. When the inlet angle increased by 93%, the (FO) outlet mass flow amplitude increased versus the baseline case, just 1.6%. Regarding the (FO) outlet mass flow oscillating frequency, it increases very slightly with the inlet angle increase, in fact, as it has been introduced in all previous cases, the frequency and amplitude variations are more relevant as the Reynolds number increases. Figure 3.21 also clarifies that the same trend is observed regardless of the Reynolds number considered.

Figure 3.22 introduces the velocity field and the pressure magnitude inside the (FO) for the maximum and minimum (MC) inlet angles evaluated. As the inlet angle increases, there is less space on both sides of the jet in the (MC) for the Coanda effect to appear, yet the jet keeps oscillating. This supports the thesis presented in this chapter and already outlined in [46, 67], which established that in reality, what forces the jet to flip is the pressure term of the net momentum acting on the lateral

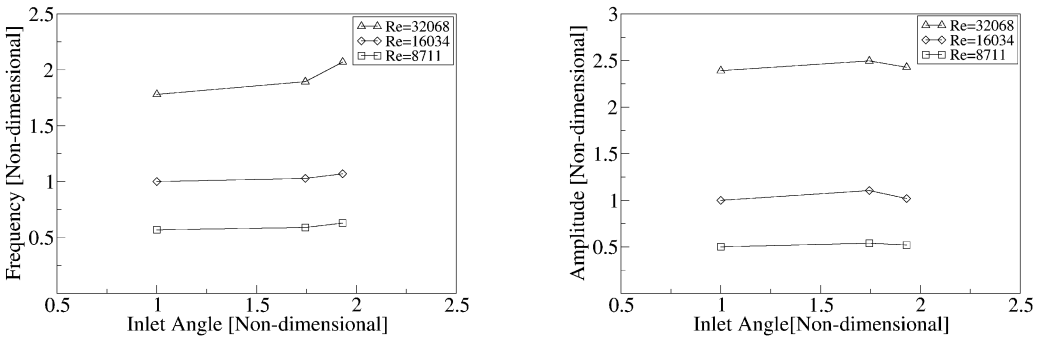

(a) (b)

Figure 3.21: Fluidic oscillator output mass flow Frequency and amplitude as a function of the mixing chamber inlet angle and for three different Reynolds numbers, 8711, 16034 and 32068.

sides of the jet entering the (MC). Regardless of the (MC) inlet inclination angle, the maximum stagnation pressure appearing at the (MC) converging walls is very similar, a peak to peak stagnation pressure increase of nearly 18% is observed when comparing the highest inlet angle evaluated with the lowest inlet angle case, compare figures 3.22c with 3.22d, see as well figure 3.25c. As a result, the net momentum peak to peak amplitude acting onto the incoming jet lateral surfaces, suffers a small increase of 2.8%, although it is difficult to distinguish the different curves, this information is presented in figure 3.25d.

From the observation of figures 3.4a, b, 3.10a, b, 3.16a, b and 3.22a, b, it is noticed that in all (FC's) 90 degrees corners small vortices appear, indicating it exists fluid recirculation in all these points. To minimize fluid recirculation it would be desirable to round all 90 degrees corners, the expected effect would be, a small increase of actuator frequency, since in reality rounding the corners would facilitate the fluid to move back and forward along the feedback channels, pressure losses would as well decrease, This observation was previously done by [43]. Figures 3.23 and 3.24 shows vortical structures appearing inside the FO by means of isosurfaces based on the Q criterion respectively for the highest and medium inlet angle. The isosurfaces are colored by the vorticity about the Z axis. The color blue indicates the structures turn clockwise, the red color is associated with counterclockwise rotation. The snapshot sequence presented in figures 3.23 and 3.24 characterizes a full oscillation period divided into six evenly spaced time steps. For the highest inlet angle, less vortical structures can be seen in the most part of the mixing chamber (MC) because there is

no space for the vortices to grow, these structures can be seen more at the end of the MC and near MC converging surfaces as shown in figure 3.23. The same phenomena happens for the medium inlet angle, in this case more vortical structures can be seen inside the MC as shown in figure 3.24.

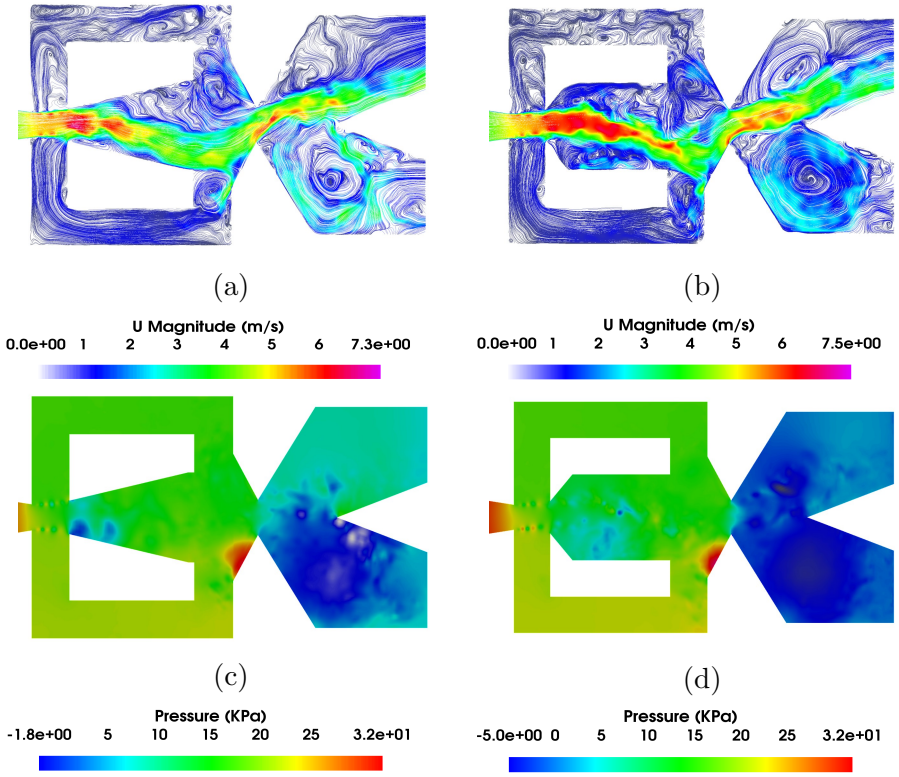

Figure 3.22: Fluidic oscillator internal velocity field (a, b) and pressure magnitude (c, d). Maximum inlet angle (a, c), minimum inlet angle (b, d). Reynolds number 16034.

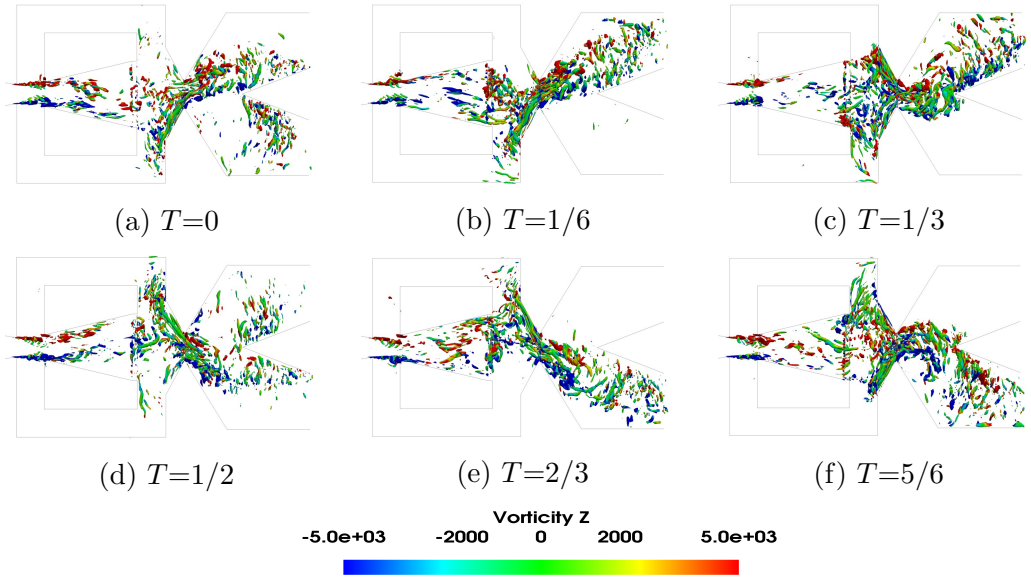

(a) T=0 (b) T=1/6 (c) T=1/3

(d) T=1/2 (e) T=2/3 (f) T=5/6

Figure 3.23: Q criterion at the mixing chamber period of oscillation divided into six equally spaced times, Reynolds number 16,034. Maximum inlet angle.

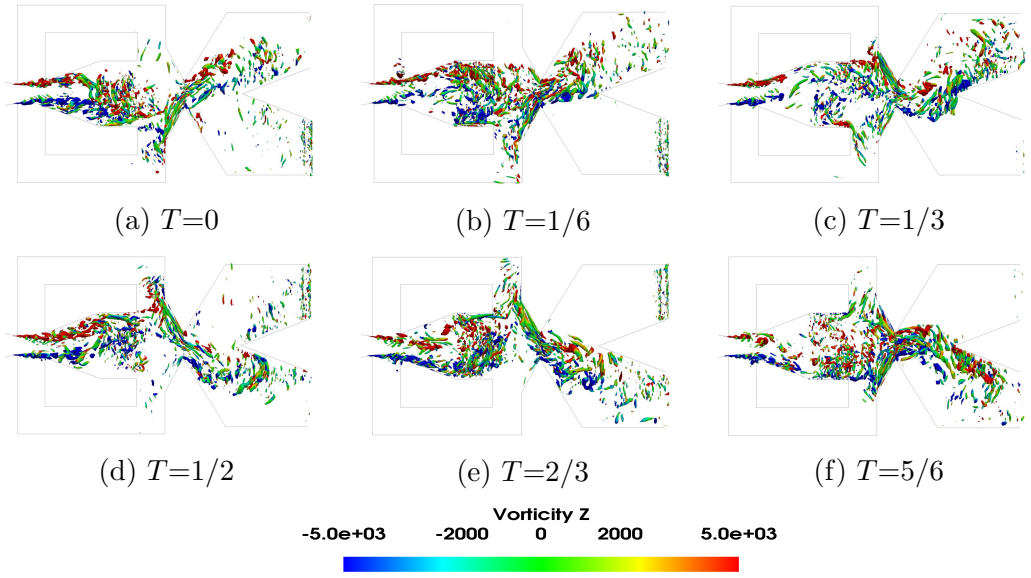

(a) T=0 (b) T=1/6 (c) T=1/3

(d) T=1/2 (e) T=2/3 (f) T=5/6

Figure 3.24: Q criterion at the mixing chamber period of oscillation divided into six equally spaced times, Reynolds number 16,034. Medium inlet angle.

Based on the results obtained in the present section, see figure 3.25, it can be concluded that the effect of modifying the (MC) inlet angle, does not generate very relevant changes on any of the studied fluid flow parameters. In fact, the (MC) inlet angle seems to be particularly linked with the Coanda effect alternatively appearing on both sides of the mixing chamber. Yet, and based on the results obtained in the

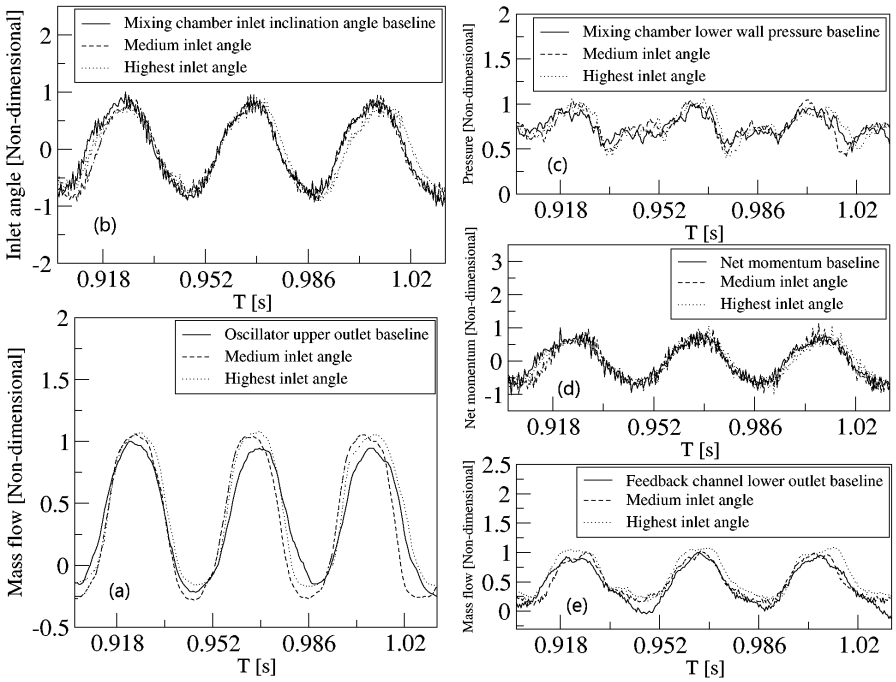

Figure 3.25: Dynamic effects of the (MC) inlet angle modification on the main flow parameters, Reynolds number 16034. Each graph presents three non-dimensional curves characterizing results from the baseline, the medium and highest inlet angle cases, and as a function of the dimensional time. In figure (a) the mass flow across the upper oscillator outlet is presented. Figure (b) introduces the temporal variation of the (MC) inlet inclination angle. Figures (c) presents the pressure at the (MC) lower inclined wall. The net momentum acting on the lateral sides of the main jet is presented in figure (d). Figure (e) characterizes the mass flow at the lower feedback channel outlet.

present set of simulations, the Coanda effect has a minor effect on the (FO) flow dynamic performance. It is important to realize, when observing figure 3.25, that the minor (MC) inlet angle, corresponds to the baseline case, therefore, the other two angles studied are called medium and highest angles. The feedback channels mass flow peak to peak amplitude, suffered a decrease versus the baseline case of 14.5%, when the medium inlet angle was used, the (FC) peak to peak amplitude decreased a 16% when the inlet angle increase was of 93%, see figure 3.25e. The reverse flow at the (FO) outlets suffered an initial increase as the inlet angle increased, and slightly reduced when the inlet angle reached its maximum value, see figure 3.25a. The jet inclination angle inside the (MC), suffered a small decrease of 9% when comparing the minimum and maximum (MC) inlet angles evaluated, see figure 3.25b. Notice that the jet inclination angle inside the (MC) is in reality delimited by the (MC) internal walls, as the inlet angle increases there is less space in the (MC) for the

jet to fluctuate. From this particular study it is observed that, small stagnation pressure variations at the (MC) converging walls, generate clear (FO) outlet mass flow modifications, compare figures 3.25a with 3.25c. Figure 3.26 shows the forces acting on the main jet lateral sides, the pressure and the mass flow terms of the net momentum acting on the main jet lateral sides are compared for the baseline, medium and highest inlet angles. Regardless of the outlet width studied, the pressure term of the net-momentum is much larger than the net-momentum mass flow term, indicating that the (FO) is pressure driven. As shown in figure 3.26, the net momentum not changing much, having more or less the same frequency and amplitude as shown in figure 3.21.

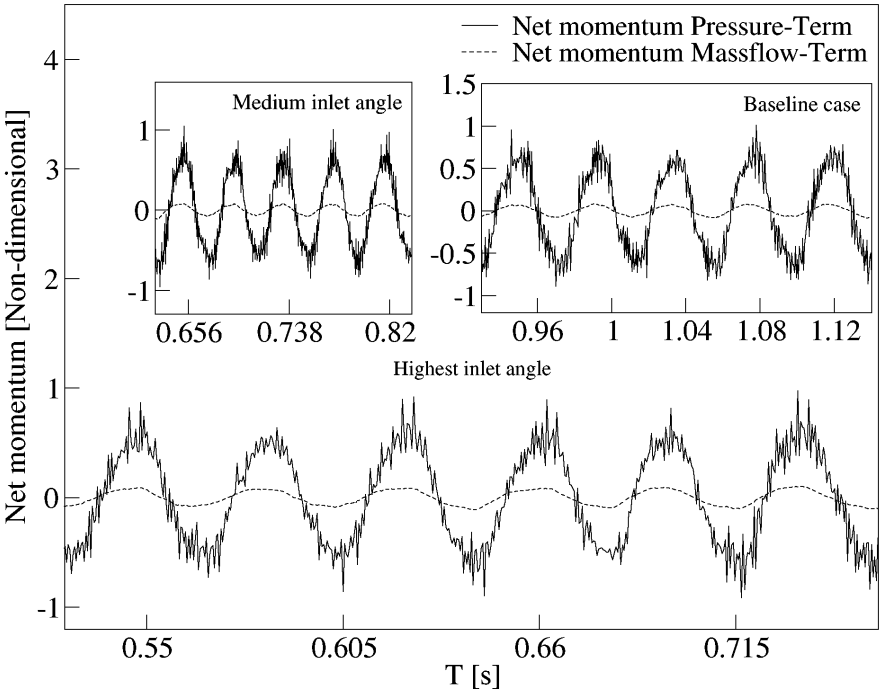

Figure 3.26: Comparison of the pressure and mass flow terms of the net-momentum and for three characteristic inlet angles, Reynolds number 16034.

3.5.5 Relation Reynolds frequency for all dimensional modifications performed

After evaluating the fluidic oscillator output mass flow frequency and amplitude as a function of the different internal modifications and at several Reynolds numbers, one of the conclusions from the present paper is, that the conventional Reynolds-frequency linear behaviour for a given oscillator, can be expressed of a set of linear functions.

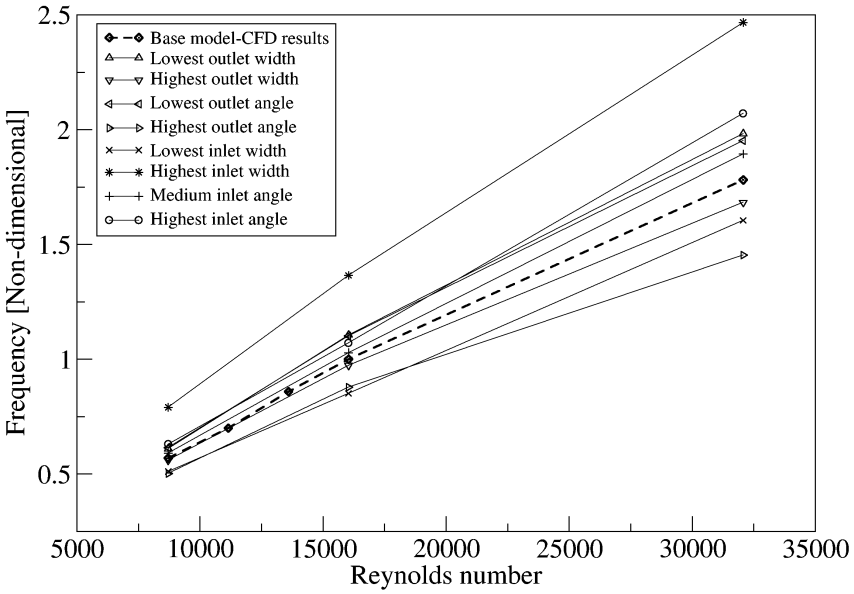

Figure 3.27: Relation Reynolds number versus mass flow output frequency, for all dimensional modifications studied.

Each line represents the operating conditions of the fluidic oscillator once a particular modification is undertaken, notice that in almost all cases, a linear relation is obtained, see figure 3.27. For example, the increase of the inlet width, and regardless of the Reynolds number employed, generates output frequencies considerably higher than the baseline case. The (FO) outlet mass flow oscillating frequency, increases versus the baseline case one, by around 40% when the maximum inlet width is employed. The outlet frequency also increases when employing the lowest output angle or the lowest output width, although for these particular cases the increase is smaller than 7%. The rest of the internal modifications, generate frequencies slightly smaller than the baseline case ones, the trend is the same for all Reynolds numbers studied. It is also interesting to observe that, when the highest (MC) outlet angle is used, the expected Reynolds-frequency linearity disappears at high Reynolds numbers, the frequency for this case is smaller than what could be expected. The authors believe this particular reduction of frequency at Reynolds 32068, is due to the channel effect caused by the highest outlet angle, this particular angle directs the fluid from the (MC) to the oscillator outlets, minimizing the generation of a stagnation pressure point at the (MC) converging walls, in other words, just an small amount of the kinetic energy

associated to the fluid is being transformed into stagnation pressure. The result is, it requires a longer time to build the required momentum at the (FC) outlets for the jet to flip. Under these conditions, the fluid is directed to the lateral sides of the oscillator external chamber wedge and flows almost parallel to them, see figure 3.16a.

It is at this point interesting to remember that, according to [34], the (FO) angled configuration, which is the one used in this study, looses its linearity at Reynolds 30000, this helps to explain why the curves presented in figure 3.27, are not fully linear. As Reynolds number increases, the flow inside the (FO) goes from quasi-periodic to chaotic, being this the reason why linearity disappears. It is also interesting to recall, that according to [56], the fluidic oscillator internal performance is essentially the same for different outlet configurations, whether one or two outlets are considered.

3.5.6 Stagnation pressure at the (MC) converging walls and net momentum acting on the (MC) incoming jet as a function of the Reynolds number.

In the present section, the net momentum acting onto the jet entering the mixing chamber will be evaluated and compared with the stagnation pressure variations at the (MC) converging walls. The momentum of the fluid acting on a given surface was defined as equation 3.1. As both feedback channels, add momentum to the lateral sides of the main jet entering the (MC), equation 3.1 will need to be applied to each (FC) outlet. In order to evaluate which is the temporal net momentum applied to the incoming jet, it will be required to know the instantaneous mass flow through both (FC) outlets as well as the temporal pressure at these two sections.

In [46] it was concluded the oscillators studied appeared to be pressure driven, the same conclusion was reached in [67], where it was demonstrated that the forces triggering the oscillation were mostly due to the pressure difference at the feedback channels outlets. In the present section the different forces acting on the jet lateral surfaces will be analyzed for each of the different geometry modifications evaluated and as a function of the Reynolds number.

The average net momentum applied to the jet entering the (MC), is for all Reynolds numbers and (FO) modifications, having a value close to zero, as observed for a Reynolds number of 16034 in figures, 3.7d, 3.13d, 3.19d and 3.25d. Regarding the evolution of the average net momentum applied to the jet at the (MC) inlet, it was observed that whenever the pressure at the (MC) is particularly high and the Reynolds number increases, the average net momentum applied to the jet decreases. This happens for the following cases, lowest outlet width, lowest outlet angle and for

Table 3.3: Equations characterizing the evolution of non dimensional average pressure at the (MC) outlet converging walls, and as a function of the Reynolds number. These equations are valid in the range $8711 < \mathrm{Re} < 32068$. The coefficient of determination was $(R)^2 = 1$ for all curves presented.

Geometry modification	Non-dimensional average pressure at the (MC) converging walls, as a function of the Reynolds number
Baseline	$2.12561E-9*Re^2-7.13644E-6*Re+0.56795$
Highest inlet angle	$2.09249E-9*Re^2-3.78849E-6*Re+0.54447$
Lowest outlet angle	$2.05449E-9*Re^2-6.89096E-7*Re+0.48405$
Highest outlet angle	$1.93563E-9*Re^2-9.36739E-7*Re+0.85368$
Lowest outlet width	$1.14444E-7*Re^2-4.10206E-4*Re+2.92727$
Highest outlet width	$1.21442E-11*Re^2+3.80462E-6*Re+0.48910$
Lowest inlet width	$1.94488E-9*Re^2-3.32478E-6*Re+0.53530$
Highest inlet width	$1E-9*Re^2+1.65524E-5*Re+0.41953$

the baseline case. On the other hand, whenever the pressure at the (MC) is particularly low, which happens for the highest outlet width, the lowest inlet width, the highest inlet width and the highest outlet angle, the average net momentum increases with the Reynolds number increase. Nevertheless, and as a general trend it can be stated that, regardless of the (FO) modification performed, as the Reynolds number increases the average pressure in the (MC) also increases. The equations characterizing the evolution of the average non-dimensional stagnation pressure at the (MC) converging walls, and the average non-dimensional net momentum acting on the jet entering the (MC), are respectively presented as a function of the Reynolds number in tables 3.3 and 3.4. These equations are valid for a range of Reynolds numbers between $8711<\mathrm{Re}<32068$, and were obtained from the data presented in figures 3.7, 3.13, 3.19 and 3.25, as well as from similar figures obtained at Reynolds numbers 8711 and 32068. Some geometry modifications, regardless of the Reynolds number, generate a decrease of the (MC) average pressure when compared to the one existing in the baseline case, these are, the highest and lowest inlet widths, the highest outlet angle and the highest outlet width. At Reynolds number 32068, the (MC) average pressure decrease versus the baseline one was respectively of 23.5%, 3.8%, 30% and 75%. On the other hand, the geometry modification generating a drastic increase of the (MC) average pressure, was the lowest outlet width, which increased the baseline

Table 3.4: Equations characterizing the evolution of non-dimensional average net momentum acting on the jet entering the (MC), and as a function of the Reynolds number. These equations are valid in the range 8711 < Re < 32068. The coefficient of determination was $(R)^2 = 1$ for all curves presented.

Geometry modification	Average non-dimensional net momentum acting on the jet entering the (MC), as a function of the Reynols number
Baseline	$1E-9*Re^2-8.37587E-5*Re+0.58993$
Highest inlet angle	$1.24383E-8*Re^2-1.53242E-4*Re+0.22188$
Lowest outlet angle	$3.37456E-9*Re^2-1.14474E-4*Re+0.99111$
Highest outlet angle	$7.50840E-11*Re^2-4.28247E-5*Re+0.32902$
Lowest outlet width	$-3.84280E-8*Re^2+8.76204E-4*Re-4.29897$
Highest outlet width	$4.83380E-9*Re^2-6.42540E-5*Re-0.30568$
Lowest inlet width	$2.18933E-9*Re^2-2.47378E-5*Re+0.20356$
Highest inlet width	$9.22674E-9*Re^2-3.57369E-4*Re+2.37742$

pressure by almost 42 times at Reynolds 32068. When employing the lowest outlet angle and for the same Reynolds number, the average pressure increase was of 11.4%.

The analysis of the peak to peak amplitude of the stagnation pressure at the (MC) outlet converging walls, and the peak to peak net momentum amplitude acting on the lateral sides of the jet entering the (MC), provides a significant information on the flow dynamics inside the (MC). Tables 3.5 and 3.6, introduce the equations characterizing the evolution of these parameters as a function of the Reynolds number and for the different geometry modifications studied. The first thing to observe is that, the stagnation pressure and the net momentum amplitudes, increase as a function of the Reynolds number almost to the power 2. It is also interesting to observe that, in nearly all the cases studied, the exponent associated to the Reynolds number when considering the stagnation pressure peak to peak amplitude, is smaller than the one associated to the net momentum amplitude for the same case. This is particularly relevant for the following cases, highest inlet width, highest inlet angle, lowest outlet angle and lowest outlet width. In any case, and regardless of the case studied, the equations from tables 3.5 and 3.6, show a direct link between the peak to peak stagnation pressure amplitude and the net momentum amplitude, giving therefore strength to the thesis established in references [46, 67] and in the present paper, regarding the origin of the forces driving the oscillation. To understand, for each of the cases studied, the origin of the net momentum driving the oscillation, the relation

Table 3.5: Equations characterizing the evolution of non-dimensional peak to peak stagnation pressure amplitude at the (MC) outlet converging walls, and as a function of the Reynolds number. These equations are valid in the range 8711 < Re < 32068.

Geometry modification	Non-dimensional peak to peak pressure amplitude at the (MC) converging walls	Coefficient of determination $(R)^2$
Baseline	$4.59756E-9*Re^{1.98634}$	0.99945
Highest inlet angle	$7.49338E-9*Re^{1.95698}$	0.99981
Lowest outlet angle	$1.93949E-8*Re^{1.85146}$	0.99811
Highest outlet angle	$1.23730E-9*Re^{2.06682}$	0.99738
Lowest outlet width	$2.12603E-8*Re^{1.86529}$	0.99786
Highest outlet width	$6.07789E-9*Re^{1.93720}$	0.99997
Lowest inlet width	$2.82056E-9*Re^{2.02025}$	0.99320
Highest inlet width	$1.87225E-8*Re^{1.83988}$	0.99335

between the peak to peak net momentum term due to the static pressure acting on the (FC) outlets, was compared with the peak to peak net momentum term due to the feedback channels mass flow. This comparison given as the ratio between the static pressure divided by the (FC) mass flow tern, is presented in table 3.7. There are four geometry modifications, highest inlet width, highest inlet angle, lowest outlet angle and lowest outlet width, at which the pressure/mass flow momentum ratio is particularly small, indicating that under these conditions, the feedback channel mass flow plays a more relevant role regarding the net momentum applied to the jet. Notice that these four geometry modifications, are the same ones generating a particular increase in the exponent associated to the Reynolds number, observed when comparing tables 3.6 and 3.5. The conclusion is that, for these particular geometry modifications, the (FC) mass flow plays a more relevant role, although small, on the net momentum driving the oscillation. Yet, regardless of the geometry modification and the Reynolds number studied, the oscillation of the jet in the (MC) is mostly driven by the pressure difference at the (FC) outlets. Finally, and based on the results presented in table 3.7 it can be concluded that, the pressure/mass flow momentum ratio is highly dependent on the geometry modification, but it is not particularly affected by the Reynolds number.

Regarding the inlet width variations, from the results obtained it is observed that, the stagnation pressure and the net momentum peak to peak amplitudes, suffer

Table 3.6: Equations characterizing the evolution of non-dimensional peak to peak net momentum amplitude at the (MC) incoming jet, and as a function of the Reynolds number. These equations are valid in the range 8711 < Re < 32068.

Geometry modification	Non-dimensional peak to peak net momentum amplitude at the (MC) incoming jet	Coefficient of determination $(R)^2$
Baseline	$4.65284E-9*Re^{1.98324}$	0.99987
Highest inlet angle	$2.70649E-9*Re^{2.04466}$	0.99944
Lowest outlet angle	$5.63381E-9*Re^{1.97122}$	0.99999
Highest outlet angle	$1E-9*Re^{1.92907}$	0.98941
Lowest outlet width	$4.29860E-9*Re^{2.00206}$	0.99997
Highest outlet width	$2.90893E-9*Re^{2.00411}$	0.99724
Lowest inlet width	$2E-9*Re^{2.00637}$	0.99724
Highest inlet width	$1.86488E-9*Re^{2.03883}$	0.99894

a minor increase as the inlet width increases. When comparing the minimum and maximum inlet widths studied, at Reynolds number 16034, the peak to peak stagnation pressure and momentum increase, were respectively of 17% and 31% versus their minimum values. When considering the outlet width effects on the (MC) converging walls peak to peak stagnation pressure amplitude, it was observed that as the outlet width decreases, the peak to peak stagnation pressure amplitude keeps increasing, also the net momentum amplitude acting on the lateral surfaces of the (MC) incoming jet, increases as the outlet width decreases. When comparing the minimum and maximum outlet widths studied, the increase of the peak to peak stagnation pressure and momentum, at Re=16034, was respectively of 39% and 36%. The same trend is observed under all Reynolds numbers studied. As Reynolds number increases, the variation in percentage for both parameters decreases.

When evaluating the (MC) outlet angle and for all the cases studied, the minimum peak to peak (MC) converging walls stagnation pressure, was obtained when the highest outlet angle was employed. As the outlet angle decreased, the peak to peak stagnation pressure at the (MC) outlet converging walls, as well as the peak to peak momentum amplitude at the (FC) outlets, kept increasing. The increase versus the minimum value was respectively of 68% and 38% at Re=16034. As Reynolds number grows, the variation in percentage reduces. When using the highest outlet angle, the peak to peak net momentum amplitude associated was higher than for the case

Table 3.7: Evaluation of the peak to peak net momentum amplitude at the (MC) incoming jet due to the pressure term, divided by the net momentum amplitude due to the (FC) mass flow term, and for the three Reynolds numbers studied.

Geometry modification	Reynolds number 8711	Reynolds number 16034	Reynolds number 32068
Baseline	11.96	12.58	9.88
Highest inlet angle	8.72	9.38	8.1
Lowest outlet angle	9.73	10.71	9.25
Highest outlet angle	16.86	17.14	14.97
Lowest outlet width	10.63	10.77	9.32
Highest outlet width	12.93	13.29	10.88
Lowest inlet width	13.61	12.38	14.52
Highest inlet width	3.78	3.74	4.12

where the lowest inlet width was used. The decrease of the inlet width, appears to particularly reduce the net momentum applied to the (MC) incoming jet. The mass flow along the (FC's) is effectively controlled by the inlet width. Regardless of the Reynolds number, as the inlet angle increases, the stagnation pressure peak to peak amplitude at the (MC) converging walls, also increases. The increase is more relevant at high Reynolds numbers. It is interesting to see that the peak to peak amplitude of the net momentum acting on the lateral sides of the jet entering the (MC), initially increases with the inlet angle increase, but as the inlet angle reaches its maximum value, the momentum amplitude slightly decreases. At the highest inlet angle, the stagnation pressure waves generated at the (MC) converging walls, are not efficiently being transferred to the (FC's) outlets. In fact, the pressure at both (FC's) outlets, is very much the same under these conditions. Regardless of the (FO) geometry modification performed, the same trend on peak to peak pressure and momentum, appeared at all Reynolds numbers evaluated, therefore, for a given (FO) modification, the same physical phenomenon is driving the oscillations at all Reynolds numbers.

In order to properly understand the effect of the inlet width variation on the net momentum acting onto the (MC) incoming jet, figure 3.28 is introduced. The first point to realize is that, for the lowest inlet width, the noise associated to the pressure wave generated at the stagnation points appearing alternatively at the (FC) outlets, see figures 3.4d and 3.7d, is much higher than in the rest of the cases studied. For this particular case, see figure 3.7e, there is a large amount of mass flow traveling

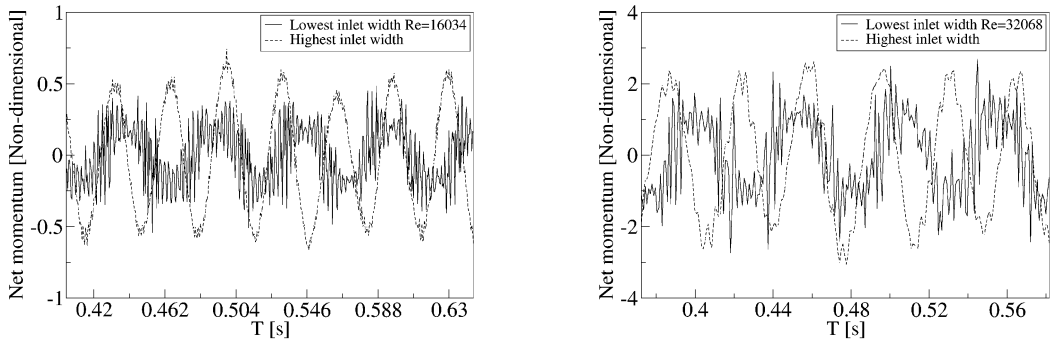

(a) (b)

Figure 3.28: Net momentum acting on the fluidic oscillator inlet jet and for two different mixing chamber inlet widths, two different Reynolds numbers, 16034 and 32068, were considered.

backwards along the feedback channels. The authors believe, the weak pressure waves originated at the (MC) outlet converging walls, which travel along the (FC) and also inside the (MC), are being disrupted by the particularly high mass flow moving along the (FC) and in opposite direction to the pressure waves, the result is a highly noisy pressure fluctuation at the (FC) outlets. In reality, and for this particular case, pressure waves are being generated at the same time on the (MC) outlet converging walls and at the (FC's) outlet internal vertical walls, these pressure waves collide inside the (FC's) enhancing the noise spectrum. Notice as well from figure 3.28 that, the noise generated reduces to a minimum whenever the maximum inlet width is being employed. For this case, the mass flow traveling along the (FC's), always goes from the (FC's) inlets to the outlets, see figure 3.7e, and pressure waves are not generated alternatively at the (FC's) outlet internal vertical walls. The direction of the (FC's) mass flow, always coincides with the traveling direction of the pressure waves, which are generated at the (MC) outlet converging walls.

3.6 Conclusions

A careful 3D-CFD evaluation of a fluidic oscillator under turbulent conditions has been performed. The study allows identifying, which dimensional parameters are more relevant regarding the modification of the fluidic actuator frequency and output amplitude. When modifying the (MC) inlet width, a threshold in both directions was observed at which fluidic oscillator was simply not oscillating. By increasing

the (MC) outlet width or the (MC) outlet angle, the (FO) output frequency and amplitude decreased. The maximum (FO) outlet mass flow amplitude, was always obtained whenever reverse flow at the (FO) outlets existed, the higher the reverse flow value, the higher the (FO) outlet mass flow amplitude.

The pressure term of the net momentum acting onto the lateral sides of the mixing chamber incoming jet, directs under all conditions studied, the oscillation of the jet inside the (MC) and therefore the oscillation at the (FO) outlets. The actuator is pressure driven. The net momentum oscillation is mostly due to the stagnation pressure fluctuation occurring at the (MC) converging surfaces, the net momentum due to the mass flow flowing along the feedback channels was observed to be negligible in all cases studied, the amplitude of the net momentum oscillation is directly linked with the maximum and minimum values of the stagnation pressure appearing at the (MC) outlet converging surfaces.

Low inlet widths, have associated a considerable reverse flow along the (FC's), reverse flow also appears at the (FO) outlets, therefore the (FO) mass flow amplitude is higher than the one existing at high inlet widths. The net momentum required to flip the jet over in the (MC), is particularly low at small inlet widths. The modification of the inlet width, drastically affects the magnitude and direction of the (FC) mass flow. At very small inlet widths, pressure waves are generated on both ends of the (FC's), generating high levels of noise which affects the net momentum acting onto the (MC) incoming jet. The variation of the (MC) outlet width, affects mostly the (FO) output amplitude, from all cases studied, the highest outlet width generates the smallest stagnation pressure peak to peak amplitude, the smallest peak to peak net momentum, the smallest peak to peak (FO) output mass flow, the smallest peak to peak inlet angle amplitude and the smallest (FC) mass flow amplitude.

As the (MC) outlet angle increases, the average stagnation pressure at the (MC) converging walls, as well as its peak to peak amplitude decreases, a reduction of all peak to peak parameters is observed. In general it can be said that, the trend defined by the (MC) outlet converging walls stagnation pressure amplitude, is followed by the amplitude of the rest of the variables, the (MC) inlet angle, the net momentum applied to the (MC) incoming jet, the (FO) output mass flow and the (FC) mass flow.High frequencies are linked with high stagnation pressure values. Oscillator mass flow amplitude directly depends on the reverse flow appearing at the (FO) outlets. Reverse flow is particularly high at lowest outlet widths.

Chapter 4

Feedback channel effect under compressible flow conditions.

4.1 Introduction

Most of the recent studies on fluidic oscillators focused on two main very similar, canonical geometries, what Ostermann et al [34] called, the angled and the curved oscillator geometries. Some very recent studies on the angled geometry are, [9,10,34, 39–45], the curved geometry was mainly studied by [6,8,11,34,37,47–50]. Ostermann et al. [34], compared both geometries concluding that the curved one was energetically more efficient.

One of the first analysis of the internal flow in an angled fluidic oscillator, was undertaken by Bobusch et al [41]. PIV Experiments were performed using water as working fluid. The results provided detailed insight into the oscillation mechanism and also of the interaction between the mixing chamber fluid and the feedback channels flow.

Employing the same fluidic oscillator configuration previously analyzed by Bobbusch et al [41], Gartlein et al [42], carefully evaluated the internal fluid structures as well as the output jet oscillation parameters using high speed PIV, they also used time-resolved pressure measurements. The Reynolds numbers studied ranged between 10000 and 50000, air was employed as working fluid. They observed a linear dependency between the oscillation frequencies and the input Reynolds number. Several fluid properties such as the deflection angle, jet width and jet velocity were examined. It was found that these properties remained rather constant for a certain range of Reynolds numbers, and suffered a strong change once a certain Reynolds number was overcome.

Gokoglu et al [10], analyzed via 2D-CFD a very similar fluidic actuator configuration to the one evaluated by Bobusch et al [41] and Gartlein et al [42], but under supersonic flow conditions. Two fluids, helium and air, were considered as compressible and the SST k-omega turbulence model was employed for all the cases evaluated. The Mach numbers evaluated ranged between 0 and 2.5. No buffer zone was considered in the simulations, Dirichlet boundary conditions for pressure were employed at the outlet. When evaluating the relation Strouhal versus Reynolds numbers and regardless of the flow conditions, subsonic or supersonic, a linear relation was observed. Under subsonic conditions the Strouhal dependency on Reynolds number was much more relevant for helium than for air, such dependency was less relevant at supersonic conditions. It was observed that the time required for the oscillations to start, sharply decreased with the Mach number increase, this time remained almost constant at supersonic flow conditions.

The same configuration previously employed by [41], although now using a single exit, was numerically evaluated in 3D at Reynolds 30000 using the SST turbulent model by Pandley and Kim [45]. Two geometry parameters, the mixing chamber inlet and outlet widths were modified. They observed a significant effect of the flow structure and the feedback channel flow rate when modifying the inlet width, negligible effects were observed when modifying the outlet width.

Woszidlo et al [43], studied the same configuration previously evaluated by Gartlein et al [42]. Both configurations resemble the one studied by Bobbush et al [41], the main differences resided in the output shape. In Woszidlo et al [43] and Gartlein et al [42], just a single output was considered. In this new paper, Woszidlo et al [43], focused their attention in analyzing the flow phenomena inside the mixing chamber (MC) and the feedback channels (FC). They also highlighted that, the increase of the (MC) inlet width was tending to increase the output frequency and rounding the feedback channels diminished the generation of the separation bubbles on these channels corners.

The fluidic oscillator output frequency and amplitude, whenever the feedback channel and the mixing chamber lengths were modified, was studied using a 2D numerical model by Seo et al. [9], the fluid was considered as incompressible. An increase of the feedback channel length generated no modifications on the output frequency, the same observation was previously obtained by [56]. In both cases the flow was considered as incompressible, which is likely to be the reason why such outcome was obtained. Slupski and Kara [11], studied using 2D-URANS with the software Fluent a

range of feedback channel (FC) geometry parameters, the sweeping jet actuator configuration was the same as the one analyzed by Aram et al [8]. The effects of varying the feedback channel height and width for different mass flow rates were studied. All the simulations were performed for a fully-turbulent compressible flow, using SST k-omega turbulence model. It was found that, oscillation frequencies increased with increasing feedback channel height, up to a certain point and then remained unaffected, however, frequencies decreased by further increasing the feedback channel width.

Via using stereoscopic PIV, the velocity field properties emitted by a (FO) rounded configuration, was studied by Ostermann et al [50] at Reynolds <50000. Among the conclusions of their study, it was observed the necessity of performing compressible flow simulations to properly understand the flow physics inside the oscillator.

An experimental and numerical study of a fluidic oscillator which could generate a wide range of frequencies (50-300 Hz), was studied by Wang et al [35]. Their study focused on the oscillation frequency response for different lengths of the feedback channels. 2D compressible simulations were performed using sonicFoam with k-epsilon as turbulence model. An inverse linear relation between frequency and the length of feedback loops was observed, frequency increased by decreasing the feedback channel length. In Hirsch and Gharib [36], it was analyzed via Schlieren visualizations the dynamics of an sweeping jet actuator. Subsonic Mach numbers and the transition to sonic conditions was evaluated. They observed the oscillations started from small asymmetries caused by small differences in geometry.

The present chapter is presenting a 3D-DNS numerical evaluation of the same fluidic oscillator configuration employed in [41]. The effect on the oscillator dynamic characteristics of four different feedback channel lengths and two inlet velocities, will be be studied. The flow is considered as compressible and subsonic.

4.2 Fluidic oscillator test of independence and cases studied

According to the authors knowledge, on the present fluidic oscillator configuration, no previous 3D-DNS simulations considering the fluid as compressible have been undertaken. In the present paper and knowing that for the operating conditions chosen no comparisons with previous experimental or numerical results are possible, initially a mesh independence test study using the baseline fluidic oscillator configuration for a velocity of 97m/s measured at the fluidic oscillator (FO) power nozzle, see figure

4.1e, was performed. Three different mesh densities were evaluated, their respective number of cells were 5933900, 19600672 and 23882040, being their respective maximum Y+, obtained after the simulations of, 23.86, 3.16 and 2.6. For each mesh, the (FO) upper outlet mass flow oscillating frequency was measured and presented in figure 4.1d, where it is observed that the (FO) oscillating frequency has a small dependency on the mesh density chosen. When comparing the results obtained using the medium and the finest mesh, the frequency varied 0.96%, the variation increased to 5% when the coarsest and the finest mesh results were compared. The authors decided the medium mesh, having 19600672 cells, was accurate enough for the present purposes and it was used for the rest of the simulations. The time step used for all simulations was of 1e-8 seconds. Figures 4.1a, b, c, introduce the 3D medium mesh employed for the baseline (FO). In figure 4.1a, the different main parts of the (FO) are presented along with the entire mesh, figure 4.1b shows the mesh inside the (MC) and the (FC's), the vertical line depicted in figure 4.1b shows the exact location of the mesh section presented in figure 4.1c. The definition of the main geometry parameters is presented in figure 4.1e. The different boundary conditions employed in all simulations were, Dirichlet boundary condition (BC) for velocity and temperature at the (FO) inlet, Neumann (BC) for pressure. At the (FO) outlet Neumann (BC) for temperature and velocity as well as Dirichlet (BC) for pressure were used. At the walls, Neumann (BC) for pressure and temperature as well as Dirichlet (BC) for velocity were chosen. Air was employed as working fluid and two fluid velocities of 65 and 97 m/s defined at the (FO) power nozzle were considered, the respective Reynolds and Mach number at the same section was Re=12410, Re=18617, M=0.188 and M=0.282. The definition of these two dimensional numbers is given in the next section of the chapter. Based on these Mach numbers, the fluid could be considered as incompressible, yet as it will be presented in results, the maximum Mach number observed inside the mixing chamber (MC) leaves no doubt regarding the fluid compressibility.

Figure 4.2 introduces the different feedback channel lengths evaluated in the present study. Defining as L the length of the feedback channels (FC's) for the baseline case, the other three (FC's) represented in figures 4.2b, c and d, are having lengths of 2L, 3L and 9L respectively, the rest of the (FO) dimensions were kept constant for all cases. The number of cells employed for the (FO) with different feedback channels lengths, represented in figures 4.2b, c and d, were respectively of 21736832, 22394112 and 32417632. The mesh in the (FO) main body remained the same in all cases, just the (FC's) mesh was modified to accommodate the different

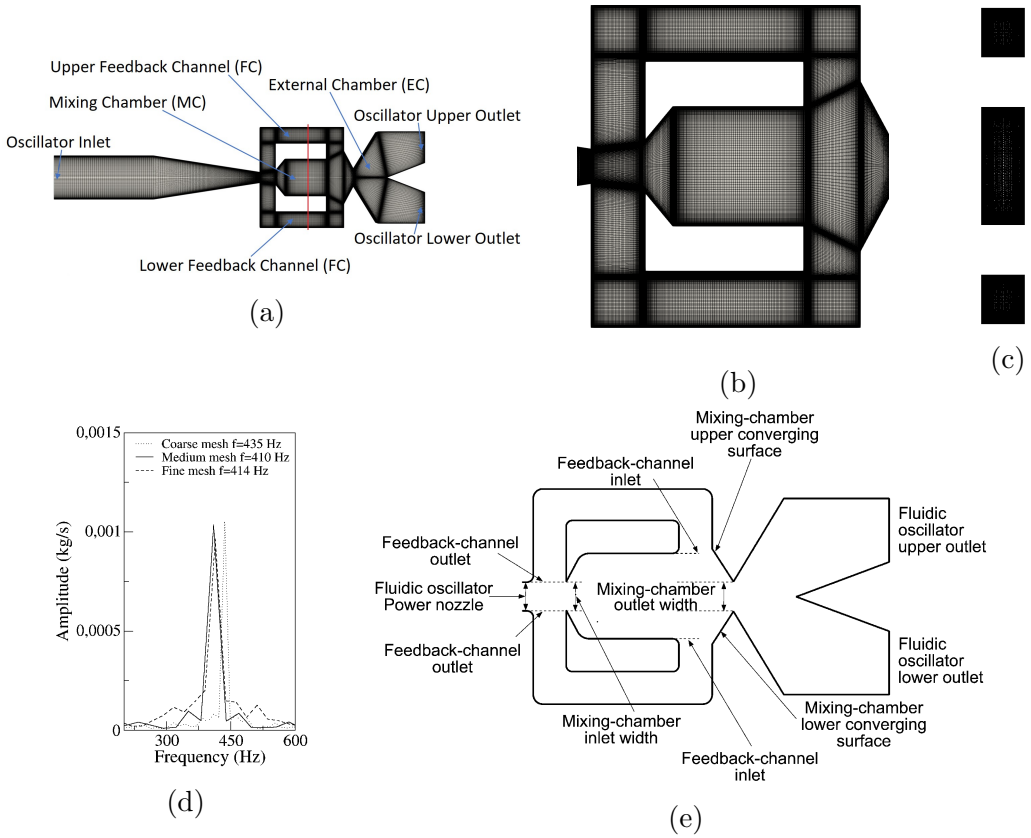

Figure 4.1: (a) Fluidic oscillator mesh, main view; (b) mixing chamber computational domain; (c) mesh side view; (d) fluidic oscillator output frequency for the three meshes studied; (e) mixing chamber main zones.

Figure 4.2: Baseline case fluidic oscillator with the different feedback channel lengths studied. (a) Original feedback channel length L; (b) feedback channel length 2L; (c) feedback channel length 3L; (d) feedback channel length 9L.

(FC) lengths. Three dimensional Direct Numerical Simulation (3D-DNS) is employed in all the cases studied, the fluid is considered as compressible.

4.3 Non-dimensional parameters

Despite the fact that most of the graphs presented in the present paper are given in dimensional form, it is required to define the different parameters used for non-dimensionalization as well as the non dimensional numbers used in the present manuscript. The Reynolds number definition used to characterize the main flow, was: $R_e = \frac{\rho V D_h}{\mu}$, ρ and μ are the density and dynamic viscosity of the fluid, respectively, D_h is the hydraulic diameter and V is the spatial averaged fluid velocity, in the present paper all these parameters were defined at the (FO) power nozzle. The definition employed for the Mach number was $M = \frac{V}{C}$, where for an ideal gas $C = \sqrt{\gamma RT}$. T being the fluid temperature, R the real gas constant and γ the adiabatic index. Despite the fact that the Mach number and the Reynolds number are defined at the power nozzle, the maximum fluid velocity was found under all conditions evaluated, at the (MC) outlet width, this is why the maximum Mach number is defined based on the fluid conditions in this particular section.

To be able to compare the relation between several parameters triggering the oscillations, some of the graphs presented were made non-dimensional, the non-dimensionalization was done by dividing each variable by the maximum value of the same variable obtained by the baseline case oscillator at the smallest Reynolds number studied.

Another parameter which will be employed in the present manuscript is the momentum associated to the fluid at the (FC's) outlet. According to the momentum equation it can be stated:

$$M = \dot{m}V + PS = \dot{m}^2/(S\rho) + PS \tag{4.1}$$

where $\dot{m}, V, S$, and P are respectively the mass flow, the spatial averaged fluid velocity, the surface where the momentum needs to be evaluated and the instantaneous spatial averaged pressure, ρ is the spatial averaged fluid density.

Based on the previous equation it can be seen that, the momentum associated to the flow at any given section consists of two parts, the momentum due to the fluid mass flow and the one associated to the pressure. In order to evaluate the mass flow momentum term, it is required to know the instantaneous mass flow, the fluid density, and the section through which the fluid flows. In the present paper, the instantaneous mass flow flowing though each grid cell belonging to the surface to be evaluated was determined. The total mass flow was obtained simply by adding the elementary mass flow of each mesh cell belonging to the chosen surface. The momentum pressure term

was obtained when multiplying the instantaneous pressure acting on each cell by the cell surface, and then adding the elemental momentum pressure terms corresponding to the surface under study. The different momentum terms were obtained at the feedback channel outlets. The net momentum characterizing the overall forces acting on the main jet lateral surfaces, will consider the instantaneous pressure and mass flow momentum terms acting on both feedback channels outlets.

4.4 Results

4.4.1 Baseline case at two different inlet velocities

The main vortical structures inside the (FO) mixing and external chambers, given for a period of oscillation divided in six equally-spaced time steps, are presented based on the Q criterion in figures 4.3 and 4.4 for the two power nozzle velocities evaluated, 65 and 97m/s, respectively. Both figures show how the positive and negative vortical structures are alternatively appearing inside the mixing chamber and being shed downstream. Particularly large positive three dimensional vortical structures in the (MC) are clearly seen at times $T = 0$, $T = 2/3$ and $T = 5/6$, large negative vortical structures are observed at times $T = 1/6$ and $T = 1/3$, see figures 4.3 and 4.4. The dimension of the vortical structures is very much the same for the two velocities studied, but the maximum vorticity associated to the main vortical structures increases about 66% when the power nozzle velocity is increased from 65 to 97m/s. Notice that the vortical structures having associated the maximum and minimum vorticity values, appear alternatively inside the mixing chamber, just after the (MC) inlet width, in the locations where the minimum pressure is observed. The main vortical structures break and become more random as they are being shed downstream. Inside the feedback channels, weak vortical structures appear alternatively at the (FC's) inlet and also at the opposite (FC) upstream corner, see figures 4.3b, e and 4.4b, e, indicating the locations where the flow is generating eddies. As already indicated by [43], the (FC's) eddies could be minimized by rounding the (FC's) corners. Rather weak vortical structures appear at the external chamber (EC), indicating that although large vortices are generated in this chamber, see figure 4.5a and 4.6a, their intensity is much weaker than the vortical structures generated inside the (MC).

Figures 4.5 and 4.6 show an instantaneous velocity, pressure, density and temperature fields, in the (FO) mixing and external chambers, the power nozzle velocities are 65 and 97m/s, respectively. A respective three dimensional Q criterion plot and generated at the same instant is as well presented in these figures. The instant shown

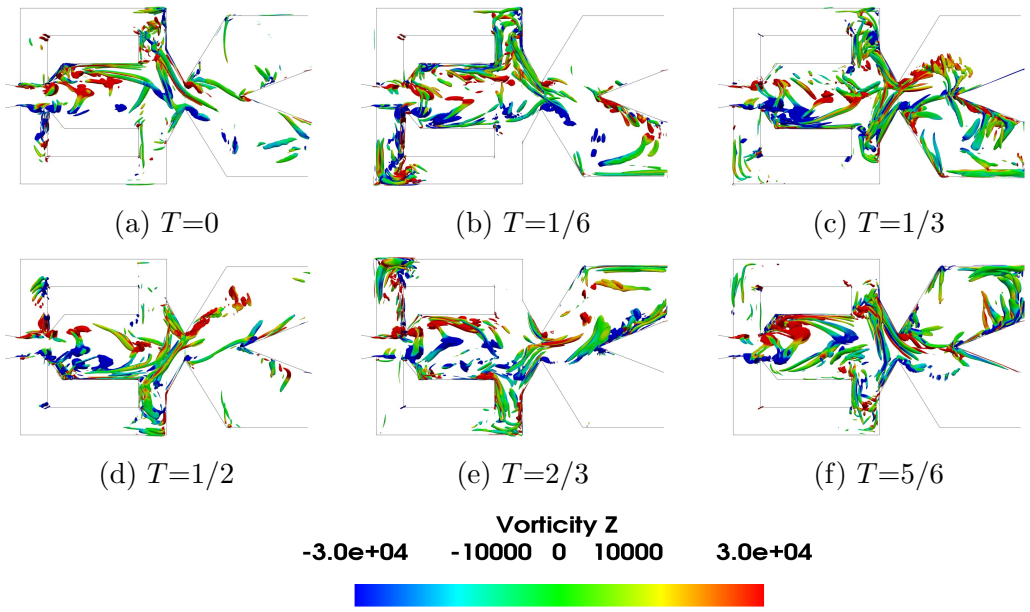

Figure 4.3: Q criterion at the mixing chamber period of oscillation divided into six equally spaced times, power nozzle velocity 65m/s. Baseline case.

in figures 4.5 and 4.6 corresponds to the period T=0 presented figures 4.3 and 4.4, respectively. It is interesting to see that the fluid expands inside the mixing chamber, the pressure decreases about 10000Pa in figure 4.5 and about 13000Pa in figure 4.6, versus the respective one at the power nozzle. The maximum velocity and Mach number at the (MC) outlet, reach values 35% and 44% higher than the power nozzle ones, respectively. The fluid suffers a second expansion when reaches the external chamber, being the pressure rather homogeneous across this chamber. In both figures, 4.5a and 4.6a, a large vortical structure of nearly the same size is observed at the external chamber upper side. When comparing these two figures it can be clearly stated that the vortical structure shown in figure 4.6 has a higher turning speed associated than the one appearing in figure 4.5. Notice that the pressure at the vortex central core is about 3000Pa lower than the one at the borders in figure 4.6 and just about 1000Pa in figure 4.5.

The feedback channels are alternatively pressurized, but due to the fluid compressibility it can be seen that just parts of the feedback channels are pressurized, in other words, pressure waves can be seen moving along the (FC's). At the instant presented in figure 4.5, the lower (FC) outlet is slightly pressured while the upper one is not, therefore suggesting that the jet inside the mixing chamber is moving upwards. Figure 4.6 shows the opposite, the upper (FC) outlet is slightly pressurized while the lower one is not, now indicating that in figure 4.6 the main jet is at this instant

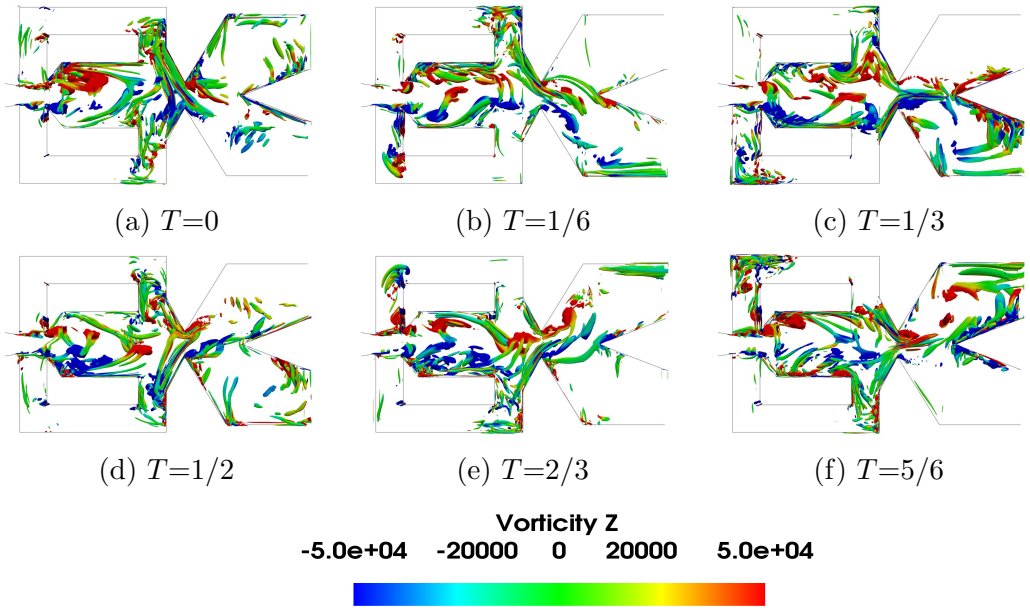

(a) T=0 (b) T=1/6 (c) T=1/3

(d) T=1/2 (e) T=2/3 (f) T=5/6

Figure 4.4: Q criterion at the mixing chamber period of oscillation divided into six equally spaced times, power nozzle velocity 97m/s. Baseline case.

moving down. At this point it needs to be clarified that although figures 4.5 and 4.6 are defined at time T=0, also represented in figures 4.3 and 4.4, respectively, this instantaneous initial time is different for each figure. As already established in [67], the pressure difference at the (FC's) outlets appears to be generating the required force which drives the jet oscillations in the (MC). This point will be further clarified in the remaining part of the present chapter.

Pressure waves originate at the (MC) converging walls and are due to the stagnation pressure points appearing alternatively at these surfaces. When carefully looking at figures 4.5b,c,d and 4.6b,c,d, it is seen that pressure waves also originate at the (FC's) outlets, see the small red point at the lower (FC) outlet internal vertical wall. Notice that from this point pressure waves are being generated and move from the (FC) outlet to the (FC) inlet. Figure 4.5b clearly shows the two pressure waves, one is moving along the upper (FC) from (FC) inlet to the outlet and the other is moving along the lower (FC) from the (FC) outlet to the (FC) inlet. This second pressure wave has associated a smaller intensity than the previous one. As it will be clarified later on, whenever pressure waves originate at each side of the (FC's), the resulting net momentum acting over the main jet as well as the stagnation pressure dynamics at the (MC) converging walls, will have particularly high fluctuations associated. The pressure waves generated at the (MC) converging walls, do not appear to be moving downstream towards the external chamber (EC), the fluid flowing across the mixing

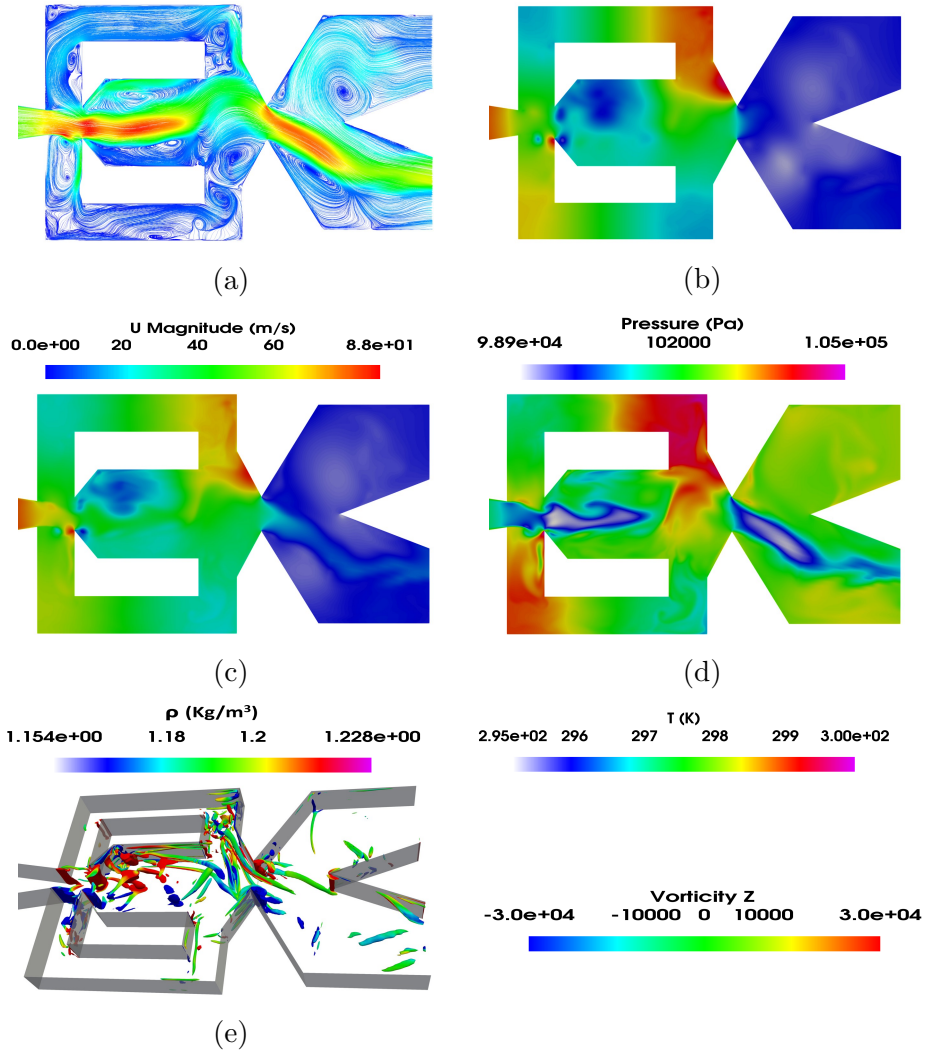

Figure 4.5: Mixing chamber instant velocity field (a), pressure distribution (b), density (c), temperature (d) and (e) Q criterion fields. Power nozzle velocity 65m/s. Baseline case.

chamber outlet width prevents this from happening. The expansion the fluid is suffering at the (EC) is also reducing the pressure waves effect in this chamber. The same happens at the (FC's) outlet, the pressure waves generated at the (FC's) outlet internal vertical walls, appear to be moving along the (FC), not towards the (MC), again it seems the main jet acts as a barrier. From the three dimensional Q criterion plots presented in figures 4.5e and 4.6e, the three dimensional structures already presented in two dimensions in figures 4.3a and 4.4a respectively, are now seen in greater detail. Notice that the main three dimensional structures alternatively appearing at the (MC) inlet, maintain their form along the spanwise direction. Mixing chamber instant velocity, pressure, density and tempreture fields can be seen in figures 4.7

and 4.8 for the feedback channel length L2 and figures 4.9 and 4.10 for the feedback channel length of L3 at power nozzle velocity of 65m/s and 97m/s respectively.

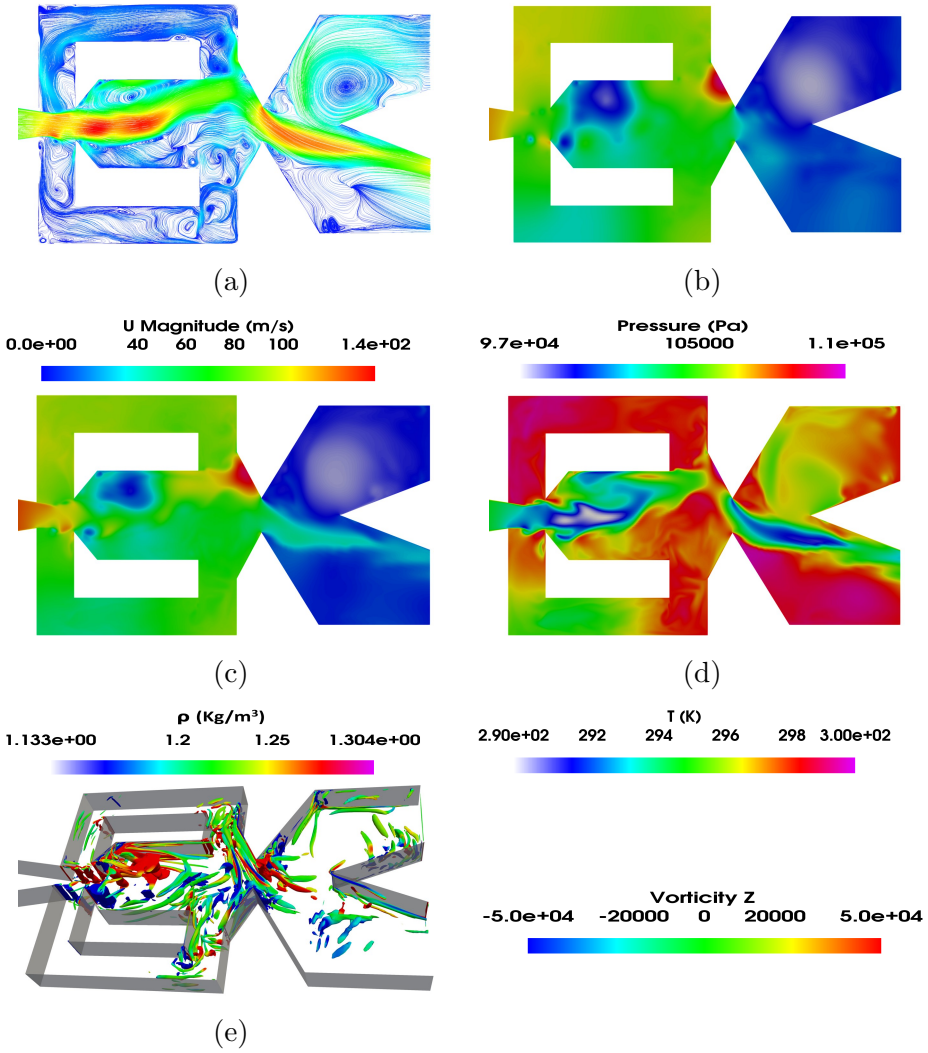

Figure 4.6: Mixing chamber instant velocity field (a), pressure distribution (b), density (c), temperature (d) and (e) Q criterion fields. Power nozzle velocity 97m/s. Baseline case.

In order to determine the origin of the forces generating the jet oscillations inside the (MC), figure 4.11a, b was created. This figure presents for the two velocities studied and in non-dimensional form, the dynamics of the maximum stagnation pressure measured at the (MC) lower converging wall, the (FO) upper outlet mass flow, the lower (FC) mass flow and the net momentum applied to the jet entering the (MC). Figures 4.11a, b, characterize the baseline case, figure 4.11c, d characterize the feedback channel length 2L, figure 4.12a, b characterize the feedback channel length 3L and figures 4.12c, d characterize the maximum feedback channel length studied, 9L.

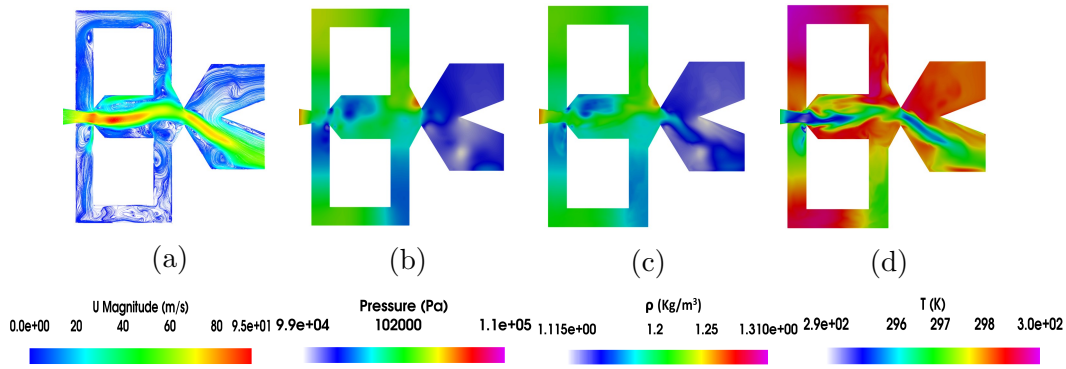

Figure 4.7: Mixing chamber instant velocity field (a), pressure distribution (b), density (c), temperature (d). Power nozzle velocity 65m/s.feedback channel length L2.

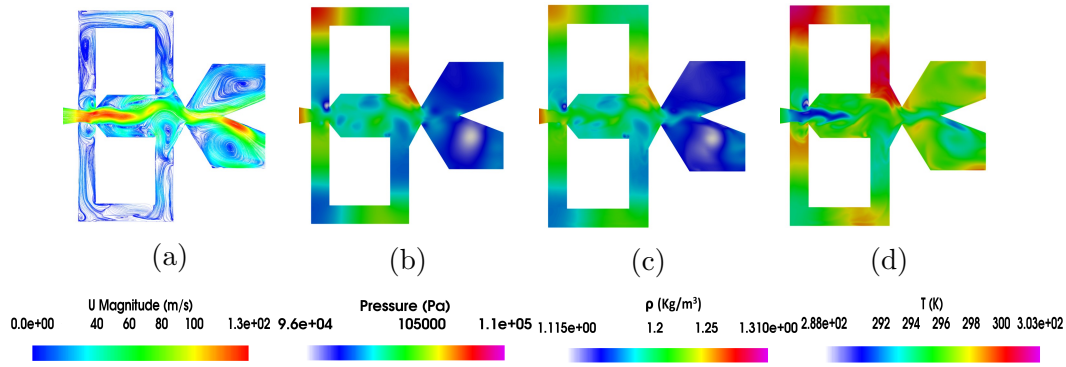

Figure 4.8: Mixing chamber instant velocity field (a), pressure distribution (b), density (c), temperature (d). Power nozzle velocity 97m/s.feedback channel length L2.

The first thing to realize is that, for the baseline case and for both Reynolds numbers studied, all these parameters follow the same trend. These parameters also following the same trend at the feedback length of 2L and 3L for the power nozzle velocity of 65m/s as shown in figures 4.11c and 4.12a. For the longest (FC) length studied, the main jet oscillations are deeply affected by random fluctuations, under these conditions the main jet inside the (MC) is mostly fluctuating although performing a low amplitude oscillation. These random fluctuations can also be seen for the feedback lengths of 2L and 3L at the power nozzle velocity of 97m/s as shown in figures 4.11d and 4.12b. In figures 4.11a, b,c and 4.12a the stagnation pressure oscillations measured at the (MC) lower converging wall, appear at the same frequency as the rest of the parameters, indicating there must be a correlation between them, although there is a small phase lag for the cases of 2L and 3L at power nozzle velocity of 65m/s. Also the amplitude of these parameters appears to be correlated. The oscillating frequencies of baseline cases and for all these parameters when the power nozzle velocities are 65 and 97m/s are respectively of 275.4 and 410 Hz.

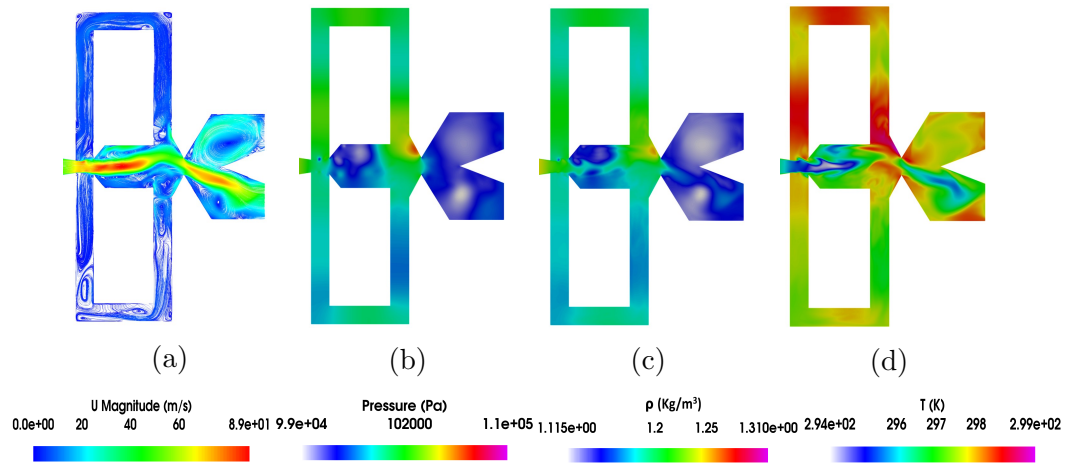

Figure 4.9: Mixing chamber instant velocity field (a), pressure distribution (b), density (c), temperature (d). Power nozzle velocity 65m/s.feedback channel length L3.

When the power nozzle inlet velocity is of 65m/s, figure 4.11a ,the stagnation pressure oscillations are particularly scattered, the (FC) mass flow and the net momentum acting on the jet entering the (MC) show as well very scattered curves, which appear to be affected by very high frequency fluctuations. For this particular inlet velocity, as shown in figure 4.5, a stagnation pressure point is observed at the (FC) lower outlet internal vertical wall. From this point, pressure waves are being generated and move from the (FC) outlet towards the (FC) inlet, these pressure waves interact with the ones generated at the (MC) converging walls and create the high frequency fluctuations observed in the pressure, net momentum and (FC) mass flow curves shown in figure 4.11a. All these pressure waves bounce on the different (FC) walls and help in generating high frequency fluctuations. As the power nozzle velocity increases to 97m/s, the stagnation pressure point appearing at the (FC) outlet internal vertical wall reaches a smaller value than in the previous case, see figure 4.6, less fluid particles from the incoming jet are impinging in this vertical wall, as a conclusion the pressure waves generated at this particular point are weaker than in the previous case. The result is, a much neater stagnation pressure oscillation at the (MC) converging walls and at the (FC) mass flow, as observed in figure 4.11b. Now the fluctuations associated to all these curves show a much smaller frequency than in the previous case. Yet, the net-momentum acting on the (MC) incoming jet is still showing large fluctuation waves, this is due to the pressure waves periodically generated at the (MC) converging walls and bouncing on the (FC's) walls, pressurizing and de-pressurizing the (FC's) outlets. From figures 4.11a,b, it can be stated that the stagnation pressure peak-to-peak oscillations are about 3.5% of the maximum stagnation pressure for a

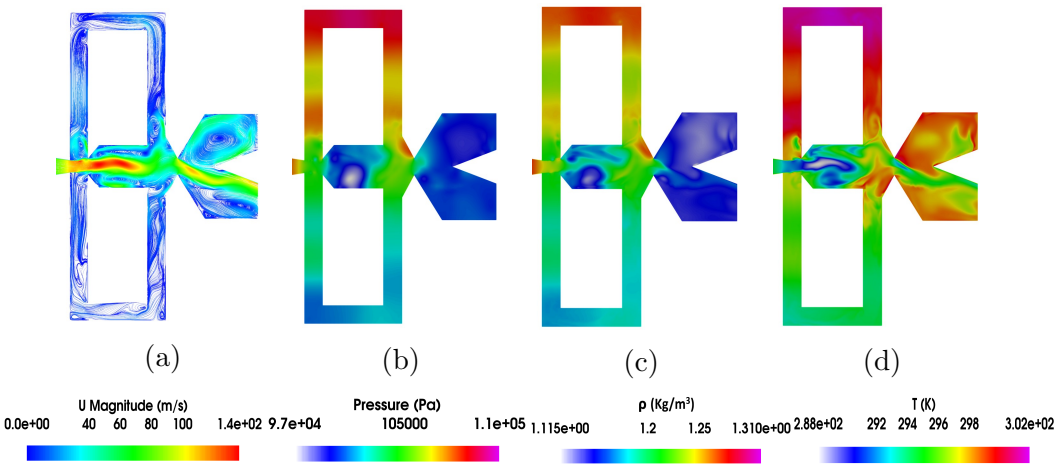

Figure 4.10: Mixing chamber instant velocity field (a), pressure distribution (b), density (c), temperature (d). Power nozzle velocity 97m/s.feedback channel length L3.

power nozzle velocity of 65m/s, the peak-to-peak stagnation pressure oscillations increase to about 5% when the power nozzle velocity reaches 97m/s. In reality, both pressure waves, show a main oscillating peak and a smaller one, this second one coincides with the instants the main jet impinges on the opposite (MC) converging wall, therefore pressurizing the opposite (FC). The increase of the peak-to-peak stagnation pressure amplitude at the (MC) converging walls, is triggering the amplitude increase of the (FO) outlet mass flow, the (FC) mass flow and the net momentum evaluated at the (FC) outlets. Notice that all these parameters show a much larger peak-to-peak amplitude in figures 4.11b, d and 4.12b ,d when compared to the ones in figure 4.11a, c and 4.12a ,c. The net momentum peak-to-peak amplitude, almost doubles the value observed at 65m/s. From figures 4.11a, b it can also be observed that for any of the two velocities studied, the (FO) outlet mass flow, the (FC) mass flow and the net momentum, have during approximately 1/4 of the oscillating cycle, negative values. This clearly indicates there is reverse flow at the (FO) outlet and inside the (FC's). The increase of the power nozzle velocity, do not seem to affect much the maximum negative value of the (FC) mass flow or the (FO) mass flow, even the time the oscillating parameters remain negative, 1/4 of the oscillating cycle, appears to be unaffected by the power nozzle inlet velocity. The (FC) reverse flow can be clearly seen at the lower (FC) outlet in figure 4.5a.

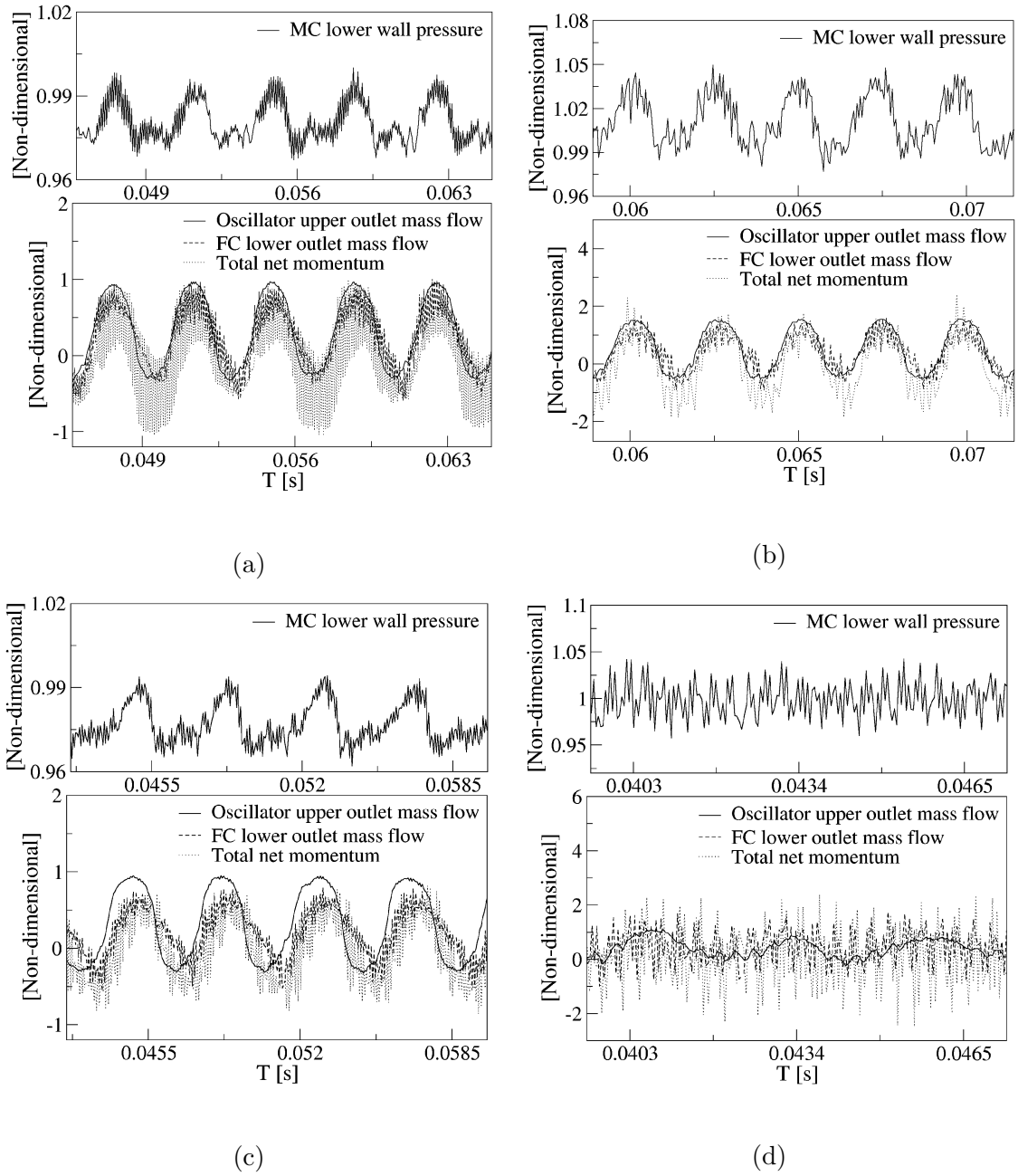

Figure 4.11: Non dimensional pressure at the mixing chamber lower converging wall, oscillator mass flow, feedback channels mass flow and total net momentum applied to the incoming jet from both feedback channel outlets. (a) (b) Baseline case. (c) (d) Feedback channels length 2L . (a) (c) Power nozzle velocity 65m/s. (b) (d) Power nozzle velocity 97m/s.

4.4.2 The effect of the feedback channel length

When comparing figures 4.11a,b, baseline case, with figures 4.12c,d, feedback channel length 9L, it is observed that regardless of the inlet velocity employed, the (FO) out-

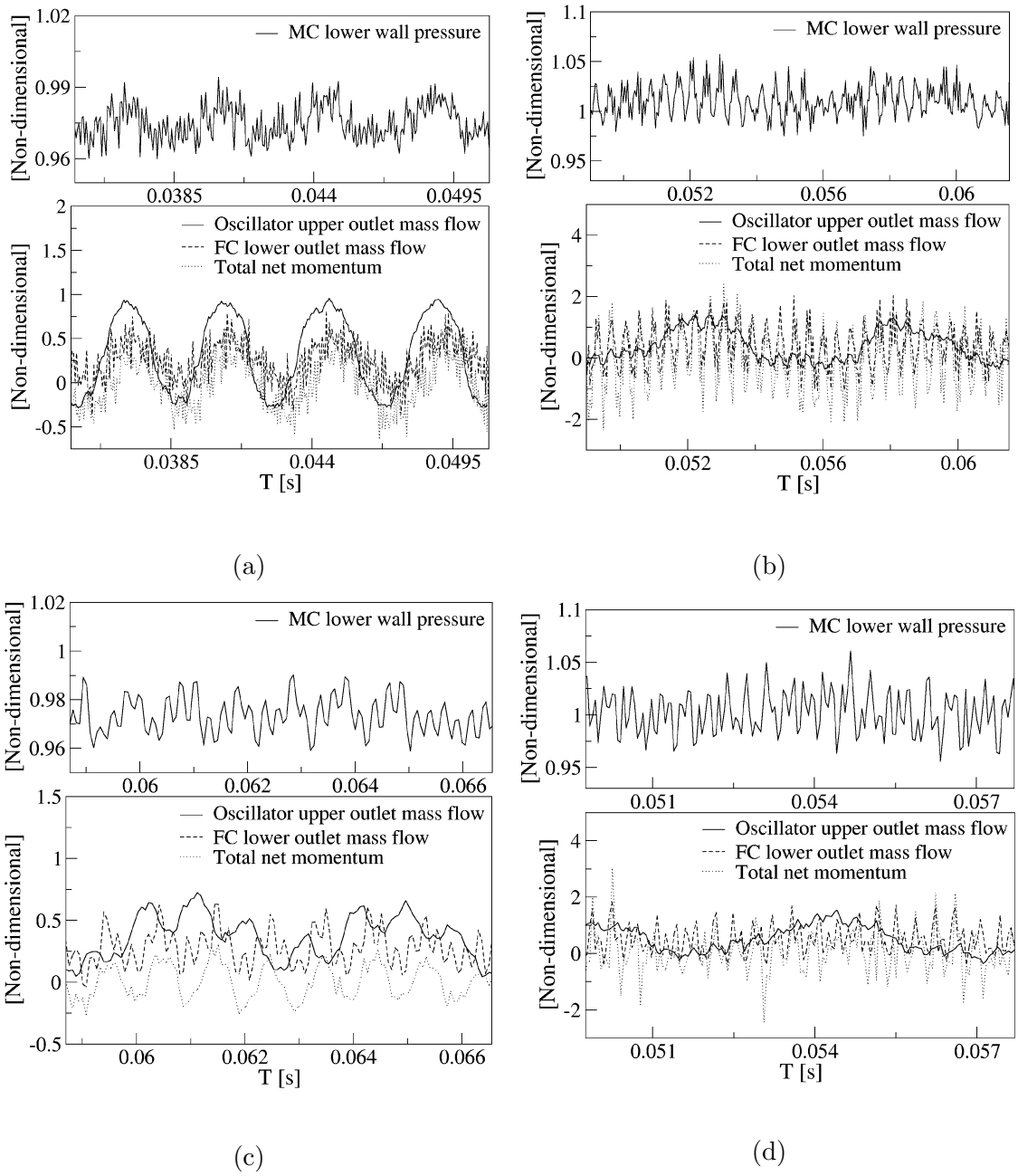

Figure 4.12: Non dimensional pressure at the mixing chamber lower converging wall, oscillator mass flow, feedback channels mass flow and total net momentum applied to the incoming jet from both feedback channel outlets. (a) (b) Feedback channels length 3L. (c) (d) Feedback channels length 9L. (a) (c) Power nozzle velocity 65m/s. (b) (d Power nozzle velocity 97m/s.

let flow suffers a minor oscillation for the longest feedback channel length is used, it was observed that the (FO) oscillation amplitude decreased as the feedback channel length increased. The second major observation is that unlike in the baseline case, at (FC) length 9L, there is not an apparent link between stagnation pressure at the (MC) convergent walls and the rest of the parameters. But if we closely look at the different curves presented in figures 4.12c, d, it can be observed the different curves tend to follow, although with a phase lag, the pressure fluctuations appearing at the (MC) converging walls. Again this appears to indicate the origin of the oscillations and even the fluctuations, is the pressure variations at the (MC) converging walls. At this particularly long (FC) length, the jet inside the (MC) is mostly fluctuating at high frequencies, the fluctuation amplitude is of the same order as the oscillation amplitude. The fluctuation frequency increases with the inlet velocity increase, in fact for the highest velocity studied, random oscillations dominate the flow, the randomness increases with the Reynolds number increase.

To be able to further understand the effect of the (FC) length on the (FO) outlet mass flow frequency and amplitude, figure 4.13 was generated. It is relevant to see that for the two power nozzle velocities studied, as the (FC) length increases the peak-to-peak amplitude as well as the oscillating frequency tends to decrease. The oscillating frequency variation is in full agreement with the observations made by [35], although they used a different (FO) configuration.

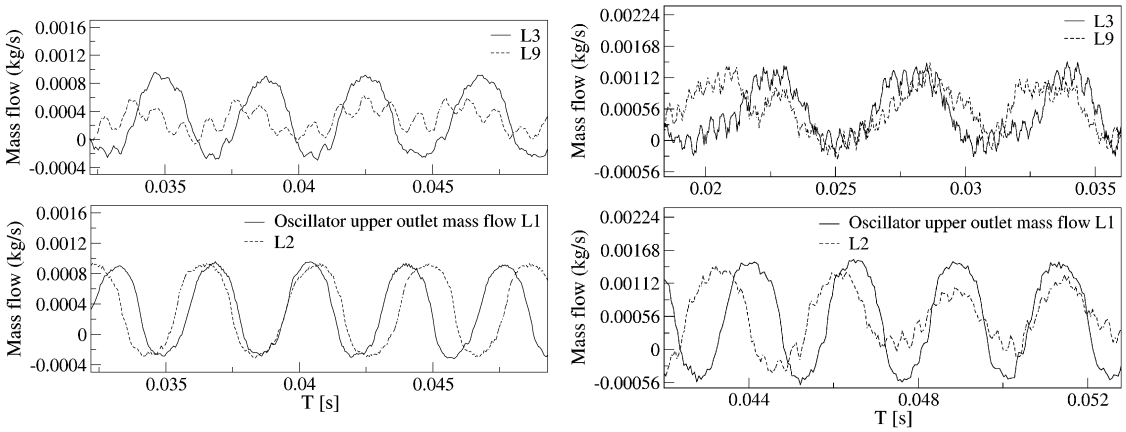

(a) (b)

Figure 4.13: Fluidic oscillator outlet mass flow as a function of the different feedback channels length. (a) Power nozzle velocity 65m/s. (b) Power nozzle velocity 97m/s.

In fact and regardless of the velocity studied, the curves showing the (FO) outlet mass flow and (FC) outlet mass flow become scattered as (FC) length increases as

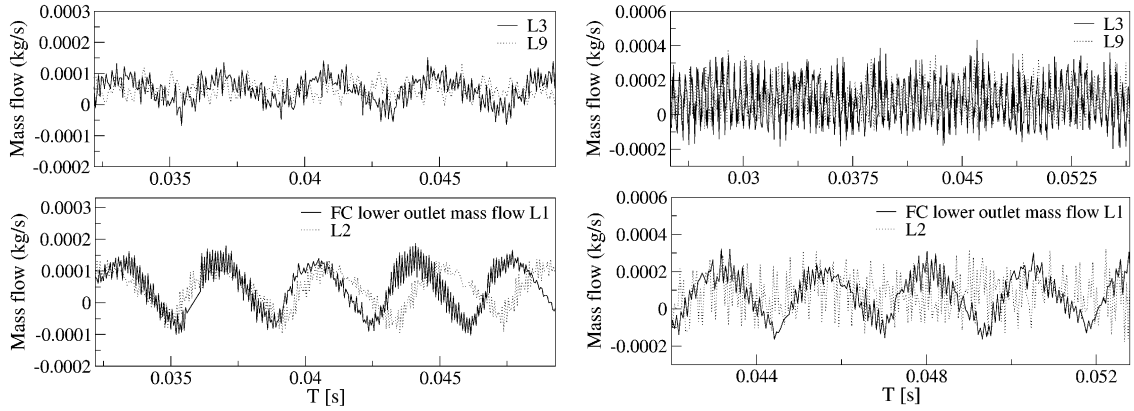

(a) (b)

Figure 4.14: Feedback channel outlet mass flow as a function of the different feedback channels length. (a) Power nozzle velocity 65m/s. (b) Power nozzle velocity 97m/s.

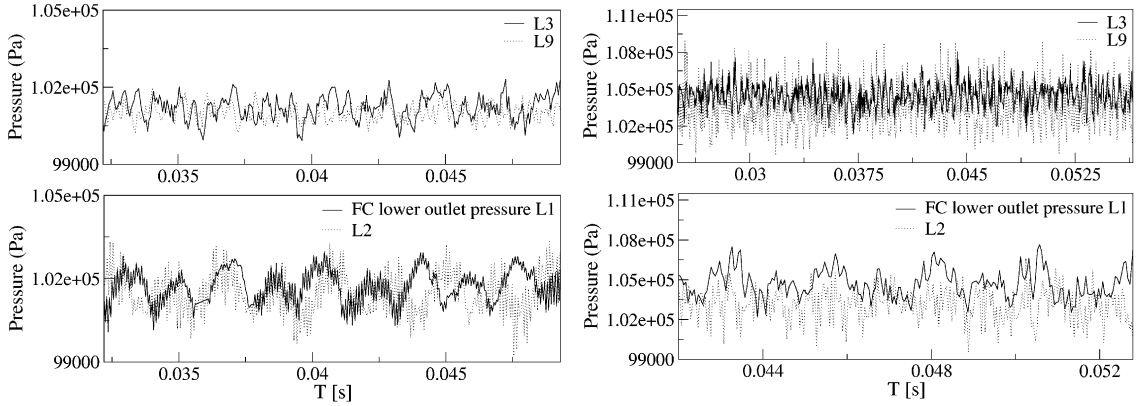

(a) (b)

Figure 4.15: Feedback channel outlet pressure as a function of the different feedback channels length. (a) Power nozzle velocity 65m/s. (b) Power nozzle velocity 97m/s.

shown in figures 4.13 and 4.14, it appears as if instead of clear oscillations the main jet undergoes some vibrational movement, although still maintaining a low amplitude oscillatory displacement. When the power nozzle velocity of 65m/s, figure 4.13a, the jet fluctuations (vibrational movement) can be clearly seen when the (FC) length is 3L and they are almost as large as the peak-to-peak oscillation cycle when the (FC) length is 9L. Under these conditions, the main jet inside the (MC) undergoes a fluctuating movement while performing a small oscillation cycle. For a (FC) length of 9L, the frequencies associated to the respective fluctuating and oscillating movements measured at the (FO) outlet mass flow are of 1037.4Hz and 251.6Hz.

When the power nozzle velocity is of 97m/s, the fluctuating wave can be clearly seen for a (FC) length of 2L, see figure 4.13b. Whenever the (FC) length is 3L, the jet fluctuations are having a peak-to-peak amplitude of about 25% of the oscillation one. For this particular case, the frequencies associated to the fluctuating and oscillating movements are 2401.8Hz and 179.3Hz, respectively. For the longest (FC) length L9, the peak-to-peak amplitude associated to the fluctuations are smaller than for the (FC) length L3, in reality the fluctuations as well as the oscillations have become quite random, a set of different frequencies appear, the maximum and minimum frequencies associated to the major flow fluctuations and to the jet main oscillating displacement, are respectively of 2708.8Hz and 132.1Hz.

In any case it can be concluded that the randomness associated to the oscillations, increases with the (FC) length increase, and or with the (FO) inlet velocity increase. Based on these results it can be estimated that a further increase of the (FC) length would make the oscillations to stop, as it is about to happen in figure 4.13b for the maximum (FC) length L9. The simulations demonstrate reverse flow has to be expected at the (FO) outlet, the reverse flow at the (FO) outlet tends to disappear as the (FC) length increases, figures 4.13a, b demonstrate there is no reverse flow at the (FO) outlet for a (FC) length of 9L. Figure 4.15 shown (FC) outlet pressure for the different lenghts studied, as for the previous case, the random fluctuations seems to be increases as the length of the feedback channel increases and the oscillation cycle disappear. This is more visible for the power nozzle velocity of 97m/s as shown in figure 4.15b.

Table 4.1 presents for the two power nozzle velocities and the four (FC) lengths, the evolution of the oscillating frequencies, the different fluctuating frequencies and the oscillation amplitudes of both of them. Information obtained based on the (FO) outlet mass flow. At 65m/s, the oscillation amplitude decreases by about 80% when comparing the results for the longest (FC) length, 9L with the baseline case. For the same conditions the oscillation frequency decreases by 9%. For a (FC) length of 9L a clear fluctuating frequency of 1037.4Hz, which is superposed to the oscillating wave, can be observed. Whenever the power nozzle velocity is of 97m/s, and when comparing the longest (FC) length results with the baseline case, the oscillation amplitude decreases by about 72% and the frequency by 67%. At high speeds, the compressibility effect along with the nearer chaotic stage, make the oscillating frequency highly dependent on the (FC) length, generating a drastic decrease of the oscillating frequency and the appearance of several fluctuating frequencies. Clearly at high speeds the (FO) outlet mass flow fluid oscillations become chaotic as the (FC)

length increases, oscillations are rather chaotic at (FC) length 9L. The fluctuating frequencies are one or several orders of magnitude higher than the oscillation ones. Figures 4.16 and 4.17 shows the frequency and amplitude evaluated in the table 4.1 based on the oscillator outlet mass flow for the power nozzle velocity of 65m/s and 97m/s respectively.

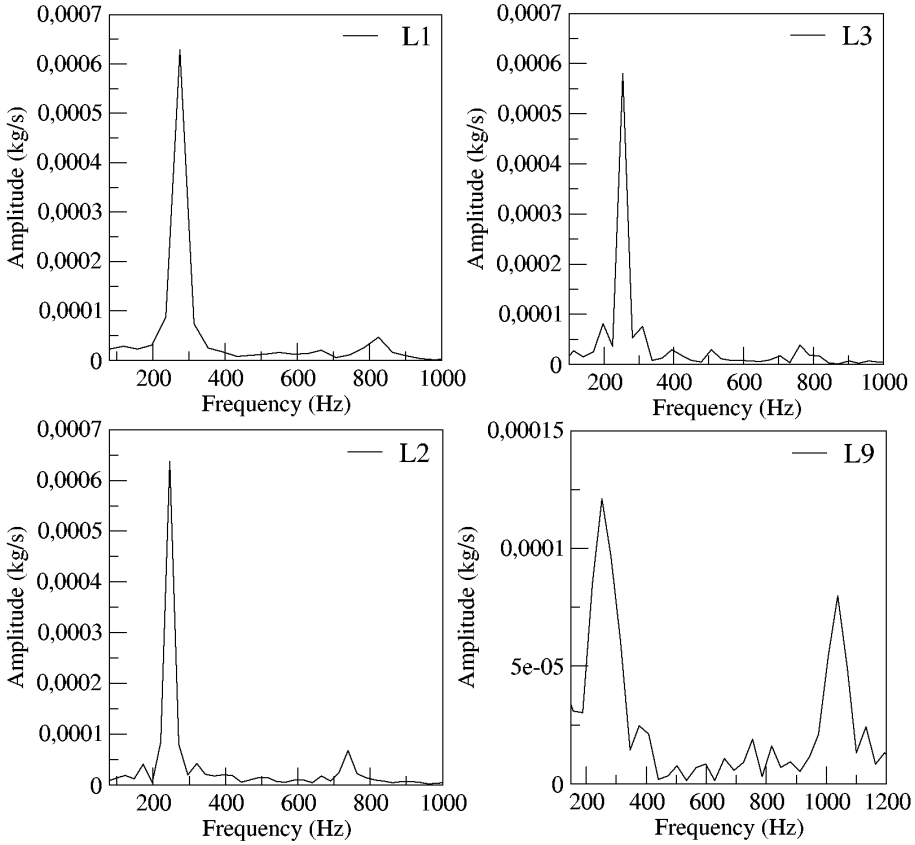

Figure 4.16: Fluidic oscillator outlet mass flow frequency (FFT) and amplitude for different feedback channel lengths. Power nozzle velocity 65m/s.

Once the main (FO) output flow characteristics are evaluated, it is interesting to analyze the fluid evolution inside the (MC) and the feedback channels. For the two power nozzle velocities and the four (FC) lengths, the overall forces acting on the main jet at the (FC's) outlets, expressed as the net momentum acting onto the (MC) incoming jet, are presented in figure 4.18. For the two power nozzle velocities studied, the net momentum oscillation amplitude and frequency associated decreases with the (FC) length increase. The net momentum oscillation becomes highly random as the (FC) length increases, the (FO) inlet velocity increase enhances this effect. In reality the net momentum it is expected to follow the stagnation pressure oscillation at the (MC) converging surfaces, as introduced in figure 4.11a, b for the baseline

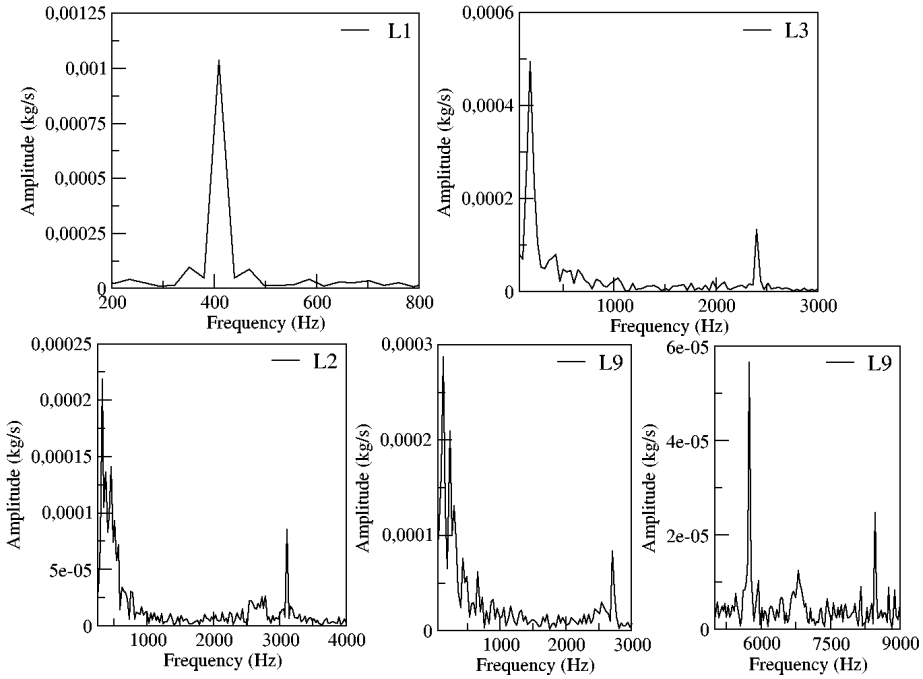

Figure 4.17: Fluidic oscillator outlet mass flow frequency (FFT) and amplitude for different feedback channel lengths. Power nozzle velocity 97m/s.

case, but at high (FC) lengths, just large amplitude pressure fluctuations can be observed in the (MC) converging walls, these fluctuations take control of the flow and of the net momentum acting on the jet. For the baseline case and for the smaller velocity studied, 65 m/s, the net-momentum oscillating displacement appears to be particularly noisy, the frequency associated to the fluctuations (noise) is of 9988.6Hz, about 35 times the oscillating frequency, which is of 273Hz. This very high frequency is likely to be associated to the pressure waves generated on both ends of the (FC), and to the bouncing of the waves on the (FC) walls. In the previous section has already been explained that under these conditions, a particularly high stagnation pressure point appears at the (FC) outlet internal vertical wall, pressure waves are periodically generated at this point and at the (MC) converging walls. Figure 4.18b for (FC) lengths L3 and L9, show that the main net-momentum oscillation is almost gone and the main jet is affected by very high frequency fluctuations, which peak to peak amplitude is larger than the oscillating one. Notice that for these particular cases the (FO) output mass flow, figure 4.13b, presents a highly random oscillation and several high fluctuating frequencies which in reality dominate the main jet movement inside the (MC) and are being transfered downstream.

Table 4.2 introduces the different frequencies obtained when performing the fast Fourier transformation of the net momentum signals obtained at the (FC's) outlets.

Table 4.1: Fluidic Oscillator output mass flow frequency and peak to peak amplitude as a function of the power nozzle velocity and the feedback channel length.

Power nozzle velocity (m/s)	**Variable**	**(FC) length L1**	**(FC) length L2**	**(FC) length L3**	**(FC) length L9**
65	Frequency (Hz)	275.4	246.3	253.5	251.6; 1037.4;
65	Amplitude (kg/s)	0.000628	0.000637	0.00058	0.000121; 0.0000797
97	Frequency (Hz)	410	324.6; 460; 3111.5	179.3; 2401.8	132.1; 231.2; 429.5; 660.7; 2708.8; 5747.8; 8456.6
97	Amplitude (kg/s)	0.00103	0.000218; 0.00014; 0.000085	0.000494; 0.000134	0.00028; 0.0002; 0.000075; 0.000061; 0.0000834; 0.0000566; 0.0000246

The results for both power nozzle velocities and the four (FC's) lengths are presented. From the comparison of tables 4.1 and 4.2 it is seen, the frequencies inside the (FC's) and the (MC) are higher than the ones obtained at the (FO) outlet, frequencies around 9000Hz are spotted under all conditions. The main oscillating frequencies appear at both tables, but the very high frequencies which appear to be associated to the pressure waves fluctuations, do not appear to be transfered to the output flow, it seams the main jet flowing thought the (MC) outlet width acts as a barrier of most of the fluctuating waves existing inside the (MC). This effect can be seen when observing figures 4.12d and 4.18b, notice that the fluctuations appearing in these figures are not fully transfered to the downstream flow figure 4.13b and therefore are not observed in table 4.1. Notice that the oscillator net momentum frequency (FFT) and amplitude are presented in figures 4.20 and 4.21 for the power nozzle velocity of 65m/s and 97m/s respectively.

An important point to clarify is, which of the two terms characterizing the net momentum acting onto the jet is the dominant one. In a previous work done by Baghaei and Bergada [67], using the same oscillator configuration but under incompressible flow conditions, water was used as working fluid, it was stated that the net-momentum pressure term, see equation 4.1, was the dominating one and therefore was driving the main jet oscillations. Under compressible flow conditions, figure

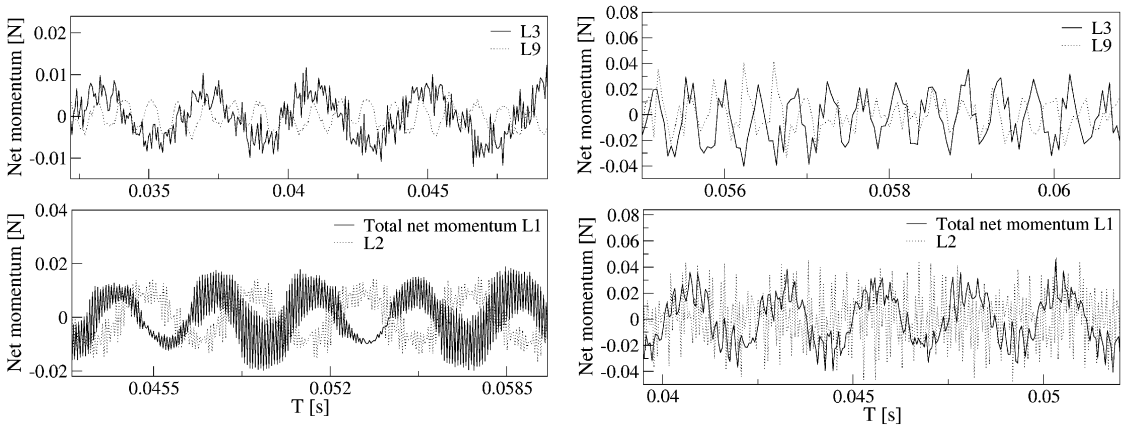

(a) (b)

Figure 4.18: Net momentum applied to the jet entering the mixing chamber as a function of the different feedback channels length. (a) Power nozzle velocity 65m/s. (b) Power nozzle velocity 97m/s.

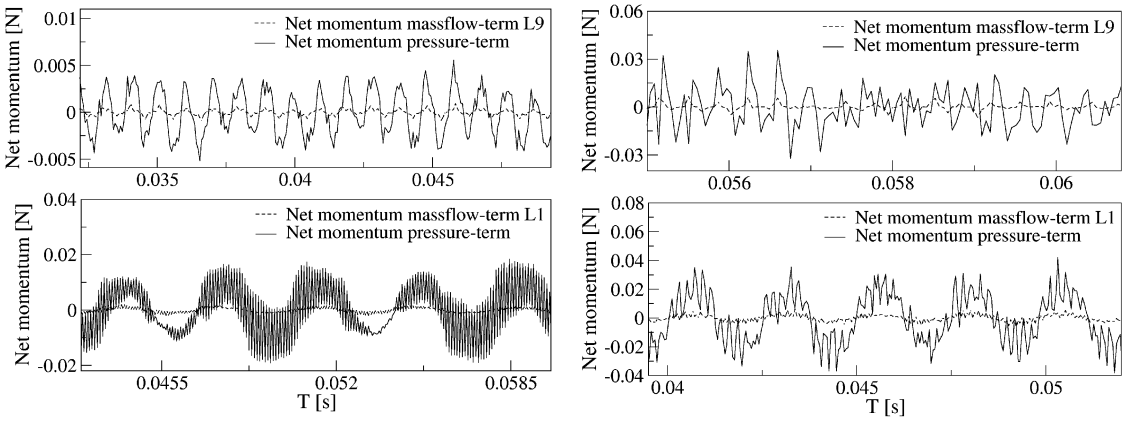

(a) (b)

Figure 4.19: Comparison of the net momentum pressure term with the mass flow term, for the baseline case L1, and for the maximum (FC) length L9. (a) Power nozzle velocity 65m/s. (b) Power nozzle velocity 97m/s.

4.19, which compares for the baseline case and the maximum (FC) length L9, the net momentum mass flow term with the net momentum pressure term at the (FC) outlets, shows that the same happens regardless of the feedback channel length and the power nozzle velocities studied. This figure clearly shows that the net momentum due to the pressure term, is over an order of magnitude higher than the one generated by the mass flow term. The conclusion is, the forces driving the oscillations in this

particular (FO) configuration are due to the pressure difference generated at the (FC) outlets. Changing the (FC) length, the inlet velocity or evaluating the fluid under compressible or incompressible conditions, do not change this statement. Figures 4.18a, b and 4.19a, b, for a (FC) length of 9L, clearly show that the jet fluctuating movement is dominating the flow, the pressure at the (FC) outlets and therefore the net momentum is driven by the main jet fluctuations, the oscillation movement has almost disappeared.

In order to be able to visualize the flow topology at different (FC) lengths, an instantaneous velocity, pressure, density and temperature fields for the maximum (FC) length evaluated and for the two power nozzle velocities of 65 and 97m/s is presented in figures 4.22 and 4.23, respectively. From figure 4.22 it is observed there are several pressure waves traveling along the feedback channels, at this instant the waves can be particularly seen at the upper feedback channel, lower intensity waves are observed in the lower (FC). Notice as well that the waves are observed at regular distances, the distance between two consecutive waves coincides with the sound speed divided by a particularly high amplitude (FO) oscillating or fluctuating frequency, $d = C/f = \sqrt{\gamma RT}/f$. Considering the maximum fluctuating frequency presented in table 4.2 for the smallest power nozzle velocity and considering the fluid temperature at the (MC) converging walls, the distance between two consecutive pressure waves can be determined, being of 45.6 mm, this is the distance between two consecutive waves observed in figure 4.22. Using the same procedure, the distance between two consecutive waves in figure 4.23, for which the power nozzle velocity is of 97m/s, is of 39.5mm. When comparing figures 4.22 and 4.23, it can be seen that the pressure waves appearing along the feedback channels are not generated regularly when the power nozzle velocity is of 97m/s, figure 4.23, this fully coincides with the (MC) converging wall stagnation pressure presented in figure 4.12d, where it is clearly seen that the degree of randomness is very high. The jet fluctuation randomness can also be seen in figure 4.18b for (FC) lengths of 3L and 9L. The relation between the maximum and minimum pressure observed in figure 4.22 shows a variation of about 6%, the fluid density changes about 7% while the maximum to minimum temperature variation is of about 2%. In figure 4.22, the maximum fluid velocity has increased by 40% versus the power nozzle one. For a power nozzle velocity of 97m/s, the pressure variation observed in figure 4.23 is of 15%, the density variation is of about 16% and the temperature variation is of about 4.5%. The percentage of velocity increase inside the (MC) is of around 54% versus the power nozzle one. As expected, the percentage variation of the different parameters is higher for higher power nozzle

Table 4.2: Frequencies obtained from the net-momentum signals measured at the feedback channels outlets.The two power nozzle velocities 65m/s and 97m/s and all feedback channels lengths are evaluated.

Power nozzle velocity (m/s)	**Variable**	**(FC) length L1**	**(FC) length L2**	**(FC) length L3**	**(FC) length L9**
65	Frequency (Hz)	273; 819.1; 9442.8; 9988.6	240; 7534.8; 8013.9; 8493.1	251.5; 1313.4; 2179.8; 5728.9; 7293.8; 8635.1	259.3; 1037.3; 2874.3; 4927.4; 6785.9; 7563.9
65	Amplitude (N)	0.00956; 0.00071; 0.001; 0.0059	0.0088; 0.0016; 0.004; 0.00087	0.0062; 0.00069; 0.00089; 0.001; 0.00146; 0.00081	0.00057; 0.002; 0.00047; 0.000185; 0.00025; 0.000182
97	Frequency (Hz)	410; 1228.9; 4389.8; 5208.3; 9714.4	311.3; 422.6; 3113.3; 5893.1; 9962.6; 10007.1	159.8; 2078.5; 2398.4; 8839.6; 10210; 10552.8	136.64; 2717.5; 3027; 4958; 5266; 8737
97	Amplitude (N)	0.023; 0.003; 0.0066; 0.0022; 0.0027	0.002; 0.00205; 0.0096; 0.0017; 0.0168; 0.011	0.0032; 0.00337; 0.019; 0.00253; 0.00188; 0.00546	0.00053; 0.00472; 0.00294; 0.00154; 0.00116; 0.00265

velocities. Another question which may arise is whether the maximum and minimum values of the velocity, pressure, density and temperature are affected by the feedback channel length as shown in table 4.3. It can be concluded that the maximum and minimum values af all these parameters remain very stable for all different feedback channel lengths studied, their variation just depends on the power nozzle velocity.

4.5 Conclusions

For the present fluidic oscillator configuration operating under compressible flow conditions, the oscillations are pressure driven, the forces due to the mass flow flowing along the feedback channels and acting on the main jet at the feedback channels

Table 4.3: Maximum and minimum values of the velocity, pressure, density and temperature variables inside the mixing chamber. Both power nozzle velocities and the four feedback channel lengths are considered.

	(FC) length L1.		**(FC) length L2.**		**(FC) length L3.**		**(FC) length L4.**	
Power nozzle velocity ($65m/s$)	**Min.**	**Max.**	**Min.**	**Max.**	**Min.**	**Max.**	**Min.**	**Max.**
Velocity (m/s)	0	98.75	0	95.3	0	98.61	0	98.22
Pressure (Pa)	94458	105840	95380	105720	93538	105630	94780	105050
Density (Kg/m^3)	1.1068	1.2339	1.1161	1.2343	1.0940	1.2316	1.1088	1.2284
Temperature (K)	292.83	300.2	293.5	300.7	293.42	300.1	293.56	300.3
Power nozzle velocity ($97m/s$)	**Min.**	**Max.**	**Min.**	**Max.**	**Min.**	**Max.**	**Min.**	**Max.**
Velocity (m/s)	0	166.52	0	169.44	0	165.94	0	163.79
Pressure (Pa)	87085	114840	83030	113050	852.46	114470	85968	114510
Density (Kg/m^3)	1.0211	1.3318	1.0219	1.3179	1.0044	1.3345	1.0099	1.3350
Temperature (K)	284.16	302.92	285.35	305.21	284.39	303.52	287.37	305.04

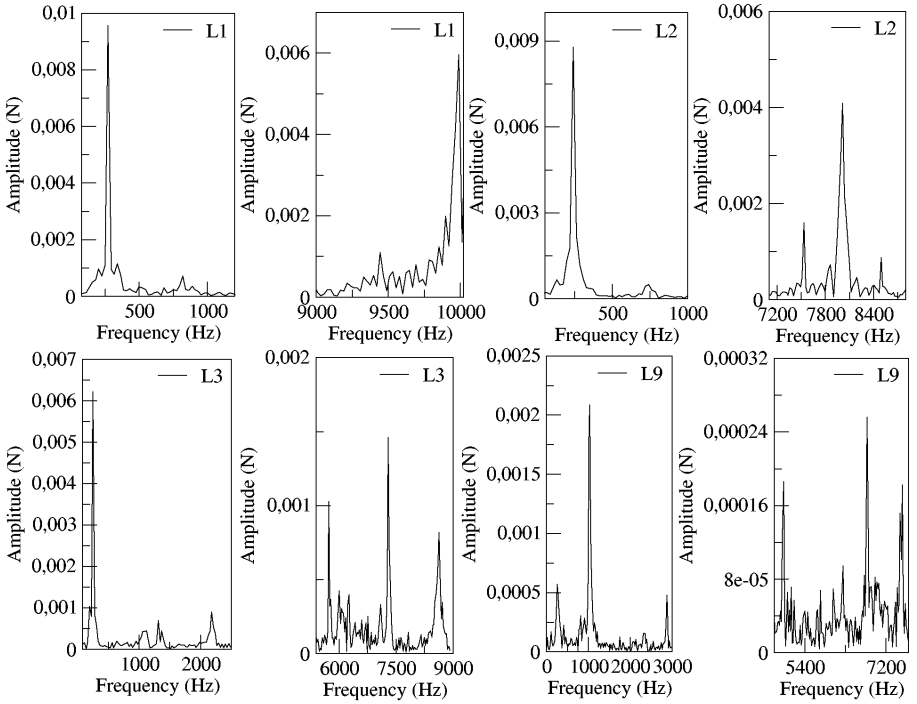

Figure 4.20: Fluidic oscillator net momentum frequency (FFT) and amplitude for different feedback channel lengths. Power nozzle velocity 65m/s.

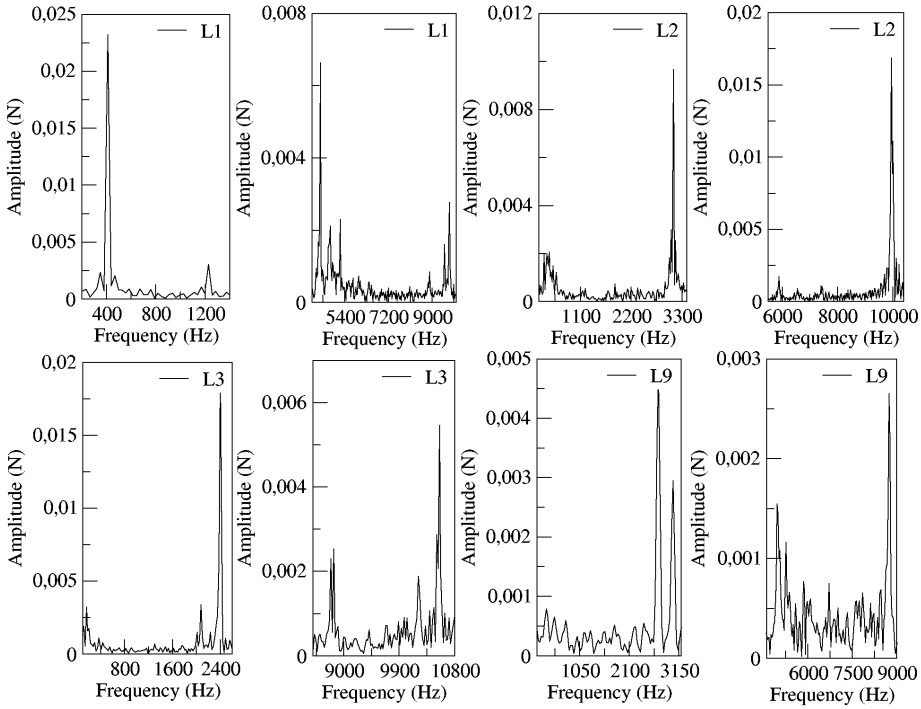

Figure 4.21: Fluidic oscillator net momentum frequency (FFT) and amplitude for different feedback channel lengths. Power nozzle velocity 97m/s.

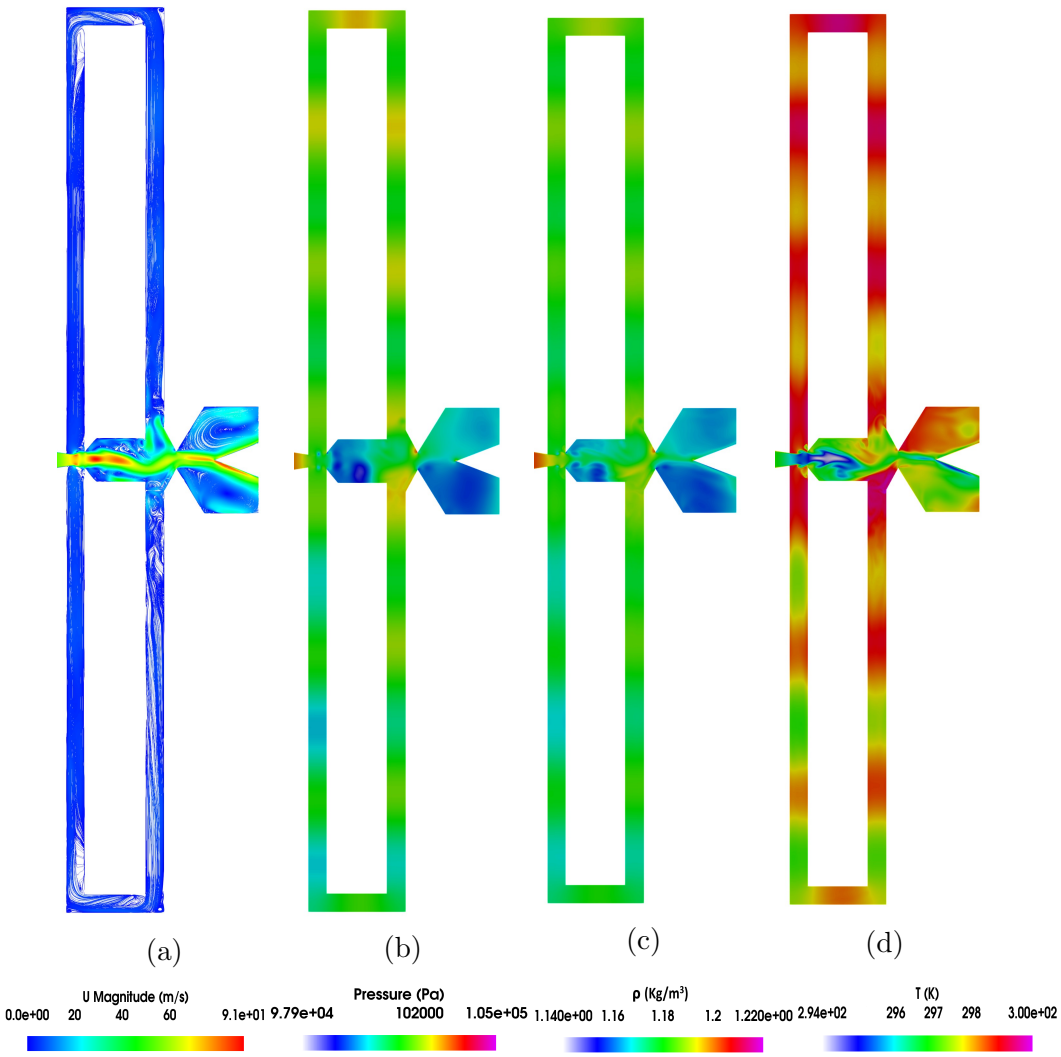

Figure 4.22: Mixing chamber instant density and temperature fields. Power nozzle velocity 65m/s, feedback channel length L9.

outlets, are an order of magnitude smaller than the ones due to the pressure. At high feedback channel lengths and high power nozzle velocities, the main jet fluctuations inside the mixing chamber are generating pressure waves which travel along the feedback channels. Under compressible flow conditions, the fluid suffers an expansion inside the mixing chamber. Pressure waves are generated alternatively at the mixing chamber converging walls. Under some conditions, pressure waves are also alternatively generated at the feedback channels outlet vertical internal walls. When this happens the dynamic net momentum, feedback channel mass flow and stagnation pressure signals are particularly scattered, this is due to the pressure waves appearing simultaneously on both sides of the feedback channels, and bouncing on the feedback channel walls. As feedback channel length increases, the outlet mass flow peak-to-

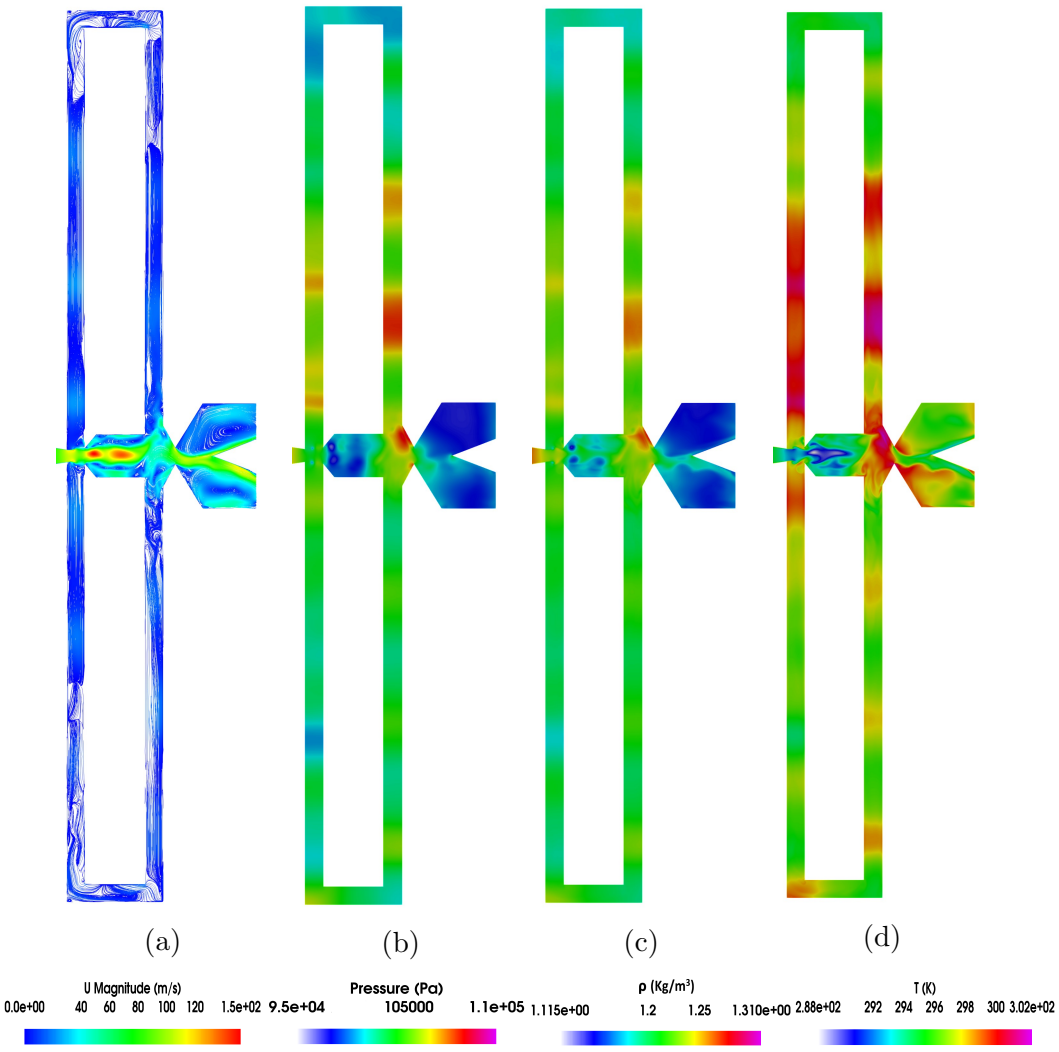

Figure 4.23: Mixing chamber instant density and temperature fields. Power nozzle velocity 97m/s, feedback channel length L9.

peak amplitude and frequency decreases. The oscillation would eventually stop if a certain feedback channel length is overcome. Under compressible flow conditions, the pressure waves can be clearly seen evolving along the feedback channels. For a power nozzle velocity of 97m/s and a feedback channel length 9L the oscillations have a high degree of randomness, as a results the pressure waves inside the feedback channels are irregularly distributed. At high feedback channel lengths, a high frequency fluctuating component is controlling the main jet movement, the typical jet oscillatory movement is almost gone, the jet mostly undergoes random fluctuations. The amplitude of the fluctuations and their frequency raises with the feedback channel length increase, higher power nozzle inlet velocities also tend to increase the fluctuations amplitude and frequency.

At small feedback channel lengths the flow dynamics of all parameters are correlated, the stagnation pressure oscillations at the mixing chamber convergent walls, drive the rest of the flow parameters. At high feedback channel lengths and high power nozzle velocities, due to the highly chaotic fluctuations associated to the main jet inside the mixing chamber, the direct link between the stagnation pressure oscillations/fluctuations measured at the mixing chamber convergent walls and the dynamics of the rest of the parameters cannot be directly establish. The different frequencies associated to the fluctuations appearing inside the (MC) and the (FC's), are not being transfered to the flow at the (FO) outlets. It seems the main jet is acting as a barrier preventing the displacement of these flow fluctuations to the Mixing chamber outlet.

Chapter 5

Thesis conclusions.

5.1 Conclusions

In the first stage, the dynamic performance and the flow characteristics inside the oscillator were analyzed and compared with the experimental results from previous studies. In the second stage, internal geometry modifications were applied to examine how the dynamic behavior was affected, and finally in the third stage, the evaluation of how fluidic oscillators operate under compressible conditions was investigated. The performance of a given fluidic oscillator was evaluated at incompressible flow conditions and at different Reynolds numbers via a 3D-computational fluid dynamics (CFD) analysis. The net momentum applied to the incoming jet was compared with the dynamic maximum stagnation pressure in the mixing chamber, to the dynamic output mass flow, to the dynamic feedback channels mass flow, to the pressure acting to both feedback channels outlets, and to the mixing chamber inlet jet oscillation angle. A perfect correlation between these parameters was obtained, therefore indicating the oscillation was triggered by the pressure momentum term applied to the jet at the feedback channels outlets. This study proves that the stagnation pressure fluctuations appearing at the mixing chamber inclined walls are responsible for the pressure momentum term acting at the feedback channels outlets. Until now it was thought that the oscillations were driven by the mass flow flowing along the feedback channels, however, in this study it is proved that the oscillations are pressure-driven. The peak to peak stagnation pressure fluctuations increases with increasing Reynolds number, and so does the pressure momentum term acting onto the mixing chamber inlet incoming jet. All the simulations were performed in this thesis are using 3D models. Three-dimensional models helped in clarifying the real 3D vortical structures appearing in the fluidic oscillator (the Q criterion), these structures could not be seen in 2D models.

For each application, a particular pulsating frequency and amplitude are required to minimize/maximize the variable under study, force, Nusselt number, etc. For a given range of Reynolds numbers, fluidic oscillators present a linear relationship between the output frequency and the incoming fluid flow, yet it appears the modification of the internal fluidic oscillator geometry may affect this relation. In chapter 3 of this thesis and for a given fluidic oscillator, several performance parameters were numerically evaluated as a function of different internal modifications via using 3D-CFD incompressible simulations. This study has evaluated the relation between the momentum applied to the mixing chamber incoming jet and the oscillator output characteristics. The evaluation was based on studying the output mass flow frequency and amplitude whenever several internal geometry parameters were modified. The geometry modifications considered were: the mixing chamber inlet and outlet widths, and the mixing chamber inlet and outlet wall inclination angles. The concept behind this study was, to evaluate how much the fluidic oscillator internal dimensions affected the device's main characteristics, and to analyze which parts of the oscillator produced a higher impact on the fluidic oscillator output characteristics. For the different internal modifications evaluated, special care was taken in studying the forces required to flip the jet. The entire study was performed for three different Reynolds numbers, 8711, 16034, and 32068. Among the conclusions reached it is to be highlighted that, for a given Reynolds number, modifying the internal shape affects the oscillation frequencies and amplitudes. Any oscillator internal modification generates a much relevant effect as Reynolds number increases. Among the conclusions from this study are, modifying the mixing chamber inlet width can sharply increase/decrease the frequency and amplitude of the oscillations and after a threshold reached in both directions, the oscillator stops oscillating. The modification of the inlet width can affect the direction and magnitude of the flow inside feedback channels. Low inlet widths associated with the large reverse flow along feedback channels. By increasing the mixing chamber outlet angle and outlet width, the frequency and amplitude decrease. Modifying the mixing chamber inlet angle has a small effect on the frequency and amplitude of the oscillation. For all modifications performed, the net momentum due to the pressure and the net momentum due to the mass flow calculated at the feedback channels outlets, it was observed that the net momentum is mostly due to the pressure, therefore, the oscillation is pressure driven. The net momentum is mostly due to the stagnation pressure fluctuations appearing at the mixing chamber converging surfaces.

Regarding the fluidic oscillator's main performance, a problem that is not yet clarified is the understanding of the feedback channel effect on the oscillator output mass flow frequency and amplitude, especially under compressible flow conditions. To bring light to this point, a set of three dimensional Direct Numerical Simulations under compressible flow conditions, were introduced in chapter four of this thesis. Four different feedback channel lengths and two inlet fluid velocities were considered. From the results obtained it is observed that as the inlet velocity increases, the fluidic oscillator output mass flow frequency and amplitude increase. An increase of the feedback channel length, decreases the output mass flow oscillating frequency. At high feedback channel lengths, the form of the main oscillation tends to disappear, the jet inside the mixing chamber simply fluctuates at high frequencies, for these cases the mass flow and pressure signals are very scattered due to the pressure waves appearing on mixing chamber converging surfaces and both feedback channels at the same time. Once the FC length exceeds a certain threshold, the oscillation stops. Under compressible conditions, the oscillations are pressure-driven as previously stated for the incompressible cases. The forces due to the pressure are much stronger than the mass flow flowing along the feedback channels.

5.2 Future work

In the present thesis, a specific design of the fluidic oscillator was studied numerically under incompressible and compressible conditions with different geometry modifications. The buffer zone was employed just for the baseline case, and just the frequency was compared with the case without the buffer zone. The flow behavior and its characteristics can be further studied inside the buffer zone and when the flow is leaving the oscillator outlets. Also, the buffer zone can be employed for different internal geometry modifications as discussed in chapter 3 of this thesis, for frequency and amplitude comparison with and without the buffer zone. Furthermore, the buffer zone can be used in chapter 4 of the present thesis, for compressible cases studied. The frequency and amplitude can be compared with and without the buffer zone under compressible conditions, although it requires a very large mesh and a lot of computational power to use the buffer zone under these conditions. The flow characteristics can also be studied inside the buffer zone with compressible cases. Different internal geometry modifications can be applied as discussed in chapter 3 for the compressible cases to understand the effect of these modifications on the frequency and amplitude

of the oscillation. As for future work, it is interesting to study other fluidic oscillator configurations and understand if they are mass flow or pressure-driven.

Furthermore, the current oscillator design under study with different internal geometry modifications and even under compressible conditions can be further investigated experimentally using the Particle image velocimetry (PIV) technology to validate the results obtained numerically with the experimental data. This fluidic oscillator design also can be tested in different applications such as flow separation improvements and drag reduction on the aircraft and vehicles, to understand the probability of using these devices on real-world applications.

Bibliography

[1] Gi-Hun Kim. *A study of fluidic oscillators as an alternative pulsed vortex generating jet actuator for flow separation control*. PhD thesis, The University of Manchester (United Kingdom), 2011.

[2] John C Lin, Marlyn Y Andino, Michael G Alexander, Edward A Whalen, Marc A Spoor, John T Tran, and Israel J Wygnanski. An overview of active flow control enhanced vertical tail technology development. In *54th AIAA aerospace sciences meeting*, page 0056, 2016.

[3] Marcel Staats, Staphan Löffler, Carola Ebert, Thomas Grund, and Julien Weiss. A fluidic device for active flow control: Simulation vs. experiment with emphasis on application. In *2018 Applied Aerodynamics Conference*, page 3336, 2018.

[4] S Shun and NA Ahmed. Wind turbine performance improvements using active flow control techniques. *Procedia engineering*, 49:83–91, 2012.

[5] Laurence Joseph Clancy. *Aerodynamics*. Halsted Press, 1975.

[6] Ganesh Raman and Surya Raghu. Cavity resonance suppression using miniature fluidic oscillators. *AIAA journal*, 42(12):2608–2612, 2004.

[7] Roman Seele, Philipp Tewes, René Woszidlo, Michael A McVeigh, Nathaniel J Lucas, and Israel J Wygnanski. Discrete sweeping jets as tools for improving the performance of the v-22. *Journal of Aircraft*, 46(6):2098–2106, 2009.

[8] Shawn Aram, Yu-Tai Lee, Hua Shan, and Abel Vargas. Computational fluid dynamic analysis of fluidic actuator for active flow control applications. *AIAA Journal*, pages 1–10, 2017.

[9] JH Seo, C Zhu, and R Mittal. Flow physics and frequency scaling of sweeping jet fluidic oscillators. *AIAA Journal*, pages 1–12, 2018.

[10] Suleyman Gokoglu, Maria Kuczmarski, Dennis Culley, and Surya Raghu. Numerical studies of a supersonic fluidic diverter actuator for flow control. In *5th Flow control conference*, page 4415, 2010.

[11] Bartosz Z Slupski and Kursat Kara. Effects of geometric parameters on performance of sweeping jet actuator. In *34th AIAA Applied Aerodynamics Conference*, page 3263, 2016.

[12] Louis N Cattafesta III and Mark Sheplak. Actuators for active flow control. *Annual Review of Fluid Mechanics*, 43:247–272, 2011.

[13] Thomas C Corke, C Lon Enloe, and Stephen P Wilkinson. Dielectric barrier discharge plasma actuators for flow control. *Annual review of fluid mechanics*, 42:505–529, 2010.

[14] Dominik J Bell, TJ Lu, Norman A Fleck, and Simon M Spearing. Mems actuators and sensors: observations on their performance and selection for purpose. *Journal of Micromechanics and Microengineering*, 15(7):S153, 2005.

[15] Adam Huang, Chris Folk, Chris Silva, Brian Christensen, Yih-Far Chen, Chih-Ming Ho, Fukang Jiang, Charles Grosjean, and Yu-Chong Tai. Applications of mems devices to delta wing aircraft-from concept development to transonic flight test. In *39th Aerospace Sciences Meeting and Exhibit*, page 124, 2001.

[16] Ari Glezer and Michael Amitay. Synthetic jets. *Annual review of fluid mechanics*, 34(1):503–529, 2002.

[17] John E Cater and Julio Soria. The evolution of round zero-net-mass-flux jets. *Journal of Fluid Mechanics*, 472:167–200, 2002.

[18] Reni Raju, Ehsan Aram, Rajat Mittal, and Louis Cattafesta. Simple models of zero-net mass-flux jets for flow control simulations. *International Journal of Flow Control*, 1(3):179–197, 2009.

[19] Rupesh B Kotapati, Rajat Mittal, and Louis N Cattafesta Iii. Numerical study of a transitional synthetic jet in quiescent external flow. *Journal of Fluid mechanics*, 581:287–321, 2007.

[20] Hassan M Nagib, John W Kiedaisch, Israel J Wygnanski, Aaron D Stalker, Tom Wood, and Michael A McVeigh. First-in-flight full-scale application of active flow control: the xv-15 tiltrotor download reduction. Technical report, ILLINOIS

INST OF TECH CHICAGO MECHANICAL MATERIALS AND AEROSPACE ENGINEERING DEPT, 2004.

[21] Brian D Giles. Fluidics, the coanda effect, and some orographic windsder coanda-effekt und spezielle orographische winde. *Archiv für Meteorologie, Geophysik und Bioklimatologie, Serie A*, 25(3):273–279, 1977.

[22] Ciro Cerretelli and Kevin Kirtley. Boundary layer separation control with fluidic oscillators. *Journal of Turbomachinery*, 131(4):041001, 2009.

[23] Daniel Guyot, Bernhard Bobusch, Christian Oliver Paschereit, and Surya Raghu. Active combustion control using a fluidic oscillator for asymmetric fuel flow modulation. In *44th AIAA/ASME/SAE/ASEE Joint Propulsion Conference & Exhibit*, page 4956, 2008.

[24] Dennis E Culley, Michelle M Bright, Patricia S Prahst, and Anthony J Strazisar. Active flow separation control of a stator vane using embedded injection in a multistage compressor experiment. *Journal of Turbomachinery*, 126(1):24–34, 2004.

[25] A Seifert, O Stalnov, D Sperber, G Arwatz, V Palei, S David, I Dayan, and I Fono. Large trucks drag reduction using active flow control. In *The Aerodynamics of Heavy Vehicles II: Trucks, Buses, and Trains*, pages 115–133. Springer, 2009.

[26] Elisa Phillips, René Woszidlo, and Israel Wygnanski. The dynamics of separation control on a rapidly actuated flap. In *5th Flow Control Conference*, page 4246, 2010.

[27] Rene Woszidlo and Israel Wygnanski. Parameters governing separation control with sweeping jet actuators. In *29th AIAA Applied Aerodynamics Conference*, page 3172, 2011.

[28] Junhui Huang, Thomas C Corke, and Flint O Thomas. Plasma actuators for separation control of low-pressure turbine blades. *AIAA journal*, 44(1):51–57, 2006.

[29] CM Rhie and W Li Chow. Numerical study of the turbulent flow past an airfoil with trailing edge separation. *AIAA journal*, 21(11):1525–1532, 1983.

[30] Oguz Uzol and Cengiz Camci. Experimental and computational visualization and frequency measurements of the jet oscillation inside a fluidic oscillator. *Journal of visualization*, 5(3):263–272, 2002.

[31] Rachid Khelfaoui, Stephane Colin, Stephane Orieux, Robert Caen, and Lucien Baldas. Numerical and experimental analysis of monostable mini-and micro-oscillators. *Heat Transfer Engineering*, 30(1-2):121–129, 2009.

[32] Rong Fung Huang and Kuo Tong Chang. Fluidic oscillation influences on v-shaped bluffbody flow. *AIAA journal*, 43(11):2319–2328, 2005.

[33] James W Gregory, Ebenezer P Gnanamanickam, John P Sullivan, and Surya Raghu. Variable-frequency fluidic oscillator driven by a piezoelectric bender. *AIAA journal*, 47(11):2717–2725, 2009.

[34] Florian Ostermann, Rene Woszidlo, C Nayeri, and Christian O Paschereit. Experimental comparison between the flow field of two common fluidic oscillator designs. In *53rd AIAA Aerospace Sciences Meeting*, page 0781, 2015.

[35] Shiqi Wang, Lucien Baldas, Stéphane Colin, Stéphane Orieux, Azeddine Kourta, and Nicolas Mazellier. Experimental and numerical study of the frequency response of a fluidic oscillator for active flow control. In *8th AIAA Flow Control Conference*, page 4234, 2016.

[36] Damian Hirsch and Morteza Gharib. Schlieren visualization and analysis of sweeping jet actuator dynamics. *AIAA Journal*, 56(8):2947–2960, 2018.

[37] G Raman, S Packiarajan, G Papadopoulos, C Weissman, and S Raghu. Jet thrust vectoring using a miniature fluidic oscillator. *The Aeronautical Journal*, 109(1093):129–138, 2005.

[38] Mohammad A Hossain, Robin Prenter, Ryan K Lundgreen, Ali Ameri, James W Gregory, and Jeffrey P Bons. Experimental and numerical investigation of sweeping jet film cooling. *Journal of Turbomachinery*, 140(3):031009, 2018.

[39] Suleyman Gokoglu, Maria Kuczmarski, Dennis Culley, and Surya Raghu. Numerical studies of an array of fluidic diverter actuators for flow control. In *41st AIAA Fluid Dynamics Conference and Exhibit*, page 3100, 2011.

[40] Oliver Krüger, Bernhard C Bobusch, Rene Woszidlo, and Christian O Paschereit. Numerical modeling and validation of the flow in a fluidic oscillator. In *21st AIAA Computational Fluid Dynamics Conference*, page 3087, 2013.

[41] Bernhard C Bobusch, René Woszidlo, JM Bergada, C Navid Nayeri, and Christian Oliver Paschereit. Experimental study of the internal flow structures inside a fluidic oscillator. *Experiments in fluids*, 54(6):1559, 2013.

[42] Sarah Gaertlein, Rene Woszidlo, Florian Ostermann, C Nayeri, and Christian O Paschereit. The time-resolved internal and external flow field properties of a fluidic oscillator. In *52nd Aerospace Sciences Meeting*, page 1143, 2014.

[43] Rene Woszidlo, Florian Ostermann, CN Nayeri, and CO Paschereit. The time-resolved natural flow field of a fluidic oscillator. *Experiments in Fluids*, 56(6):125, 2015.

[44] Florian von Gosen, Florian Ostermann, Rene Woszidlo, C Nayeri, and Christian O Paschereit. Experimental investigation of compressibility effects in a fluidic oscillator. In *53rd AIAA Aerospace Sciences Meeting*, page 0782, 2015.

[45] Raunak Jung Pandey and Kwang-Yong Kim. Numerical modeling of internal flow in a fluidic oscillator. *Journal of Mechanical Science and Technology*, 32(3):1041–1048, 2018.

[46] Yongjia Wu, Shifeng Yu, and Lei Zuo. Large eddy simulation analysis of the heat transfer enhancement using self-oscillating fluidic oscillators. *International Journal of Heat and Mass Transfer*, 131:463–471, 2019.

[47] Kursat Kara. Numerical study of internal flow structures in a sweeping jet actuator. In *33rd AIAA Applied Aerodynamics Conference*, page 2424, 2015.

[48] Matthew Metka, James Gregory, Aaron Sassoon, and James McKillen. Scaling considerations for fluidic oscillator flow control on the square-back ahmed vehicle model. *SAE International Journal of Passenger Cars-Mechanical Systems*, 8(2015-01-1561):328–337, 2015.

[49] Arvin Shmilovich, Yoram Yadlin, and Edward A Whalen. Numerical simulations of an airplane with an active flow control system. In *8th AIAA Flow Control Conference*, page 3929, 2016.

[50] Florian Ostermann, Rene Woszidlo, C Navid Nayeri, and C Oliver Paschereit. Properties of a sweeping jet emitted from a fluidic oscillator. *Journal of Fluid Mechanics*, 857:216–238, 2018.

[51] Rene Woszidlo, Florian Ostermann, and Hanns-Joachim Schmidt. Fundamental properties of fluidic oscillators for flow control applications. *AIAA Journal*, 57(3):978–992, 2019.

[52] Florian Ostermann, Rene Woszidlo, C Navid Nayeri, and C Oliver Paschereit. The interaction between a spatially oscillating jet emitted by a fluidic oscillator and a cross-flow. *Journal of Fluid Mechanics*, 863:215–241, 2019.

[53] Mehmet N Tomac and Elias Sundström. Adjustable frequency fluidic oscillator with supermode frequency. *AIAA Journal*, pages 1–11, 2019.

[54] Mehmet N Tomac and James W Gregory. Phase-synchronized fluidic oscillator pair. *AIAA Journal*, 57(2):670–681, 2018.

[55] Veer Vatsa, Mehti Koklu, and Israel Wygnanski. Numerical simulation of fluidic actuators for flow control applications. In *6th AIAA Flow Control Conference*, page 3239, 2012.

[56] Bernhard C Bobusch, Rene Woszidlo, Oliver Krüger, and Christian O Paschereit. Numerical investigations on geometric parameters affecting the oscillation properties of a fluidic oscillator. In *21st AIAA Computational Fluid Dynamics Conference*, page 2709, 2013.

[57] Václav Tesař. *Pressure-driven microfluidics*. Artech House Boston/London, 2007.

[58] Václav Tesař. Taxonomic trees of fluidic oscillators. In *EPJ Web of Conferences*, volume 143, page 02128. EDP Sciences, 2017.

[59] David C Wilcox et al. *Turbulence modeling for CFD*, volume 2. DCW industries La Canada, CA, 1998.

[60] Rodney O Fox and Herbert L.. Stiles. *Computational models for turbulent reacting flows*, volume 1. Cambridge university press Cambridge, 2003.

[61] Philippe Spalart and Steven Allmaras. A one-equation turbulence model for aerodynamic flows. In *30th aerospace sciences meeting and exhibit*, page 439, 1992.

[62] Matthieu Boudreau, Guy Dumas, and Jean-Christophe Veilleux. Assessing the ability of the ddes turbulence modeling approach to simulate the wake of a bluff body. *Aerospace*, 4(3):41, 2017.

[63] Philippe R Spalart. Comments on the feasibility of les for wings, and on a hybrid rans/les approach. In *Proceedings of first AFOSR international conference on DNS/LES*. Greyden Press, 1997.

[64] Philippe R Spalart, Shur Deck, Michael L Shur, Kyle D Squires, M Kh Strelets, and Andrei Travin. A new version of detached-eddy simulation, resistant to ambiguous grid densities. *Theoretical and computational fluid dynamics*, 20(3):181, 2006.

[65] Philippe R Spalart. Detached-eddy simulation. *Annual review of fluid mechanics*, 41:181–202, 2009.

[66] James Gregory and Mehmet N Tomac. A review of fluidic oscillator development. In *43rd AIAA Fluid Dynamics Conference*, page 2474, 2013.

[67] Masoud Baghaei and Josep M Bergada. Analysis of the forces driving the oscillations in 3d fluidic oscillators. *Energies*, 12(24):4720, 2019.

Appendices

Appendix A

Published journal papers

The followings are the papers published in the Energies Journal and the Applied Sciences Journal:

1.Baghaei, Masoud, and Josep M. Bergada. "Analysis of the forces driving the oscillations in 3D fluidic oscillators." Energies 12, no. 24 (2019): 4720.

2.Baghaei, Masoud, and Josep M. Bergada. "Fluidic Oscillators, the Effect of Some Design Modifications." Applied Sciences 10, no. 6 (2020): 2105.

energies

MDPI

Article

Analysis of the Forces Driving the Oscillations in 3D Fluidic Oscillators

Masoud Baghaei and Josep M. Bergada *

Department of Fluid Mechanics, Universitat Politècnica de Catalunya, 08034 Barcelona, Spain; masoud.baghaei@upc.edu

* Correspondence: josep.m.bergada@upc.edu; Tel.: +34-937398771

Received: 19 November 2019; Accepted: 7 December 2019; Published: 11 December 2019

Abstract: One of the main advantages of fluidic oscillators is that they do not have moving parts, which brings high reliability whenever being used in real applications. To use these devices in real applications, it is necessary to evaluate their performance, since each application requires a particular injected fluid momentum and frequency. In this paper, the performance of a given fluidic oscillator is evaluated at different Reynolds numbers via a 3D-computational fluid dynamics (CFD) analysis. The net momentum applied to the incoming jet is compared with the dynamic maximum stagnation pressure in the mixing chamber, to the dynamic output mass flow, to the dynamic feedback channels mass flow, to the pressure acting to both feedback channels outlets, and to the mixing chamber inlet jet oscillation angle. A perfect correlation between these parameters is obtained, therefore indicating the oscillation is triggered by the pressure momentum term applied to the jet at the feedback channels outlets. The paper proves that the stagnation pressure fluctuations appearing at the mixing chamber inclined walls are responsible for the pressure momentum term acting at the feedback channels outlets. Until now it was thought that the oscillations were driven by the mass flow flowing along the feedback channels, however in this paper it is proved that the oscillations are pressure driven. The peak to peak stagnation pressure fluctuations increase with increasing Reynolds number, and so does the pressure momentum term acting onto the mixing chamber inlet incoming jet.

Keywords: fluidic oscillators design; 3D-computational fluid dynamics (CFD); flow control; forces driving the oscillation

1. Introduction

Flow control actuators have traditionally been a research topic in the fluid mechanics field. Their use on bluff bodies allows modifying lift and drag, reducing flow instabilities, as well as the energy required for the body to move. From the different existing actuators, plasma actuators, ZNMF (zero net mass flow), MEMS (Micro-Electro-Mechanical Systems), fluidic oscillators, and combustion driven jet actuators [1,2], only plasma, pulsed combustion actuators, and fluidic oscillators do not have moving parts, which a priori gives confidence regarding their reliability.

Plasma actuators are just beginning to be able to produce the required momentum to interact with the boundary layer in real applications, but the voltage differential used often does not sufficiently ionize the fluid to create the required fluid jet momentum. Pulsed combustion actuators provide a large flow momentum, but, due to the high temperatures associated with them, these actuators can only be used in very particular applications in which high fluid temperatures are acceptable. Fluidic oscillators are able to produce pulsating jets with the required momentum to interact with the main flow boundary layer, although it appears that their design needs to be adapted to each particular application.

Original fluidic oscillators design goes back to the 60 s and 70 s. Their outlet frequency ranges from several Hz to KHz and the flow rate is usually of a few dm^3/min. From their applications in flow control, it is interesting to mention their use in combustion control [3], flow deflection and mixing enhancement [4], flow separation modification in airfoils [5], boundary layer modification on hump diffusers used in turbomachinery [6], flow separation control on compressors stator vanes [7], gas turbine cooling [8], drag reduction on lorries [9], and noise reduction in cavities [10].

Despite the existence of particular fluidic oscillator configurations, like the one introduced by Uzol and Camci [11], which was based on two elliptical cross-sections placed transversally and an afterbody located in front of them, or the one proposed by Huang and Chang [12], which was a V-shaped fluidic oscillator, most of the recent studies on oscillators focused on two main, very similar, canonical geometries, which Ostermann et al. [13] called the angled and the curved oscillator geometries. Some very recent studies on the angled geometry are [13–23], while the curved geometry was studied by [4,10,13,23–33]. Ostermann et al. [13], compared both geometries, concluding that the curved one was energetically the most efficient.

One of the first analyses of the internal flow on an angled fluidic oscillator was undertaken by Bobusch et al. [17]. Experiments were performed using water to visualize and quantify the internal flow patterns. The results provided detailed insight into the oscillation mechanism and also of the interaction between the mixing chamber and the feedback channels.

Via employing the same fluidic oscillator configuration previously analyzed by Bobbusch et al. [17], Gartlein et al. [18] carefully evaluated the internal fluid structures as well as the output jet oscillation parameters using high speed PIV, and they also used time-resolved pressure measurements. The Reynolds numbers studied ranged between 10,000 and 50,000, and air was employed as working fluid. They observed a linear dependency between the oscillation frequencies and the input Reynolds number. Several fluid properties, such as the deflection angle, jet width, and jet velocity, were examined. It was found that these properties remained rather constant for a certain range of Reynolds numbers, and suffered a strong change once a certain Reynolds number was overcome. Woszidlo et al. [19] studied the same configuration previously evaluated by Gartlein et al. [18]. Their attention focused on analyzing the flow phenomena inside the mixing chamber and the feedback channels, and highlighted that increasing the mixing chamber inlet width tended to increase the output frequency, and rounding the feedback channels should diminish the generation of the separation bubbles on these channels.

Vatsa et al. [34] studied the same two fluidic oscillators recently analyzed by [13], which resemble the ones previously studied by Bobusch et al. [17] and Aram et al. [28]. Results showed that the fluidic oscillator with sharp internal corners generated a much more homogeneous output velocity distribution than the actuator with rounded internal corners.

Aram et al. [28] studied numerically the curved geometry sweeping jet fluidic oscillator, and a large buffer zone was also considered in the simulation. The simulations were performed in 2D and 3D using the URANS-K-omega turbulence model, additionally a 3D simulation was undertaken using the IDDES turbulence model. An oscillator with an outlet diameter of 25 mm using air as working fluid and at Reynolds 12,000 and 50,000 was initially studied, but a second oscillator with an outlet diameter of 1.3 mm using water as working fluid at Reynolds number 12,000 was considered. Based on the computational results validated against experiments undertaken by previous researchers, it was found that the IDDES model provided the most accurate prediction of the flow field.

Ostermann et al. [13] experimentally studied, via PIV, the internal and external flow fields of the same two oscillator configurations previously studied by Vatsa et al. [34]. Both oscillators were characterized by a linear dependence of the oscillation frequency on the supply flow—in fact, and for the Reynolds numbers studied, the output frequency of both configurations was almost identical. The curved configuration studied by Aram et al. [28] had a larger mixing chamber inlet width than the angled one employed by Bobusch et al. [17] and Gokoglu et al. [14], which prevented the existence of reversed flow into the feedback channel. This configuration also prevented the flow

separation on the feedback channel's corners. As a result, this particular configuration appeared to be more efficient in terms of energy requirements. In fact, there are considerable differences in external flow fields caused by the different external chamber configurations. The configurations of Bobusch et al. [17] and Gokoglu et al. [14] have a smaller deflection angle and a higher homogeneous distribution of the output flow field, when compared with the flow distribution generated by the Aram et al. [28] configuration.

Slupski and Kara [27] studied a range of feedback channel geometric parameters, where the actuator configuration was the same as the one analyzed by Aram et al. [28]. The effects of varying the feedback channel height and width for different fluidic oscillator mass flow rates were studied. Oscillation frequencies increased when increasing the feedback channel height up to a certain point and then remained unaffected, however, frequencies decreased by further increasing the feedback channel width.

The oscillation frequency response for different lengths of the feedback channels of a fluidic oscillator which could generate a wide range of frequencies (50–300 Hz) was studied by Wang et al. [35]. An inverse linear relation between frequency and the length of the feedback channels was observed.

The same configuration previously employed by [17], although using a single exit, was numerically evaluated in 3D by [21]. Two geometrical parameters, the mixing chamber inlet and outlet widths, were modified. They observed a significant effect of the flow structure and the feedback channel flow rate when modifying the inlet width, while negligible effects were observed when modifying the outlet width. The effect of modifying the feedback channel and mixing chamber lengths on the oscillator mass flow frequency and amplitude was studied using a 2D numerical model by Seo et al. [22], where the fluid was considered as incompressible. Increasing the mixing chamber length generated a clear reduction in the actuator output frequency. An increase of the feedback channel length generated no modifications on the output frequency, the same observation that was previously obtained by [36].

In Hirsch and Gharib [37], the dynamics of a sweeping jet actuator were analyzed via Schlieren visualizations. Subsonic Mach numbers and the transition to sonic conditions were evaluated. They observed the oscillations started from small asymmetries caused by small differences in geometry. The properties of a sweeping jet emitted by a fluidic oscillator were recently investigated by Ostermann et al. [29]. They observed the maximum jet velocity decays much faster than a comparable steady jet, and the entrainment rate was four times the one of a steady jet. Among the latest studies on fluidic oscillators, it is relevant to highlight the ones performed by [32,33], where novel phase-synchronized and adjustable frequency fluidic oscillators were introduced. In Staats et al. [38], a new array of six Fluidic Oscillators (FOs) connected together was designed, and they simulated it using OpenFOAM in order to understand the flow physics inside the actuators. The array was employed to experimentally modify the side forces acting on a model of a vertical stabilizer.

The current paper presents a numerical evaluation of the same fluidic oscillator configuration employed in [17]. Initially, the experimental results obtained in [17] are compared with the 3D-computational fluid dynamics (CFD) simulations performed. A discussion regarding why the stagnation pressure generated at the mixing chamber converging surfaces and why the pressure momentum term acting onto the main jet at the mixing chamber inlet are responsible of the jet oscillations is undertaken. The effect of the Reynolds number on the dynamic stagnation pressure and on the pressure momentum term acting on the jet shall further clarify the origin of the oscillations. At this point it is very relevant to recall the work done by Wu et al. [23], where they applied the curved and angled fluidic oscillator configurations to enhance heat transfer. As in the present paper, they presented the temporal pressure fields inside the oscillator and concluded that for the two configurations they studied, the oscillations were pressure driven. As a matter of a fact, in microfluidics there are several fluidic oscillator configurations which are known to be pressure driven [39,40]. In the present paper and for a different angled configuration than the ones evaluated by [23], the same conclusion is obtained and is proven fully.

2. Fluidic Oscillator Main Characteristics and Model Validation

According to the introduction just presented, fluidic oscillators were mostly studied experimentally. The vast majority of the CFD simulations were carried out in two dimensions, although some recent three dimensional simulations were performed by [21,23,28,32]. In the present study, the flow was considered as turbulent, incompressible, and isothermal, all simulations were 3D, and the fluid used was water. The 3D Fluidic Oscillator (FO) considered in the present paper is introduced in Figure 1. The incoming flow enters the actuator Mixing Chamber (MC) (2) through the flattered pipe (1), and on both sides of the MC there are the Feedback Channels (FC) (3), their function is to allow transporting fluid from the downstream mixing chamber site to the upstream one and vice-versa. The fluid leaves the oscillator alternatively through the two exit surfaces located on both sides of the External Chamber (EC) (4). Notice that a second FO with a buffer zone (5) is also presented in Figure 1b. This second configuration was used to evaluate the effects of the outlet boundary conditions on the FO outlet mass flow frequency. In order to properly understand the following explanations, Figure 1c was generated, and the different sections, actuator angles, and relevant walls are defined in this figure.

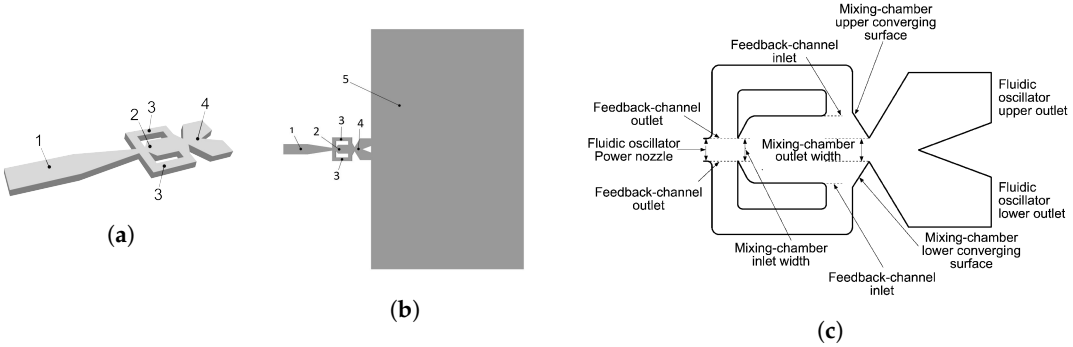

Figure 1. Fluidic oscillator general view and its different parts, (**a**) original fluidic oscillator, (**b**) fluidic oscillator with buffer zone, (**c**) fluidic oscillator main parts. Flattered pipe, 1; mixing chamber (MC), 2; feedback channels (FC), 3; external chamber (EC), 4; buffer zone (BZ), 5.

A zoomed view of the grid used to perform the 3D simulations is presented in Figure 2. Initial simulations were done employing three different grid sizes—the number of cells were respectively 142,000, 2,242,000, and 5,933,900—and the Reynolds number was set to 16,034. The Reynolds number definition used to characterize the main flow was $R_e = \frac{\rho V D_h}{\mu}$, where ρ and μ are the density and dynamic viscosity of the fluid respectively. The characteristic length was chosen to be the oscillator's power nozzle hydraulic diameter D_h, and the fluid velocity at the same section was employed as the dimensional characteristic velocity.

The output oscillation frequencies obtained with the three different meshes were 24.6 Hz, 22.7 Hz, and 22.63 Hz respectively. When comparing these values with the experimental results undertaken by [17], it was noticed that for the coarsest grid, the error produced was 12.8%, when using the intermediate mesh, the error reduced to around 4.1%, and this error further reduced to 3.8% for the finest mesh. The typical computational time required for each of these simulations was respectively 2480 CPUh for the coarsest grid, 9950 CPUh for the medium one, and 14,900 CPUh when using the finest mesh, where the computational time was calculated based on a 16 core CPUs server, and each processor had a speed of 2.3 GHz. All three grids were structured, for a Reynolds number of 16,034, the maximum respective $x+$, $y+$, and $z+$ were 5.2, 8.4, and 14.8 when employing the coarsest grid, 1.8, 4.7, and 1.2 for the case of the medium mesh, and 0.5, 0.65, and 0.4 when the finest mesh was employed. The locations of the maximum $x+$, $y+$, and $z+$ were, for the coarsest grid case, at the actuator inlet section, just before the mixing chamber entrance. For the other two meshes, the location of the maximum $x+$ was the same, yet the locations of the maximum $y+$ and $z+$ were found at the mixing chamber outlet section. The definition of $y+$ is given as $y+ = (\rho y U_\tau)/\mu$, where $U_\tau = \sqrt{\tau_w/\rho}$,

and τ_w characterizes the shear stresses at the wall point where $y+$ is determined, y is the distance to the first grid cell measured in the y direction. To obtain the $x+$ and $z+$ values, the cell distances in these respective directions were used instead of y, and the maximum shear stresses at each particular point were used for all cases. Based on the previous simulations undertaken in this paper, it was concluded that the medium grid was precise enough to evaluate the cases under study and when using Reynolds numbers below 16,034. The mesh with 5,933,900 cells was used to perform simulations at Reynolds number of 32,068. The maximum values of $x+$, $y+$, and $z+$ obtained with the finest mesh at Reynolds 32,068 were 0.9, 1.2, and 0.7 respectively. Table 1 summarizes this information.

Table 1. Main characteristic parameters of the initial simulations done in 3D using DDES turbulent model.

Reynolds Number	Number of Grid Cells	Output Frequency (Hz)	Error (%)	Time CPUh	$x+$	$y+$	$z+$
16,034	142,000	24.6	12.8	2480	5.2	8.4	14.8
16,034	2,242,000	22.7	4.1	9950	1.8	4.7	1.2
16,034	5,933,900	22.63	3.8	14,900	0.5	0.65	0.4
16,034	11,292,000 (buffer zone)	22.38	2.7	26,100	1.8	4.7	1.2
16,034	Experimental [17]	21.8	0	-	-	-	-
32,068	5,933,900	40.43	-	17,700	0.9	1.2	0.7

As previously stated, and in order to characterize the possible effect of the boundary conditions on the flow performance, a fluidic actuator with a buffer zone was generated. For this particular case, the outlet boundary conditions were maintained the same as in the original case, but the outlet was located at the end of the buffer zone. The total number of cells used in this new model was 11,292,000. A single Reynolds number of 16,034 was studied, being the maximum $x+$, $y+$, and $z+$ values, the same as the ones obtained for the medium mesh previously introduced. The frequency obtained when using this particular buffer zone model increased by 2.7% versus the one obtained experimentally [17]. The use of the buffer zone increased the computational time by 162% and the oscillation frequency obtained differed by 1.4% versus the one obtained without buffer and using the medium mesh. Considering the number of 3D simulations to be undertaken, it was decided to simulate the FO without the buffer zone.

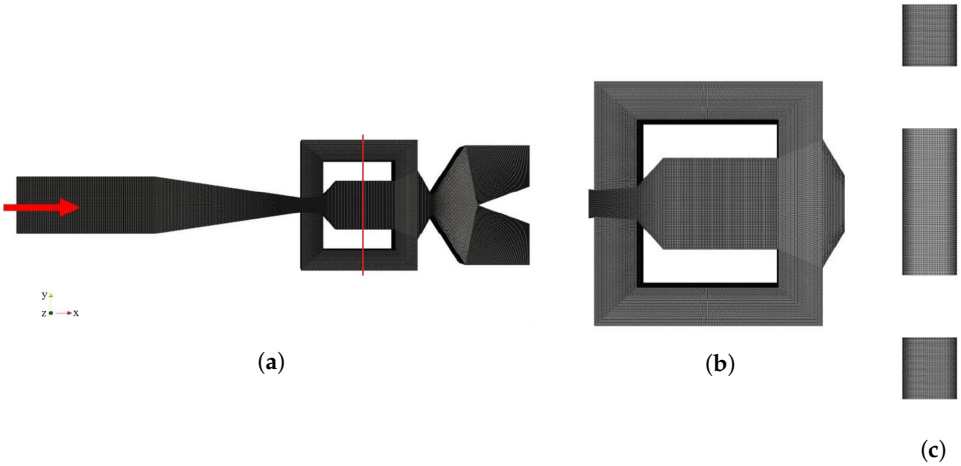

Figure 2. Grid used in the present study, (**a**) plane view, (**b**) zoom view, (**c**) side view of the mesh at the center of the mixing chamber, see the vertical line.

The boundary conditions employed in all simulations were Dirichlet conditions for velocity and Neumann for pressure at the inlet. A relative pressure of 10^4 Pa and Neumann conditions for velocity were employed at the two outlets. The same boundary conditions were used at the single outlet when the buffer zone was employed. Dirichlet boundary conditions for velocity and Neumann

for pressure were set to all walls. The different velocities evaluated and defined at the inlet of the flattered pipe where the section was $10.3 \times 3.25 = 33.475$ mm^2, see Figure 1a, were 0.671 m/s, 0.8588 m/s, 1.0479 m/s, 1.2347 m/s, and 2.46 m/s. Their respective associated volumetric flows were 22.47 cm^3/s, 28.75 cm^3/s, 35.08 cm^3/s, 41.33 cm^3/s, and 82.349 cm^3/s, with the corresponding Reynolds numbers being 8711, 11,152, 13,593, 16,034, and 32,068. The Reynolds numbers are based on the hydraulic diameter D_h and the fluid velocity V at the power nozzle, mixing chamber inlet, and the same location was already used by [17]. One of the main characteristics of a fluidic oscillator is its linear frequency behavior versus the inlet mass flow, usually represented as a function of the Reynolds number. The results obtained from the first four Reynolds numbers were used for comparison with the experimental results obtained by [17]. This comparison is presented in Figure 3, and clarifies that the expected linear behavior appears in both cases. The frequency obtained when simulating the Reynolds number 32,068 with a mesh of 5,933,900 cells is also plotted in the same figure, proving that the oscillator linearity still exists at this particular Reynolds number. Notice that the straight line showing the relation between the FO outlet frequency with the Reynolds number, see Figure 3a, would have been even better if the finest mesh was used for all Reynolds numbers evaluated.

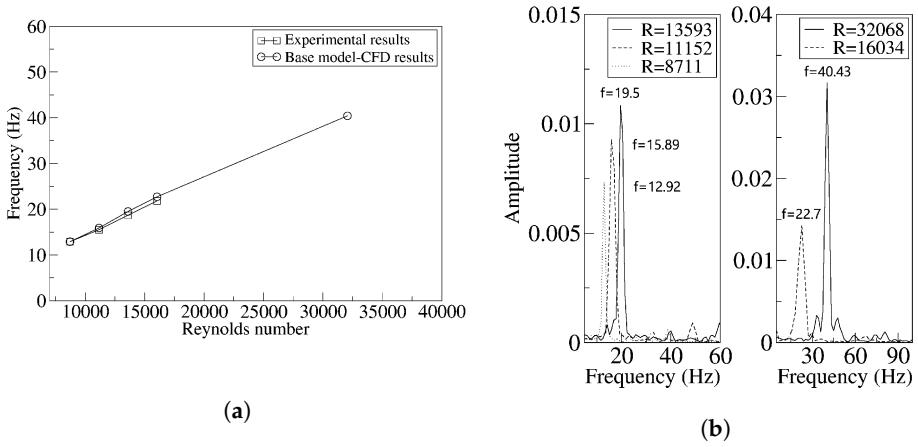

(**a**) (**b**)

Figure 3. (**a**) Comparison of experimental and computational fluid dynamics (CFD) results, (**b**) FFT of the different Reynolds numbers studied.

Fluid dynamic viscosity was chosen as 0.001003 Kg/(m s), with the fluid density being 998.2 Kg/m^3. The software OpenFOAM was employed for all 3D simulations, and finite volumes is the approach OpenFOAM uses to discretize Navier Stokes equations. Inlet turbulence intensity was set to 0.05% in all cases, Pressure Implicit with Splitting Operators (PISO) was used to solve the Navier Stokes equations, the time step being 10^{-6} s, and spatial discretization was set to second order.

3. Parameters Used to Non-Dimensionalize the Results

In order to be able to compare the present results with the previous researchers' ones, the majority of the graphs introduced in this paper were made dimensional, yet, the final graphs in which for a given Reynolds number several parameters are compared, the results are presented in non-dimensional form. To proceed with the non-dimensionalization and in order to generate graphs showing values around unity, the following dimensional parameters were employed. All dimensional parameters are based on values obtained for the baseline oscillator case at Reynolds number 16,034.

The FO outlet mass flow was non-dimensionalized using the maximum value of the mass flow measured at one of the FO outlets. The maximum inclination angle of the main jet at the mixing chamber inlet was used to non-dimensionalize the jet inclination angle at the mixing chamber inlet. The maximum momentum measured at one of the FC outlets was employed to non-dimensionalize the momentum acting over the jet. The maximum value of the stagnation pressure measured at the mixing chamber outlet converging walls was defined as the characteristic pressure for non

dimensionalization. The characteristic length was chosen to be the oscillator's power nozzle inlet hydraulic diameter D_h, and the fluid velocity at the oscillator's power nozzle was employed as the dimensional characteristic velocity.

One of the main concepts which needs to be understood in the present paper is the momentum associated with the fluid in a given section. Equation (1) defines this concept for any of the two FC outlets.

$$M = \dot{m}_{out} \times V_{out} + P_f \times S_{out} = \dot{m}_{out}^2 / (S_{out} \times \rho) + P_f \times S_{out} \quad (1)$$

where $\dot{m}_{out}, V_{out}, S_{out}$, and P_f are respectively the mass flow, the spatial average fluid velocity, the surface at the FC outlet, and the pressure instantaneously appearing at any of the FC outlets, and ρ is the fluid density.

The momentum associated with the flow at any given section consists of two parts: the momentum associated with the fluid mass flow and the one associated with the fluid pressure. To evaluate the mass flow momentum term, it is required to know the instantaneous mass flow, the fluid density, and the section through which the fluid flows. In the present paper, the instantaneous mass flow flowing though each grid cell belonging to the surface to be evaluated was determined. The total mass flow was obtained simply by adding the elementary mass flow of each cell corresponding to the chosen surface. The pressure momentum term was obtained when multiplying the instantaneous pressure acting on each cell by the cell surface, and then adding the elemental pressure momentum terms corresponding to the surface under study. The different momentum terms will be obtained at the feedback channel outlets. The net momentum characterizing the overall forces acting on the main jet lateral surfaces will consider the pressure and mass flow momentum terms acting on both feedback channels outlets.

4. Results

4.1. Original Fluidic Oscillator at Reynolds Number 16,034

As already presented in many of the studies on FO, see for example [17–19,21–23,32], the MC and FC internal flow configuration along a complete oscillation period was divided in several equally spaced time steps. In the present study, the streamlines and pressure contour plots at Reynolds number 16,034 are divided into six time steps, which correspond to 1/6 of a typical oscillation period. This information is introduced in Figure 4. Notice that the streamline plots are almost identical to the ones experimentally obtained by [17], although in the present case, the pressure contours are also implemented and will be used to clarify the origin of the forces responsible of the oscillation. In order to properly understand the flow configuration and the forces acting inside the FO, Figures 5 and 6, which introduce the dimensional values of the oscillator and FC volumetric flows, the MC inlet, and outlet jet inclination angles, the pressure at different locations inside the MC, and the net momentum acting on the jet at the feedback channels outlet will be linked with Figure 4. Each graph in Figures 5 and 6 is divided into six equally spaced time steps, see the dotted vertical lines, which correspond to each of the time periods described in Figure 4. This will allow to carefully evaluate the value of each parameter at each time period.

The initial time in Figure 4, $T = 0$, was chosen at the instant at which the volumetric flow across the FO upper outlet was minimum. At this particular instant there is some negative flow entering the oscillator across the oscillator upper outlet, see Figure 5a at a dimensional time of 1.255 s. The jet inside the MC is moving down and it is about to reach its lowest position, Figure 5c clarifies this point. According to Figure 4a, there is a considerable flow along the upper feedback channel, from Figure 5b it is observed that such volumetric flow is almost at its maximum value and it tends to decrease over time. When comparing Figure 5a,b, it is stated that the FC volumetric flow is one order of magnitude smaller than the oscillator volumetric flow. This characteristic agrees perfectly well with what was found in [13,19] working with air, comparing Figure 5a,b from the present paper with Figures 6 and 8

in [19] or with Figures 3 and 5 from [13]. At this initial instant, the volumetric flow along the lowest FC is almost zero, see Figure 5b. The spatially averaged pressure at the MC upper converging surface is about 4000 Pa higher than the one corresponding to the lower converging wall, this can be seen in Figures 4d and 6a, and both pressures are about to decrease versus time. Also, the pressure at the upper FC outlet, see Figure 6b, is about 4000 Pa higher than the one appearing at the lower FC outlet, indicating there must be a force acting on the main jet inlet which pushes the jet down. The net momentum acting onto the lateral sides of the jet at the MC inlet is obtained when considering the pressure and mass flow on both FC outlets. The pressure at each grid cell multiplied by the cell area and summed across a feedback channel outlet provides the momentum due to the pressure at this particular section. However, the momentum due to the pressure needs to be added to the momentum due to the FC mass flow, which was determined via dividing the instantaneous mass flow raised to the power of two by the section of the feedback channel outlet and the fluid density, $M = ps + \dot{m}v = ps + \dot{m}^2/(\rho s)$. Each separate net momentum, pressure, and mass flow term on both FC outlets, and the addition of both terms, is presented in Figure 6d, from which it is stated that the net momentum due to the mass flow is almost negligible when compared to the one generated by the pressure. The net momentum presented in Figure 6d is almost the same as the net momentum due to pressure term, then the forces due to the FC mass flow are over an order of magnitude smaller. The net momentum at this initial time is negative, indicating the jet is being pushed down, in fact the net momentum has just reached its maximum negative value. Notice there is a very good agreement between Figure 6b,d, in fact, the origin of Figure 6d is the temporal pressure difference between both feedback channel outlets.

Going back to Figure 4a, it is observed that the bubble located between the jet and the MC lower borders is about to reach its minimum volume, while the bubble above the jet is almost at its maximum dimension. Notice that these bubbles consist of a series of small vortical structures, instead of a main large structure as defined in previous papers, see for example [17,19]. This is probably due to the high accuracy of the turbulent model employed along with a very realistic three dimensional model presented in this research. When analyzing the vortical structures generated, it needs to be considered that the Reynolds number studied is relatively high, hence the flow is chaotic. Evaluating a different FO configuration and using the Q criterion, the internal vortical structures were presented in [32].

At this initial instant, the jet leaves the FO through the lower outlet. On both sides of the (EC), a large vortex is observed, the lower vortex is smaller than the upper one and has a much higher intensity, see from Figure 4d that the pressure is about 32% smaller than the upper one, indicating that the lower vortex turns much faster. The pressure inside the mixing chamber is quite homogeneous, and some particular low pressure spots are to be seen where the main lower and upper bubbles are located. The particularly low pressure spot located below the jet indicates the Coanda effect appears in this location. According to [41], from this low pressure location and when the flow is considered as compressible, weak expansion waves are being generated.

At this initial instant, on the MC upper converging surface, the pressure is about 16% higher than the one existing on the MC lower converging surface. This particularly high stagnation pressure point will move to the lower converging surface in the next time period $T = 1/6$, compare Figure 4d,e. It appears the jet impinges alternatively on these surfaces during a small period of time. According to Gregory and Tomac [41], under compressible flow conditions, weak compression pressure waves are generated alternatively at these locations. The FC upper branch has a slightly higher pressure than the lower branch, see Figure 4d, and this pressure difference between both feedback channels and measured at the feedback channels outlets is presented in Figure 6b. The particular pressure difference between the upper feedback channel inlet and outlet is introduced in Figure 6c. The pressure is very much alike along the channel, being just slightly higher at the inlet, but this small pressure difference is what drives the flow along the feedback channel. It is at this point relevant to clarify that all graphs presented, especially the pressure ones, show very scattered curves. The origin of this lack of smoothness is the intrinsic instabilities associated with the chaotic flow. Another point to discuss

is that the curves presented are not fully sinusoidal. As the flow inside the mixing chamber is fully turbulent, the jet inside the mixing chamber does not follow a perfect and symmetrical displacement, therefore the periods of all variables are not completely sinusoidal.

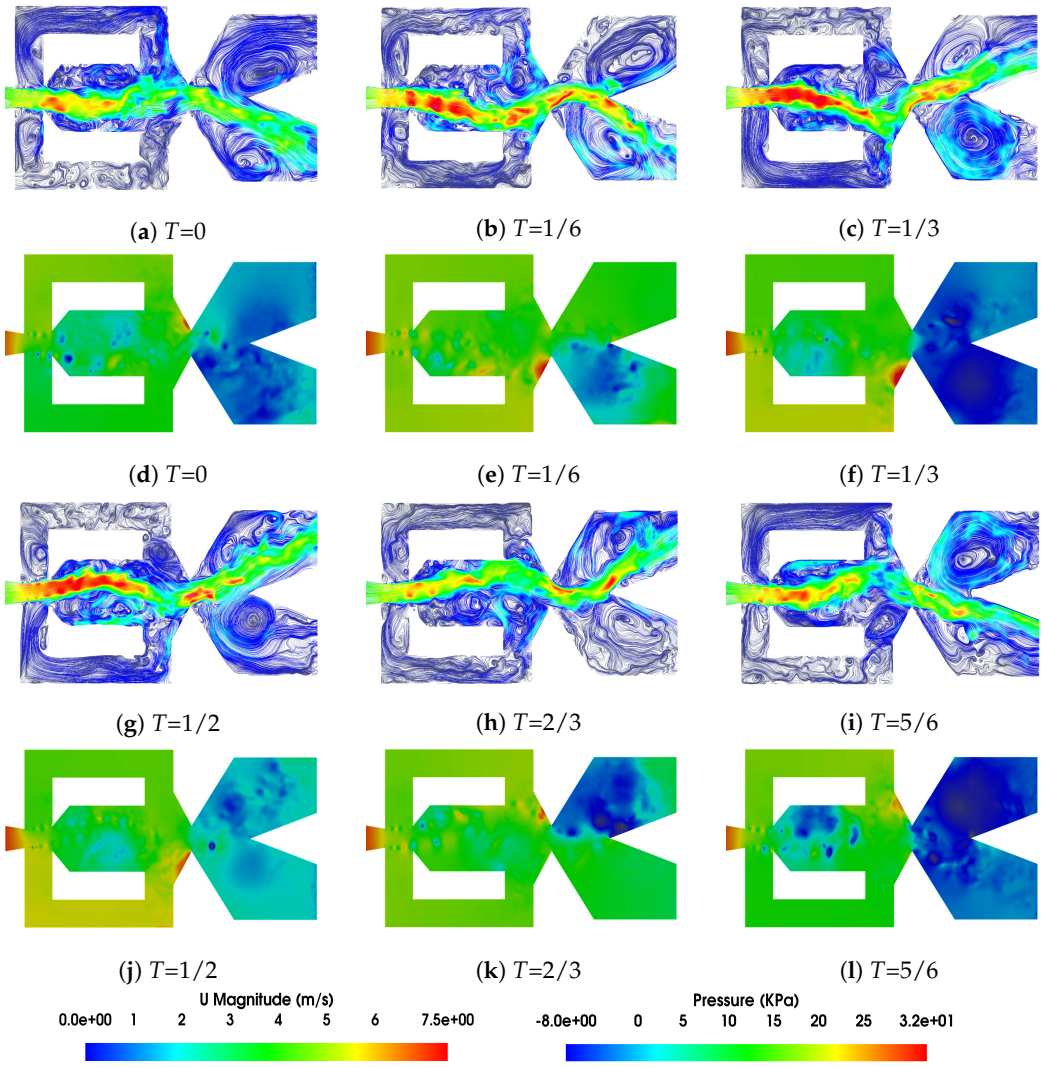

Figure 4. Mixing chamber period of oscillation divided in six equally spaced times, Reynolds number 16,034. Figures (**a**–**c**,**g**–**i**), present the streamlines plots, figures (**d**–**f**,**j**–**l**), introduce the pressure contours.

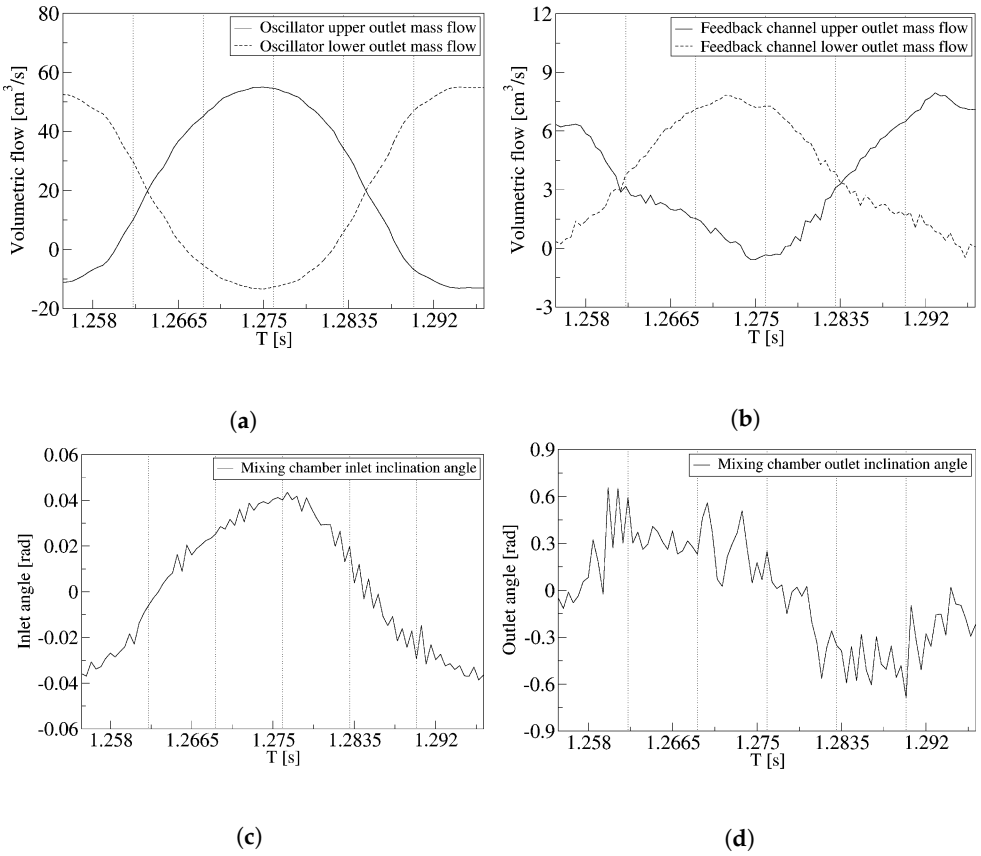

Figure 5. Mass flow through the oscillator upper and lower outlets, (**a**); mass flow through the feedback channels, (**b**); mixing chamber inlet jet inclination angle, (**c**); and mixing chamber outlet jet inclination angle, (**d**). Reynolds number 16,034.

In the next time period $T = 1/6$, the jet inside the MC has reached its lowest position and it is starting to move up. Most of the flow is leaving the oscillator through the lower oscillator outlet, but some amount of flow exits the oscillator through the upper outlet, see Figures 4b and 5a. Two large vortices can be observed at the external chamber upper and lower outlets. The vortex associated with the upper outlet is much bigger than the one appearing at the lower outlet, yet the intensity associated with the lower vortex is higher, as can be extracted from the observation of the pressure field in Figure 4e. In any case, when comparing Figure 4d,e it is observed that the external chamber lower vortex has decreased its intensity versus the previous time period, which is because the mass flow leaving through the lower outlet is now smaller than the previous time period. The volumetric flow along both feedback channels is very similar and flows in both cases from the feedback channels inlets to the outlets. This fact can be observed from the streamlines plot presented in Figure 4b and from the FC volumetric flow at a dimensional time of 1.2635 s, Figure 5b. The maximum pressure is now to be observed at the MC lower converging wall, see Figures 4e and 6a, which is why the lower FC has a slightly higher pressure than the upper one, yet as already mentioned, the volumetric flow is almost the same in both feedback channels, which seems to indicate that there is a phase lag between the instant an FC is pressurized and the instant the flow starts moving along the FC. In fact, at this particular instant and according to Figure 6b, the pressure on both feedback channel outlets is almost the same, although on the verge of being higher at the lower FC outlet. From the information presented in Figure 6b, the pressure term of the net momentum applied to the jet entering the FO is obtained, see Figure 6d, where it can be stated that at this instant, the net momentum is almost zero. Figure 5c,d presents the jet inclination angle at the mixing chamber inlet and outlet, as already introduced by Seo et al. [22]. The jet inclination angle at the MC inlet is still negative and tending to zero, while at the MC outlet the jet inclination angle is now positive, see Figures 4b and 5d. It is interesting to realize that

at this instant the jet leaving the MC is facing upwards, but the jet still leaves the oscillator through the lower outlet, which is due to the reattachment the jet is having to the external chamber lower wedge surface.

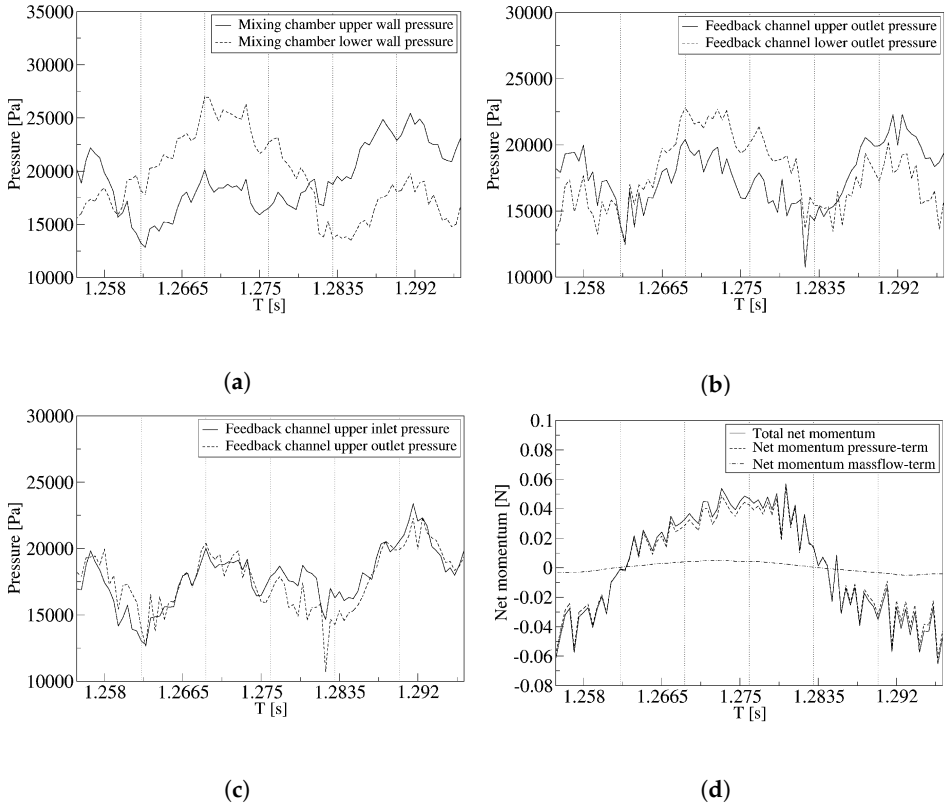

Figure 6. Mixing chamber outlet converging walls pressure, (**a**); pressure at both feedback channels outlets, (**b**); and pressure at the feedback channel inlet and outlet, (**c**). Overall momentum at the feedback channels outlet, which is acting on the jet entering the mixing chamber. The momentum is split in the component due to the mass flow flowing along the feedback channels and due to the pressure acting onto the feedback channels outlet, (**d**). Reynolds number 16,034.

When moving to the next time period, $T = 1/3$, it is observed that the jet is now entering the MC almost perpendicular to it, see Figure 4c and also Figure 5c, where it can be stated that the jet inclination angle at the mixing chamber inlet is slightly positive. The flow is leaving the oscillator through the upper outlet, see Figures 4c and 5a. This is why at the MC outlet, the jet inclination angle is positive and having almost its maximum value, Figure 5d. The two typical vortices respectively appearing at each side of the external chamber are clearly seen, at this particular instant. The lower vortex, which is located at the center of the lower outlet, has a slightly higher intensity than the upper one, see Figure 4f. This is particularly relevant because at this instant the jet leaves the actuator through the upper outlet, which in reality indicates that the jet has just flipped from the lower outlet to the upper one. Inside the MC, the maximum pressure is localized at the lower converging surface, notice that the jet impinges on this surface, Figure 4f. As a result of the location of the maximum stagnation pressure point, the lower feedback channel is pressurized and a large amount of flow is going from the feedback channel inlet to the outlet, with Figures 4c,f and 5b are showing this situation. Despite the fact that the flow on the lower FC is almost at its maximum, on the upper FC there is still a small amount of flow from the FC inlet to the outlet. Regarding the streamlines at the lower FC, it is interesting to recall the work undertaken by Woszidlo et al. [19], where they defined the existence of a bubble at the FC inlet, which perfectly fits with what can be seen in Figure 4c. At this particular instant, the pressure between the lower and upper mixing chamber converging walls is about 6500 Pa, also the pressure difference between the feedback channel lower and upper outlets reached a particularly high

value of about 3000 Pa, see Figure 6a,b. As a result of the relevant pressure difference at the feedback channel outlets, the positive net momentum acting on the jet is about to reach its maximum value, see Figure 6d.

The next time period corresponds to $T = 1/2$, see Figure 4g,j. The jet inside the MC is about to reach its maximum position, the flow is leaving the actuator through the upper outlet, and the jet inside the MC is still impinging onto the lower converging surface. The stagnation pressure is lower than the one existing in the previous time period. The pressure on the lower converging wall, see Figures 4j and 6a, is much higher than the one in the upper converging wall. The lower FC is still pressurized, and the flow rate going from the lower FC inlet to the outlet is still very high, on the other hand the flow flowing along the upper FC is almost zero, see Figures 4g and 5b. The pressure on the lower FC outlet is, according to Figure 6b, about 4000 Pa higher than the one on the upper FC outlet. This is why the net momentum acting on the jet inlet is positive, pushing the jet upwards, Figure 6d represents this case.

At $T = 2/3$, Figure 4h,k, the jet at the MC has reached its highest position and is beginning to move down. At the MC inlet, the jet inclination angle is still positive, but tending to zero, see Figure 5c. At the MC outlet, the jet inclination angle has changed from positive to negative, see Figures 4h and 5d, but the jet still leaves the FO through the upper outlet, the volumetric flow through the FO upper outlet is represented in Figure 5a. The vortex generated at the upper part of the external chamber is now more energetic than the one appearing at the lower external chamber outlet, and Figure 4h,k clarifies this point. From Figure 6a it is observed that the maximum stagnation pressure has moved to the upper converging wall, and the upper FC is about to be pressurized. The pressure at both feedback channel outlets is very much the same (Figure 6b), as a result the volumetric flow along both feedback channels is also very similar, see Figure 5b, and flows from the feedback channels inlets to outlets. The net momentum applied to the jet entering the MC, as can be observed in Figure 6d, is almost null, this is clearly understandable when realizing that the pressure on both feedback channels outlets is nearly the same, as represented in Figure 6b.

Finally, when the time period is $T = 5/6$, the jet is located at the center of the MC and descending down, the jet inclination angle at the MC inlet is slightly negative and so is the jet at the MC outlet, see Figures 4i and 5c,d. The flow is leaving the FO through the lower outlet, in fact, there is some reverse flow entering the FO through the upper outlet, as presented in Figure 5a. At the external chamber upper outlet, a clear vortex is being observed, as can be seen in Figure 4l. This vortex has a higher intensity than the one appearing at the external chamber lower outlet. This is particular because, as previously mentioned, the fluid leaves the oscillator through the lower outlet, which in reality indicates that the jet at the external chamber has just flipped over from up to down. Inside the MC, the jet is still impinging on the upper converging surface, Figure 4l, as a result there is a relatively large flow moving along the upper FC. On the lower FC there is a small amount of flow still going from the FC inlet to the outlet, see Figure 5b. The pressure difference between the upper and lower converging walls is at its maximum, about 6000 Pa, and so is the pressure difference between the feedback channel upper and lower outlets, about 3000 Pa, see Figure 6a,b, respectively. As a result of the pressure difference existing between the feedback channels outlets, the net momentum acting on the lateral surfaces of the jet entering the mixing chamber is negative, see Figure 6d, and the jet is being pushed down. Two videos presenting the dynamic velocity field and the pressure distribution are given as Supplementary Materials.

Based on the previous explanations, the following statement is made: What is needed to flip the jet from one side to another is a pressure gradient between the feedback channel outlets. Once a pressure threshold is overcome, the jet starts bending and the mass flow through the feedback channels provides the required volume for the mixing chamber bubbles to expand. The required pressure threshold originates at the mixing chamber outlet converging surfaces.

Figure 7 introduces, for the three Reynolds numbers studied, 8711, 16,034, and 32,068, the volume of fluid transferred through each FC during half cycle and during a full cycle. The estimated mixing

chamber bubble volume increase, as the main jet flips from one side to the other, is also presented. According to the work undertaken by [18,19], the maximum bubble volume remains constant and independent of the Reynolds number employed, and the volume of fluid transferred by the feedback channel, according to [18,19,22], was always equal to the bubble volume growth. Figure 7a shows that both volumes are independent of the Reynolds number, yet they are not equal, which means the volume of fluid required for the mixing chamber bubble to expand may not be fully provided by one of the feedback channels flow, in fact both FCs are responsible for the MC bubble growth. It also appears that some of the required volume is provided by the mixing chamber incoming jet, and Figure 7b clarifies this point. Notice that the jet expands as it enters the MC, filling up part of it.

At this point, it is necessary to remember that most of the previous work on fluidic oscillators was done in 2D, and even the results obtained experimentally were based on 2D PIV measurements. The present simulations are 3D, and this fact is likely to explain the small discrepancies found regarding the origin of the fluid required for the mixing chamber bubble to grow. In order to highlight the importance of performing the study in 3D, Figure 8 introduces instantaneous slices of the mixing chamber and of the FO output exits. Clearly, the flow cannot be considered two dimensional at any point and clarifies the difficulty of measuring the exact bubble growth in the mixing chamber.

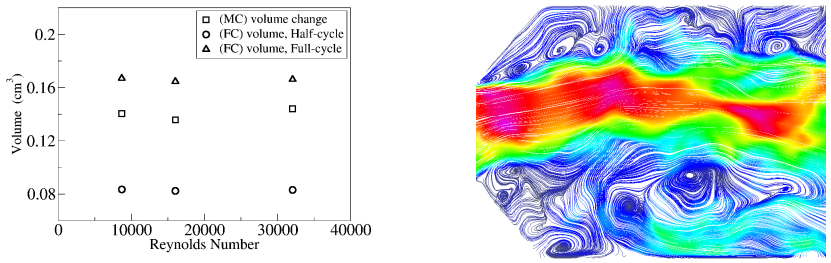

Figure 7. (**a**) Mixing chamber volume growth at three different Reynolds numbers, 8711, 16,034, and 32,068. Comparison with the fluid volume provided by the FC. (**b**) Zoomed view of the mixing chamber inlet, where it is seen that part of the incoming fluid helps the mixing chamber bubble to grow.

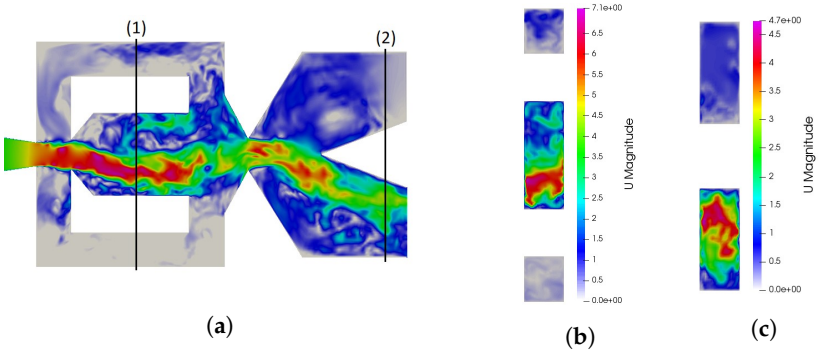

Figure 8. Instantaneous velocity fields at the, (**a**) mixing chamber, (**b**) spanwise section, slice (1), (**c**) spanwise section at the fluidic oscillator outlet, slice (2). Reynolds number 16,034.

A good way to illustrate the vortical structures appearing inside the FO is by means of isosurfaces based on the Q criterion, as presented in Figure 9. The isosurfaces are colored by the vorticity about the Z axis. The color blue indicates the structures turn clockwise, the red color is associated with counterclockwise rotation. The snapshot sequence presented in Figure 9 characterizes a full oscillation period divided into six evenly spaced time steps, which match with the time steps introduced in Figure 4. It is interesting to see the coexistence of positive and negative structures at any instant. When the jet inside the MC is inclined downwards, $T = 0$ and $T = 1/6$, the negative structures dominate the flow, but the counterclockwise structures are the predominant ones when the jet inside the MC faces

upwards, $T = 1/2$ and $T = 2/3$. The vortical structures inside the FCs and the external chamber (EC), which could clearly be seen in Figure 4, can hardly be seen in Figure 9, indicating that their vorticity is at least an order of magnitude smaller than the one associated with the MC vortical structures. The large coherent negative structures which can be seen in Figure 9a,b break and move downstream of the MC at time $T = 1/3$. In the next two time periods, in Figure 9d,e, coherent positive structures dominate the MC flow, also moving downstream, while breaking up on the next time step.

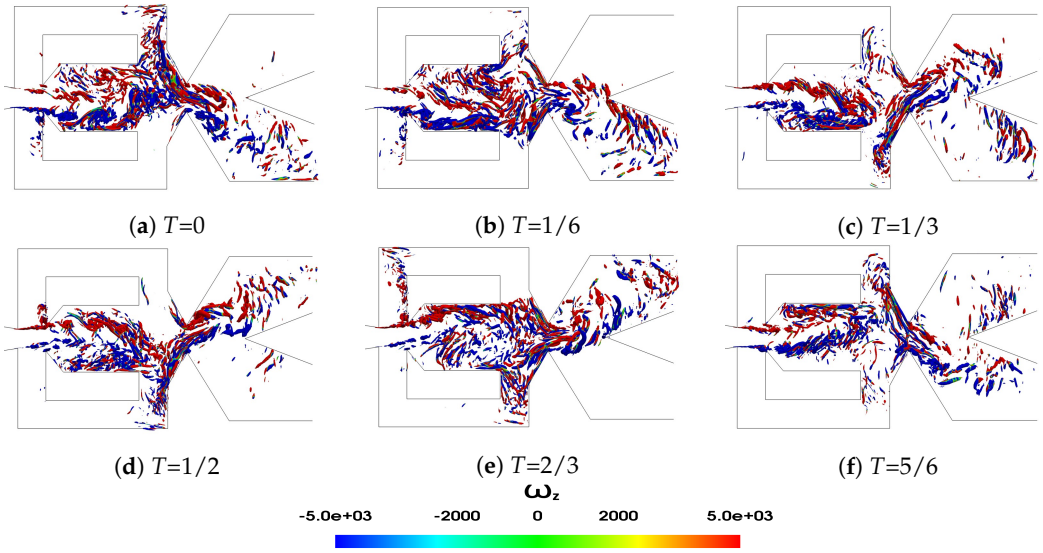

Figure 9. Q criterion at the mixing chamber period of oscillation divided into six equally spaced times, Reynolds number 16,034.

4.2. Variation of the Fluidic Oscillator Momentum with the Reynolds Number

When evaluating the forces which trigger the flapping motion of the incoming jet inside the mixing chamber, and according to previous studies, it seemed that the mass flow flowing along the feedback channels had a high degree of relevance. In the previous section, see Figure 6d, the net momentum generated by the FC mass flow was compared with the one generated by the pressure, and both net momentums were determined at the feedback channels outlets. The conclusion was that the net momentum due to pressure is the relevant one. But one question still remains: Is the net momentum due to the pressure always the relevant one? In the present section and for three different Reynolds numbers, 8711, 16,034, and 32,068, the net momentum acting on the fluidic oscillator incoming jet and due to the feedback channels flow is compared with the net momentum generated by the static pressure. Figure 10 presents, for the three Reynolds numbers evaluated, both net momentums acting on the MC incoming jet lateral sides. The net momentum due to the static pressure and regardless of the Reynolds number studied is over one order of magnitude higher than the one generated by the feedback channel mass flow. The overall net momentum is mostly due to the pressure term, as shown in Figure 6d for Reynolds number 16,034. The conclusion is, that for the present FO configuration, the mass flow transported by the FCs plays a negligible role when considering the flapping movement of the jet inside the MC. The flapping movement is driven by the pressure difference acting onto the main jet lateral surfaces, the feedback channel output surfaces.

From Figure 10 it is also observed that the net momentum due to the pressure field appears to be rather scattered. The curve is not smooth, and the authors believe this is due to the turbulence intensity associated with the chaotic flow. Another point to be highlighted from Figure 10 is that the amplitude of the net momentum due to the pressure term increases as the Reynolds number increases. To understand why this is so, it just needs to be remembered that the kinetic energy $V^2/2$, and therefore the dynamic term of the stagnation pressure $P_{0d} = \rho V^2/2$, increases with the fluid velocity to the power of two. The peak to peak amplitude of the stagnation pressure, measured in Pascals, at the

mixing chamber converging walls and as a function of the Reynolds number, was found to be having the following relation, $PA_{peaktopeak} = 6.476 \times 10^{(-5)} \times (Re)^{1.985}$. The reason why it is not increasing as a function of the velocity to the power two is due to the inclination of the MC converging walls where the jet impinges.

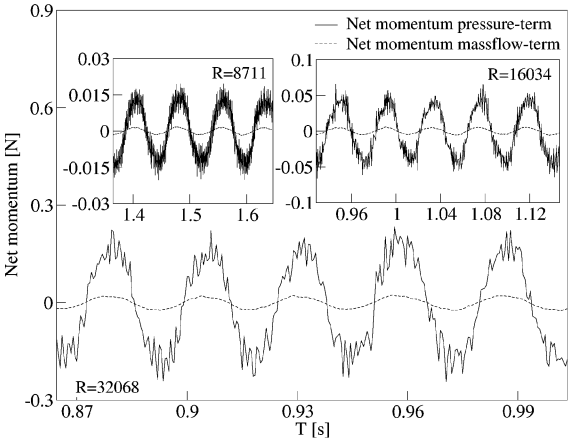

Figure 10. Net momentum pressure and mass flow terms for different Reynolds numbers.

For the Reynolds numbers studied, the net momentum peak to peak amplitude, given in Newtons, increases with the Reynolds number increase and obeys to the following expression, $MA_{peaktopeak} = 6.267 \times 10^{(-10)} \times (Re)^{1.981}$. At this point, it is important to recall that the fluid net momentum has two terms, the static pressure term and the mass flow one, the second being much smaller than the first. The fluid velocity increases linearly with the Reynolds number increase, the net momentum amplitude increases with the stagnation pressure increase at the MC converging walls, and the stagnation pressure increase is a function of the square of the fluid velocity, $P_{0d} = \rho V^2/2$. Therefore, it seems the net momentum amplitude should increase as a function of the Reynolds number to the power of two, yet this is not happening and the reason why is related to the stagnation pressure increase, which in reality increases to the power of 1.985 as presented in the previous paragraph. The reason why the momentum increases to the power 1.981 instead of 1.985, which is the power increase of the pressure amplitude, is due to the pressure losses existing between the MC outlet inclined walls and the FC outlet. In reality, the fluidic oscillator internal configuration, and especially the angle of the MC converging walls, play a decisive role in the relation fluid velocity and stagnation pressure.

The statements made in the previous section were: the oscillation of the FO is triggered by the pressure difference between the FC outlets, and this pressure difference is generated at the MC outlet converging surfaces. In order to properly understand these statements, the following dynamic non-dimensional parameters were compared in Figure 11: the stagnation pressure at the MC lower converging surface, the net momentum acting on the jet, the MC incoming jet oscillation angle, and the FO upper outlet mass flow. These parameters were compared for the three Reynolds numbers studied, 8711, 16,034, and 32,068.

The first thing to realize, when comparing the Figure 11a–c, is that the outlet mass flow frequency and peak to peak amplitude increase as the Reynolds number increases. During approximately one fourth of the period the volumetric flow at the FO outlet enters the oscillator, the volumetric flow entering the oscillator increases as the Reynolds number increases, yet the time at which this is happening keeps being approximately one fourth of the oscillation period. The main conclusion from Figure 11a–c is that there is a perfect agreement between the dynamic parameters evaluated. This agreement exists regardless of the Reynolds number studied. The stagnation pressure peak to peak amplitude increases as the Reynolds number increases, and the exact dimensional relation previously defined was $PA_{peaktopeak} = 6.476 \times 10^{(-5)} \times (Re)^{1.985}$. The net momentum applied to the jet, the FO output mass flow, and the MC inlet inclination angle follow the pressure dynamics generated at the

MC outlet converging walls. Yet a small phase-lag between the stagnation pressure fluctuation and the net momentum acting on the MC incoming jet, to the order of 0.0017 s, is to be observed at Reynolds number 16,034, the phase-lag increases to 0.00287 s for a Reynolds number of 32,068.

Under compressible flow conditions, the time required by the pressure waves to travel from the FC inlet to outlet directly depends on the speed of the pressure waves, which is defined as $C = \sqrt{\beta/\rho}$, and considering the bulk modulus and the density for the working fluid, water, the resultant speed is of $C = 1460$ m/s. This speed is meant to be infinite when the fluid is considered incompressible. In any case and considering the actual FC length, the phase lag between all parameters studied has to be negligible regardless of the Reynolds number employed. Therefore, the phase lag observed in Figure 11 is believed to estimate the time required for the pressure to be established at the FC outlets. In Figure 7, it was shown that the maximum volume between the MC oscillating jet and the lateral walls remained constant and independent of the Reynolds number. Figure 11 also presents the jet inclination angle at the MC inlet. Notice that the maximum inlet inclination angle remains constant and independent of the Reynolds number, therefore explaining why the maximum volume at the MC remains constant.

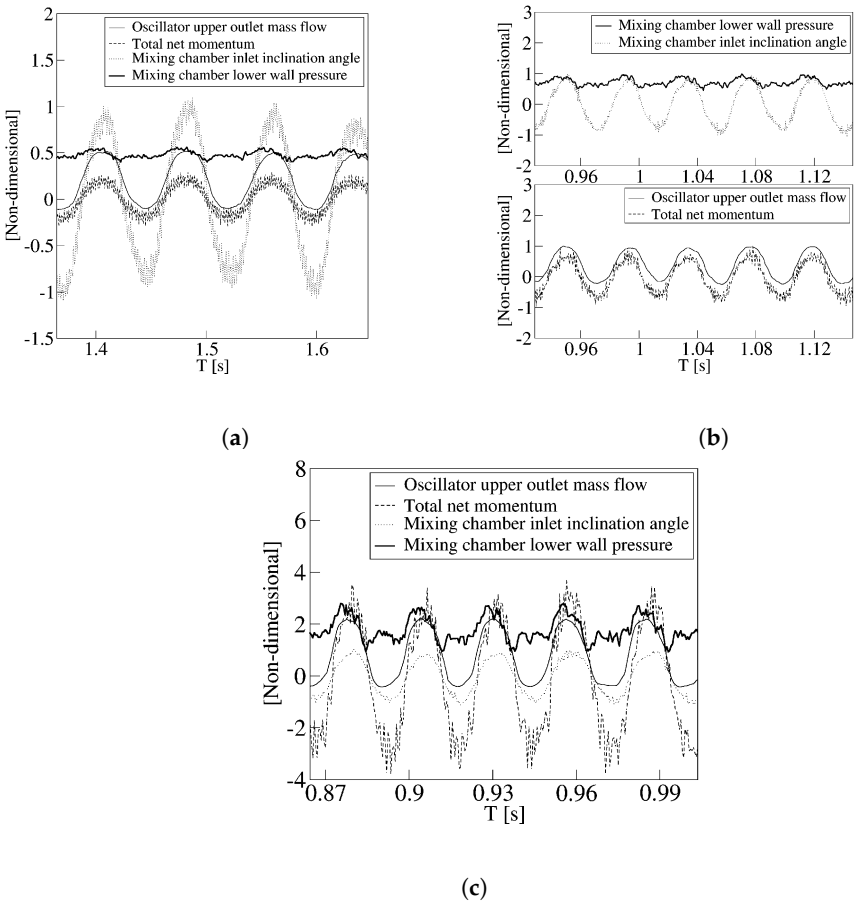

Figure 11. Comparison of the stagnation pressure at the mixing chamber lower converging surface, the total momentum acting on the jet, the mixing chamber inlet oscillation angle, and the oscillator output mass flow. Reynolds numbers, 8711 (**a**), 16,034 (**b**), 32,068 (**c**).

5. Conclusions

A careful 3D-CFD evaluation of a fluidic oscillator under turbulent conditions has been performed. Numerical results obtained were compared with previous experimental works, showing good agreement. For the Reynolds numbers studied, the flow is chaotic, therefore three dimensional simulations are needed to properly characterize the flow structures. The main jet oscillation at the mixing chamber inlet and outlet has been linked with the feedback channels mass flow, the oscillator

mass flow, the pressure at the mixing chamber converging walls, and the pressure at the feedback channels outlet. The conclusion is that the forces acting onto the incoming jet at the mixing chamber inlet and feedback channel outlets are mostly due to the static pressure.

The net momentum pressure term acting onto the lateral sides of the mixing chamber incoming jet directs the oscillation of the jet in the MC, and therefore the oscillation at the fluidic oscillator output. For the actual FO, the momentum oscillation is generated by the stagnation pressure oscillation occurring at the mixing chamber outlet converging surfaces. The momentum due to the mass flow flowing along the feedback channels plays a negligible role, when considering the forces driving the oscillation. The amplitude of the net momentum oscillation is directly linked with the maximum and minimum values of the stagnation pressure appearing at the mixing chamber outlet converging surfaces, and the amplitude of the stagnation pressure increases the Reynolds number increases, according to the function $PA_{peaktopeak} = 6.476 \times 10^{(-5)} \times (Re)^{1.985}$. Regardless of the Reynolds number employed, the total dynamic momentum acting on the jet always follows the stagnation pressure dynamics observed at the mixing chamber converging walls, therefore indicating that the origin of the fluctuations is the same for all Reynolds numbers studied.

Supplementary Materials: The following are available online at http://www.mdpi.com/1996-1073/12/24/4720/s1, Two videos introducing the velocity field and pressure distribution at Reynolds number 16,034, are also provided. Video S1: Velocity Field, Video S2: Pressure Distribution.

Author Contributions: Conceptualization, M.B. and J.M.B.; methodology, M.B. and J.M.B.; software, M.B.; validation, M.B.; formal analysis, M.B. and J.M.B.; investigation, M.B. and J.M.B.; data curation, M.B.; writing—original draft preparation, M.B. and J.M.B.; writing—review and editing, M.B. and J.M.B.; visualization, M.B. and J.M.B.; supervision, J.M.B.; project administration, J.M.B.; funding acquisition, J.M.B.

Funding: This work was supported by the Spanish and Catalan Governments under grants FIS2016-77849-R and 2017-SGR-00785, respectively. Part of the computations were done in the Barcelona Supercomputing Center under grants FI-2016-3-0038, FI-2017-2-0020, FI-2017-3-0009 and FI-2018-3-0036.

Conflicts of Interest: The authors declare no conflicts of interest.

References

1. Cattafesta, L.N., III; Sheplak, M. Actuators for active flow control. *Annu. Rev. Fluid Mech.* **2011**, *43*, 247–272. [CrossRef]
2. Corke, T.C.; Enloe, C.L.; Wilkinson, S.P. Dielectric barrier discharge plasma actuators for flow control. *Annu. Rev. Fluid Mech.* **2010**, *42*, 505–529. [CrossRef]
3. Guyot, D.; Bobusch, B.; Paschereit, C.O.; Raghu, S. Active combustion control using a fluidic oscillator for asymmetric fuel flow modulation. In Proceedings of the 44th AIAA/ASME/SAE/ASEE Joint Propulsion Conference & Exhibit, Hartford, CT, USA, 21–23 July 2008; p. 4956.
4. Raman, G.; Packiarajan, S.; Papadopoulos, G.; Weissman, C.; Raghu, S. Jet thrust vectoring using a miniature fluidic oscillator. *Aeronaut. J.* **2005**, *109*, 129–138. [CrossRef]
5. Seele, R.; Tewes, P.; Woszidlo, R.; McVeigh, M.A.; Lucas, N.J.; Wygnanski, I.J. Discrete sweeping jets as tools for improving the performance of the V-22. *J. Aircr.* **2009**, *46*, 2098–2106. [CrossRef]
6. Cerretelli, C.; Kirtley, K. Boundary layer separation control with fluidic oscillators. *J. Turbomach.* **2009**, *131*, 041001. [CrossRef]
7. Culley, D.E.; Bright, M.M.; Prahst, P.S.; Strazisar, A.J. Active flow separation control of a stator vane using embedded injection in a multistage compressor experiment. *J. Turbomach.* **2004**, *126*, 24–34. [CrossRef]
8. Hossain, M.A.; Prenter, R.; Lundgreen, R.K.; Ameri, A.; Gregory, J.W.; Bons, J.P. Experimental and numerical investigation of sweeping jet film cooling. *J. Turbomach.* **2018**, *140*, 031009. [CrossRef]
9. Seifert, A.; Stalnov, O.; Sperber, D.; Arwatz, G.; Palei, V.; David, S.; Dayan, I.; Fono, I. Large trucks drag reduction using active flow control. In *The Aerodynamics of Heavy Vehicles II: Trucks, Buses, and Trains*; Springer: Berlin/Heidelberg, Gemany, 2009; pp. 115–133.
10. Raman, G.; Raghu, S. Cavity resonance suppression using miniature fluidic oscillators. *AIAA J.* **2004**, *42*, 2608–2612. [CrossRef]

11. Uzol, O.; Camci, C. Experimental and computational visualization and frequency measurements of the jet oscillation inside a fluidic oscillator. *J. Vis.* **2002**, *5*, 263–272. [CrossRef]
12. Huang, R.F.; Chang, K.T. Fluidic oscillation influences on v-shaped bluffbody flow. *AIAA J.* **2005**, *43*, 2319–2328. [CrossRef]
13. Ostermann, F.; Woszidlo, R.; Nayeri, C.; Paschereit, C.O. Experimental comparison between the flow field of two common fluidic oscillator designs. In Proceedings of the 53rd AIAA Aerospace Sciences Meeting, Kissimmee, FL, USA, 5–9 January 2015; p. 0781.
14. Gokoglu, S.; Kuczmarski, M.; Culley, D.; Raghu, S. Numerical studies of a supersonic fluidic diverter actuator for flow control. In Proceedings of the 5th Flow Control Conference, Chicago, IL, USA, 28 June–1 July 2010; p. 4415.
15. Gokoglu, S.; Kuczmarski, M.; Culley, D.; Raghu, S. Numerical studies of an array of fluidic diverter actuators for flow control. In Proceedings of the 41st AIAA Fluid Dynamics Conference and Exhibit, Honolulu, HI, USA, 27–30 June 2011; p. 3100.
16. Krüger, O.; Bobusch, B.C.; Woszidlo, R.; Paschereit, C.O. Numerical Modeling and Validation of the Flow in a Fluidic Oscillator. In Proceedings of the 21st AIAA Computational Fluid Dynamics Conference, San Diego, CA, USA, 24–27 June 2013; p. 3087.
17. Bobusch, B.C.; Woszidlo, R.; Bergada, J.; Nayeri, C.N.; Paschereit, C.O. Experimental study of the internal flow structures inside a fluidic oscillator. *Exp. Fluids* **2013**, *54*, 1559. [CrossRef]
18. Gaertlein, S.; Woszidlo, R.; Ostermann, F.; Nayeri, C.; Paschereit, C.O. The time-resolved internal and external flow field properties of a fluidic oscillator. In Proceedings of the 52nd Aerospace Sciences Meeting, National Harbor, MD, USA, 13–17 January 2014; p. 1143.
19. Woszidlo, R.; Ostermann, F.; Nayeri, C.; Paschereit, C. The time-resolved natural flow field of a fluidic oscillator. *Exp. Fluids* **2015**, *56*, 125. [CrossRef]
20. von Gosen, F.; Ostermann, F.; Woszidlo, R.; Nayeri, C.; Paschereit, C.O. Experimental investigation of compressibility effects in a fluidic oscillator. In Proceedings of the 53rd AIAA Aerospace Sciences Meeting, Kissimmee, FL, USA, 5–9 January 2015; p. 0782.
21. Pandey, R.J.; Kim, K.Y. Numerical modeling of internal flow in a fluidic oscillator. *J. Mech. Sci. Technol.* **2018**, *32*, 1041–1048. [CrossRef]
22. Seo, J.; Zhu, C.; Mittal, R. Flow Physics and Frequency Scaling of Sweeping Jet Fluidic Oscillators. *AIAA J.* **2018**, *56*, 1–12. [CrossRef]
23. Wu, Y.; Yu, S.; Zuo, L. Large eddy simulation analysis of the heat transfer enhancement using self-oscillating fluidic oscillators. *Int. J. Heat Mass Transf.* **2019**, *131*, 463–471. [CrossRef]
24. Kara, K. Numerical study of internal flow structures in a sweeping jet actuator. In Proceedings of the 33rd AIAA Applied Aerodynamics Conference, Dallas, TX, USA, 22–26 June 2015; p. 2424.
25. Metka, M.; Gregory, J.; Sassoon, A.; McKillen, J. Scaling considerations for fluidic oscillator flow control on the square-back Ahmed vehicle model. *SAE Int. J. Passeng. Cars-Mech. Syst.* **2015**, *8*, 328–337. [CrossRef]
26. Shmilovich, A.; Yadlin, Y.; Whalen, E.A. Numerical Simulations of an Airplane with an Active Flow Control System. In Proceedings of the 8th AIAA Flow Control Conference, Atlanta, GA, USA, 25–29 June 2018; p. 3929.
27. Slupski, B.Z.; Kara, K. Effects of Geometric Parameters on Performance of Sweeping Jet Actuator. In Proceedings of the 34th AIAA Applied Aerodynamics Conference, Washington, DC, USA, 13–17 June 2016; p. 3263.
28. Aram, S.; Lee, Y.T.; Shan, H.; Vargas, A. Computational Fluid Dynamic Analysis of Fluidic Actuator for Active Flow Control Applications. *AIAA J.* **2017**, *56*, 1–10. [CrossRef]
29. Ostermann, F.; Woszidlo, R.; Nayeri, C.N.; Paschereit, C.O. Properties of a sweeping jet emitted from a fluidic oscillator. *J. Fluid Mech.* **2018**, *857*, 216–238. [CrossRef]
30. Woszidlo, R.; Ostermann, F.; Schmidt, H.J. Fundamental properties of fluidic oscillators for flow control applications. *AIAA J.* **2019**, *57*, 978–992. [CrossRef]
31. Ostermann, F.; Woszidlo, R.; Nayeri, C.N.; Paschereit, C.O. The interaction between a spatially oscillating jet emitted by a fluidic oscillator and a cross-flow. *J. Fluid Mech.* **2019**, *863*, 215–241. [CrossRef]
32. Tomac, M.N.; Sundström, E. Adjustable Frequency Fluidic Oscillator with Supermode Frequency. *AIAA J.* **2019**, *57*, 1–11. [CrossRef]
33. Tomac, M.N.; Gregory, J.W. Phase-synchronized fluidic oscillator pair. *AIAA J.* **2018**, *57*, 670–681. [CrossRef]

34. Vatsa, V.; Koklu, M.; Wygnanski, I. Numerical simulation of fluidic actuators for flow control applications. In Proceedings of the 6th AIAA Flow Control Conference, New Orleans, LA, USA, 25–28 June 2012; p. 3239.
35. Wang, S.; Baldas, L.; Colin, S.; Orieux, S.; Kourta, A.; Mazellier, N. Experimental and numerical study of the frequency response of a fluidic oscillator for active flow control. In Proceedings of the 8th AIAA Flow Control Conference, Washington, DC, USA, 13–17 June 2016; p. 4234.
36. Bobusch, B.C.; Woszidlo, R.; Krüger, O.; Paschereit, C.O. Numerical Investigations on Geometric Parameters Affecting the Oscillation Properties of a Fluidic Oscillator. In Proceedings of the 21st AIAA Computational Fluid Dynamics Conference, San Diego, CA, USA, 24–27 June 2013; p. 2709.
37. Hirsch, D.; Gharib, M. Schlieren Visualization and Analysis of Sweeping Jet Actuator Dynamics. *AIAA J.* **2018**, *56*, 2947–2960. [CrossRef]
38. Staats, M.; Löffler, S.; Ebert, C.; Grund, T.; Weiss, J. A Fluidic Device for Active Flow Control: Simulation vs. Experiment with Emphasis on Application. In Proceedings of the 2018 Applied Aerodynamics Conference, Atlanta, GA, USA, 25–29 June 2018; p. 3336.
39. Tesař, V. *Pressure-Driven Microfluidics*; Artech House: Boston, MA, USA; London, UK, 2007.
40. Tesař, V. Taxonomic trees of fluidic oscillators. *EPJ Web Conf. EDP Sci.* **2017**, *143*, 02128. [CrossRef]
41. Gregory, J.; Tomac, M.N. A review of fluidic oscillator development. In Proceedings of the 43rd AIAA Fluid Dynamics Conference, San Diego, CA, USA, 24–27 June 2013; p. 2474.

applied sciences

MDPI

Article

Fluidic Oscillators, the Effect of Some Design Modifications

Masoud Baghaei and Josep M. Bergada *

Department of Fluid Mechanics, Universitat Politècnica de Catalunya, 08034 Barcelona, Spain; masoud.baghaei@upc.edu

* Correspondence: josep.m.bergada@upc.edu; Tel.: +34-937398771

Received: 12 February 2020; Accepted: 17 March 2020; Published: 20 March 2020

Abstract: The number of applications where fluidic oscillators are expected to be used in the future, is raising sharply, then their ability of interacting with the boundary layer to modify forces on bluff bodies, enhancing heat transfer or decreasing noise generation, are just few of the applications where fluidic oscillators can be used. For each application a particular pulsating frequency and amplitude are required to minimize/maximize the variable under study, force, Nusselt number, etc. For a given range of Reynolds numbers, fluidic oscillators present a linear relationship between the output frequency and the incoming fluid flow, yet it appears the modification of the internal fluidic oscillator geometry may affect this relation. In the present paper and for a given fluidic oscillator, several performance parameters will be numerically evaluated as a function of different internal modifications via using 3D-CFD simulations. The paper is also evaluating the relation between the momentum applied to the mixing chamber incoming jet and the oscillator output characteristics. The evaluation is based on studying the output mass flow frequency and amplitude whenever several internal geometry parameters are modified. The geometry modifications considered were: the mixing chamber inlet and outlet widths, and the mixing chamber inlet and outlet wall inclination angles. The concept behind this paper is, to evaluate how much the fluidic oscillator internal dimensions affect the device main characteristics, and to analyze which parts of the oscillator produce a higher impact on the fluidic oscillator output characteristics. For the different internal modifications evaluated, special care is taken in studying the forces required to flip the jet. The entire study is performed for three different Reynolds numbers, 8711, 16034 and 32068. Among the conclusions reached it is to be highlighted that, for a given Reynolds number, modifying the internal shape affects the oscillation frequencies and amplitudes. Any oscillator internal modification generates a much relevant effect as Reynolds number increases. Under all conditions studied, it was observed the fluidic oscillator is pressure driven.

Keywords: fluidic oscillators design; Computational Fluid Dynamics (CFD); flow control

1. Introduction

The reduction or enhancement of the lift and drag forces on any bluff-body via modifying the boundary layer employing Active Flow Control (AFC), must be regarded as a novel technology. The use of pulsating flow in (AFC) applications, allows reducing the energy required to modify the boundary layer around a given bluff body. Zero Net Mass Flux Actuators (ZNMFA) and Fluidic Oscillators (FO), are two good candidates to generate pulsating jets, the later having the advantage of employing no moving parts, therefore increasing its reliability. Although there exist few canonical shapes on (FO), it is of major interest to investigate the (FO's) performance when modifying their internal dimensions, then oscillation amplitude and frequency are expected to change. The present paper aims to bring some light to this matter. One of the initial evaluations of the fluidic oscillators

performance when modifying its internal shape, was made in 2013 by Bobusch et al. [1], they made some suggestions regarding the mixing chamber inlet width in order to modify the fluidic actuator output frequency. Vatsa et al. [2] studied, using the lattice Boltzmann method and based on the solver PowerFLOW, two different configurations of sweeping jet fluidic oscillators (FO), which were further analyzed in 2015 by Ostermann et al. [3]. The two (FO) considered, resemble the ones studied by Bobusch et al. [1] and Aram et al. [4] respectively. Velocity profiles generated by the (FO) in quiescent air were compared with experimental data, results showed that the (FO) having sharp internal corners, similar to the one employed in [1], generated an output velocity distribution much more homogeneous than the oscillator having rounded internal corners. The results from the two different configurations were compared to identify similarities and differences between the designs, suggestions of how these differences may affect applications, were made.

Woszidlo et al. [5], studied the same configuration previously evaluated by Gartlein et al. [6]. Both configurations resemble the one studied by Bobbush et al. [1], the main differences resided in the output shape. In Woszidlo et al. [5] and Gartlein et al. [6], just a single output was considered. In this new paper, Woszidlo et al. [5], focused their attention in analyzing the flow phenomena inside the mixing chamber and the feedback channels. They also observed that, the increase of the mixing chamber inlet width was tending to increase the output frequency, and rounding the feedback channels would diminish the generation of the separation bubbles on these channels.

Slupski and Kara [7], studied using 2D-URANS with the software Fluent a range of feedback channel (FC) geometry parameters, the sweeping jet actuator configuration was the same as the one analyzed by Aram et al. [4]. The effects of varying the feedback channel height and width for different mass flow rates were studied. All the simulations were performed for a fully-turbulent compressible flow, using SST k-omega turbulence model. It was found that, oscillation frequencies increased with increasing feedback channel height, up to a certain point and then remained unaffected, however, frequencies decreased by further increasing the feedback channel width.

An experimental and numerical study of a fluidic oscillator which could generate a wide range of frequencies (50–300 Hz), was studied by Wang et al. [8]. Their study focused on the oscillation frequency response for different lengths of the feedback channels, 2D compressible simulations were performed using sonicFoam with k-epsilon as turbulence model. An inverse linear relation between frequency and the length of feedback loops was observed, frequency increased when decreasing the feedback channel length.

In 2018, the same configuration previously employed by [1], although now using a single exit, was numerically evaluated in 3D at Reynolds 30000 using the SST turbulent model by Pandley and Kim [9]. Two geometry parameters, the mixing chamber inlet and outlet widths were modified. They observed a significant effect of the flow structure and the feedback channel flow rate when modifying the inlet width, negligible effects were observed when modifying the outlet width. The output frequency and amplitude effects whenever the (FC) and the mixing chamber (MC) lengths were modified, was studied using a 2D numerical model by Seo et al. [10], the fluid was considered as incompressible, the Reynolds number employed was 5000. They observed that an increase of the feedback channel length generated no modifications on the output frequency, the same observation was previously obtained by [11], in both cases the flow was defined as incompressible, being the reason why the simulations could not provide the correct information. On the other hand, the increase of the mixing chamber length, generated a clear reduction on the actuator output frequency. They defined the length scale to be employed to properly non-dimensionalize the oscillation frequency.

The present paper is presenting a numerical evaluation of the same fluidic oscillator (FO) configuration experimentally evaluated in [1]. The effects on the stagnation pressure, net momentum acting onto the jet, output mass flow and mixing chamber incoming jet inclination angle, among other parameters, are analyzed for four different internal geometry modifications, the (MC) inlet and outlet widths and the (MC) inlet and outlet wall inclination angles. Three different Reynolds numbers are considered. The four geometry modifications chosen have a considerable impact on the flow inside

the (MC) and the (FC's). The (MC) inlet width decisively affects the reverse flow in the (FC's) and the Coanda effect in the (MC), the (MC) outlet width drastically modifies the pressure inside the (MC), the (MC) inlet inclination angles, affect the Coanda effect and the bubble volume inside the (MC), finally, the (MC) outlet inclined walls drastically change the stagnation pressure in these particular walls, changing as well the (FC) dynamic pressure and amplitude.

2. Fluidic Oscillator Main Characteristics

The central part of the (FO) considered in the present study is introduced in Figure 1, the four internal geometries modified, the mixing chamber (MC) inlet and outlet widths and angles, are clearly shown. Figure 1 also introduces the positive and negative directions taken for each geometry modification.

Regardless of the configuration evaluated, an orthogonal 3D mesh with 2,242,000 cells was used to evaluate the flow at Reynolds numbers up to 16,034, for the baseline case configuration the respective maximum x+, y+ and z+ were of 1.8, 4.7 and 1.2, very similar values were obtained for the rest of the configurations. A mesh with 5,933,900 cells was used to perform all simulations at Reynolds number 32,068. The maximum values of x+, y+ and z+ obtained with this mesh and for the baseline case at Reynolds number 32,068, were of 0.9, 1.2 and 0.7, respectively. The rest of the configurations evaluated at Reynolds number 32068 generated very similar x+, y+ and z+ values. Figure 2 presents the mesh used for the simulations, showing as well the entire computational domain. The mesh independence test performed to validate the meshes used in the present paper, was presented in the authors previous paper [12], where the fluidic oscillator baseline case was analyzed for a set of different Reynolds numbers, including the largest Reynolds numbers analyzed in the present manuscript.

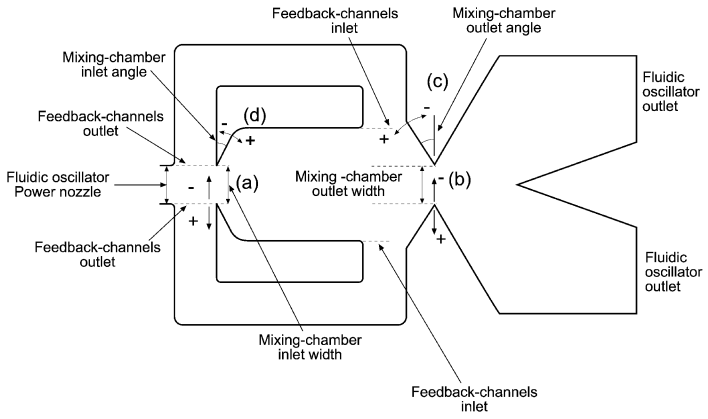

Figure 1. Fluidic oscillator mixing chamber internal dimensions modifications.

The boundary conditions employed in all simulations were, Dirichlet conditions for velocity and Neumann for pressure at the inlet. A relative pressure of 10^4 Pa and Neumann conditions for velocity were considered at the two outlets. Dirichlet boundary conditions for velocity and Neumann for pressure were set to all walls.

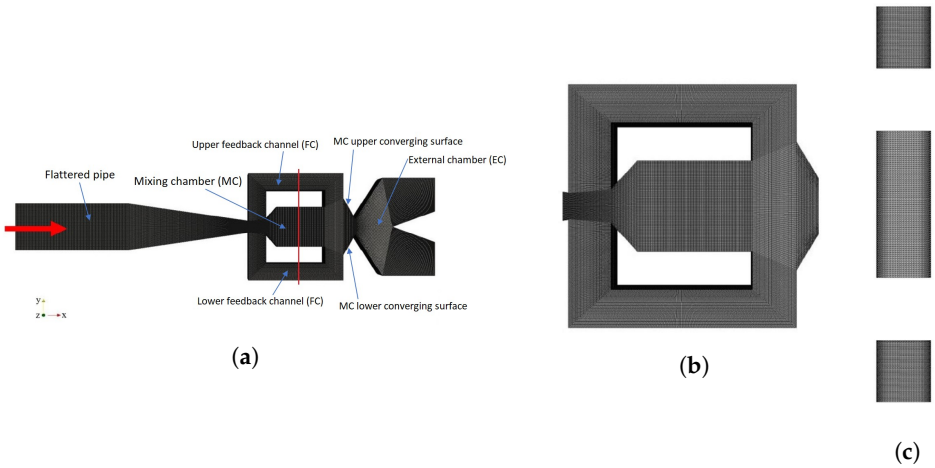

Figure 2. Grid used in the present study, (**a**) plane view, (**b**) zoom view, (**c**) side view of the mesh at the center of the mixing chamber, see the vertical line.

In the present study the flow was considered as turbulent, incompressible and isothermal, all simulations were three dimensional. The fluid used was water. Fluid dynamic viscosity was chosen to be 1.003×10^{-3} Kg/(m s), the fluid density was 998.2 Kg/m^3. The turbulence model used was the DDES, which is a hybrid RANS-LES model, since according to the research undertaken by [4], this model generates a very close approach to the experimental results. The Spalart-Allmaras turbulent model was used for the RANS approach, while the Subgrid Scale (SGS) model was employed as the LES one. The parameter defining which turbulent model RANS-LES needs to be used is the distance between a given cell and the nearest wall, d. In the DES model, When $d < (C_{DES}\Delta)$, being $C_{DES} = 0.65$ a constant of the model and Δ the generic cell length, the RANS approach was used, and whenever $d > (C_{DES}\Delta)$ then the SGS model was employed. The DDES model is a modified version of the DES one, in which a new formulation with a filter function f_d was introduced to avoid the so called grid-induced separation (GIS). In the DDES model, the switching mechanism between RANS and LES is not only dependent on the wall distance and grid spacing but also on the flow itself. The filter function f_d is designed to take a value of 0 in the region where the boundary layer is attached, under this conditions the RANS model is used, and a value of 1 in the region where the flow is separated, under these conditions the switching criteria to employ whether the RANS or the LES model, is the one just defined for the DES model. The different constants involved in the turbulent models are, $c_{b1} = 0.1355$; $c_{b2} = 0.622$; $\sigma = \frac{2}{3}$; $\kappa = 0.41$; $c_{w1} = \frac{c_{b1}}{\kappa^2} + \frac{1+c_{b2}}{\sigma}$; $c_{w2} = 0.3$; $c_{w3} = 2$; $c_{v1} = 7.1$. Further information of the DDES model mathematical background employed along with the different constants involved is to be found in [13–17].

The software OpenFOAM was considered for all 3D simulations, finite volume method is the approach OpenFOAM uses to discretize Navier Stokes equations. Inlet turbulence intensity was set to 0.05% in all cases, Pressure Implicit with Splitting Operators (PISO), was used to solve the Navier Stokes equations, the time step being of 10^{-6} s, spatial discretization was set to second order.

The different velocities evaluated and defined at the inlet of the flattered pipe where the section was $10.3 \times 3.25 = 33.475$ mm^2, see Figure 2a, were 0.671 m/s, 1.2347 m/s, and 2.46 m/s, being the corresponding Reynolds numbers 8711, 16034 and 32068 respectively. The Reynolds numbers were based on the hydraulic diameter D_h and the fluid velocity V at the power nozzle, the same location was already used by [1]. One of the main characteristics of a fluidic oscillator is its linear output mass flow frequency behavior versus the inlet mass flow, usually represented as a function of the Reynolds number. The results obtained from the first four Reynolds numbers were used for comparison with the experimental results obtained by [1]. This comparison is presented in Table 1, further validating the 3D-CFD model introduced. Notice that in Table 1 the results obtained using two more Reynolds numbers 11152, 13593, are also presented. To compare the results, the Reynolds numbers presented in Table 1 were chosen to be exactly the ones employed by [1] in their experimental work. In fact

the code validation was previously presented in [12], see Figure 3 of this previously published paper. Another point which requires further discussion is the possible necessity of using a buffer zone. Also in the previously published paper [12] and for the baseline case at Reynolds number 16034, the fluidic oscillator outlet mass flow frequency obtained with and without a buffer zone was compared. The use of a buffer zone, involving an increase of over 9 million cells in the domain, gave an outlet frequency 1.4% smaller than the one obtained without a buffer zone. When considering the number of 3D cases to be studied in the present paper, and the small variation of the output frequency obtained when using a buffer zone, the authors decided not to implement the buffer zone in the present simulations.

Table 1. Comparison experimental and simulated results.

Reynolds Number	8711	11152	13593	16034	32068
(CFD) Mass Flow Output Frequency (Hz)	12.92	15.89	19.5	22.7	40.43
Eperimental Output Frequency (Hz) [1]	12.9	15.5	18.7	21.8	-
Error in %	0.15	2.5	4.2	4.1	-

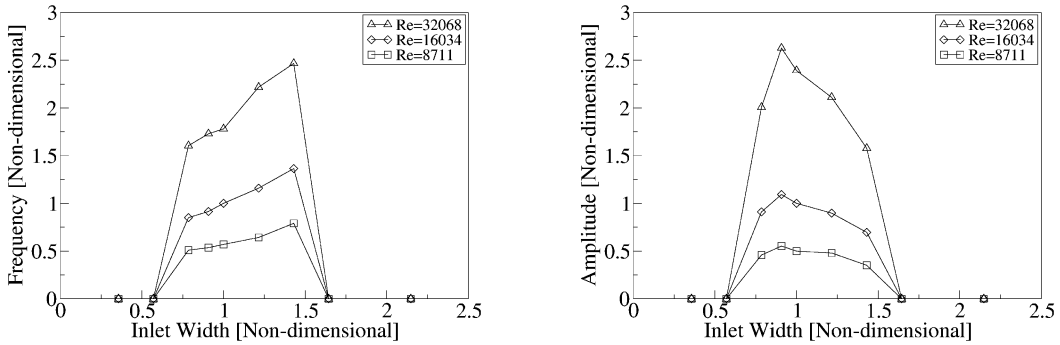

(**a**) (**b**)

Figure 3. Fluidic oscillator output mass flow frequency (**a**) and peak to peak amplitude (**b**) as a function of the mixing chamber inlet width and for three different Reynolds numbers, 8711, 16034 and 32068.

To proceed with the non-dimensionalization and in order to generate graphs showing values around unity, the following dimensional parameters were employed. All dimensional parameters are based on values obtained for the baseline oscillator case at Reynolds number 16034. The (FO) outlet mass flow, was non-dimensionalised using the maximum value of the mass flow measured at one of the (FO) outlets. The maximum inclination angle of the main jet at the mixing chamber inlet, was used to non-dimensionalise the jet inclination angle at the mixing chamber inlet. The maximum momentum measured at one of the (FC) outlets, was employed to non-dimensionalise the momentum acting over the jet. The maximum value of the stagnation pressure measured at the mixing chamber outlet converging walls, was defined as the characteristic pressure for non dimensionalization. The characteristic length was chosen to be the oscillator's power nozzle hydraulic diameter D_h, as already employed in [1]. The fluid velocity at the (FO) power nozzle was employed as the dimensional characteristic velocity. The Reynolds number definition used to characterize the main flow, was: $Re = (\rho V D_h)/\mu$, where μ is the dynamic viscosity of the fluid. Time was maintained dimensional in all graphs.

3. Geometry Modifications Considered

The present study, is based on analyzing the effect of several geometry modifications on the (FO) outlet dynamic mass flow, frequency and amplitude. Four different modifications were evaluated, see Figure 1 and Table 2. Fluidic oscillator (MC) inlet width (a), was the first modification to be computed.

Eight different widths were analyzed, the maximum and minimum width ratio was respectively 2.14 and 0.35. Width ratio was defined as the generic inlet width divided by the original one. The inlet width was decreased by 64.4% and increased by 114.7%.

The (MC) outlet width (b), was respectively increased and decreased by a ratio of 1.82 and 0.17. Outlet width ratio was defined as the generic outlet width divided by the original one. A total of 8 different outlet width ratios were analyzed. The outlet width increase and decrease was of 82.3%. The (MC) outlet angle (c), was progressively increased and decreased versus its original value until reaching an outlet angular ratio respectively of 2 and 0.63, the definition of the outlet angular ratio is similar to the previous definitions already given. A total of 8 different outlet angular ratios were studied. The outlet angle maximum increase and decrease was respectively of 100% and 36.6%. Finally, the (MC) inlet internal angle (d) was as well modified, two different angles which increase versus the original one was respectively of 74.3%, and 93% were evaluated. It is interesting to mention that the inlet angles are directly linked with the position, shape an intensity of the Coanda vortices generated alternatively at both sides of the (MC). This angles also modify the shape and dimension of the (MC) bubble generated alternatively on both sides of the main jet, and according to [5,10,11] among others, there is a direct link between the (MC) bubble volume increase and the feedback channels mass flow. Table 2 summarizes all the different internal geometry modifications performed. All geometry modifications presented were evaluated for three different Reynolds numbers, 8711, 16034 and 32068.

Table 2. List of the different geometry ratios evaluated.

Inlet Width/Reference Inlet Width	Outlet Width/Reference Outlet Width	Outlet Angle/Reference Outlet Angle	Inlet Angle/Reference Inlet Angle
0.35	0.17	0.63	1
0.57	0.38	0.82	1.74
0.78	0.58	1	1.93
0.9	0.79	1.16	
1	1	1.31	
1.21	1.2	1.44	
1.42	1.41	1.56	
1.64	1.61	1.66	
2.14	1.82	2	

4. Momentum Acting on the Jet Entering the Mixing Chamber

In order to carefully evaluate the forces acting onto the main jet lateral surfaces, the momentum acting on any of the (FC) outlets is employed. The momentum is characterized by two terms, the (FC) mass flow and the static pressure at this particular location, Equation (1) defines each of the two terms.

$$M = \dot{m}_{out} * V_{out} + P_f * S_{out} = \dot{m}_{out}^2 / (S_{out} * \rho) + P_f * S_{out} \quad (1)$$

where, $\dot{m}_{out}, V_{out}, S_{out}$ and P_f, are respectively the instantaneous mass flow defined as $\dot{m} = \int_s \rho \vec{V} \vec{ds}$, the spatial averaged fluid velocity, the (FC) outlet surface and the pressure instantaneously appearing at any of the (FC) outlets, ρ is the fluid density. The net momentum acting on the jet entering the (MC), is obtained when considering the forces defined by Equation (1) acting instantaneously on both (FC) outlets. The net momentum acting on the jet is composed by two terms, the net momentum due to the pressure term, which considers at each instant the pressure acting on both (FC) outlets, and the net momentum generated by the mass flow flowing along the (FC) and acting instantaneously on both (FC) outlets. At this point it is important to clarify that the momentum generated by the (FC) mass flow was obtained using the instantaneous mass flow to the power 2, divided by the section of the feedback channel and the fluid density, see the second term of Equation (1).

In the following sections and thanks to the simulations undertaken, it will be clarified, for the different geometry modifications considered, which is the role played by the net momentum due to the mass flow transferred across the (FC). This net momentum will be compared with the role undertaken by the net momentum due to the pressure difference acting onto the jet at the (FC) outlets. The role of the Coanda effect generated alternatively on both sides of the mixing chamber will also be investigated, in fact, this point will be particularly addressed when evaluating the effect of the (MC) inlet angle.

5. Results

5.1. Modifying the (Mc) Inlet Width

The first modification to be considered is the variation of the mixing chamber inlet width. Figure 3 introduces the variation of (FO) output mass flow peak to peak amplitude and frequency as a function of the different inlet widths evaluated. The first thing to notice is that whenever the inlet width falls below a minimum or is higher than a maximum value, the actual (FO) is not producing any outgoing frequency, see Figure 3a. The explanation why there is no flow oscillation when the actuator inlet width falls to a minimum, is based on the fact that, the mixing chamber incoming jet borders impinge onto the feedback channels (FC's) outlet internal vertical walls, creating a flow stream in the (FC's) which goes from left to right, from upstream to downstream, and along both (FC's) at the same time. At both (FC's) outlet internal vertical walls, a stagnation pressure point is generated, from this point, pressure waves are generated and sent from the feedback channels outlets to the inlets. The combination of these two effects prevents any feedback flow to move from downstream to upstream. On the other hand, when the mixing chamber inlet width is too large, a gap appears between the incoming jet and the mixing chamber inlet width borders. This small gap is enough to prevent a pressure increase at the (FC's) outlets, then it allows the fluid coming up from the (FC) inlet, to escape through this gap towards the mixing chamber.

In Figure 3b, is presented the effect of modifying the inlet width on the (FO) outlet mass flow peak to peak amplitude. As previously presented, for inlet widths exceeding a limit in any direction, whether too big or too small, the flow stops oscillating and the amplitude decays to zero. For the intermediate values it is seen that the amplitude is initially being highly affected by the inlet width, but as the width keeps increasing the amplitude decreases. It is also seen that the amplitude tendency is opposed to that of the frequency, small frequencies are linked with high oscillation amplitudes and vice versa. The reason why this is happening, it is clearly seen when applying the mass conservation equation between the (FO) inlet and outlets. For the present modification, when high widths are considered, the jet entering the mixing chamber (MC), suffers a relatively small oscillation inside the mixing chamber (MC), causing a small variation of amplitude at the oscillator exit. As the mixing chamber (MC) inlet width decreases, the jet oscillation amplitude inside the mixing chamber increases, the jet deflection angle at the mixing chamber inlet and outlet also increases and so does the fluidic oscillator output amplitude, see Figures 3–5. Based on the results presented in Figure 3, it can also be stated that the effects on output frequency and amplitude, are more relevant as the Reynolds number increases, but the trend already presented remains the same. The threshold at which the oscillation stops, appears to be rather independent of the Reynolds number.

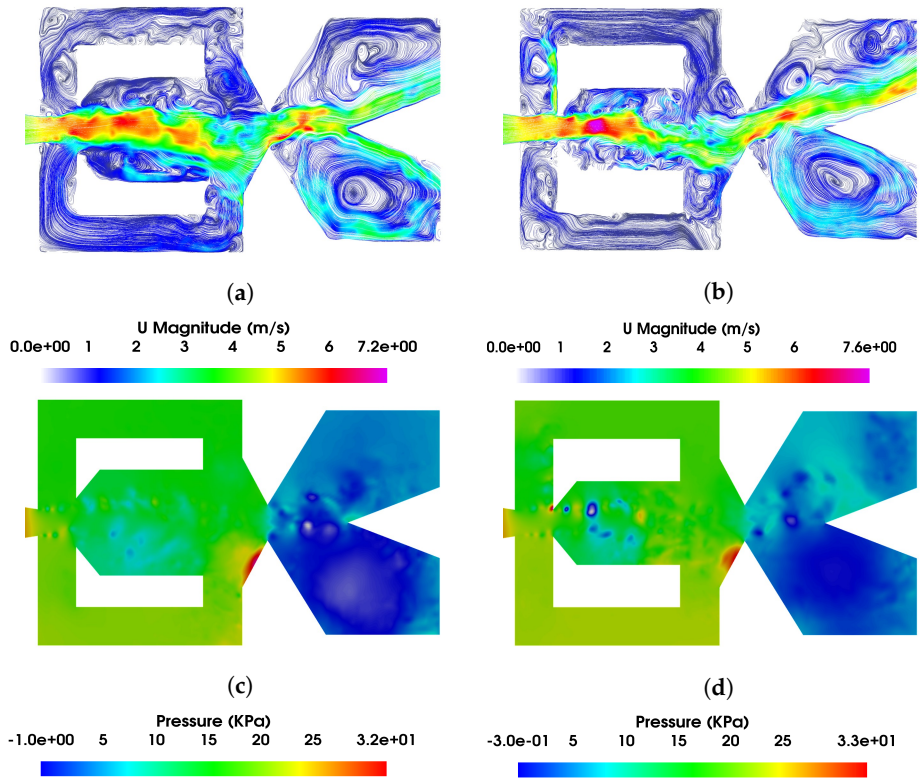

Figure 4. Fluidic oscillator internal velocity field (**a**,**b**), and pressure magnitude (**c**,**d**). Maximum inlet width (**a**,**c**), minimum inlet width (**b**,**d**). Reynolds number 16034.

Figure 4 introduces the flow field and pressure distribution inside the (FO), for the minimum and maximum (MC) inlet widths at which oscillation still appears, the Reynolds number is 16034. For the maximum inlet width, Figure 4a,c, the jet bending inside the (MC) is supported by the low pressure below the jet generated by the Coanda effect, see Figure 4c, at the external chamber the jet flows reattached to the surface of the wedge, generating two alternative vortices of nearly the same size on both sides of the external chamber. From Figure 5a, it is observed that no reverse flow appears at the (FO) upper outlet, see the curve characterizing the highest inlet width. Regarding the pressure distribution, the pressure is very much the same along the entire (MC), very small pressure fluctuations appear on the (FC's), alternatively pressurizing one (FC) or the other. The origin of the pressure waves, responsible of the (FC's) periodic pressurization, are the stagnation pressure points appearing alternatively at the (MC) outlet converging walls, see the red spots observed in Figure 4c,d.

At small inlet widths, Figure 4b,d, the (MC) incoming jet impinges alternatively at the (FC's) outlet internal vertical walls, generating an stagnation pressure point from which pressure waves are being sent alternatively from both (FC) outlets to the inlets, see the small red spot observed at the upper feedback channel outlet, Figure 4d. Reverse flow, from (FC) outlets to inlets is therefore generated, although for this particular case, the oscillation still exists. This is because the stagnation pressure at the (MC) converging walls, is acting over a surface about 20 times bigger than the one affected by the pressure at the (FC's) outlet internal vertical walls, and despite the fact the maximum pressure at the (MC) outlet converging walls, is for the present case, about 22% smaller than the maximum pressure existing at the (FC's) outlet internal walls, the time the stagnation pressure is acting on the (MC) converging walls, is 6.4 times longer than the time the stagnation pressure point appears at the (FC) outlet internal vertical walls, being this time difference along with the area the stagnation pressure acts, what maintains the oscillation. Although no figure related is presented in the present manuscript, if the inlet width would be further reduced, the stagnation pressure points at the (FC's) outlet vertical walls, would be appearing simultaneously on both vertical walls, generating reverse flow on both

feedback channels at the same time. Pressure waves would also be continuously transfered from the (FC's) upstream to downstream. Under these particular conditions oscillation would stop.

The evaluation of the dynamic values of the, net-momentum acting onto the jet entering the mixing chamber, the pressure at the (MC) outlet converging walls, the (MC) inlet inclination angle, the (FC's) mass flow and the (FO) output flow, greatly helps in understanding the (FO) dynamic performance. Figure 5 introduces the non-dimensional dynamic values of the mass flow through one of the (FO) outlets, the lower (FC) mass flow, the stagnation pressure at the (MC) outlet lower convergent wall, the net-momentum acting on the (MC) incoming jet and the (MC) inlet jet inclination angle. The Reynolds number was kept constant at 16,034. In each graph it is presented the non-dimensional dynamic value obtained for the baseline case, original actuator, and the corresponding ones characterizing the maximum and minimum inlet widths evaluated at which pulsating flow was observed. The first thing to notice is, that the dynamic stagnation pressure appearing alternatively at the (MC) converging walls, Figure 5c, is driving the oscillation, the rest of the graphs presented simply follow these pressure pulsations. From the oscillator upper outlet mass flow graph, Figure 5a, it is observed that the mass flow amplitude is directly linked with the reverse flow appearing at the (FO) outlets, the higher the reverse flow the higher the mass flow outlet amplitude, large reverse flows are associated to small inlet widths. This direct relationship is obvious when considering that the incoming (FO) mass flow is constant and given by the inlet boundary conditions, and at each instant, the mass flow through the two (FO) outlets must be the same as the inlet mass flow, the fluid is considered as incompressible. Therefore, if at some particular time, reverse flow appears at one of the (FO) outlets, the (FO) mass flow amplitude must increase to fulfill the continuity equation at each time instant.

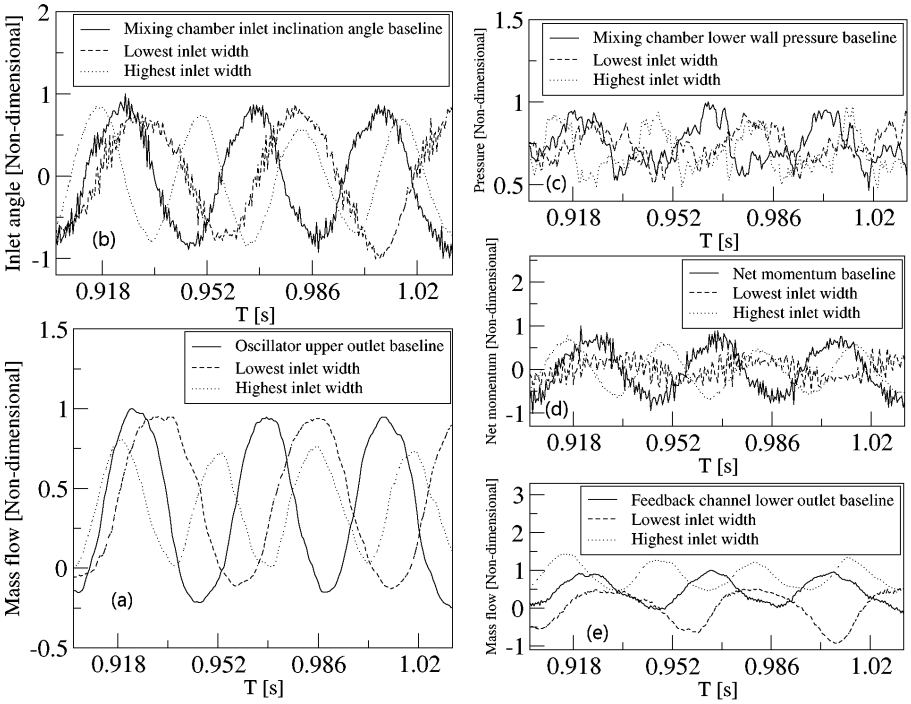

Figure 5. Dynamic effects of the (MC) inlet width modification on the main flow parameters, Reynolds number 16034. Each graph presents three non-dimensional curves characterizing results from the baseline, the lowest inlet width and the highest inlet width cases, and as a function of the dimensional time. In figure (**a**) the mass flow across the upper oscillator outlet is presented. Figure (**b**) introduces the temporal variation of the (MC) inlet inclination angle. Figure (**c**) presents the pressure at the (MC) lower inclined wall. The net momentum acting on the lateral sides of the main jet is presented in figure (**d**). Figure (**e**) characterizes the mass flow at the lower feedback channel outlet.

When observing the effects of the inlet width on the (FC's), Figure 5e, it is seen that, at small inlet widths the average mass flow is about zero, the flow inside the (FC's) is moving in both directions, yet the mass flow entering the (FC) outlet, reverse or negative flow, appears to be higher than the flow leaving such surface. If the inlet width would be further decreased, the reversed flow would keep increasing, eventually stopping the oscillation. As the inlet width increases, the mass flow inside the (FC's), although periodic, has a positive average value, meaning, there is a net mass flow moving from the feedback channels inlet to the outlet, at high inlet widths there is no reverse flow in the (FC's). The reason why at small inlet widths there is reverse flow in the (FC's), is the small stagnation pressure points generated alternatively at the (FC's) outlet internal vertical walls.

It is also relevant to highlight that, the peak to peak amplitude of the net momentum driving the jet oscillations inside the mixing chamber, is particularly small when the lowest inlet width is employed, Figure 5d, the jet is prone to fluctuate under these conditions, therefore a small pressure difference at the (FC's) outlets is sufficient to flip the jet. The jet oscillation amplitude inside the (MC) appears not to be affected by this fact, then the amplitude is higher than the one appearing at highest inlet widths. In other words, small inlet widths require small net momentums to flip the jet and the jet oscillation amplitude inside the mixing chamber is maximum. The (MC) incoming jet inclination angle, Figure 5b, suffers a reduction in the peak to peak amplitude of about 4.6% when comparing the maximum and minimum inlet widths, for the same conditions, the variation of the outlet mass flow amplitude, is about 16%. It appears the oscillation inside the (MC) is delimited by the (MC) upper and lower internal horizontal walls.

To properly understand the forces acting on the main jet lateral sides, the pressure and the mass flow terms of the net momentum acting on the main jet lateral sides are compared for the lowest, baseline and highest inlet widths, see Figure 6. Regardless of the inlet width studied, the pressure term of the net-momentum is much larger than the net-momentum mass flow term, indicating that the (FO) is pressure driven. Based on their observations and studying two different configurations of (FO), wu et al. [18] reached the same conclusion, although they could not bring a clear prove of it. From Figure 6, it is also important to realize that at low inlet widths, the pressure term of the net momentum is particularly scattered, as previously explained under these conditions in any of the feedback channels there is reverse flow and pressure waves travel in opposite directions.

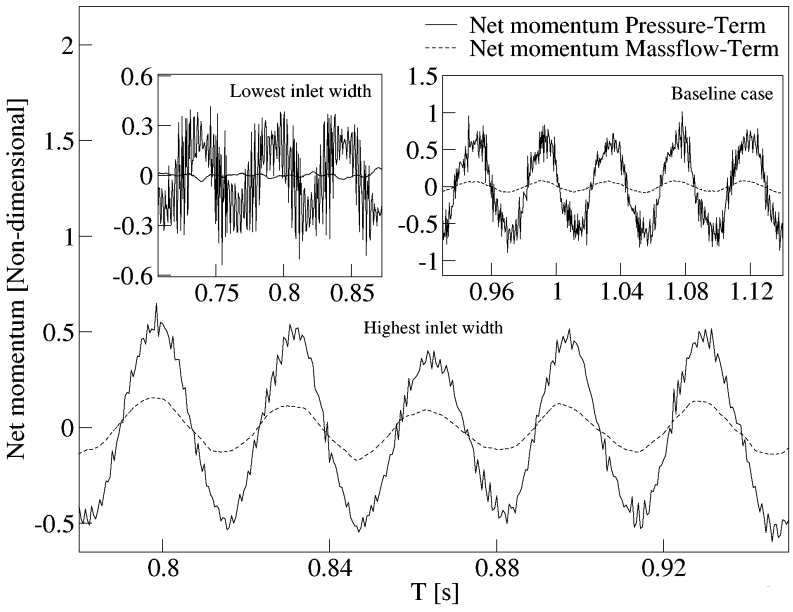

Figure 6. Comparison of the pressure and mass flow terms of the net-momentum and for three characteristic inlet widths, Reynolds number 16034.

From the dimensional temporal pressure plots at the (FC's) outlets, not presented in Figure 5, and when comparing the highest and smallest inlet widths studied, it was observed that the average static pressure at both (FC) outlets, decreased about 3000 Pa when the highest inlet width was used. Regarding the pressure fluctuation at both (FC) outlets, when the lowest inlet width was employed, the pressure was at any time, almost identical on both feedback channel outlets. While when the inlet width was maximum, the maximum pressure difference between the two (FC) outlets increased to about 2000 Pa. From the results obtained, it can be stated that at higher inlets widths, a higher net momentum onto the mixing chamber incoming jet lateral sides is required to bend the jet towards the opposite direction and therefore generate flapping. This phenomenon is understood when realizing that at small inlet widths, the Coanda effect helps in generating the required pressure difference inside the mixing chamber, to flip the incoming jet.

As Reynolds number increases to 32,064, there is an increase of the average pressure across the entire (MC) and therefore at the (FC's) outlets. The peak to peak amplitude of the mass flow inside the feedback channels, also increases. This is because the stagnation pressure is likely to increase with the velocity increase $P_0 = \rho V^2/2$. At Reynolds number 32,064 and for the lowest inlet width evaluated, the feedback channel mass flow reaches higher negative values than at Reynolds 16,034, but its average value remains quite constant and close to zero. In other words, at high Reynolds numbers, a higher net momentum acting on the (MC) incoming jet is required, to produce the jet flapping. The effect of Reynolds number on all (FO) dynamic parameters studied is presented in the last section of the paper.

5.2. Modifying (Mc) Outlet Width

The second dimensional evaluation undertaken consisted in analyzing the effect of modifying the mixing chamber outlet width. Figure 7, introduces the results obtained for the three Reynolds numbers studied. The first thing to observe, is that, an outlet width increase involves a reduction of the (FO) output frequency and amplitude, such reduction is more relevant as the Reynolds number increases. For example, at Reynolds 8711 and when comparing the values of the maximum and minimum outlet widths evaluated, the maximum decrease in frequency and amplitude was of about 7% and 60% respectively. At Reynolds 32,068, the respective decrease of frequency and amplitude was about 9% and 74%. In other words, the range of frequencies and amplitudes a given fluidic oscillator can produce, when modifying the outlet width, increases with the Reynolds number increase. The variation of the outlet width affects mostly the (FO) outlet amplitude. A point to consider when comparing Figures 3 and 7, is that the increase of the inlet width was bringing an increase in frequency and a decrease in amplitude, while an increase of outlet width generates a decrease in outlet frequency and amplitude. This opposite effect needs to be understood when evaluating the velocity fields under these four extreme conditions, these instantaneous velocity and pressure fields are presented in Figure 8.

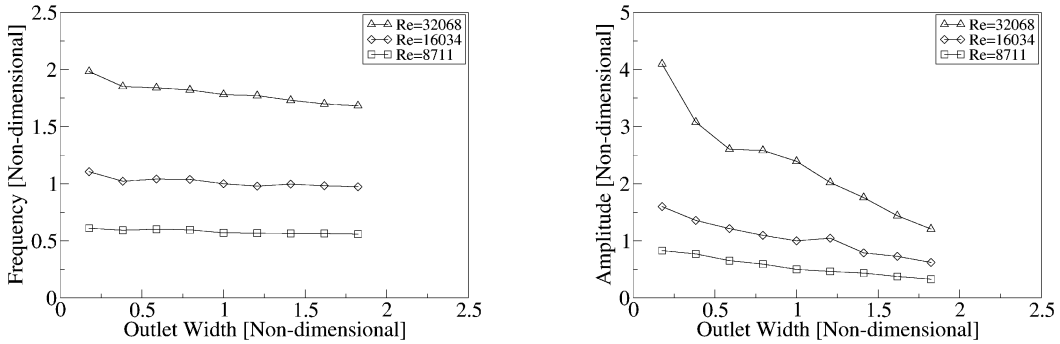

(**a**) (**b**)

Figure 7. Fluidic oscillator output mass flow frequency (**a**) and peak to peak amplitude (**b**) as a function of the mixing chamber outlet width and for three different Reynolds numbers, 8711, 16034 and 32068.

Figure 8a,b, show the velocity vectors magnitude inside the oscillator for the highest and lowest outlet widths evaluated. Notice that when the (MC) outlet width is minimum, the velocity of the jet leaving the external chamber is maximum, more than four times the maximum velocity found for the rest of the cases studied in this paper. The average pressure in the (MC) is about nineteen times higher than for the rest of the cases studied. The fluid is pressurized due to the restriction effect caused by the small outlet width. The fluid stiffness in the (MC) and therefore its dynamic response is particularly high, explaining why high frequencies are linked to small outlet widths. At the (EC) the pressure is particularly low, see Figure 8d, in fact the relative negative pressure is of about 120 KPa, which is physically not possible and in reality shows that for small outlet widths cavitation is likely to appear at the (EC). Under these conditions, at the (FO) outlets, the section used by the flow to leave the oscillator is being reduced, leaving a large part of the outlet section in which reverse flow exists, huge spatial velocity differences are to be seen at the (FO) outlets. As a result, high (FO) outlet mass flow amplitudes are expected.

Figure 8c shows, for the highest outlet width studied, there is a low pressure area generated below the jet due to the Coanda effect, it can also be seen that the (FC) located below the (MC) is beginning to be pressurized, a clear stagnation pressure point is observed at the (MC) outlet lower converging wall. The mass flow spatial distribution at the (FO) outlets, appears to be much uniform, the (FO) outlets have a smaller surface through which reverse flow exists, being this directly linked to smaller outlet amplitudes. The (MC) is slightly pressurized, the fluid stiffness is low and so it is the (FO) outlet mass flow oscillating frequency. For the present (FO) and regardless of the dimensional modification, the maximum mass flow amplitudes at the (FO) outlets, are directly linked with the reverse flow existing at the outlets, the bigger the reverse flow the higher the (FO) outlet oscillation amplitude. The outlet width can be effectively used to control the outlet oscillations amplitude.

Regardless of the outlet width, a vortex at the external chamber upper side, can be spotted, yet its intensity and turning speed associated are much smaller for the highest than for the lowest outlet widths studied. The turning speed of this particular vortex for the lowest and highest outlet widths studied, was respectively of 301 and 59 rad/s, which explains why the pressure at the (EC) is particularly low at small outlet widths.

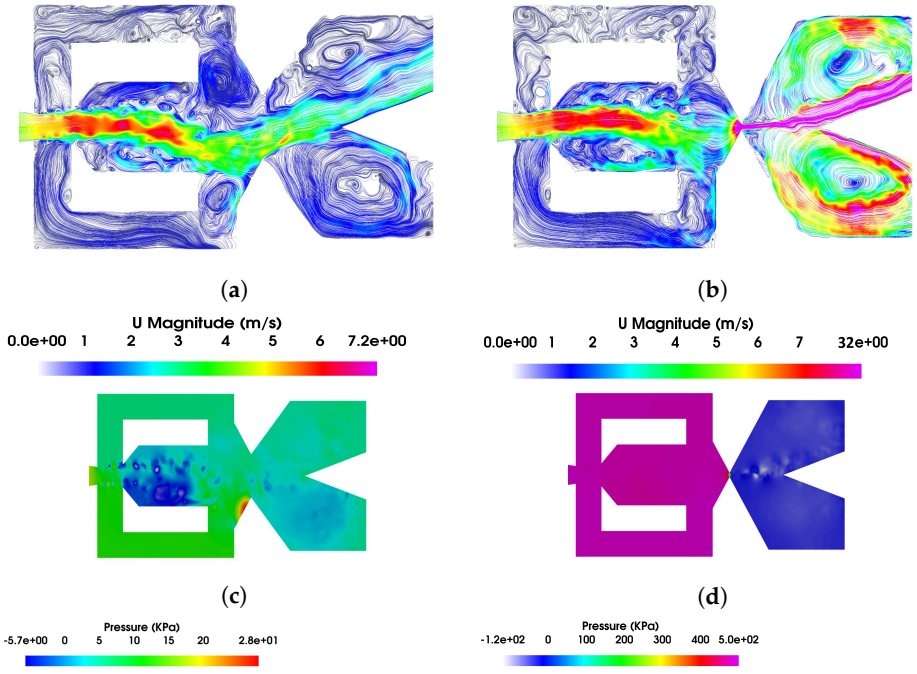

Figure 8. Fluidic oscillator internal velocity field (**a**,**b**) and pressure magnitude (**c**,**d**). Maximum outlet width (**a**,**c**), minimum outlet width (**b**,**d**). Reynolds number 16034.

The same dynamic parameters evaluated in the previous section and introduced in Figure 5, are now being presented in Figure 9 for the maximum, minimum and baseline (MC) outlet widths studied. When the highest (MC) outlet width is employed, the (FO) outlet mass flow amplitude is minimum, there is no reverse flow at any time. As the (MC) outlet width decreases, the reverse flow at the (FO) outlets keeps increasing, consequently the (FO) mass flow amplitude increases, see Figure 9a. Another relevant effect associated to the decrease of the outlet width, is the progressive increase of the (MC) pressure, notice that the average value of the stagnation pressure fluctuations presented in Figure 9c, increases around 19 times when comparing the maximum and minimum outlet width values. For the lowest outlet width evaluated, the stagnation pressure fluctuations at the (MC) lower converging wall, show a quasi-chaotic behaviour, probably due to the stagnation pressure points appearing simultaneously on both (MC) converging walls, see Figures 8d and 9c, although clear oscillation signs are still to be seen. Under these conditions, the curve representing the net momentum is particularly scattered. This fact is clearly understood when considering that the main term of the net momentum is the pressure term, as observed in Figure 6 for the previous case. Regarding the net momentum responsible of the jet fluctuations inside the (MC), see Figure 9d, its amplitude is about 38% smaller for high outlet widths than for the smaller ones. Notice as well that for the highest outlet width, the stagnation pressure peak to peak amplitude is about 40% smaller than for the smallest outlet width evaluated. These values suggest a direct relation between the stagnation pressure peak to peak amplitude and the net momentum driving the jet oscillations.

Another point to be discussed may be, why the net momentum shows rather a sinusoidal curve when the stagnation pressure oscillations, specially at the lowest outlet width, looks rather chaotic. The reason is the integration effect the (FC's) outlets are having on the pressure oscillations. The study of the (MC) incoming jet oscillation angle, see Figure 9b, shows that the smallest oscillation amplitude appears when the highest outlet width is employed. The maximum jet oscillation angle amplitude, obtained for the minimum outlet width, is about 3% higher than the one generated for the baseline case, and about 29% higher than the one obtained when using the maximum outlet width. From Figure 9, a direct correlation between the peak to peak stagnation pressure, the (MC) inlet angle amplitude, the (FO) output and (FC) mass flows amplitude, as well as the net momentum amplitude, appears to exist. Small stagnation pressure amplitudes generates small amplitudes in all these parameters.

When evaluating the feedback channel mass flow, Figure 9e, regardless of the outlet width, it is observed there is an average mass flow flowing from both feedback channel inlets to the outlets. Its average value remains pretty much constant regardless of the outlet width chosen, although it was observed it increased with the Reynolds number increase. For the smallest (MC) outlet width evaluated, just a very small reverse mass flow exists on both feedback channel outlets, the reverse flow increases with the Reynolds number increase. (FC) reverse flow is associated to the alternative appearance of the stagnation pressure points at the (FC) outlets internal vertical walls, as it was observed in Figures 4d and 5e for the smallest inlet width. At high mixing chamber outlet widths, there is no (FC) reverse flow. Regarding the (FC) mass flow amplitude, a decrease of about 32% is observed, when comparing the values of the highest outlet width with the ones obtained at the lowest outlet width. The decrease in feedback channel mass flow amplitude as outlet width increases can be more clearly seen at high Reynolds numbers, in general it can be said that all differences can be seen more clearly at high Reynolds numbers, the dynamic values at several Reynolds numbers are not presented in the present paper. The phase lag between the oscillator output mass flow and the feedback channel mass flow is about 4.4×10^{-3} and 2.4×10^{-3} s, respectively for the lowest and highest outlet widths at Reynolds 16034. It seems high phase lag values are related to high (FO) output mass flow amplitudes.

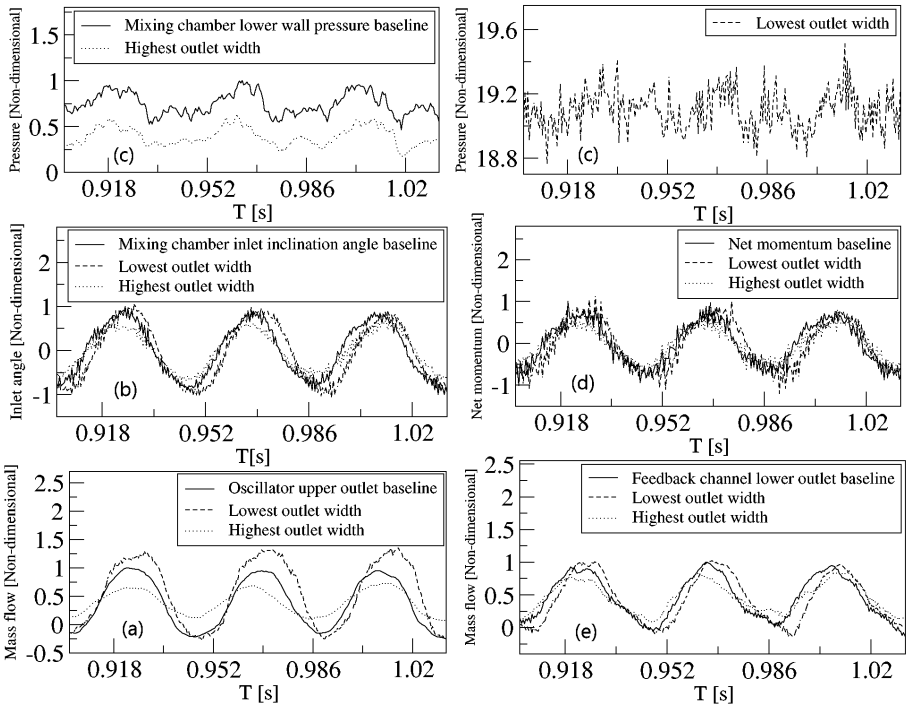

Figure 9. Dynamic effects of the (MC) outlet width modification on the main flow parameters, Reynolds number 16034. Each graph presents three non-dimensional curves characterizing results from the baseline, the lowest and highest outlet width cases, and as a function of the dimensional time. In figure (**a**) the mass flow across the upper oscillator outlet is presented. Figure (**b**) introduces the temporal variation of the (MC) inlet inclination angle. Figures (**c**) presents the pressure at the (MC) lower inclined wall. The net momentum acting on the lateral sides of the main jet is presented in figure (**d**). Figure (**e**) characterizes the mass flow at the lower feedback channel outlet.

Although not directly presented in the present manuscript, at low (MC) outlet widths, the pressure difference between the upper and lower (FC) channel outlets, was particularly high, a maximum pressure difference of 4200 Pa was measured. For the highest outlet width studied, this maximum pressure difference was of 2500 Pa. The peak to peak stagnation pressure oscillations amplitude at the (MC) converging walls, was specially high at low outlet widths and high Reynolds numbers. From Figure 9b,d, it is observed that for the lowest outlet width studied, the peak to peak net momentum amplitude acting onto the jet entering the (MC), and the peak to peak inlet angle amplitude of the jet at the same point, are respectively of 43% and 30% higher than the respective values obtained when evaluating the highest outlet width. A final relevant point to highlight on the average pressure, is that for most of the cases presented in this paper, and regardless of the modification considered, as Reynolds number increases from 16034 to 32068, the average pressure at the (MC) outlet converging walls, increased by approximately 150%. Yet there are two exceptions, one of them is whenever the highest (MC) outlet width is employed, for this particular case, the same increase of Reynolds number brings an increase of the average pressure of about 12.7%. The second exception appears when the lowest (MC) outlet width is employed, being the increase of average pressure of 316% for the same increase of the Reynolds number. For highest outlet widths, the central core of the main jet flows towards the (EC) without impinging on the (MC) converging walls, just some fluid particles located at the lateral sides of the jet impinge on the (MC) converging walls, therefore explaining why the average spatial pressure on these walls is particularly small. Regardless of the geometry modification evaluated, the stagnation pressure peak to peak amplitude at the (MC) converging walls, increases with the Reynolds number increase. The detailed evaluation of this particular parameter is to be found in the final part of this paper.

5.3. Modifying the (Mc) Outlet Angle

Figure 10 presents the results obtained when modifying the (MC) outlet angle and for the three Reynolds numbers evaluated. The (FO) output mass flow frequency and amplitude keeps decreasing as the inclination angle increases. The frequency effect is perfectly understandable once it is realized that the (MC) outlet converging walls, play a key role regarding the flow directed towards the (FC's) and the pressure waves transmission. Not only the position of the stagnation pressure point is modified by this angle but also its magnitude will be affected. The stagnation pressure maximum value as well as the peak to peak pressure amplitude, was observed to decrease with the (MC) angle increase. High frequencies are linked to high stagnation pressure values and vice versa. Furthermore, high (MC) outlet angles tend to direct the pressure waves towards the (FC) located opposite to the wall where the main jet impinges, the main flow stream is directed towards the (FO) outlet. On the other hand, small (MC) outlet angles, have associated a much wider area where stagnation pressure exists, maximum stagnation pressure values and peak to peak amplitudes are obtained under these conditions. Small angles direct the mass flow and specially the pressure waves towards the (FC) located next to the wall the main jet impinges, periodically pressurizing the (FC), compare Figure 11a,c with Figure 11b,d. This is the reason why, small (MC) outlet angles, have associated higher frequencies and amplitudes.

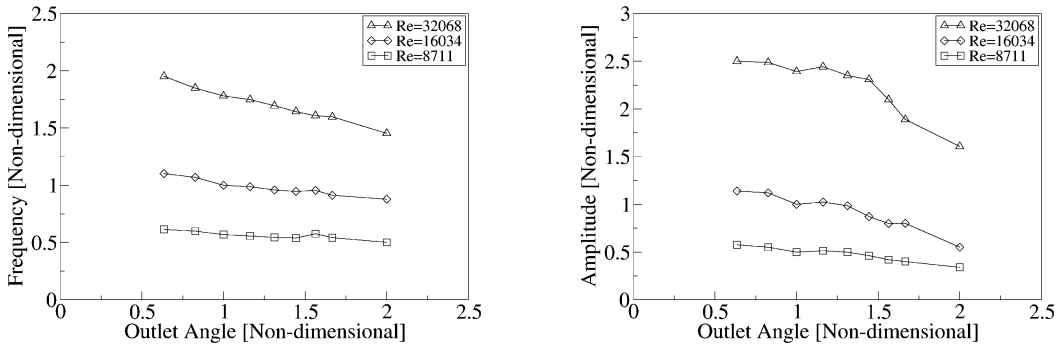

(**a**) (**b**)

Figure 10. Frequency (**a**) and amplitude (**b**) of the (FO) outlet dynamic mass flow, as a function of the mixing chamber outlet angle and for three different Reynolds numbers, 8711, 16034 and 32068.

The effect of the (MC) outlet angle on the (FO) outlet mass flow amplitude, can be further explained when taking into account that, higher angles tend to direct the main flow towards the (FO) outlet central horizontal axis, therefore tending to decrease the jet deflection. Notice from Figure 12 that the amplitude of all parameters is particularly small at high outlet angles. The flow leaves the (EC) rather tangentially to the wedge walls and across one of the outlets at a time, generating a large vortex on the opposite outlet of the (EC). For high (MC) outlet angles, the fluid velocity at the (FO) outlets, is rather uniform across one of the exits at a time and always leaves the oscillator, there is no reverse flow, see Figure 12a. As the angle decreases, the outlet maximum fluid velocity magnitude increases, for a given oscillation period and during approximately one third of the period, the mass flow in any of the two exits enters the oscillator, for the rest of the period the fluid leaves the oscillator at a relatively high speed, the peak to peak output mass flow amplitude is maximum under these conditions, see Figure 12a. Again we are observing that large (FO) output mass flow amplitudes, have associated reverse flow at the (FO) outlets.

Figure 11 represents the oscillator overall velocity and pressure fields when the outlet angles are respectively the largest and smallest studied. From Figure 11b, which characterizes the smallest angle evaluated, it is noticed that the jet impinges nearly perpendicular to the (MC) lower converging wall, generating a large area where the stagnation pressure acts, see Figure 11d. The stagnation pressure and its peak to peak amplitude, reach their respective maximums under these conditions, see

Figure 12c. Pressure waves and some fluid flow are directed from the lower (FC) inlet to the outlet. the lower feedback channel is pressurized, Figure 11d. On the other hand, whenever the output angle increases, Figure 11a, the jet leaving the (MC), tends to run tangential to the (MC) converging walls, therefore directing a smaller amount of fluid through the feedback channels, and even more important, the formation of a high pressure stagnation point is reduced to a very small converging walls section, its peak to peak amplitude and maximum value are also minimized, see Figures 11c and 12c. As a result the time needed for the main jet to flip over increases, and accordingly the oscillation frequency decreases. It is also interesting to realize that at the external chamber (EC), a large vortex is generated at the opposite exit from the one the flow is leaving the amplifier. In fact the vortex covers the entire opposite exit, preventing flow from outside the (FO) to enter into the (EC). This vortex intensity was observed to be slightly higher as the angle decreased. For the smallest (MC) outlet angle, the turning speed associated to this particular vortex was of 117 rad/s, while when highest outlet angle is used, the turning speed was of 67 rad/s.

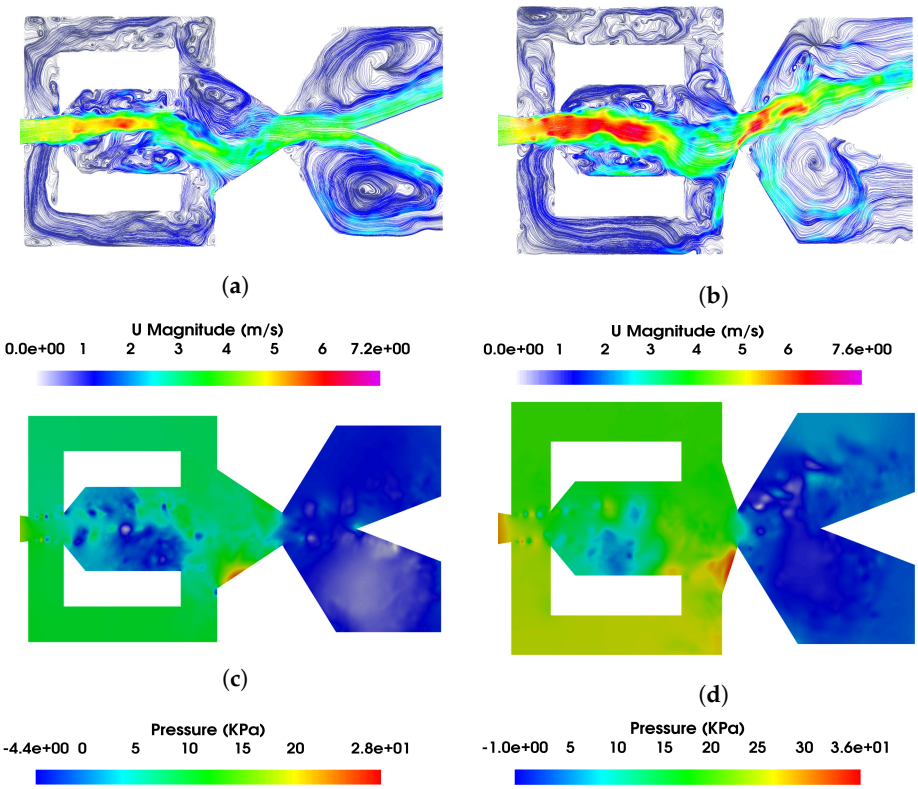

Figure 11. Fluidic oscillator internal velocity field (**a**,**b**) and pressure magnitude (**c**,**d**). Maximum outlet angle (**a**,**c**), minimum outlet angle (**b**,**d**). Reynolds number 16034.

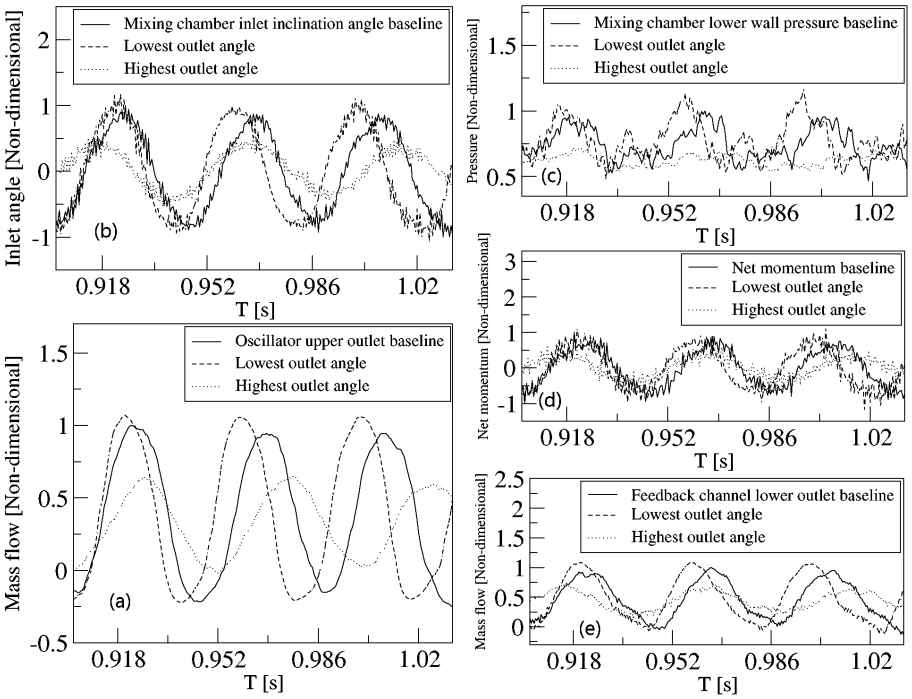

Figure 12. Dynamic effects of the (MC) outlet angle modification on the main flow parameters, Reynolds number 16034. Each graph presents three non-dimensional curves characterizing results from the baseline, the lowest and highest outlet angle cases, and as a function of the dimensional time. In figure (**a**) the mass flow across the upper oscillator outlet is presented. Figure (**b**) introduces the temporal variation of the (MC) inlet inclination angle. Figures (**c**) presents the pressure at the (MC) lower inclined wall. The net momentum acting on the lateral sides of the main jet is presented in figure (**d**). Figure (**e**) characterizes the mass flow at the lower feedback channel outlet.

The effects on the (FO) outlet mass flow, the (FC) mass flow, the net momentum acting on the (FC) outlets, the stagnation pressure on the (MC) converging walls, and the (MC) jet oscillation angle, for the baseline case, the lowest and highest mixing chamber outlet angles evaluated, at Reynolds number 16034, are presented in Figure 12. The first thing to observe is that the (MC) outlet angle modification, generates a clear effect on the (FO) main parameters. As the outlet angle increases, a clear peak to peak amplitude reduction of all measured parameters was observed. For the (MC) smallest outlet angle studied, the mass flow frequency and amplitude at the (FO) outlet are maximum, the reverse flow is also the largest. The peak to peak mass flow amplitude at the (FC's), is about 53% smaller when using the highest (MC) outlet angle than when using the smallest one. Under all (MC) outlet angles studied, the (FC) mass flow always goes from the (FC) inlets to outlets, for the lowest outlet angle, the minimum (FC) mass flow is about zero, see Figure 12e. The average pressure at the (MC) lower converging wall, is around 22% lower for the highest (MC) outlet angle than for the lowest one. When the lowest (MC) outlet angle was employed, a clear difference between the static pressure at the (FC) outlets was observed, a maximum pressure difference between both outlets of over 3000 Pa was measured. For the lowest (MC) outlet angle, the net momentum acting onto the lateral sides of the main jet entering the (MC), is about 38% higher than when the highest angle is used, Figure 12d. This effect helps in generating a much larger jet oscillation amplitude in the (MC) and at the (FO) outlet mass flow, see Figure 12a,b. The conclusion is that high oscillation amplitudes are linked with high pressure variations on the (MC) converging walls and therefore on the (FC) outlets.

5.4. Modifying the (Mc) Inlet Angle

The flow effects caused by the modification of the (MC) inlet angle is presented in this section, just three angles including the baseline case, were considered, see Figure 13. It was observed that,

the (FO) outlet mass flow peak to peak oscillation amplitude, when compared with the baseline case, increased an 8.9% for an inlet angle increase of 74%. When the inlet angle increased by 93%, the (FO) outlet mass flow amplitude increased versus the baseline case, just 1.6%. Regarding the (FO) outlet mass flow oscillating frequency, it increases very slightly with the inlet angle increase, in fact, as it has been introduced in all previous cases, the frequency and amplitude variations are more relevant as the Reynolds number increases. Figure 13 also clarifies that the same trend is observed regardless of the Reynolds number considered.

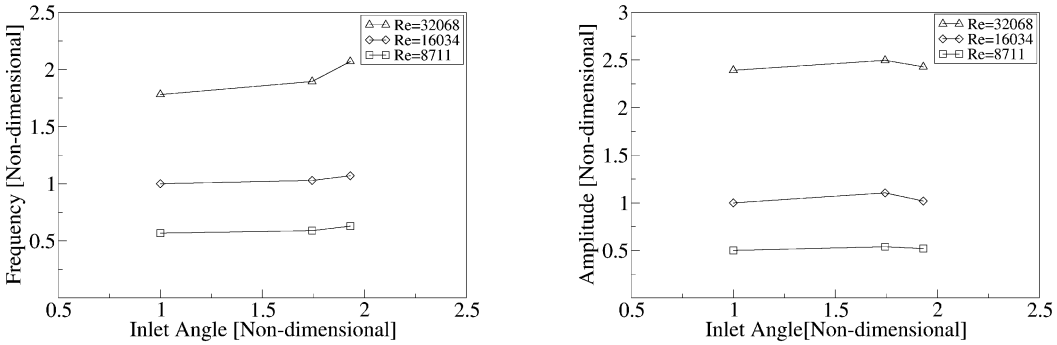

(**a**) (**b**)

Figure 13. Fluidic oscillator output mass flow Frequency (**a**) and amplitude (**b**) as a function of the mixing chamber inlet angle and for three different Reynolds numbers, 8711, 16034 and 32068.

Figure 14 introduces the velocity field and the pressure magnitude inside the (FO) for the maximum and minimum (MC) inlet angles evaluated. As the inlet angle increases, there is less space on both sides of the jet in the (MC) for the Coanda effect to appear, yet the jet keeps oscillating. This supports the thesis presented in this paper and already outlined in [12,18], which established that in reality, what forces the jet to flip is the pressure term of the net momentum acting on the lateral sides of the jet entering the (MC). Regardless of the (MC) inlet inclination angle, the maximum stagnation pressure appearing at the (MC) converging walls is very similar, a peak to peak stagnation pressure increase of nearly 18% is observed when comparing the highest inlet angle evaluated with the lowest inlet angle case, compare Figure 14c with Figure 14d, see as well Figure 15c. As a result, the net momentum peak to peak amplitude acting onto the incoming jet lateral surfaces, suffers a small increase of 2.8%, although it is difficult to distinguish the different curves, this information is presented in Figure 15d.

From the observation of Figures 4a,b, 8a,b, 11a,b and 14a,b, it is noticed that in all (FC's) 90 degrees corners small vortices appear, indicating it exists fluid recirculation in all these points. To minimize fluid recirculation it would be desirable to round all 90 degrees corners, the expected effect would be, a small increase of actuator frequency, since in reality rounding the corners would facilitate the fluid to move back and forward along the feedback channels, pressure losses would as well decrease, This observation was previously done by [5].

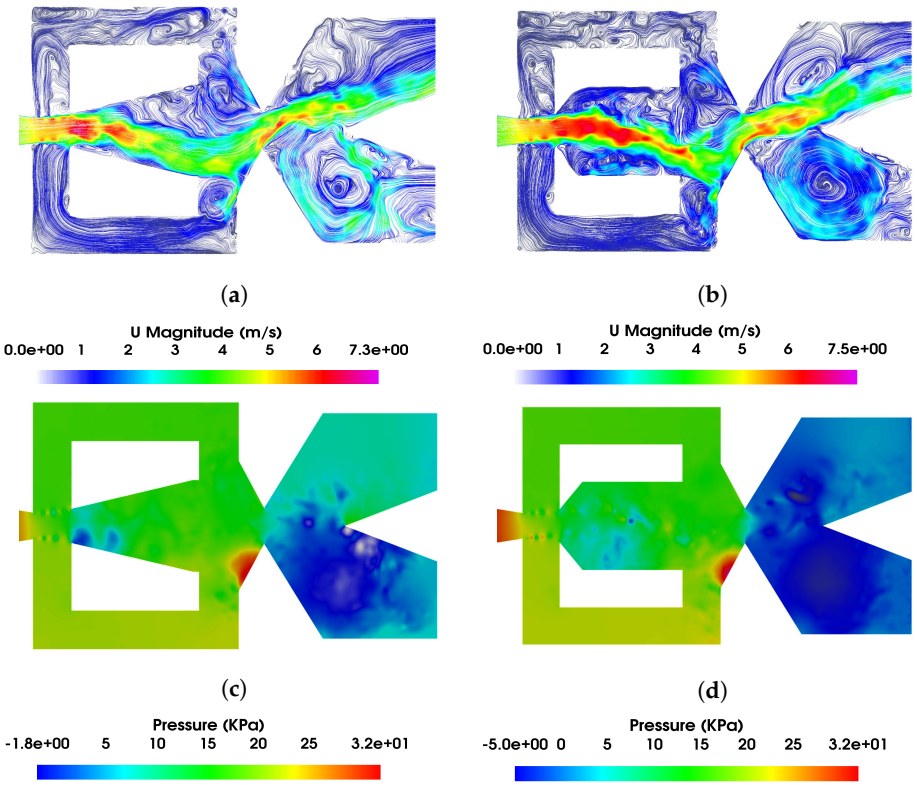

Figure 14. Fluidic oscillator internal velocity field (**a**,**b**) and pressure magnitude (**c**,**d**). Maximum inlet angle (**a**,**c**), minimum inlet angle (**b**,**d**). Reynolds number 16034.

Based on the results obtained in the present section, see Figure 15, it can be concluded that the effect of modifying the (MC) inlet angle, does not generate very relevant changes on any of the studied fluid flow parameters. In fact, the (MC) inlet angle seems to be particularly linked with the Coanda effect alternatively appearing on both sides of the mixing chamber. Yet, and based on the results obtained in the present set of simulations, the Coanda effect has a minor effect on the (FO) flow dynamic performance. It is important to realize, when observing Figure 15, that the minor (MC) inlet angle, corresponds to the baseline case, therefore, the other two angles studied are called medium and highest angles. The feedback channels mass flow peak to peak amplitude, suffered a decrease versus the baseline case of 14.5%, when the medium inlet angle was used, the (FC) peak to peak amplitude decreased a 16% when the inlet angle increase was of 93%, see Figure 15e. The reverse flow at the (FO) outlets suffered an initial increase as the inlet angle increased, and slightly reduced when the inlet angle reached its maximum value, see Figure 15a. The jet inclination angle inside the (MC), suffered a small decrease of 9% when comparing the minimum and maximum (MC) inlet angles evaluated, see Figure 15b. Notice that the jet inclination angle inside the (MC) is in reality delimited by the (MC) internal walls, as the inlet angle increases there is less space in the (MC) for the jet to fluctuate. From this particular study it is observed that, small stagnation pressure variations at the (MC) converging walls, generate clear (FO) outlet mass flow modifications, compare Figure 15a with Figure 15c.

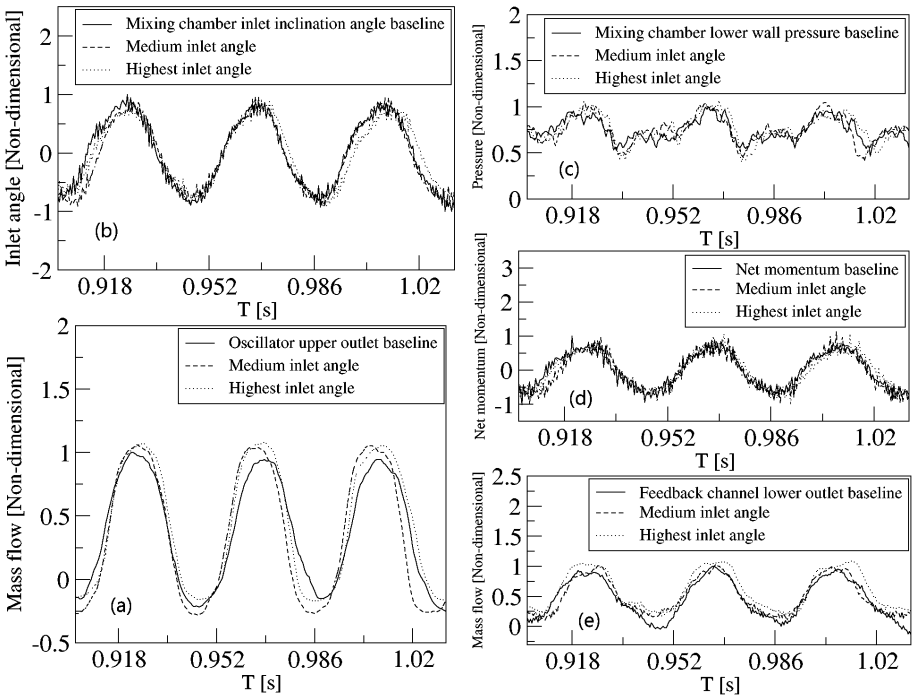

Figure 15. Dynamic effects of the (MC) inlet angle modification on the main flow parameters, Reynolds number 16034. Each graph presents three non-dimensional curves characterizing results from the baseline, the medium and highest inlet angle cases, and as a function of the dimensional time. In figure (**a**) the mass flow across the upper oscillator outlet is presented. Figure (**b**) introduces the temporal variation of the (MC) inlet inclination angle. Figures (**c**) presents the pressure at the (MC) lower inclined wall. The net momentum acting on the lateral sides of the main jet is presented in figure (**d**). Figure (**e**) characterizes the mass flow at the lower feedback channel outlet.

The corresponding videos presenting the velocity and pressure fields for the eight different cases evaluated, see Figures 4, 8, 11 and 14, are given in Supplementary Materials; a total of sixteen videos are introduced.

5.5. Relation Reynolds Frequency for All Dimensional Modifications Performed

After evaluating the fluidic oscillator output mass flow frequency and amplitude as a function of the different internal modifications and at several Reynolds numbers, one of the conclusions from the present paper is, that the conventional Reynolds-frequency linear behaviour for a given oscillator, can be expressed of a set of linear functions. Each line represents the operating conditions of the fluidic oscillator once a particular modification is undertaken, notice that in almost all cases, a linear relation is obtained, see Figure 16. For example, the increase of the inlet width, and regardless of the Reynolds number employed, generates output frequencies considerably higher than the baseline case. The (FO) outlet mass flow oscillating frequency, increases versus the baseline case one, by around 40% when the maximum inlet width is employed. The outlet frequency also increases when employing the lowest output angle or the lowest output width, although for these particular cases the increase is smaller than 7%. The rest of the internal modifications, generate frequencies slightly smaller than the baseline case ones, the trend is the same for all Reynolds numbers studied. It is also interesting to observe that, when the highest (MC) outlet angle is used, the expected Reynolds-frequency linearity disappears at high Reynolds numbers, the frequency for this case is smaller than what could be expected. The authors believe this particular reduction of frequency at Reynolds 32068, is due to the channel effect caused by the highest outlet angle, this particular angle directs the fluid from the (MC) to the oscillator outlets, minimizing the generation of a stagnation pressure point at the (MC) converging walls, in other words, just an small amount of the kinetic energy associated to the fluid is being transformed into stagnation

pressure. The result is, it requires a longer time to build the required momentum at the (FC) outlets for the jet to flip. Under these conditions, the fluid is directed to the lateral sides of the oscillator external chamber wedge and flows almost parallel to them, see Figure 11a.

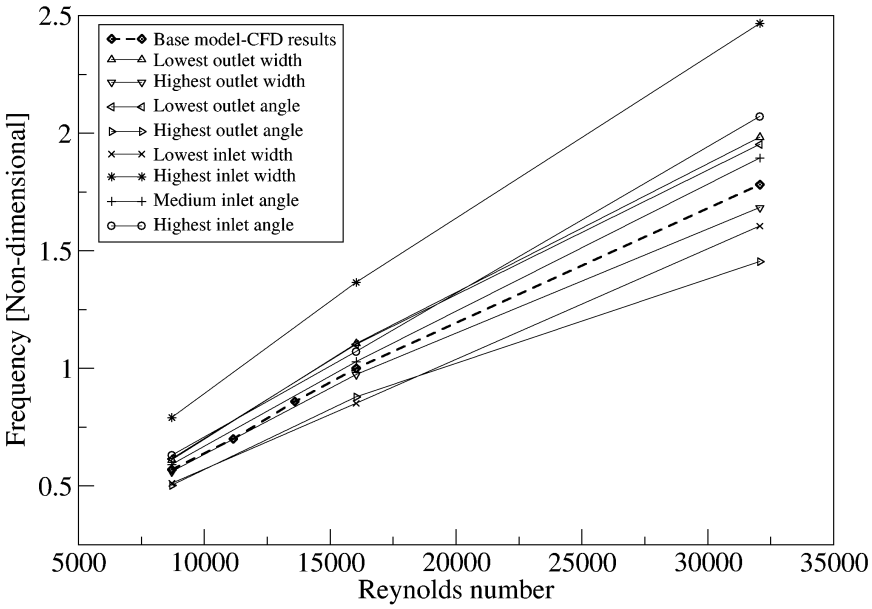

Figure 16. Relation Reynolds number versus mass flow output frequency, for all dimensional modifications studied.

It is at this point interesting to remember that, according to [3], the (FO) angled configuration, which is the one used in this study, looses its linearity at Reynolds 30000, this helps to explain why the curves presented in Figure 16, are not fully linear. As Reynolds number increases, the flow inside the (FO) goes from quasi-periodic to chaotic, being this the reason why linearity disappears. It is also interesting to recall, that according to [11], the fluidic oscillator internal performance is essentially the same for different outlet configurations, whether one or two outlets are considered.

5.6. Stagnation Pressure at the (MC) Converging Walls and Net Momentum Acting on the (MC) Incoming Jet as a Function of the Reynolds Number

In the present section, the net momentum acting onto the jet entering the mixing chamber will be evaluated and compared with the stagnation pressure variations at the (MC) converging walls. The momentum of the fluid acting on a given surface was defined as Equation (1). As both feedback channels, add momentum to the lateral sides of the main jet entering the (MC), Equation (1) will need to be applied to each (FC) outlet. In order to evaluate which is the temporal net momentum applied to the incoming jet, it will be required to know the instantaneous mass flow through both (FC) outlets as well as the temporal pressure at these two sections.

In [18] it was concluded the oscillators studied appeared to be pressure driven, the same conclusion was reached in [12], where it was demonstrated that the forces triggering the oscillation were mostly due to the pressure difference at the feedback channels outlets. In the present section the different forces acting on the jet lateral surfaces will be analyzed for each of the different geometry modifications evaluated and as a function of the Reynolds number.

The average net momentum applied to the jet entering the (MC), is for all Reynolds numbers and (FO) modifications, having a value close to zero, as observed for a Reynolds number of 16034

in Figures 5d, 9d, 12d and 15d. Regarding the evolution of the average net momentum applied to the jet at the (MC) inlet, it was observed that whenever the pressure at the (MC) is particularly high and the Reynolds number increases, the average net momentum applied to the jet decreases. This happens for the following cases, lowest outlet width, lowest outlet angle and for the baseline case. The equations presented in Table 4 characterize this evolution. On the other hand, whenever the pressure at the (MC) is particularly low, which happens for the highest outlet width, the lowest inlet width, the highest inlet width and the highest outlet angle, the average net momentum increases with the Reynolds number increase, Table 4 states this evolution. Nevertheless, and as a general trend it can be stated that, regardless of the (FO) modification performed, as the Reynolds number increases the average pressure in the (MC) also increases. The equations characterizing the evolution of the average non-dimensional stagnation pressure at the (MC) converging walls, and the average non-dimensional net momentum acting on the jet entering the (MC), are respectively presented as a function of the Reynolds number in Tables 3 and 4. These equations are valid for a range of Reynolds numbers between $8711 < \mathrm{Re} < 32068$, and were obtained from the data presented in Figures 5, 9, 12 and 15, as well as from similar figures obtained at Reynolds numbers 8711 and 32068. Some geometry modifications, regardless of the Reynolds number, generate a decrease of the (MC) average pressure when compared to the one existing in the baseline case, these are, the highest and lowest inlet widths, the highest outlet angle and the highest outlet width. At Reynolds number 32068, the (MC) average pressure decrease versus the baseline one was respectively of 23.5%, 3.8%, 30% and 75%. On the other hand, the geometry modification generating a drastic increase of the (MC) average pressure, was the lowest outlet width, which increased the baseline pressure by almost 42 times at Reynolds 32068. From the equation presented in Table 3, characterizing the evolution of the average stagnation pressure at the (MC) converging walls, as a function of the Reynolds number and for the lowest outlet width case, it is clearly observed that the pressure increase is much higher under these conditions than for the rest of the cases studied. Nevertheless the rest of the equations presented in Table 3 show an increase of the average stagnation pressure at the (MC) converging walls with the Reynolds number increase. When employing the lowest outlet angle and for the same Reynolds number 32068, the average pressure increase was of 11.4%.

Table 3. Equations characterizing the evolution of non dimensional average stagnation pressure at the (MC) outlet converging walls, and as a function of the Reynolds number. These equations are valid in the range $8711 < \mathrm{Re} < 32068$. The coefficient of determination was $(R)^2 = 1$ for all curves presented.

Geometry Modification	Non-Dimensional Average Pressure at the (MC) Converging Walls, as a Function of the Reynolds Number
Baseline	$2.125E-9*Re^2-7.136E-6*Re+0.5679$
Highest inlet angle	$2.092E-9*Re^2-3.788E-6*Re+0.5444$
Lowest outlet angle	$2.054E-9*Re^2-6.890E-7*Re+0.4840$
Highest outlet angle	$1.935E-9*Re^2-9.367E-7*Re+0.8536$
Lowest outlet width	$1.144E-7*Re^2-4.102E-4*Re+2.9272$
Highest outlet width	$1.214E-11*Re^2+3.804E-6*Re+0.4891$
Lowest inlet width	$1.944E-9*Re^2-3.324E-6*Re+0.5353$
Highest inlet width	$1E-9*Re^2+1.655E-5*Re+0.4195$

The analysis of the peak to peak amplitude of the stagnation pressure at the (MC) outlet converging walls, and the peak to peak net momentum amplitude acting on the lateral sides of the jet entering the (MC), provides a significant information on the flow dynamics inside the (MC). Tables 5 and 6, introduce the equations characterizing the evolution of these parameters as a function of the Reynolds number and for the different geometry modifications studied. The first thing to observe is that, the stagnation pressure and the net momentum amplitudes, increase as a function of the Reynolds number almost to the power 2. It is also interesting to observe that, in nearly all the cases studied, the exponent associated to the Reynolds number when considering the stagnation pressure peak to

peak amplitude, is smaller than the one associated to the net momentum amplitude for the same case. This is particularly relevant for the following cases, highest inlet width, highest inlet angle, lowest outlet angle and lowest outlet width. In any case, and regardless of the case studied, the equations from Tables 5 and 6, show a direct link between the peak to peak stagnation pressure amplitude and the net momentum amplitude, giving therefore strength to the thesis established in references [12,18] and in the present paper, regarding the origin of the forces driving the oscillation. To understand, for each of the cases studied, the origin of the net momentum driving the oscillation, the relation between the peak to peak net momentum term due to the static pressure acting on the (FC) outlets, was compared with the peak to peak net momentum term due to the feedback channels mass flow. This comparison given as the ratio between the static pressure divided by the (FC) mass flow term, is presented in Table 7. There are four geometry modifications, highest inlet width, highest inlet angle, lowest outlet angle and lowest outlet width, at which the pressure/mass flow momentum ratio is particularly small, indicating that under these conditions, the feedback channel mass flow plays a more relevant role regarding the net momentum applied to the jet. Notice that these four geometry modifications, are the same ones generating a particular increase in the exponent associated to the Reynolds number, observed when comparing Tables 5 and 6. The conclusion is that, for these particular geometry modifications, the (FC) mass flow plays a more relevant role, although small, on the net momentum driving the oscillation. Yet, regardless of the geometry modification and the Reynolds number studied, the oscillation of the jet in the (MC) is mostly driven by the pressure difference at the (FC) outlets. Finally, and based on the results presented in Table 7 it can be concluded that, the pressure/mass flow momentum ratio is highly dependent on the geometry modification, but it is not particularly affected by the Reynolds number.

Table 4. Equations characterizing the evolution of non-dimensional average net momentum acting on the jet entering the (MC), and as a function of the Reynolds number. These equations are valid in the range $8711 < \mathrm{Re} < 32068$. The coefficient of determination was $(R)^2 = 1$ for all curves presented.

Geometry Modification	Average Non-Dimensional Net Momentum Acting on the Jet Entering the (MC), as a Function of the Reynols Number
Baseline	$1E-9*Re^2-8.375E-5*Re+0.5899$
Highest inlet angle	$1.243E-8*Re^2-1.532E-4*Re+0.2218$
Lowest outlet angle	$3.374E-9*Re^2-1.144E-4*Re+0.9911$
Highest outlet angle	$7.508E-11*Re^2-4.282E-5*Re+0.3290$
Lowest outlet width	$-3.842E-8*Re^2+8.762E-4*Re-4.2989$
Highest outlet width	$4.833E-9*Re^2-6.425E-5*Re-0.3056$
Lowest inlet width	$2.189E-9*Re^2-2.47378E-5*Re+0.2035$
Highest inlet width	$9.226E-9*Re^2-3.57369E-4*Re+2.3774$

Table 5. Equations characterizing the evolution of non-dimensional peak to peak stagnation pressure amplitude at the (MC) outlet converging walls, and as a function of the Reynolds number. These equations are valid in the range $8711 < \mathrm{Re} < 32068$.

Geometry Modification	Non-Dimensional Peak to Peak Pressure Amplitude at the (MC) Converging Walls	Coefficient of Determination $(R)^2$
Baseline	$4.597E-9*Re^{1.986}$	0.999
Highest inlet angle	$7.493E-9*Re^{1.956}$	0.999
Lowest outlet angle	$1.939E-8*Re^{1.851}$	0.998
Highest outlet angle	$1.237E-9*Re^{2.066}$	0.997
Lowest outlet width	$2.126E-8*Re^{1.865}$	0.997
Highest outlet width	$6.077E-9*Re^{1.937}$	0.999
Lowest inlet width	$2.820E-9*Re^{2.020}$	0.993
Highest inlet width	$1.872E-8*Re^{1.839}$	0.993

Table 6. Equations characterizing the evolution of non-dimensional peak to peak net momentum amplitude at the (MC) incoming jet, and as a function of the Reynolds number. These equations are valid in the range $8711 < \mathrm{Re} < 32068$.

Geometry Modification	Non-Dimensional Peak to Peak Net Momentum Amplitude at the (MC) Incoming Jet	Coefficient of Determination $(R)^2$
Baseline	$4.652E-9*Re^{1.983}$	0.999
Highest inlet angle	$2.706E-9*Re^{2.044}$	0.999
Lowest outlet angle	$5.633E-9*Re^{1.971}$	0.999
Highest outlet angle	$1E-9*Re^{1.929}$	0.989
Lowest outlet width	$4.298E-9*Re^{2.002}$	0.999
Highest outlet width	$2.908E-9*Re^{2.004}$	0.997
Lowest inlet width	$2E-9*Re^{2.006}$	0.997
Highest inlet width	$1.864E-9*Re^{2.038}$	0.998

Table 7. Evaluation of the peak to peak net momentum amplitude at the (MC) incoming jet due to the pressure term, divided by the net momentum amplitude due to the (FC) mass flow term, and for the three Reynolds numbers studied.

Geometry Modification	Reynolds Number 8711	Reynolds Number 16034	Reynolds Number 32068
Baseline	11.96	12.58	9.88
Highest inlet angle	8.72	9.38	8.1
Lowest outlet angle	9.73	10.71	9.25
Highest outlet angle	16.86	17.14	14.97
Lowest outlet width	10.63	10.77	9.32
Highest outlet width	12.93	13.29	10.88
Lowest inlet width	13.61	12.38	14.52
Highest inlet width	3.78	3.74	4.12

Regarding the inlet width variations, from the results obtained it is observed that, the stagnation pressure and the net momentum peak to peak amplitudes, suffer a minor increase as the inlet width increases. When comparing the minimum and maximum inlet widths studied, at Reynolds number 16034, the peak to peak stagnation pressure and momentum increase, were respectively of 17% and 31% versus their minimum values. When considering the outlet width effects on the (MC) converging walls peak to peak stagnation pressure amplitude, it was observed that as the outlet width decreases, the peak to peak stagnation pressure amplitude keeps increasing, also the net momentum amplitude acting on the lateral surfaces of the (MC) incoming jet, increases as the outlet width decreases. When comparing the minimum and maximum outlet widths studied, the increase of the peak to peak stagnation pressure and momentum, at Re = 16034, was respectively of 39% and 36%. The same trend is observed under all Reynolds numbers studied. As Reynolds number increases, the variation in percentage for both parameters decreases.

When evaluating the (MC) outlet angle and for all the cases studied, the minimum peak to peak (MC) converging walls stagnation pressure, was obtained when the highest outlet angle was employed. As the outlet angle decreased, the peak to peak stagnation pressure at the (MC) outlet converging walls, as well as the peak to peak momentum amplitude at the (FC) outlets, kept increasing. The increase versus the minimum value was respectively of 68% and 38% at Re = 16034. As Reynolds number grows, the variation in percentage reduces. When using the highest outlet angle, the peak to peak net momentum amplitude associated was higher than for the case where the lowest inlet width was used. The decrease of the inlet width, appears to particularly reduce the net momentum applied to the (MC) incoming jet. The mass flow along the (FC's) is effectively controlled by the inlet width. Regardless of the Reynolds number, as the inlet angle increases, the stagnation pressure peak to peak amplitude at the (MC) converging walls, also increases. The increase is more relevant at high Reynolds

numbers. It is interesting to see that the peak to peak amplitude of the net momentum acting on the lateral sides of the jet entering the (MC), initially increases with the inlet angle increase, but as the inlet angle reaches its maximum value, the momentum amplitude slightly decreases. At the highest inlet angle, the stagnation pressure waves generated at the (MC) converging walls, are not efficiently being transferred to the (FC's) outlets. In fact, the pressure at both (FC's) outlets, is very much the same under these conditions. Regardless of the (FO) geometry modification performed, the same trend on peak to peak pressure and momentum, appeared at all Reynolds numbers evaluated, therefore, for a given (FO) modification, the same physical phenomenon is driving the oscillations at all Reynolds numbers.

In order to properly understand the effect of the inlet width variation on the net momentum acting onto the (MC) incoming jet, Figure 17 is introduced. The first point to realize is that, for the lowest inlet width, the noise associated to the pressure wave generated at the stagnation points appearing alternatively at the (FC) outlets, see Figures 4d and 5d, is much higher than in the rest of the cases studied. For this particular case, see Figure 5e, there is a large amount of mass flow traveling backwards along the feedback channels. The authors believe, the weak pressure waves originated at the (MC) outlet converging walls, which travel along the (FC) and also inside the (MC), are being disrupted by the particularly high mass flow moving along the (FC) and in opposite direction to the pressure waves, the result is a highly noisy pressure fluctuation at the (FC) outlets. In reality, and for this particular case, pressure waves are being generated at the same time on the (MC) outlet converging walls and at the (FC's) outlet internal vertical walls, these pressure waves collide inside the (FC's) enhancing the noise spectrum. Notice as well from Figure 17 that, the noise generated reduces to a minimum whenever the maximum inlet width is being employed. For this case, the mass flow traveling along the (FC's), always goes from the (FC's) inlets to the outlets, see Figure 5e, and pressure waves are not generated alternatively at the (FC's) outlet internal vertical walls. The direction of the (FC's) mass flow, always coincides with the traveling direction of the pressure waves, which are generated at the (MC) outlet converging walls.

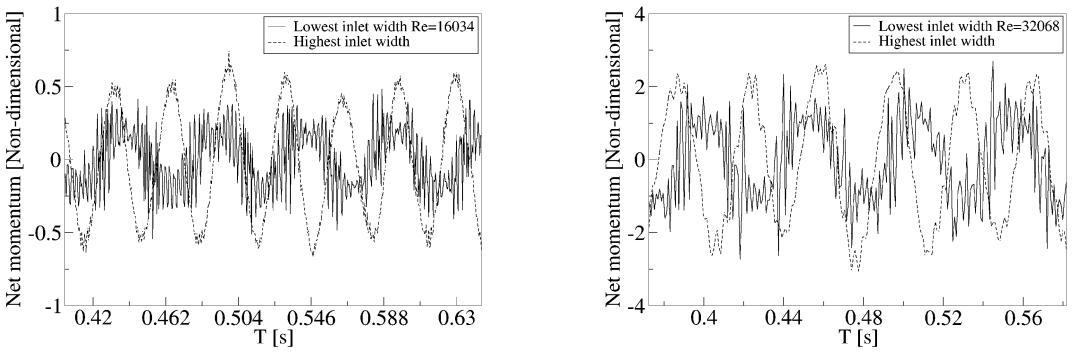

(**a**) (**b**)

Figure 17. Net momentum acting on the fluidic oscillator inlet jet and for two different mixing chamber inlet widths (the lowest and the highest), two different Reynolds numbers, 16034 Figure (**a**) and 32068 Figure (**b**), were considered.

6. Conclusions

A careful 3D-CFD evaluation of a fluidic oscillator under turbulent conditions has been performed. The study allows identifying, which dimensional parameters are more relevant regarding the modification of the fluidic actuator frequency and output amplitude. When modifying the (MC) inlet width, a threshold in both directions was observed at which fluidic oscillator was simply not oscillating. By increasing the (MC) outlet width or the (MC) outlet angle, the (FO) output frequency and amplitude decreased. The maximum (FO) outlet mass flow amplitude, was always obtained

whenever reverse flow at the (FO) outlets existed, the higher the reverse flow value, the higher the (FO) outlet mass flow amplitude.

The pressure term of the net momentum acting onto the lateral sides of the mixing chamber incoming jet, directs under all conditions studied, the oscillation of the jet inside the (MC) and therefore the oscillation at the (FO) outlets. The actuator is pressure driven. The net momentum oscillation is mostly due to the stagnation pressure fluctuation occurring at the (MC) converging surfaces, the net momentum due to the mass flow flowing along the feedback channels was observed to be negligible in all cases studied, the amplitude of the net momentum oscillation is directly linked with the maximum and minimum values of the stagnation pressure appearing at the (MC) outlet converging surfaces.

Low inlet widths, have associated a considerable reverse flow along the (FC's), reverse flow also appears at the (FO) outlets, therefore the (FO) mass flow amplitude is higher than the one existing at high inlet widths. The net momentum required to flip the jet over in the (MC), is particularly low at small inlet widths. The modification of the inlet width, drastically affects the magnitude and direction of the (FC) mass flow. At very small inlet widths, pressure waves are generated on both ends of the (FC's), generating high levels of noise which affects the net momentum acting onto the (MC) incoming jet. The variation of the (MC) outlet width, affects mostly the (FO) output amplitude, from all cases studied, the highest outlet width generates the smallest stagnation pressure peak to peak amplitude, the smallest peak to peak net momentum, the smallest peak to peak (FO) output mass flow, the smallest peak to peak inlet angle amplitude and the smallest (FC) mass flow amplitude.

As the (MC) outlet angle increases, the average stagnation pressure at the (MC) converging walls, as well as its peak to peak amplitude decreases, a reduction of all peak to peak parameters is observed. In general it can be said that, the trend defined by the (MC) outlet converging walls stagnation pressure amplitude, is followed by the amplitude of the rest of the variables, the (MC) inlet angle, the net momentum applied to the (MC) incoming jet, the (FO) output mass flow and the (FC) mass flow.High frequencies are linked with high stagnation pressure values. Oscillator mass flow amplitude directly depends on the reverse flow appearing at the (FO) outlets. Reverse flow is particularly high at lowest outlet widths.

Supplementary Materials: The following are available online at https://zenodo.org/record/3725490. A set of sixteen videos introducing the flow and pressure distribution at Reynolds number 16,034, and characterizing the different extreme cases initially described in Figure 4 for the maximum and minimum inlet width, Figure 8 for the maximum and minimum outlet width, Figure 11 characterizing the maximum and minimum outlet angle and Figure 14 for the maximum and minimum inlet angle, are also provided.

Author Contributions: Conceptualization, M.B. and J.M.B.; methodology, M.B. and J.M.B.; software, M.B.; validation, M.B.; formal analysis, M.B. and J.M.B.; investigation, M.B. and J.M.B.; data curation, M.B.; writing—original draft preparation, M.B. and J.M.B.; writing—review and editing, M.B. and J.M.B.; visualization, M.B. and J.M.B.; supervision, J.M.B.; project administration, J.M.B.; funding acquisition, J.M.B. All authors have read and agreed to the published version of the manuscript.

Funding: This work was supported by the Spanish and Catalan Governments under grants FIS2016-77849-R and 2017-SGR-00785, respectively. Part of the computations were done in the Barcelona Supercomputing Center under grants FI-2016-3-0038, FI-2017-2-0020, FI-2017-3-0009, FI-2018-3-0036 and FI-2019-1-0017.

Conflicts of Interest: The authors declare no conflicts of interest.

References

1. Bobusch, B.C.; Woszidlo, R.; Bergada, J.; Nayeri, C.N.; Paschereit, C.O. Experimental study of the internal flow structures inside a fluidic oscillator. *Exp. Fluids* **2013**, *54*, 1559. [CrossRef]
2. Vatsa, V.; Koklu, M.; Wygnanski, I. Numerical simulation of fluidic actuators for flow control applications. In Proceedings of the 6th AIAA Flow Control Conference, New Orleans, LO, USA, 25 June 2012; p. 3239.
3. Ostermann, F.; Woszidlo, R.; Nayeri, C.; Paschereit, C.O. Experimental comparison between the flow field of two common fluidic oscillator designs. In Proceedings of the 53rd AIAA Aerospace Sciences Meeting, Kissimmee, FL, USA, 9 January 2015; p. 0781.
4. Aram, S.; Lee, Y.T.; Shan, H.; Vargas, A. Computational Fluid Dynamic Analysis of Fluidic Actuator for Active Flow Control Applications. *AIAA J.* **2018**, 111–120. [CrossRef]

5. Woszidlo, R.; Ostermann, F.; Nayeri, C.; Paschereit, C. The time-resolved natural flow field of a fluidic oscillator. *Exp. Fluids* **2015**, *56*, 125. [CrossRef]
6. Gaertlein, S.; Woszidlo, R.; Ostermann, F.; Nayeri, C.; Paschereit, C.O. The time-resolved internal and external flow field properties of a fluidic oscillator. In Proceedings of the 52nd Aerospace Sciences Meeting, National Harbor, MD, USA, 17 January 2014; p. 1143.
7. Slupski, B.Z.; Kara, K. Effects of Geometric Parameters on Performance of Sweeping Jet Actuator. In Proceedings of the 34th AIAA Applied Aerodynamics Conference, Washington, DC, USA, 17 June 2016; p. 3263.
8. Wang, S.; Baldas, L.; Colin, S.; Orieux, S.; Kourta, A.; Mazellier, N. Experimental and numerical study of the frequency response of a fluidic oscillator for active flow control. In Proceedings of the 8th AIAA Flow Control Conference, Washington, DC, USA, 17 June 2016; p. 4234.
9. Pandey, R.J.; Kim, K.Y. Numerical modeling of internal flow in a fluidic oscillator. *J. Mech. Sci. Technol.* **2018**, *32*, 1041–1048. [CrossRef]
10. Seo, J.; Zhu, C.; Mittal, R. Flow Physics and Frequency Scaling of Sweeping Jet Fluidic Oscillators. *AIAA J.* **2018**, *56*, 2208–2219. [CrossRef]
11. Bobusch, B.C.; Woszidlo, R.; Krüger, O.; Paschereit, C.O. Numerical Investigations on Geometric Parameters Affecting the Oscillation Properties of a Fluidic Oscillator. In Proceedings of the 21st AIAA Computational Fluid Dynamics Conference, San Diego, CA, USA, 24 June 2013; p. 2709.
12. Baghaei, M.; Bergada, J.M. Analysis of the forces driving the oscillations in 3D fluidic oscillators. *Energies* **2019**, *12*, 4720. [CrossRef]
13. Spalart, P.R. Detached-eddy simulation. *Annu. Rev. Fluid Mech.* **2009**, *41*, 181–202. [CrossRef]
14. Spalart, P.R. Strategies for turbulence modelling and simulations. *Int. J. Heat Fluid Flow* **2000**, *21*, 252–263. [CrossRef]
15. Spalart, P.R.; Deck, S.; Shur, M.L.; Squires, K.D.; Strelets, M.K.; Travin, A. A new version of detached-eddy simulation, resistant to ambiguous grid densities. *Theor. Comput. Fluid Dyn.* **2006**, *20*, 181. [CrossRef]
16. Spalart, P.R. Comments on the feasibility of LES for wings, and on a hybrid RANS/LES approach. In Proceedings of the First AFOSR International Conference on DNS/LES. Greyden Press, Ruston, LO, USA, 4 August 1997.
17. Spalart, P.; Allmaras, S. A one-equation turbulence model for aerodynamic flows. In Proceedings of the 30th Aerospace Sciences Meeting and Exhibit, Reno, NV, USA, 6 January 1992; p. 439.
18. Wu, Y.; Yu, S.; Zuo, L. Large eddy simulation analysis of the heat transfer enhancement using self-oscillating fluidic oscillators. *Int. J. Heat Mass Transf.* **2019**, *131*, 463–471. [CrossRef]

Appendix B

Published conference papers

The followings are the papers published in the ICCFD international conference and the CMMSE international conference:

1. Baghaei, Masoud, Josep M. Bergada, David Del Campo, and Vanessa Del Campo. ”Research on fluidic amplifiers dimensional modifications via computer simulation (CFD).” In 9th International Conference on Computational Fluid Dynamics, ICCFD9, Istanbul, Turkey, July 11-15, 2016: proceedings, pp. 1-10. Istanbul Tecnical University, 2016.

2. Baghaei, Masoud, Josep Maria Bergadà Granyó, and David del Campo Sud. ”Fluidic actuator performance variation via internal dimensions modifications.” In Proceedings of the 17th International Conference on Computational and Mathematical Methods in Science and Engineering, CMMSE 2017, Costa Ballena (Rota), Cádiz, Spain, July 4-8, 2017, pp. 166-176. 2017.

Attention¡¡

The pages from 132 to the end of the thesis, must be consulted on the website of the corresponding conferences

#1: https://iccfd9.itu.edu.tr/assets/pdf/papers/ICCFD9-2016-256.pdf

#2:http://cmmse.usal.es/cmmse2018/sites/default/files/volumes/Proceedings_CMMSE_2017_vol_1_6.pdf